U.PORTO

FEUP FACULDADE DE ENGENHARIA
UNIVERSIDADE DO PORTO

Thesis Submitted To Faculdade De Engenharia Da Universidade Do Porto As A Requirement To Obtain The MSc Degree In Mechanical Engineering

Crash And Explicit Dynamic Analysis of Lightweight Structures For BEV

Author:
Ana Isabel de Jesus Pinheiro

Under the supervision of:
Professor José Joaquim da Mota Machado (FEUP)
Miguel Couto Aires (Continental Engineering Services)

Under the co-supervision of:
Professor Marco Paulo Lages Parente (FEUP)

Porto, July 2023

Agradecimentos

Como autora deste trabalho gostaria de agradecer, em primeiro lugar, aos meus orientadores e co-orientador para o desenvolvimento do mesmo, o Professor José Machado, o Engenheiro Miguel Aires e o Professor Marco Parente. O tempo, apoio e aconselhamento que me disponibilizaram no decorrer da execução deste projeto foi algo essencial para a sua conclusão. Foi um gosto trabalhar com os três.

Um obrigada aos meus colegas de equipa durante este período que passei na Continental Engineering Services, onde fui tão bem recebida. Qualquer dúvida que tivesse relativamente ao meu trabalho foi prontamente explicada, tal como qualquer outra curiosidade minha relativa a algum projeto a cargo de outrém. Espero que nos voltemos a encontrar no futuro.

Aos meus amigos, que me acompanharam durante estes cinco anos, gostaria de agradecer pela vossa constante presença nas mais diversas aventuras que esta curta etapa nos trouxe. Que a finitude da mesma não se traduza no término das memórias que já fizemos e que continuaremos a fazer pela vida, enquanto testemunhamos o sucesso de uns dos outros, a todos os níveis.

Ao meu maior suporte, Pedro, obrigada por toda a paciência, motivação e confiança que me dás sempre que duvido de mim e do quão longe as minhas capacidades me levarão. Foste uma peça essencial para o culminar do meu percurso enquanto estudante e enquanto autora desta dissertação.

Por último, gostaria de agradecer aos meus pais, Maria de Jesus e António Pinheiro, aos quais dedico este trabalho. A pessoa que sou resulta do vosso constante carinho, apoio e motivação. Um muito obrigada por personificarem o meu motor de inspiração e força, sem o qual seria impossível quer o início, quer a conclusão desta fase.

Abstract

Crashworthiness, in the automotive industry meaning the vehicle's structural ability to plastically deform and absorb abrupt impact loads while still providing enough survival room for the occupants, is a key aspect for any automobile. However, this term achieves new importance when referring to Electric Vehicles (EVs), which have found significant commercial success in recent years.

The potential crash of an EV, particularly a Battery Electric Vehicle (BEV), could entail the occurrence of severe mechanical, thermal, and electric stresses to the battery of the vehicle. If this is the case, hazardous phenomena will likely originate in the energy storage system, thereby posing a serious threat to passenger safety. This concern is prioritised by consumers, oftentimes superseding considerations on the environmental impact or long-term cost savings associated with BEVs.

Alongside the employment of safer and more reliable batteries, a matter governed by suitable regulations and the subject of extensive ongoing research, it is also crucial to develop mechanically efficient battery protection structures, often termed Battery Pack Enclosures (BPEs). In an impact scenario, the battery components' well-being is influenced by the chosen battery housing solution. The structural properties of BPEs should be coupled with low density, as the battery pack assembly is the principal contributor to the overall weight of a BEV. Thus, the latter parameter must be minimised in the BPE to reduce energy consumption and further enhance the vehicle's driving range.

In this thesis, the study of a realistic model inspired by a prominent industry solution is performed by resorting to the Finite Element Method (FEM). Subsequently, optimised models, considering weight reduction and crashworthiness abilities, are proposed and analysed. In one case, the improved model involves replacing the aluminium alloy BPE structure with one made from ABS and in another metallic foams are utilised. The efficiency of the various BPE solutions is then evaluated under real-life Euro NCAP crash test conditions using explicit dynamics analyses and complemented by other analysis techniques.

Keywords - Battery Electric Vehicles, Battery Pack Enclosure, Structural Analysis, Crash, Explicit Dynamic Simulation, FEM.

Resumo

A capacidade inerente a um veículo automóvel de absorver cargas de impacto abruptas e deformar-se plasticamente enquanto assegura o espaço necessário à sobrevivência dos ocupantes, é um aspeto fundamental para qualquer automóvel. No entanto, esta habilidade adquire renovada importância quando se tratam de veículos elétricos, que têm alcançado um sucesso comercial significativo nos últimos anos.

Uma potencial colisão envolvendo um automóvel da referida classe, especialmente um veículo elétrico a baterias, poderia resultar em elevadas cargas mecânicas, térmicas e elétricas na bateria do mesmo. Se tal ocorrer, é possível que fenómenos perigosos surjam no componente de armazenamento energético, o que representa uma séria ameaça à segurança dos passageiros. Esta preocupação é evidentemente priorizada pelos consumidores, superando muitas vezes considerações sobre o impacto ambiental ou economias financeiras a longo prazo, algo tipicamente associadas aos veículos elétricos a baterias.

Para além da utilização de baterias mais seguras e confiáveis, área governada por regulamentações adequadas e a sujeita de pesquisa extensiva, é igualmente crucial desenvolver estruturas de proteção de bateria, frequentemente denominadas "compartimentos de baterias", mecanicamente eficientes. Note-se que a saúde dos componentes da bateria em cenários de impacto muitas vezes depende ativamente da solução escolhida para o invólucro da bateria. Adicionalmente, as propriedades estruturais dos mesmos devem estar associadas a uma baixa densidade, uma vez que a bateria, e todos os componentes a ela associados, é o principal contribuinte para o peso total de um veículo elétrico. Assim, este parâmetro deve ser minimizado no referido componente estrutural, de forma a reduzir o consumo energético e, consequentemente, aumentar a autonomia do veículo.

Nesta tese, é realizado o desenvolvimento e estudo de um modelo realista inspirado numa solução proeminente da indústria automóvel utilizando o método dos elementos finitos. Depois, segue-se a proposta e análise de modelos otimizados, considerando reduções de peso e sem detrimento para o nível de segurança às mesmas associado. Os modelos aprimorados envolvem, num caso, a substituição da estrutura do compartimento da bateria, originalmente em liga de alumínio, por uma feita de ABS e, noutro caso, a utilização de espumas metálicas. A avaliação dos diversos modelos, em condições de testes de colisão do Euro NCAP, é conduzida via análises dinâmicas explícitas, complementadas por outras técnicas de análise.

Palavras-Chave - Veículo Elétrico a Bateria, Compartimento da Bateria, Análise Estrutural, Crash, Simulação Dinâmica Explícita, Método dos Elementos Finitos.

Contents

List of Acronyms **xix**

List of Notations **xxi**

1 Introduction **1**
1.1 Background and Motivation . . . 1
1.2 Purpose and Novelty of the Thesis . . . 2
1.3 Contextualisation of the Thesis in Continental Engineering Services . . . 3
1.4 Structure of the Thesis . . . 3

2 Scientific Review **5**
2.1 Importance of Crashworthiness Assessment in EVs . . . 5
2.2 Crashworthiness Testing . . . 11
2.2.1 Crashworthiness Testing Historical Assessment . . . 11
2.2.2 Euro NCAP Crash Tests . . . 12
2.2.3 Crashworthiness Testing of Electric Vehicles . . . 14
2.2.3.1 Recent Research on Crashworthiness Testing on EVs . . . 15
2.3 Crashworthiness Analysis Using the Finite Element Method . . . 16
2.3.1 The Origin of the Finite Element Method . . . 16
2.3.2 Finite Element Method in Dynamic Analysis . . . 17
2.3.3 Recent Research on Crashworthiness FEM Simulation on EVs . . . 18
2.3.3.1 Crashworthiness Analysis in FEM at Vehicle Level . . . 19
2.3.3.2 Crashworthiness Analysis in FEM at Battery Pack Level . . . 20
2.3.3.3 Research Gaps and Future Directions . . . 22

3 Fundamentals of Solid Mechanics **25**

4 Fundamentals of the Finite Element Method **29**
4.1 Finite Element Method . . . 29
4.1.1 Principal of Minimum Potential Energy . . . 31
4.1.2 Formulation of Finite Element Equations . . . 32
4.1.3 Mesh Generation . . . 35
4.1.4 Numerical Integration . . . 38
4.2 Dynamic Analysis in FEM . . . 39
4.2.1 Time discretisation . . . 41
4.2.2 Explicit Integration Method . . . 42
4.2.2.1 Central Difference Integration . . . 42
4.2.2.2 Stability Condition and Time Step Size . . . 44
4.2.2.3 Mass Scaling . . . 46

4.2.2.4 Lumped Mass Matrix 47

5 Electric Vehicle and Battery Design 49
5.1 Battery Electric Vehicles 49
5.1.1 Environmental impact of the BEV 52
5.1.2 Cost Structure of the BEV 54
5.1.3 Charging times and infrastructure of the BEV 55
5.1.4 Energy and power densities of the BEV 56
5.2 Battery Pack Enclosure 60
5.2.1 Design of the Battery Pack Enclosure 62
5.2.2 Battery Pack Placement and Fixation 65
5.2.3 Materials of the Battery Pack Enclosure 66
5.2.3.1 Aluminium in Battery Pack Enclosure Manufacturing 69
5.2.3.2 Steel in Battery Pack Enclosure Manufacturing 72
5.2.3.3 Composites in Battery Pack Enclosure Manufacturing 72
5.2.4 Summary of State-of-the-art Battery Pack Enclosure Solutions 74

6 Numerical Analysis Procedure 77
6.1 Industry Inspiration for the Study 79
6.1.1 Battery Pack Enclosure Structure 80
6.1.2 Battery Pack Enclosure Model 84
6.1.2.1 Model Geometry: Design Parameters 84
6.1.2.2 Assumptions and Limitations 87
6.1.2.3 Battery Pack Enclosure Model Materials 89
6.1.2.4 Body Connections 91
6.1.2.5 Mesh Metrics 92
6.2 Static Structural Analysis 93
6.3 Modal Analysis 95
6.3.1 Modal analysis: Theoretical Context 95
6.3.2 Modal analysis: Analysis Settings 96
6.4 Transient Structural Analysis 99
6.4.1 Transient structural analysis: theoretical context 99
6.4.2 Transient Structural Analysis: Analysis Settings 100
6.4.2.1 Acceleration Pulse 101
6.5 Explicit Dynamic Analysis 104
6.5.1 Explicit Dynamics Analysis: analysis settings 104
6.5.1.1 Side Pole Test 104

7 Convergence Study 111
7.1 Partial Penetration of a Bullet to a Wall 112
7.1.1 Geometry, Boundary and Load Conditions 112
7.1.2 Mechanical Properties 113
7.1.3 Mesh Discretisation 114
7.1.4 Explicit Analysis Settings Definition 115
7.1.5 Convergence Results 116
7.1.5.1 Directional Deformation in x axis 116
7.1.5.2 Equivalent von Mises Stress 118
7.1.5.3 Internal Energy 120
7.1.5.4 Hourglass energy 120

7.1.5.5 Simulation Elapsed Time . . . 121

8 Phase 1: Original Geometry in Al 6061-T6 123
8.1 Phase 1: Static Analysis . . . 124
8.1.1 Total and Directional Deformation . . . 126
8.1.2 Equivalent von Mises Stress . . . 128
8.2 Phase 1: Modal Analysis . . . 129
8.2.1 Natural Mode Shapes: Deformation . . . 131
8.3 Phase 1: Transient Analysis . . . 133
8.3.1 Total and Directional Deformation . . . 133
8.3.2 Equivalent von Mises Stress . . . 137
8.3.3 Equivalent von Mises Strain . . . 138
8.4 Phase 1: Explicit Dynamics Analysis . . . 139
8.4.1 Side Impact at 32 km/h . . . 140
8.4.1.1 Total and Directional Deformations . . . 141
8.4.1.2 Equivalent von Mises Stress . . . 147
8.4.1.3 Equivalent Elastic Strain and Equivalent Plastic Strain . . . 150
8.4.2 Side Impact at 100 km/h . . . 151
8.4.2.1 Total and Directional Deformations . . . 152
8.4.2.2 Equivalent von Mises Stress . . . 157
8.4.2.3 Equivalent Elastic Strain and Equivalent Plastic Strain . . . 159

9 Phase 2: Original Geometry with ABS 163
9.1 Phase 2: ABS Material Properties . . . 163
9.2 Phase 2: Static Analysis . . . 165
9.2.1 Total and Directional Deformation . . . 165
9.2.2 Equivalent von Mises Stress . . . 166
9.3 Phase 2: Modal analysis . . . 167
9.3.1 Natural Mode Shapes: Deformation . . . 167
9.4 Phase 2: Transient Analysis . . . 169
9.4.1 Total and Directional Deformation . . . 169
9.4.2 Equivalent von Mises Stress . . . 173
9.4.3 Equivalent von Mises Strain . . . 174
9.5 Phase 2: Explicit Dynamics Analysis . . . 175
9.5.1 Side Impact at 32 km/h . . . 175
9.5.1.1 Total and Directional Deformations . . . 176
9.5.1.2 Equivalent von Mises Stress . . . 182
9.5.1.3 Equivalent Elastic Strain and Equivalent Plastic Strain . . . 184
9.5.2 Side Impact at 100 km/h . . . 185
9.5.2.1 Total and Directional Deformations . . . 187
9.5.2.2 Equivalent von Mises Stress . . . 192
9.5.2.3 Equivalent Elastic Strain and Equivalent Plastic Strain . . . 193

10 Phase 3: Multimaterial Honeycomb Geometry 197
10.1 Phase 3: Novel Geometry and Al-SiC Material Properties . . . 197
10.2 Phase 3: Static Analysis . . . 201
10.2.1 Total and Directional Deformation . . . 203
10.2.2 Equivalent von Mises Stress . . . 205
10.3 Phase 3: Modal Analysis . . . 206

10.3.1 Natural Mode Shapes: Deformation 208
10.4 Phase 3: Transient Analysis 209
10.4.1 Total and Directional Deformation 209
10.4.2 Equivalent von Mises Stress 212
10.4.3 Equivalent von Mises Strain 213
10.5 Phase 3: Explicit Dynamics Analysis 214
10.5.1 Side Impact at 32 km/h 215
10.5.1.1 Total and directional deformation 215
10.5.1.2 Equivalent von Mises Stress 220
10.5.1.3 Equivalent von Mises Strain 222
10.5.2 Side Impact at 100 km/h 223
10.5.2.1 Total and Directional Deformations 224
10.5.2.2 Equivalent von Mises Stress 230
10.5.2.3 Equivalent Elastic Strain and Equivalent Plastic Strain . . . 231

11 Conclusions **235**

List of Figures

2.1 Euro NCAP "Full-Width Rigid Barrier" frontal crash test on the Tesla Model X [23]. 14
2.2 Flowchart indicating the preparation and assessment process of high voltage vehicles (Adapted from [26]). 15
2.3 Examples of FEM models elaborated to evaluate the EV crash behaviour. **(a)** Full frontal barrier crash against a rigid impact wall at 50 km/h [64]. **(b)** Frontal pole test with rigid pole at 50 km/h [60] 20
2.4 Examples of FEM models elaborated to evaluate the battery pack's and BPE's behaviour in crash situations. **(a)** Effective stress on the battery pack model after the crash simulation [66]. **(b)** Stress and displacement, respectively, distributions in the battery pack under bump, acceleration, deceleration, and turning conditions [68]. **(c)** Deformed models of empty packs (rectangular, hexagonal, and trapezoidal, respectively) under dynamic impacts [65]. 21

3.1 Two-dimensional representation of an infinitesimal element of a body, with stresses and body forces (Adapted from [71]). 26

4.1 Iterative modelling approach based on numerical approximations of physical problems (Adapted from [74]). 30
4.2 Continuous body subjected to body and surface forces (Adapted from [76]). . 31
4.3 1D elements and respective local degrees of freedom. **(a)** Two-noded generalised rod element. **(b)** Two-noded generalised beam element. **(c)** Two-noded generalised frame element. 36
4.4 Linear and quadratic, Serendipity and Lagrange 2D elements (left, centre and right) **(a)** Triangular elements. **(b)** Quadrangular elements. 37
4.5 Linear and quadratic 3D elements (left and right). **(a)** Tetrahedron elements. **(b)** Hexahedron elements. 37
4.6 Time integration events (Adapted from [81]). 43
4.7 Explicit finite element algorithm (Adapted from [81]). 44
4.8 Characteristic length for critical time step calculation in beam element, shell element, and solid element (left, centre and right) (Adapted from [80]). 46

5.1 Vehicle spectrum with regards to propulsion device, energy source, and corresponding utilisation level (Adapted from [84]). 50
5.2 Diagram of a BEV's powertrain (Adapted from [87]). 50
5.3 Sales and registrations of electric cars in China, US, Europe, and other regions, from 2016 to 2021 [88]. 51
5.4 Greenhouse gas emissions from transport sectors in the EU, by transport mode and scenario (Adapted from [3]). 53

5.5 Comparison of the environmental footprint of an ICEV and an EV, based on CO_2 emissions during production and over the entire lifespan [87]. 54
5.6 Cost structure of present-day and future BEVs, in comparison to ICEVs (Adapted from [94]). 55
5.7 Schematic illustration of a battery pack and its main components [97]. 57
5.8 Ragone plot of various battery technologies with specification at the cell level for automotive applications without lithium-sulfur, and metal-air batteries [7]. SuperCap: supercapacitor; Pb: lead; Li-ion: lithium-ion; NiCd: nickel-cadmium; NiMH: nickel–metal hydride; NaNiCl2: sodium–nickel chloride; ZEBRA: Zero Emission Battery Research Activities. 58
5.9 Various cell shapes: cylindrical, prismatic and pouch (left, centre and right) [7]. 59
5.10 Stresses arising during LIB exploitation (Adapted from [1]). 60
5.11 Functional tree diagram of the battery pack enclosure (Adapted from [103]). . 61
5.12 Battery packs of state-of-the-art of commercial EVs [105]. **(a)** Audi Q4 e-tron Quattro. **(b)** BMW iX xDrive40. **(c)** Chevrolet Bolt Premier. **(d)** Dacia Spring Comfort Plus. **(e)** Nissan Ariya B6 Variant. **(f)** Tesla Model 3 Long Range RWD. . 63
5.13 Safety zones based on data from vehicle intrusions from accidents and laboratory tests (Adapted from [107]). 65
5.14 Battery pack positioning in a Nissan Leaf [102]. 66
5.15 Materials used in battery pack enclosure of state-of-the-art commercial car and their range (Adapted from [108]). 68
5.16 Drivers for material selection and lightweight design (Adapted from [108]). . . 69
5.17 Material plot of aluminium alloys used in the automotive industry, in terms of tensile yield strength and elongation (Adapted from [117]). 71
5.18 Properties of fibre-reinforced polymers set side by side with those of steel, aluminium, and wood (*for a fibre orientation of $0/\pm 45 = 1/1$) (Adapted from [123]). 73

6.1 Structure of the numerical portion of the work being performed. 78
6.2 Industry inspiration for the battery pack enclosure in this study [105]. **(a)** Battery protection structure fully closed. **(b)** Battery protection structure without the top cover. **(c)** Position of the battery pack (enclosure) in the vehicle. 81
6.3 Attachment of the battery pack enclosure to the rocker panel (and cross-section of the latter) [128]. 82
6.4 Battery pack tier-down, considering its main components [105]. 83
6.5 Battery modules used in the industry inspiration for this study [105]. **(a)** A module unit. **(b)** Positioning of the fifteen modules within the BPE. 84
6.6 CAD of the BPE structure. **(a)** Battery protection structure fully closed. **(b)** Battery protection structure without the top cover. 84
6.7 Dimensions of the CAD of the battery pack enclosure. **(a)** Top view. **(b)** Frontal view. 86
6.8 Attribution of a distributed mass in the bottom surface of the module cavities to represent their presence in the BPE. 88
6.9 Al 6061-T6: Steinberg-Guinan strength (Adapted from [129]). 90
6.10 Al 6061-T6: shock EOS linear (Adapted from [129]). 91
6.11 Loads and boundary conditions defined for the static analyses. 94
6.12 Natural response of an undamped system (Adapted from [133]). 96
6.13 Loads and boundary conditions defined for the modal analyses. 97
6.14 Half-sine wave transient solicitation (Adapted from [133]). 99

6.15 Pulse shape and limits of tolerance for a half-sine pulse [136]. 101
6.16 Acceleration profile applied in the model. 102
6.17 Loads and boundary conditions defined for the transient analyses. 103
6.18 Rigid pole configuration and positioning. 105
6.19 Distance in between the rocker panel and the rigid pole. 105
6.20 Loads and boundary conditions defined for the explicit dynamic analyses. . . 107

7.1 Validation and verification concept (Adapted from [140]). 111
7.2 Geometry of the studied problem [140]). 113
7.3 Addressed mesh discretisations in the impacted wall. **(a)** Mesh discretisation 1 (coarsest mesh used). **(b)** Mesh discretisation 2. **(c)** Mesh discretisation 3. **(d)** Mesh discretisation 4 (more refined mesh). 115
7.4 Directional deformation in the x axis found in the back face of the impacted wall: lateral (on the left) and frontal (on the right) view. **(a)** Mesh discretisation 1 (coarsest mesh used). **(b)** Mesh discretisation 2. **(c)** Mesh discretisation 3. **(d)** Mesh discretisation 4. 117
7.5 Maximum directional deformation, on the x axis, in the impacted wall (central node) through time. 118
7.6 Equivalent von Mises stress found in the back face of the impacted wall. **(a)** Mesh discretisation 1 (coarsest mesh used). **(b)** Mesh discretisation 2. **(c)** Mesh discretisation 3. **(d)** Mesh discretisation 4. 119
7.7 Maximum equivalent stress in the back face of the impacted wall (central node), for each of the four discretisations. 119
7.8 Internal energy of the impacted wall through time. 120
7.9 Hourglass energy of the impacted wall through time. 121
7.10 Total elapsed run time for each simulation. 122

8.1 Static analysis of Phase 1: mesh applied in the model. **(a)** BPE with cover. **(b)** BPE without cover. **(c)** Bottom case detail. **(d)** Rock panel and top cover detail. . 125
8.2 Static analysis of Phase 1: total deformation of the BPE (scale of 3600). **(a)** BPE with cover. **(b)** BPE without cover. 127
8.3 Static Analysis of Phase 1: directional deformation in y (true scale). 127
8.4 Static analysis of Phase 1: equivalent von Mises stress (true scale). **(a)** BPE with cover. **(b)** BPE without cover. 128
8.5 Static analysis of Phase 1: the most stressed region (true scale). 129
8.6 Modal analysis of Phase 1: mesh applied in the model. **(a)** BPE with cover. **(b)** BPE without cover. **(c)** Top cover and rocker panels detail. 130
8.7 Modal analysis of Phase 1: natural mode shapes coupled with the first six natural frequencies (scale of 20). **(a)** 113.85 Hz. **(b)** 145.24 Hz. **(c)** 148.05 Hz. **(d)** 169.2 Hz. **(e)** 172.05 Hz. **(f)** 172.05 Hz. 132
8.8 Transient analysis of Phase 1: total deformation distribution in the BPE and rocker panels (scale of 1000). **(a)** BPE with cover. **(b)** BPE without cover. . . . 133
8.9 Transient analysis of Phase 1: total deformation distribution at the component level (true scale). **(a)** Bottom case **(b)** Top cover. **(c)** Reinforcements. **(d)** Rocker panel. 135
8.10 Transient analysis of Phase 1: directional deformation distribution in y, at the global and component levels (true scale). **(a)** BPE with cover. **(b)** BPE without cover. **(c)** Bottom case. **(d)** Top cover. **(e)** Reinforcements. **(f)** Rocker panel. . . . 136

8.11 Transient analysis of Phase 1: equivalent von Mises stress distribution in the BPE and rocker panels (scale of 1000). **(a)** BPE with cover. **(b)** BPE without cover. 137
8.12 Transient analysis of Phase 1: equivalent von Mises stress at the component level (true scale). **(a)** Bottom case **(b)** Top cover. **(c)** Reinforcements. **(d)** Rocker panel. 138
8.13 Transient analysis of Phase 1: equivalent von Mises strain distribution in the BPE and rocker panels (true scale). **(a)** BPE with cover. **(b)** BPE without cover. 139
8.14 Explicit analysis of Phase 1, at 32 km/h: energy summary. 141
8.15 Explicit dynamic analysis of Phase 1, at 32 km/h: an overview of the deformation of the BPE in time frames (scale of 2). **(a)** $t = 0$ s. **(b)** $t = 2.5e-3$ s. **(c)** $t = 5e-3$ s. **(d)** $t = 7.5e-3$ s. **(e)** $t = 1e-2$ s. 142
8.16 Explicit dynamic analysis of Phase 1, at 32 km/h: a frontal view of the deformation of the BPE, in the $z-y$ plane, in time frames (scale of 2). **(a)** $t = 0$ s. **(b)** $t = 2.5e-3$ s. **(c)** $t = 5e-3$ s. **(d)** $t = 7.5e-3$ s. **(e)** $t = 1e-2$ s. . . 143
8.17 Explicit dynamics analysis of Phase 1, at 32 km/h: the intrusion of the pole into the automotive structure (true scale). **(a)** Global view. **(b)** Deformation in the z direction. 144
8.18 Explicit dynamics analysis of Phase 1, at 32 km/h: total deformation distribution at global and component levels (true scale). **(a)** BPE with top cover. **(b)** BPE without top cover. **(c)** Bottom case. **(d)** Top cover. **(e)** Reinforcements. **(f)** Rocker panel. 145
8.19 Explicit dynamics analysis of Phase 1, at 32 km/h: directional deformation distribution in the y direction at a global level (true scale). **(a)** BPE with top cover. **(b)** BPE without top cover. 146
8.20 Explicit dynamics analysis of Phase 1, at 32 km/h: directional deformation distribution in the y direction at the component level (true scale). **(a)** Bottom case. **(b)** Top cover. **(c)** Reinforcements. **(d)** Rocker panel. 147
8.21 Explicit dynamics analysis of Phase 1, at 32 km/h: equivalent von Mises stress (true scale). **(a)** BPE with top cover. **(b)** BPE without top cover. 148
8.22 Explicit dynamics analysis of Phase 1, at 32 km/h: equivalent von Mises stress (true scale). **(a)** Bottom case. **(b)** Top cover. **(c)** Reinforcements. **(d)** Rocker panel that endures the impact. 149
8.23 Explicit dynamics analysis of Phase 1, at 32 km/h: equivalent von Mises strain (true scale). **(a)** Rocker panels and BPE. **(b)** Exclusively the BPE structure. . . . 150
8.24 Explicit dynamics analysis of Phase 1, at 32 km/h: plastic strain (true scale). **(a)** Rocker panels and BPE. **(b)** Rocker panel cross-section. 150
8.25 Explicit analysis of Phase 1, at 100 km/h: energy summary. 151
8.26 Explicit dynamic analysis of Phase 1, at 100 km/h: overview of the deformation of the BPE in time frames (scale of 2). **(a)** $t = 0$ s. **(b)** $t = 2.5e-3$ s. **(c)** $t = 5e-3$ s. **(d)** $t = 7.5e-3$ s. **(e)** $t = 1e-2$ s. 153
8.27 Explicit dynamic analysis of Phase 1, at 100 km/h: overview of the deformation of the BPE, in the $z-y$ plane, in time frames (scale of 2). **(a)** $t = 0$ s. **(b)** $t = 2.5e-3$ s. **(c)** $t = 5e-3$ s. **(d)** $t = 7.5e-3$ s. **(e)** $t = 1e-2$ s. 154
8.28 Explicit dynamics analysis of Phase 1, at 100 km/h: intrusion of the pole into the automotive structure (true scale). **(a)** Global view. **(b)** Deformation in the z direction. 155

8.29 Explicit dynamics analysis of Phase 1, at 100 km/h: total deformation distribution at global and component levels (true scale). **(a)** BPE with top cover. **(b)** BPE without top cover. **(c)** Bottom case. **(d)** Top cover. **(e)** Reinforcements. **(f)** Rocker panel. 156
8.30 Explicit dynamics analysis of Phase 1, at 100 km/h: directional deformation distribution in the y direction at the global and component levels (true scale). **(a)** BPE with top cover. **(b)** BPE without top cover. **(c)** Bottom case. **(d)** Top cover. **(e)** Reinforcements. **(f)** Rocker panel. 157
8.31 Explicit dynamics analysis of Phase 1, at 100 km/h: equivalent von Mises stress (true scale). **(a)** BPE with top cover. **(b)** BPE without top cover. 158
8.32 Explicit dynamics analysis of Phase 1, at 100 km/h: equivalent von Mises stress (true scale). **(a)** Bottom case. **(b)** Top cover. **(c)** Reinforcements. **(d)** Rocker panel that endures the impact. 158
8.33 Explicit dynamics analysis of Phase 1, at 100 km/h: equivalent von Mises strain (true scale). **(a)** Rocker panels and BPE. **(b)** Exclusively the BPE structure. 159
8.34 Explicit dynamics analysis of Phase 1, at 100 km/h: plastic strain (true scale). **(a)** Exterior region of the impacted rocker panel. **(b)** Exclusively the BPE structure. **(c)** Rocker panel cross-section. 160

9.1 ABS stress-strain relationship, true and engineering curves (Adapted from [144]).164
9.2 Static analysis of Phase 2: total deformation of the BPE (scale of 360). **(a)** BPE with cover. **(b)** BPE without cover. 166
9.3 Static Analysis of Phase 2: directional deformation in y (true scale). 166
9.4 Static analysis of Phase 2: equivalent von Mises stress (true scale). **(a)** BPE with cover. **(b)** BPE without cover. **(c)** Most stressed region. 167
9.5 Modal analysis of Phase 2: natural mode shapes coupled with the first six natural frequencies (scale of 20). **(a)** 25.05 Hz. **(b)** 30.448 Hz. **(c)** 35.678 Hz. **(d)** 41.456 Hz. **(e)** 43.742 Hz. **(f)** 48.957 Hz. 168
9.6 Transient analysis of Phase 2: total deformation distribution in the BPE and rocker panels (scale of 100). **(a)** BPE with cover. **(b)** BPE without cover. 170
9.7 Transient analysis of Phase 2: total deformation distribution at the component level (true scale). **(a)** Bottom case **(b)** Top cover. **(c)** Reinforcements. **(d)** Rocker panel. 171
9.8 Transient analysis of Phase 2: directional deformation distribution in y, at the global and component levels (true scale). **(a)** BPE with cover. **(b)** BPE without cover. **(c)** Bottom case. **(d)** Top cover. **(e)** Reinforcements. **(f)** Rocker panel. . . . 172
9.9 Transient analysis of Phase 2: equivalent von Mises stress distribution in the BPE and rocker panels (scale of 100). **(a)** BPE with cover. **(b)** BPE without cover.173
9.10 Transient analysis of Phase 2: equivalent von Mises stress distribution at the component level (true scale). **(a)** Bottom case. **(b)** Top cover. **(c)** Reinforcements. **(d)** Rocker panel. 174
9.11 Transient analysis of Phase 2: equivalent von Mises strain distribution in the BPE and rocker panels (true scale). **(a)** BPE with cover. **(b)** BPE without cover. 175
9.12 Explicit analysis of Phase 2, at 32 km/h: energy summary. 176
9.13 Explicit dynamic analysis of Phase 2, at 32 km/h: overview of the deformation of the BPE in time frames (scale of 2). **(a)** $t = 0$ s. **(b)** $t = 2.5e-3$ s. **(c)** $t = 5e-3$ s. **(d)** $t = 7.5e-3$ s. **(e)** $t = 1e-2$ s. 177

9.14 Explicit dynamic analysis of Phase 2, at 32 km/h: overview of the deformation of the BPE, in the $z-y$ plane, in time frames (scale of 2). **(a)** $t = 0$ s. **(b)** $t = 2.5e-3$ s. **(c)** $t = 5e-3$ s. **(d)** $t = 7.5e-3$ s. **(e)** $t = 1e-2$ s. 178
9.15 Explicit dynamics analysis of Phase 2, at 32 km/h: intrusion of the pole into the automotive structure (true scale). **(a)** Global view. **(b)** Deformation in the z direction. 179
9.16 Explicit dynamics analysis of Phase 2, at 32 km/h: total deformation distribution at global and component levels (true scale). **(a)** BPE with top cover. **(b)** BPE without top cover. **(c)** Bottom case. **(d)** Top cover. **(e)** Reinforcements. **(f)** Rocker panel. 180
9.17 Explicit dynamics analysis of Phase 2, at 32 km/h: directional deformation distribution in the y direction at global and component levels (true scale). **(a)** BPE with top cover. **(b)** BPE without top cover. **(c)** Bottom case. **(d)** Top cover. **(e)** Reinforcements. **(f)** Rocker panel. 181
9.18 Explicit dynamics analysis of Phase 2, at 32 km/h: equivalent von Mises stress (true scale). **(a)** BPE with top cover. **(b)** BPE without top cover. 182
9.19 Explicit dynamics analysis of Phase 2, at 32 km/h: equivalent von Mises stress (true scale). **(a)** Bottom case. **(b)** Top cover. **(c)** Reinforcements. **(d)** Rocker panel that endures the impact. 183
9.20 Explicit dynamics analysis of Phase 2, at 32 km/h: equivalent von Mises strain (true scale). **(a)** Rocker panels and BPE. **(b)** Bottom view. 184
9.21 Explicit dynamics analysis of Phase 2, at 32 km/h: plastic strain (true scale). **(a)** Rocker panels and BPE. **(b)** Plastic strain in the rocker panel cross-section. 185
9.22 Explicit analysis of Phase 2, at 100 km/h: energy summary. 186
9.23 Explicit dynamic analysis of Phase 2, at 100 km/h: overview of the deformation of the BPE in time frames (scale of 2). **(a)** $t = 0$ s. **(b)** $t = 2.5e-3$ s. **(c)** $t = 5e-3$ s. **(d)** $t = 7.5e-3$ s. **(e)** $t = 1e-2$ s. 187
9.24 Explicit dynamic analysis of Phase 2, at 100 km/h: an overview of the deformation of the BPE, in the $z-y$ plane, in time frames (scale of 2). **(a)** $t = 0$ s. **(b)** $t = 2.5e-3$ s. **(c)** $t = 5e-3$ s. **(d)** $t = 7.5e-3$ s. **(e)** $t = 1e-2$ s. 188
9.25 Explicit dynamics analysis of Phase 2, at 100 km/h: the intrusion of the pole into the automotive structure (true scale). **(a)** Global view. **(b)** Deformation in the z direction. 189
9.26 Explicit dynamics analysis of Phase 2, at 100 km/h: total deformation distribution at global and component levels (true scale). **(a)** BPE with top cover. **(b)** BPE without top cover. **(c)** Bottom case. **(d)** Top cover. **(e)** Reinforcements. **(f)** Rocker panel. 190
9.27 Explicit dynamics analysis of Phase 2, at 100 km/h: directional deformation distribution in the y direction at global and component levels (true scale). **(a)** BPE with top cover. **(b)** BPE without top cover. **(c)** Bottom case. **(d)** Top cover. **(e)** Reinforcements. **(f)** Rocker panel. 191
9.28 Explicit dynamics analysis of Phase 2, at 100 km/h: equivalent von Mises stress (true scale). **(a)** BPE with top cover. **(b)** BPE without top cover. 192
9.29 Explicit dynamics analysis of Phase 2, at 100 km/h: equivalent von Mises stress (true scale). **(a)** Bottom case. **(b)** Top cover. **(c)** Reinforcements. **(d)** Rocker panel that endures the impact. 193
9.30 Explicit dynamics analysis of Phase 2, at 100 km/h: equivalent von Mises strain (true scale). **(a)** Rocker panels and BPE. **(b)** Exclusively the BPE structure. 194

9.31 Explicit dynamics analysis of Phase 2, at 100 km/h: plastic strain (true scale). **(a)** Exterior region of the impacted rocker panel. **(b)** Rocker panel cross-section. 194

10.1 Al-SiC foam stress-strain relationship, true and engineering curves (Adapted from [144]). 198
10.2 Inspiration for the BPE of Phase 3 [128]. 199
10.3 Geometry of the BPE model of Phase 3. **(a)** Top view of the integration of the metal foam component in the BPE. **(b)** Metal foam component with relevant dimensions. 199
10.4 Static analysis of Phase 3: mesh applied in the model. **(a)** BPE with cover. **(b)** BPE without cover. **(c)** Bottom case detail. **(d)** Rock panel and top cover detail. . 203
10.5 Static analysis of Phase 3: total deformation of the BPE (scale of 360). **(a)** BPE with cover. **(b)** BPE without cover. 204
10.6 Static Analysis of Phase 3: directional deformation in y (true scale). 204
10.7 Static analysis of Phase 3: equivalent von Mises stress (true scale). **(a)** BPE with cover. **(b)** BPE without cover. **(c)** Most stressed region. 205
10.8 Modal analysis of Phase 3: mesh applied in the model. **(a)** BPE with cover. **(b)** BPE without cover. **(c)** Top cover and rocker panels detail. 207
10.9 Modal analysis of Phase 3: natural mode shapes coupled with the first six natural frequencies (scale of 20). **(a)** 30.882 Hz. **(b)** 44.121 Hz. **(c)** 51.269 Hz. **(d)** 70.557 Hz. **(e)** 81.014 Hz. **(f)** 103.41 Hz. 208
10.10 Transient analysis of Phase 3: total deformation distribution in the BPE and rocker panels (scale of 100). **(a)** BPE with cover. **(b)** BPE without cover. 209
10.11 Transient analysis of Phase 3: total deformation distribution at the component level (true scale). **(a)** Bottom case **(b)** Top cover. **(c)** Reinforcements. **(d)** Rocker panel. 210
10.12 Transient analysis of Phase 3: directional deformation distribution in y, at the global and component levels (true scale). **(a)** BPE with cover. **(b)** BPE without cover. **(c)** Bottom case. **(d)** Top cover. **(e)** Reinforcements. **(f)** Rocker panel. . . . 211
10.13 Transient analysis of Phase 3: equivalent von Mises stress distribution in the BPE and rocker panels (scale of 100). **(a)** BPE with cover. **(b)** BPE without cover. 212
10.14 Transient analysis of Phase 3: equivalent von Mises stress distribution at the component level (true scale). **(a)** Bottom case. **(b)** Top cover. **(c)** Reinforcements. **(d)** Rocker panel. 213
10.15 Transient analysis of Phase 3: equivalent von Mises strain distribution in the BPE and rocker panels (true scale). **(a)** BPE with cover. **(b)** BPE without cover. 214
10.16 Explicit analysis of Phase 3, at 32 km/h: energy summary. 215
10.17 Explicit dynamic analysis of Phase 3, at 32 km/h: overview of the deformation of the BPE in time frames (scale of 2). **(a)** $t = 0$ s. **(b)** $t = 2.5e-3$ s. **(c)** $t = 5e-3$ s. **(d)** $t = 7.5e-3$ s. **(e)** $t = 1e-2$ s. 216
10.18 Explicit dynamic analysis of Phase 3, at 32 km/h: overview of the deformation of the BPE, in the $z-y$ plane, in time frames (scale of 2). **(a)** $t = 0$ s. **(b)** $t = 2.5e-3$ s. **(c)** $t = 5e-3$ s. **(d)** $t = 7.5e-3$ s. **(e)** $t = 1e-2$ s. 217
10.19 Explicit dynamics analysis of Phase 3, at 32 km/h: intrusion of the pole into the automotive structure (true scale). **(a)** Global view. **(b)** Deformation in the z direction. 217

10.20Explicit dynamics analysis of Phase 3, at 32 km/h: total deformation distribution at global and component levels (true scale). **(a)** BPE with top cover. **(b)** BPE without top cover. **(c)** Bottom case. **(d)** Top cover. **(e)** Reinforcements. **(f)** Rocker panel. 218
10.21Explicit dynamics analysis of Phase 3, at 32 km/h: directional deformation distribution in the y direction at global and component levels (true scale). **(a)** BPE with top cover. **(b)** BPE without top cover. **(c)** Bottom case. **(d)** Top cover. **(e)** Reinforcements. **(f)** Rocker panel. 219
10.22Explicit dynamics analysis of Phase 3, at 32 km/h: equivalent von Mises stress (true scale). **(a)** BPE with top cover. **(b)** BPE without top cover. 220
10.23Explicit dynamics analysis of Phase 3, at 32 km/h: equivalent von Mises stress (true scale). **(a)** Bottom case. **(b)** Top cover. **(c)** Reinforcements. **(d)** Rocker panel that endures the impact. 221
10.24Explicit dynamics analysis of Phase 3, at 32 km/h: equivalent von Mises strain (true scale). **(a)** Rocker panels and BPE. **(b)** Exclusively the BPE structure. . . . 222
10.25Explicit dynamics analysis of Phase 3, at 32 km/h: plastic strain (true scale). **(a)** Exterior region of the impacted rocker panel. **(b)** Rocker panel cross-section. 222
10.26Explicit analysis of Phase 3, at 100 km/h: energy summary. 224
10.27Explicit dynamic analysis of Phase 3, at 100 km/h: overview of the deformation of the BPE in time frames (scale of 2). **(a)** $t = 0$ s. **(b)** $t = 2.5e-3$ s. **(c)** $t = 5e-3$ s. **(d)** $t = 7.5e-3$ s. **(e)** $t = 1e-2$ s. 225
10.28Explicit dynamic analysis of Phase 3, at 100 km/h: overview of the deformation of the BPE, in the $z-y$ plane, in time frames (scale of 2). **(a)** $t = 0$ s. **(b)** $t = 2.5e-3$ s. **(c)** $t = 5e-3$ s. **(d)** $t = 7.5e-3$ s. **(e)** $t = 1e-2$ s. 226
10.29Explicit dynamics analysis of Phase 3, at 100 km/h: intrusion of the pole into the automotive structure (true scale). **(a)** Global view. **(b)** Deformation in the z direction. 227
10.30Explicit dynamics analysis of Phase 3, at 100 km/h: total deformation distribution at global and component levels (true scale). **(a)** BPE with top cover. **(b)** BPE without top cover. **(c)** Bottom case. **(d)** Top cover. **(e)** Reinforcements. **(f)** Rocker panel. 228
10.31Explicit dynamics analysis of Phase 3, at 100 km/h: directional deformation distribution in the y direction at the global level (true scale). **(a)** BPE with top cover. **(b)** BPE without top cover. **(c)** Bottom case. **(d)** Top cover. **(e)** Reinforcements. **(f)** Rocker panel. 229
10.32Explicit dynamics analysis of Phase 3, at 100 km/h: equivalent von Mises stress (true scale). **(a)** BPE with top cover. **(b)** BPE without top cover. 230
10.33Explicit dynamics analysis of Phase 3, at 100 km/h: equivalent von Mises stress (true scale). **(a)** Bottom case. **(b)** Top cover. **(c)** Reinforcements. **(d)** Rocker panel that endures the impact. 231
10.34Explicit dynamics analysis of Phase 3, at 100 km/h: equivalent von Mises strain (true scale). **(a)** Rocker panels and BPE. **(b)** Exclusively the BPE structure. 232
10.35Explicit dynamics analysis of Phase 3, at 100 km/h: plastic strain (true scale). **(a)** Exterior region of the impacted rocker panel. **(b)** Rocker panel cross-section. 232

11.1 BPE optimisation methodology, based on novel material and geometry solutions.239

List of Tables

2.1 International standards and regulations and their levels of mechanical tests (Adapted from [4]) . . . 8
2.2 Hazard levels with descriptions and effects (Adapted from [10]) . . . 10
2.3 Euro NCAP tests for the assessment of Adult Occupation Protection (Adapted from [23]) . . . 13
2.4 Research gaps and future research directions on the battery pack enclosure design, with focus on crashworthiness assessment (Adapted from [70]) . . . 23

4.1 Quadrature point's locations and weights for Gauss-Legendre quadrature [77] 39

5.1 EV charging technologies (Adapted from [87]) . . . 56
5.2 EV battery chemistry and relevant characteristics as of 2018 [100] . . . 58
5.3 SAE standards regulating the mechanical design of automotive battery packs (Adapted from [106]) . . . 64
5.4 Placement of battery pack in some state-of-the-art commercial cars (Adapted from [102]) . . . 66
5.5 Realistic examples of aluminium alloys utilised in the automotive industry . . 72
5.6 Summary of materials, weight, and dimensions of commercial (Adapted from EVs [105]) . . . 75

6.1 Dimensions of the battery pack enclosure CAD . . . 86
6.2 Analysis unit system in Ansys® . . . 87
6.3 Al 6061-T6 material properties (Adapted from [129]) . . . 90
6.4 Connections setting definition . . . 92
6.5 Modal analysis: basic input analysis settings . . . 98
6.6 Transient analysis: basic input analysis settings . . . 104
6.7 Mechanical properties of the utilised structural steel in the rigid pole [129] . 106
6.8 Explicit dynamics analysis: basic input parameters . . . 108

7.1 Number of elements along the thickness of the wall and total number of elements and nodes for the whole model . . . 114
7.2 Convergence study's explicit analysis settings . . . 115
7.3 Percentage of hourglass energy present in the simulation with regards to the total energy of the system . . . 121

8.1 Mass associated with the BPE model of Phase 1 . . . 124
8.2 Phase 1: Static analysis mesh metrics . . . 126
8.3 Phase 1: Modal and transient analyses mesh metrics . . . 131
8.4 Phase 1: Explicit analysis mesh metrics . . . 140

9.1 ABS mechanical properties (Adapted from [117]) 164
9.2 Mass associated with the ABS BPE model of Phase 2 165

10.1 Al-SiC foam mechanical properties [117] 198
10.2 Dimensions of the cell cavities of the internal metal foam components of Phase 3200
10.3 Mass associated with the BPE model of Phase 3 200
10.4 Phase 3: Static analysis mesh metrics 202
10.5 Phase 3: Modal and transient analyses mesh metrics 207
10.6 Phase 3: Explicit analysis mesh metrics 214

List of Acronyms

2D	Two-Dimensional
3D	Three-Dimensional
ABS	Acrylonitrile Butadiene Styrene
AEB	Autonomous Emergency Braking
ANCAP	Australasian New Car Assessment Program
ATD	Anthropomorphic Test Device
BEV	Battery Electric Vehicle
BIW	Body-In-White
BMS	Battery Management System
BPE	Battery Pack Enclosure
CAD	Computer-Aided Design
CAE	Computer-Aided Engineering
CES	Continental Engineering Services
CFRP	Carbon Fiber Reinforced Polymer
CF-SMC	Carbon Fiber Sheet Molding Compounds
CG	Center of Gravity
CPT	Capacitive Power Transfer
CST	Constant-Strain Triangle
DoF	Degrees of Freedom
EEA	European Environment Agency
EOS	Equations Of State
EMC	Eletromagnetic Compatibility
EU	European Union
EUCAR	European Council for Automotive Research and Development
Euro NCAP	European New Car Assessment Program
EV	Electric Vehicle
EVA	Ethylene-Vinyl Acetate
FCEV	Fuel Cell Electric Vehicle
FEA	Finite Element Analysis
FEM	Finite Element Method
GBA	Granular Battery Assembly
GFRP	Glass Fiber Reinforced Polymer
GHG	Greenhouse Gas
HEV	Hybrid Electric Vehicle
HV	High Voltage
ICE	Internal Combustion Engine
ICEV	Internal Combustion Engine Vehicle
IIHS	Insurance Institute for Highway Safety

IP	Ingress Protection
IPT	Inductive Power Transfer
LCO	Lithium Cobalt Oxide
LFP	Lithium Iron Phosphate
LIB	Lithium-ion Battery
LMO	Lithium Manganese Oxide
NCA	Lithium Nickel Cobalt Aluminum Oxide
NCAP	New Car Assessment Programme
NFPA	National Fire Protection Association
NHTSA	National Highway Traffic Safety Administration
NMC	Lithium Nickel Manganese Cobalt Cxide
NVH	Noise, Vibration, and Harshness
OEM	Original Equipment Manufacturer
PDE	Partial Differential Equation
PET	Polyethylene terephthalate
PHEV	Plug-in Hybrid Electric Vehicle
PM	Particulate Matter
RESS	Rechargeable Energy Storage System
SAE	Society of Automotive Engineers
SF	Safety Factor
SLEV	Small Lightweight Electric Vehicle
SOC	State-of-charge
SOH	State-of-health
SPOC	Severe Partial Offset Crash
US	United States
VRU	Vulnerable Road User
WEM	With Existing Measures
WAM	With Additional Measures

List of Notations

$A_{bottom\ surf}$	Area associated with the bottom surface of a battery module cavity
$A_{total_{bottom\ surf}}$	Total area associated with the bottom surfaces of battery cell cavities
$\boldsymbol{a}$ or $\ddot{\boldsymbol{u}}$	Acceleration vector
$\boldsymbol{B}$	Deformation tensor
$\boldsymbol{b}$	Body forces
c	Speed of sound
$\mathbf{C}$	Constitutive matrix
$\boldsymbol{d}$	Nodal displacements vector
$\boldsymbol{\delta}_{IJ}$	Kronecker delta
$\boldsymbol{D}(t)$	Generalized time-dependent damping matrix
ε	Strain tensor
$\boldsymbol{\varepsilon}_0$	Initial strain vector
E	Young's modulus
$\boldsymbol{F_b}^{(e)}$	Element load due to body forces vector
$\boldsymbol{F_i}^{(e)}$	Element load due to initial strains vector
$\boldsymbol{F_t}^{(e)}$	Element load due to surface forces vector
$\boldsymbol{F_t}$	Total nodal forces vector
$\boldsymbol{F}^{int}$	Internal forces vector
$\boldsymbol{F}^{ext}$	External forces vector
F_{module}	Weight associated to a battery module unit
$F_{modules\ total}$	Total weight associated to the battery cells
$F(\xi)$	Polynomial function of domain $\xi \in [-1, 1]$
G	Shear modulus & Standard earth gravity
g	Standard earth gravity
Γ	Physical boundary
I	Generalized Functional
$\mathbf{I}$	Fourth-order identity tensor
$\mathbf{K}^{(e)}$	Element stiffness matrix
$\mathbf{K}$	Global, or assembled stiffness matrix
$\mathbf{K}(t)$	Generalized time-dependent stiffness matrix
L	Characteristic length
λ	Lamé's first parameter
$\boldsymbol{M}(t)$	Generalized time-dependent mass matrix
m_{module}	Mass of a battery module unit
μ	Lamé's second parameter
$\mathbf{N}$	Shape functions matrix
$n^{(e)}$	Number of elements
n^{cycle}	Number of cycles

ν	Poisson coefficient
P_{module}	Pressure associated to a battery module unit
$P_{modules\,total}$	Total pressure associated to the battery cells
ρ	Density
ρ^0	Original density
ρ^s	Scaled density
$\boldsymbol{\sigma}$	Stress tensor
t	Time
$\boldsymbol{t}$	Surface forces
U	Strain energy
$\boldsymbol{u}$	Displacement vector
$\boldsymbol{u}_0$	Initial condition of displacement vector
$\dot{\boldsymbol{u}}_0$	Initial condition of velocity vector
V	Potential energy
$V^{(e)}$	Element potential energy
$\boldsymbol{v}$ or $\dot{\boldsymbol{u}}$	Velocity vector
W_f	Work performed by external forces
t	Time
t^{sim}	Computation time for a simulation
t^{cycle}	Computation time for a cycle
$t^{(e)}$	Computation time for an element
Δt	Time step size
Δt^{crit}	Critical time step size
Δt^s	Time step associated with the scaled density
Δt^0	Time step associated with the original density
Ω	Problem domain
ω^{max}	Highest natural frequency of a system
w_i	Weight of the integration point i
w_j	Weight of the integration point j

Chapter 1

Introduction

This work consists of the study, development, and analysis of lightweight protection structures for the energy storage units in Battery Electric Vehicles (BEVs). A focus is given to the resistance of these structures to short-duration impact events through the performance of various Finite Element Method (FEM) analyses, particularly explicit dynamics.

1.1 Background and Motivation

In today's world, in light of heightened environmental awareness, there is a growing recognition of the need for significant changes in the transportation sector. The automotive industry is now actively seeking cleaner modes of transportation that contribute to reduce CO_2 and greenhouse gas emissions. This movement is being accelerated by increasingly strict environmental constraints and evolving consumer preferences, as environmentally conscious products have become an important competitive advantage [1, 2].

Electric mobility has been identified as a key element in the decarbonization of the transportation sector, particularly on road transport. Both existing and prospective environmental policies are mainly centred around the latter and place substantial emphasis on adopting Electric Vehicles (EVs) [3]. The emergence of this vehicle class as a promising solution to reduce tank-to-wheel emissions and, thus, advance in carbon-neutrality goals has been reflected, not only in their increased number of commercial sales but also in the growing body of research, conducted by both the academia and industry, to further explore and enhance these vehicles [4].

The battery can be interpreted as the heart of an Electric Vehicle (EV), particularly in the case of a BEV, which constitutes the family of electric vehicles that runs solely on energy stored in the rechargeable battery [5]. Lithium-ion Batteries (LIBs) are the preferred industry choice for employment in EVs, primarily due to their superior gravimetric and volumetric energy densities compared to other available options. These are essential characteristics for the performance and, therefore, the success of a BEV. Enhanced energy densities correspond to less weight and volume associated with the battery, which is particularly important for BEVs as the battery is already the heaviest and largest component of the vehicle. Thus, if the energy density associated with the battery is improved, the less the weight associated with the energy storage system and, subsequently, the longer the driving range characteristic of the electric vehicle [6, 7].

Other approaches can also be employed to enhance the weight efficiency of the battery pack and, consequently, of the overall vehicle. For instance, by resorting to a lightweight design of the Battery Pack Enclosure (BPE), i.e., through the obtainment of a lighter battery

housing. However, this cannot be done without proper consideration to ensure the integrity and safety of the battery pack.

In the event of a BEV crash, the occurrence of severe mechanical, thermal, and electrical stresses to the battery of the vehicle, and even its ignition as a result of the former, have been verified. Evidently, these hazardous phenomena pose a serious threat to passenger safety, making the crashworthiness of the vehicle and the battery pack a major concern. The BPE, in addition to other roles, is, after all, the battery's structural component responsible for its integrity, particularly in a crash event. Therefore, the desired above-mentioned weight reduction to this component cannot be performed to the detriment of its mechanical properties, particularly those related to impact.

The achievement of this balance between weight efficiency and mechanical robustness of the BPE is what this work strives to achieve by proposing innovative BPE designs obtained by resorting to utilising novel geometries and materials.

1.2 Purpose and Novelty of the Thesis

The focus of the present work is the obtainment of realistic lightweight battery pack enclosure solutions by utilisation of FEM.

This work emerged from the identification of a research gap in the topic of BPE crash simulations in FEM. The evaluation of BPE crashworthiness in literature has frequently relied on overly simplistic models. While these models are often used to showcase the validity of a proposed method or idea in a straightforward and efficient manner, they fail to address realistic scenarios and accurately assess the mechanical behaviour of the automotive structure. To ensure the evaluation of the safety level enabled by a particular BPE solution, it is essential to employ more complex models that yield physically meaningful results.

To fulfil the verified gap and, thus, achieve significant results, the starting point and novelty of this numerically-focused work were to obtain, by process of reverse engineering, a model representative of a well-positioned industry BPE solution. However, this could not be done without a preliminary comprehensive review of the fundamentals of Solid Mechanics, FEM, and, evidently, extensive research targeting the automotive industry and current solutions for battery housing. Aspects like the design, material selection, and positioning of the BPE within the BEV were addressed and contributed to the construction of the realistic model.

The focus of this work was then shifted to the definition of innovative weight-reduction optimisation routes for the above-mentioned model. This was to be done exclusively by resorting to alterations in the material and internal design of the BPE, excluding any changes to this component that would affect its integration into the real BEV that served as inspiration for this study. The goal is to obtain a "ready-to-use" BPE that does not require costly and time-consuming modifications to the vehicle's underlying structure.

The chosen improvement approaches involved two paths: one where the original Al 6061-T6 BPE, based on the performed industry research, was replaced with an identically-designed geometry manufactured with ABS, while the other utilised Al-SiC metal foams and introduced a more ambitious internal geometry for the BPE. The aim of these optimisation routes is to obtain increasingly weight-efficient BPE solutions with equal, or even improved, levels of mechanical and impact performance with regard to the original model, which effectively represents the current industry's state-of-the-art solutions.

1.3 Contextualisation of the Thesis in Continental Engineering Services

As discussed above, given the recently accentuated prominence of EVs, it is of the interest of any company serving the automotive industry to be at the forefront of expertise and innovation in this matter.

This work, conducted in association with Continental Engineering Services (CES), aimed to provide the company with a comprehensive workflow and innovative strategies for obtaining lightweight protection structures for the battery pack of a BEV. The findings and comprehensive knowledge obtained from this study have the potential to contribute to future projects undertaken by the company, both at internal and external levels. Hence, it is imperative to thoroughly analyse the given theme to establish the rationale for obtaining realistic and industry-aligned solutions for the specific problem. This approach ensures the reliability of the results and facilitates the development of solutions that meet industry standards and possess real-world relevance.

CES is a company within the Continental group. It offers a broad range of services, encompassing fields such as development, product supply and integration, consulting, and expertise. This enterprise offers specialised engineering in the areas of Driver Assistance, Interior Electronic Functions, Driveline & Electrification, as well as Brake Systems, which directly correspond to its existing departments. This work was developed in the context of the Driveline & Electrification department of the company's headquarters in Porto.

The reduced size of CES, compared with the extensive dimension of the Continental group, gives the company agility and momentum, especially considering that the entire technology pool of Continental AG is available to CES. These resources were also accessible to the performance of this work and have significantly contributed to its enrichment, accuracy and speed.

1.4 Structure of the Thesis

The purpose of this work is to provide the reader with all of the necessary knowledge and tools to acquire a solid understanding of the assessed theme. To achieve this, the work is organised to prioritise addressing the fundamentals of subjects, such as Solid Mechanics, before delving into the mathematical review of the Finite Element Method (FEM). Following the same philosophy, the assessment of the FEM basics will occur prior to the study of the explicit time integration method. Then, after the mathematical study, in-depth research is conducted on EVs.

After the completion of the literature review, the subsequent Chapters of this work concern the performed numerical analysis. This includes a preliminary convergence study to validate the employed method, followed by the novelty introduced by this work, corresponding to its main purpose. At this point, the reader will have a comprehensive understanding of the steps taken in this analysis as a result of the extensive theoretical research.

Thus, to conclude, the work is organised in the following manner:

- In Chapter 2, a scientific review regarding the diverse methods of vehicle crashworthiness assessment is conducted, with a focus on crash tests and FEM simulation. A historical assessment of both is performed, which then follows the presentation of relevant research projects on this theme, both at vehicle and component levels.

- Chapter 3 encompasses the fundamentals of Solid Mechanics.

- In Chapter 4, FEM is exposed in terms of its foundation and general principles that contribute to its extensive use in the industry. Then, the dynamic analysis in FEM is addressed. The explicit time integration method and its basic characteristics are assessed and its colossal application in the automotive industry is justified.
- In Chapter 5, thorough research is conducted on BEVs regarding their functioning, as well as their primary selling points and potential drawbacks in the eyes of consumers and experts. The BPE, the main subject of this work, is deeply investigated with regard to its essential functions, design, placement within the vehicle, and materials used in their manufacture in the current industry's solutions.
- Chapter 6 represents the partition between the theoretical and the numerical parts that compose this work. First, the procedure of the second part is laid out, and then, each of the analyses conducted in FEM is investigated, and the reasoning for their performance is explained. The "Original model" of the BPE, which resulted from the inspiration of a prominent industry component and that will be subject to alterations in the optimisation stages, is presented.
- In Chapter 7, a convergence study is done to validate the method that will be employed next in the BPE numerical analyses.
- Chapters 8, 9, and 10 correspond to Phases 1, 2, and 3 of the numerical portion of this work. They regard the exposition of the results of the conducted numerical analyses for the "Original model" and each of the performed optimisations. The particular specifications for the improved models will also be shown in these Chapters.
- The main conclusions of the performed work and related future works can be consulted in Chapter 11. n

Chapter 2

Scientific Review

The purpose of the present Chapter is to conduct a comprehensive literature review on the principal topics of interest of this work, particularly on the diverse methods the automotive industry employs for vehicle crashworthiness assessment. The subjects are preferably addressed chronologically to facilitate a logical and coherent understanding. Therefore, firstly, for contextualisation purposes, the importance and the necessity of vehicle crashworthiness evaluation are addressed. Then, the discussion focuses on the historical advancements and current regulations of crash testing. FEM as a tool for vehicle impact simulation follows, with the exposition of significant contributions and works for the development of the method and for its extensive use in the study of impact. Other relevant mathematical models for vehicle crashes are also briefly presented. The Chapter concludes with the exposition of recent research related to protecting battery packs in EVs in case of impact using FEM.

2.1 Importance of Crashworthiness Assessment in EVs

In the event of an EV crash, the safety of the occupants depends mainly on three factors: electrical safety, shielding against the spillage of hazardous chemicals, and protection against mechanical deformation of the vehicle structure [4].

As defined previously in this work, the term "crashworthiness" in the automotive industry refers to the vehicle's structural ability to plastically deform and absorb abrupt impact loads while still providing enough survival room for the occupants. Thus, a crashworthy vehicle structure should be stiff in bending and torsion for suitable ride and handling and minimise fore-aft vibrations that originate harshness [8].

For the case of occupant protection against the vehicle structure deformation, the task of the structural crashworthiness engineer is to ensure the vehicle is able to: 1) in the case of a frontal crash, deform plastically in the front end, absorbing the crash energy in that region and preventing intrusions into the drivers' compartment; 2) deform plastically in the rear end and be able to protect the passengers in the case of a rear impact; 3) prevent side intrusions in the passenger compartment and opening of doors due to crash loadings. Reducing occupant harm is the main objective of the safety engineer, and it is achieved through the combination of crashworthiness measures and crash avoidance, the latter being out of the scope of this work [9].

For the case of a BEV, the vehicle's safety performance is a colossal requirement for its acceptance and large-scale expansion in the market [10].

From the start of the current worldwide EV sales boost, there have been several reports of devastating fire incidents, most of which are linked to the igniting of Lithium-ion batteries,

according to research conducted by the National Highway Traffic Safety Administration (NHTSA) [11]. EV batteries are prone to failure in the event of an accident, existing the risk of the battery catching fire either immediately after its occurrence or in a delayed event [12].

There is a scarcity of data regarding the occurrences of electric vehicle fires [12]. However, Chombo et al. [4] summarised some of the publicly reported EV fire incidents that occurred on roads as of March 2021. The list included fifty-four fire incidents that, for simplification purposes, originated only from mechanical abuse. The incidents were grouped according to their abuse type, for instance, penetration, crash, drop, rollover and immersion, which allowed the identification of different phenomena and the evaluation of similarities and discrepancies between events within the same group. Forty-four of the reported accidents were based on crash abuse, and eleven were on multi-crashes. This study concluded that vehicle speed plays a crucial role in a crash's effect on the vehicle's safety level.

Although EV fire incidents are statistically rare, their occurrence represents a colossal safety concern due to the presence of intense heat release, emission of toxic noxious smoke, and risk of fire. Furthermore, as the number of EVs on the roads grows, concerns related to battery behaviour during potential vehicle collisions will likely become more prominent [4]. In fact, Spielbauer et al. [13] anticipate that incidents of battery fires and their severity will likely increase. This is explained by two factors: 1) the expected rise in energy density of newly developed cells and 2) the growing demand for EVs and the batteries used within them. Machuca et al. [14] estimate that the number of incidents involving EV battery fires can reach up to 135 000 vehicles per year by 2030, just in Germany.

Identical design strategies are employed in EVs and Internal Combustion Engine Vehicles (ICEVs); the differences rely on the replacement of the internal combustion engine with the electrified drivetrain in the front compartment, the introduction of the battery pack, and the structural alternations necessary to support the additional vehicle weight [4]. Understandably, to obtain, at least, a safety level equivalent to the one characteristic of ICEVs, potential changes in its behaviour resulting from component, structural and material modifications must be evaluated in EVs [4].

In the event of an EV accident, a multitude of phenomena can occur within the battery, owing to the associated impact loads, thereby causing its mechanical deformation, malfunction or failure. Some of these are the following: internal cell short circuit; battery charge or discharge, when the batteries surpass their upper and lower manufacturer-recommended voltage limits, respectively, also conducting to the aforesaid phenomenon; external short circuit; high-temperature exposure; thermal runaway, which is when exothermic chemical reactions in a battery are producing more heat than what is being dissipated, possibly leading to the emission of heat or fumes, ignition, or ultimately explosion of the battery [12]. Thus, one crucial aspect for reaching an adequate safety level in EVs is the development of safer and more reliable batteries.

Lithium-ion Batteries (LIBs) represent the automotive industry's preferred solution to store the electrical energy used for EV propulsion. Owing to the advanced state of EV and BPE design, it is not expected of most EV collisions to destroy the battery pack. Notwithstanding, given the elevated high energy density of LIBs, potential penetration and/or local damage resulting from external influences have the capability to lead to disastrous consequences, such as severe heat release, which in turn can originate thermal runaway.

Battery safety is regulated by several international organisations, as well as standards and legislations defined by governments, dependent on particular national requirements. Regulation ensures the uniform implementation of laws by setting out an extensive set of instructions. In turn, a standard is a directive document that outlines how to replicate something and addresses the product's technical characteristics. To formulate a safety standard,

in addition to testing in more stringent conditions than those often found in the real world, three principles should be safeguarded: the operability, repeatability, and reproducibility of the evaluations [10]. According to Kotak et al. [12], standards and regulations constitute the basis for the development and progress of EV batteries. In addition, Chen et al. [10] also highlight the role of the academia and industrial groups' joint endeavours regarding battery safety improvements in LIBs.

Focusing on the above-mentioned regulations, they often encompass different testing procedures, known as abuse tests. These consist of various testing conditions and safety criteria parameters for battery examination, for which LIBs must be certified by. As stated above, these standards ensure the required quality of commercially available LIBs and enforce that the necessary efforts for the evolution of LIBs and EVs are being exercised [4, 12, 10].

Given the principal purpose of this work, mainly the mechanical abuses on LIBs will be addressed. In fact, mechanical abuse is studied as a way to simulate the field phenomena, i.e., the diverse road circumstances that may occur during LIB exploitation, and evaluate the battery safety under all relevant cases. The level of mechanical abuse tests varies from the cell, pack to vehicle level, depending on the standard or regulation. Table 2.1 shows the list of international standards for EV batteries related to mechanical abuse tests. The letters C, M, P, and V represent Cell, Module, Pack, and Vehicle levels, respectively [4].

Table 2.1: International standards and regulations and their levels of mechanical tests (Adapted from [4])

Test Type	**International standards**					**EU**	**US**	**Korea**	**India**	**China**
	SAE J2464:2021	SAE J2929:2013	ISO 12405-4:2018	ISO 6469-1:2019	IEC 62660-3:2022	UN/ECER 100:2021	UL 2580:2022	KMVSS 18-3:2016	AIS-038:2020	QC/T 743:2006
Mechanical shock	C; M; P	C; M; P; V	P	P	C	C; M; P; V	C; M; P		M	
Drop	P	P					C; P	P		
Penetration	C; M; P									
Immersion	M; P	P		P			M; P	P	C; M	
Crash/ Crush	C; M; P	P; V		P; V	C	C; M; P; V	C; M; P			
Rollover	P	P					P		M	
Vibration		C; M; P	P	P	C	C; M; P; V	C; M; P		M	P

The letters C, M, P, and V are indicative of Cell, Module, Pack, and Vehicle levels, respectively.

Different hazard levels can emerge from the battery, dependent on its abuse type, chemistry, and internal passive protection devices. Therefore, it is pertinent to determine the response of the Rechargeable Energy Storage System (RESS) to abuse tests. The outcome of these in the abused LIB can be evaluated utilising the European Council for Automotive Research and Development's (EUCAR's) defined hazard levels (Table 2.2), and associated "pass" or "fail" criteria. This aims to ensure that the LIB does not ignite or explode within a specified time frame. In fact, "no fire", "no explosion", and "no leakage" are defined as pass criteria for the ISO 6469-1 [15], UL 2580 [16], and UN/ECE-R100.02 [17] standards [4, 10].

Table 2.2: Hazard levels with descriptions and effects (Adapted from [10])

Hazard severity level	Description	Classification criteria and effects
0	No effect	No effect or loss of functionality
1	Passive protection activated	No damage or hazard, with reversible loss of function. Normal functionality is restored with the replacement or re-setting of the protection device.
2	Defect/ Damage	No hazard but damage to the RESS. Irreversible loss of function, with needed repair or replacement.
3	Minor leakage/ Venting	Evidence of cell leakage or venting with RESS weight loss <50% of electrolyte weight.
4	Major leakage/ Venting	Evidence of cell leakage or venting with RESS weight loss >50% of electrolyte weight.
5	Rupture	Loss of mechanical integrity of the RESS container, resulting in release of contents. No physical damage external to the RESS.
6	Fire or Flame	Ignition and sustained combustion of flammable gas or liquid for more than about one second. Sparks are not flames.
7	Explosion	Very fast release of enough energy to cause pressure waves and/or projectiles that may cause considerable structural and/or bodily damage, varying on RESS size. The kinetic energy of the flying debris from the RESS may cause damage.

It is noteworthy to mention that while extensive research and standards concerning battery abuse testing have been performed and set to ensure that LIBs are safe during operation, the same cannot be said regarding requirements for extinguishing LIB fires. A study conducted by the National Fire Protection Association (NFPA) found that there is a dearth of knowledge related to battery flammability and fire protection specifications for battery packs. Moreover, the effectiveness of potential fire-extinguishing suppressants is unclear [18, 19].

2.2 Crashworthiness Testing

In accordance with most safety legislations, specialised facilities are typically utilised to conduct crash tests with the purpose of evaluating the crashworthiness parameters of vehicles. Automotive manufacturers commonly conduct full vehicle or sled tests to ensure compliance with these regulations and assess the crash performance of their designs. Despite the astonishing insight this approach enables into the crash behaviour and safety of the vehicle and its components, it is important to note that crash testing is extremely consuming in terms of time and costs, and, in addition, very few experimental data are publicly available [20].

2.2.1 Crashworthiness Testing Historical Assessment

Vehicle design aims at maximising both passive and active safety and, therefore, crashworthiness is a crucial automotive design requirement. The assessment of this parameter in vehicles dates back to the beginning of the second half of the twentieth century, as modern society urged for safer means of transportation. Governments responded to this by the implementation of suitable regulations by which novel techniques and methodologies to assess, characterise, predict, and enhance the crashworthiness of vehicle structures and, consequently, the safety of the occupants were described [8, 21]. As vehicle safety requirements have become more stringent and innovative vehicle classes, such as BEVs, have gained prominence in the market, these legislations have undergone continuous improvement.

In 1889, the first motor vehicle fatality occurred in New York City, originating the field of study of automotive safety. From there, according to Du Bois et al. [9], the development history of automotive safety can be divided into three different intervals:

- From 1900 to 1935 - A period of growth and development aiming to understand the complex process of a vehicle collision, with the first full-scale test. Basic improvements took place in areas such as the reduction of tire blowouts and the introduction of self-starters.

- From 1936 to 1965 - Crash avoidance devices, for instance, windshield wipers and turn signals, were incorporated. The seatbelt was introduced as an optional device. In addition, General Motors conducted the first car-to-barrier frontal crash.

- From 1966 to the Present - Starting from the creation of the NHTSA in the USA. Crashworthiness, crash avoidance, driver performance, and highway construction became the key aspects of vehicle safety. Multiple crashworthiness features are included in vehicles, such as rigid steel occupant cells surrounded by strategically positioned energy-absorbing components.

Full-scale crash tests were, and continue to be, the best way to assess the structural response of a vehicle structure in a collision, given the colossal complexity intrinsic to a crash event and the challenging characterisation of the structural response of a vehicle. Vehicle collision surveys show frontal crashes are the most common, followed by side, rear, and roll-over ones, respectively [22]. In addition, frontal impacts are the principal cause of death and serious injuries out of all the accident types. Side crashes are responsible for the second-highest number of death and injuries [23]. Crash tests are then performed to mimic the most common road scenarios by crashing a vehicle against a rigid or flexible, moving or fixed barrier at a defined impact velocity, angle and overlap [8].

Evidently, in the early times, these tests were rudimentary by today's standards; however, since then, technological developments allowed a more refined crashworthiness assessment [9]. Nowadays, occupant safety is studied by instrumented full-scale Anthropomorphic crash Test Dummies (ATD). These enable the obtainment of data on particular body parts which are more prone to injury. As these dummies simulate the size, proportions, weight, and articulations of a human body, through the use of load cells and accelerometers, the forces and deceleration levels the human body would be subjected to in a crash event can be obtained. Then, biomechanical injury criteria are utilised to assess the injuries [8].

Adding to the safety standards set by the government to assess the crashworthiness of a vehicle, several independent organisations, public and private, have surfaced with the objective of proposing programs that heighten consumer awareness about vehicle safety. These entities issue reports evaluating the crashworthiness performance of vehicles, rating them based on their performance in various crash tests such as frontal, side, and pedestrian impact, employing even more stringent criteria than that of vehicle certification. The publication of these reports is not a mandatory requirement for selling vehicles in the market; however, it has sparked a growing interest among consumers in vehicle safety, thereby motivating automotive manufacturers to enhance the crashworthiness of their products. The first initiative of this kind was the New Car Assessment Program (NCAP), created by the NHTSA in 1979, which introduced a crashworthiness rating consisting of awarding stars (five stars being the best and one the worst) derived from the injury measures recorded on the ATDs [8, 24].

In the 1990s, this practice was disseminated globally. The Insurance Institute for Highway Safety (IIHS) commenced utilising frontal offset crash tests to evaluate and compare frontal crashworthiness, which then followed side and rear crash evaluations. Soon after, Europe launched the European New Car Assessment Programme (Euro NCAP). The impact of these consumer-centric crash test programs on vehicle design has been paramount. For instance: enhanced seatbelt performance, substantial improvements in front-end crumple zones and occupant compartments, and improved side structures. [24].

To fulfil the main purpose of this work, the tests suggested by the Euro NCAP will be used as a basis to simulate relevant and realistic road scenarios.

2.2.2 Euro NCAP Crash Tests

Euro NCAP, which emerged in 1997, was initially criticised by automotive manufacturers, who claimed that the severe assessment criteria made it impossible for any vehicle to attain more than three out of the five-star rating system. Nevertheless, these entities now strive for a five-star evaluation from this program on all their new models, which reflects the effectiveness of the market-driven approach in enhancing vehicle safety [23, 24].

Euro NCAP's overall safety rating, starting from 2009, is based on four parameters [23]: "Adult Occupant Protection" (for both the driver and passenger), established based on three tests: frontal and lateral impacts and whiplash tests; "Child Occupant Protection"; "Vulnerable Road User (VRU) Protection"; and Safety Assist. The star rating employed at a particular time is contingent on the technological advancements accessible at that time. Consequently, if new innovations become available, the tests may undergo modifications, resulting in changes to the star ratings. Hence, it is imperative to consider the year of assessment to interpret the vehicle's overall rating accurately [23].

The tests determining the score of the Adult Occupant Protection can be consulted in Table 2.3, alongside their description and relevant parameters.

Table 2.3: Euro NCAP tests for the assessment of Adult Occupation Protection (Adapted from [23])

Impact Type	Test Name	Description	Barrier Type	Velocity [km/h]
Frontal	Full-Width Rigid Barrier	Collision between the vehicle and a rigid barrier. Places high demands on the restraint systems in front and rear seating positions. Evaluates the deceleration forces acting on the dummies, which can lead to severe injuries, especially on the chest of the more vulnerable, smaller or elderly occupants.	Rigid & Fixed	(50 +/- 1)
Frontal	Mobile Progressive Deformable Barrier	Collision between a vehicle and a mobile deformable barrier, which represents the front end of another vehicle, getting progressively stiffer the more it is deformed. Developed to estimate the risk of head, neck, chest and abdominal injury.	Deformable & Mobile	(50 +/- 1)
Side	Side Pole	Vehicle strikes a rigid narrow pole on the driver's side. Given the localized loading, severe deformation may occur and the pole can penetrate deeply into the passenger compartment. Evaluates the vehicle's ability to protect the driver's head.	Rigid & Fixed	(32 +/- 0.5)
Side	Side Mobile Barrier	The vehicle is struck on the driver's side by a mobile deformable barrier. Ensures adequate protection of critical body regions. Has driven the strengthening of structures around the B-pillar, curtain airbags, and the development of less-evident energy-absorbing structures in seats and door panels.	Deformable & Mobile	(60 +/- 1)
Side	Far-Side Impact	The vehicle is struck on the opposite side of the driver's seat by a mobile deformable barrier or a narrow pole. Two sled tests are required: one performed using a representative 32 km/h side pole test non-struck side B-pillar pulse, and another using a representative 60 km/h MDB to car non-struck side B-pillar pulse. In both sled tests, the movement of the dummy towards the impacted side of the vehicle, also known as "excursion" is measured, particularly on the head and neck. Data from full-scale testing is also required.	N/A	N/A
Rear	Whiplash	The test involves a dummy or dummies seated in the forward-facing seat(s), which are placed on a sled and accelerated to simulate a rear-end collision. The geometry is evalutated to assess the effectiveness of seat and head restraint designs.	N/A	N/A

Note that the N/A, meaning "Not Applicable", in the "Far-Side Impact" test comes from the fact that the barrier type, the velocity characteristic of the sled test are different in each test. In the "Whiplash" test, two medium and high severity pulses are employed [23].

For illustration purposes, a representation of the performance of the "Full-Width Rigid Barrier" frontal crash test on the Tesla Model X is provided in Figure 2.1

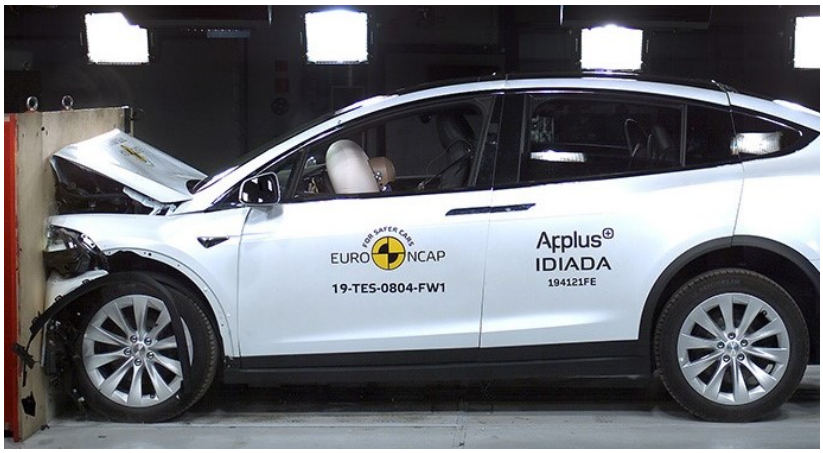


Figure 2.1: Euro NCAP "Full-Width Rigid Barrier" frontal crash test on the Tesla Model X [23].

2.2.3 Crashworthiness Testing of Electric Vehicles

Electric and hybrid vehicles are submitted to the same passive and active safety standards as conventional fossil fuel vehicles; however, they must meet a few EV-exclusive requirements added to official standards before, during, and after the testing process, to safeguard the safety of specific components [4, 25]. The results of the first safety test performed by Euro NCAP of a BEV (a Mitsubishi i-MiEV) were published in 2011. The admirable four-star rating proved the fact that, indeed, safety is not compromised by zero-emission vehicles [23].

The technical bulletin "TB011 Testing of Electric Vehicles" [26] was initially published in 2010. It has since been updated to incorporate specific requirements on two main aspects: 1) information on the vehicle's electric drive system that the Original Equipment Manufacturer (OEM) must provide to the testing laboratory; 2) the various checks that the testing laboratory should undertake in the global crash testing process [26]. For the particular case of a BEV, the OEM must provide a battery charger and declare the recharge method for the vehicle [26].

The HV vehicle assessment requires laboratories to measure the voltage of the battery during the full-scale crash test. This evaluation aims to verify the protection against electrical shock, as per UNECE R94, R95, R135, and R137 regulations. Diverse test options are allowed to attest to this safety parameter, namely the absence of high voltage, low electrical energy, physical protection, or isolation resistance, and both the pre and post-test should follow a strict protocol to ensure the well-being of the workers and infrastructure [25, 26].

A thermal evaluation, in which the temperature of the HV battery and the rate at which it increases during testing are monitored, should also be executed. The manner by which this is performed is left to the discretion of the test laboratory. Any audible or visual alerts from the vehicle indicating a possible thermal incident should be documented. If the vehicle fails to provide any warning in the event of a thermal incident, this will also be notified [26].

The overall procedure of a crash test performed in HV electric vehicles is illustrated in Figure 2.2.

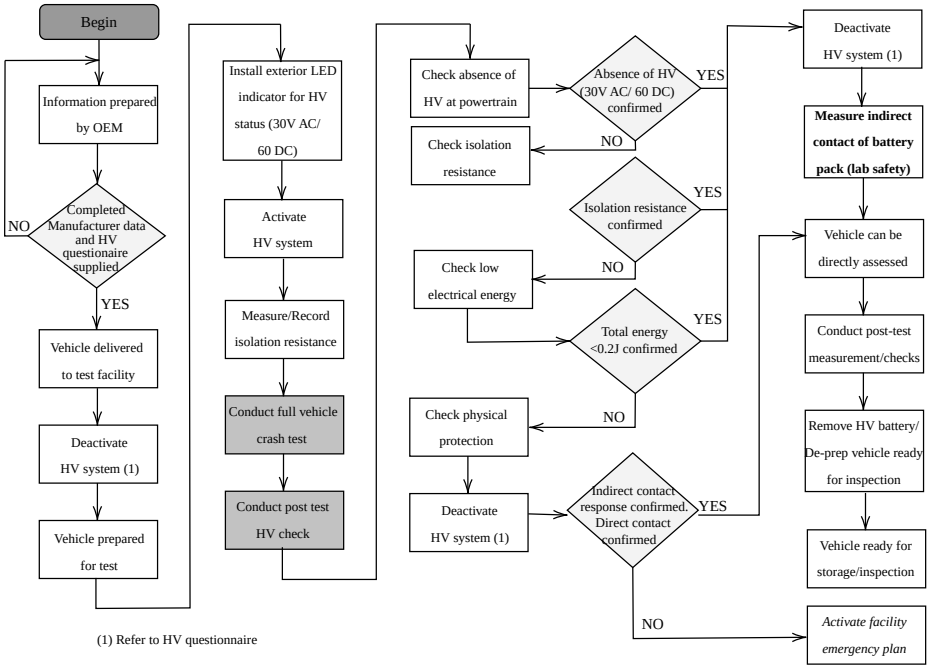


Figure 2.2: Flowchart indicating the preparation and assessment process of high voltage vehicles (Adapted from [26]).

Concluding, the testing procedure for HV electric vehicles aims at comprehensively assessing their safety level, accounting for their intrinsic differences with regards to ICEV, and enabling consumers to make informed decisions while selecting a vehicle.

2.2.3.1 Recent Research on Crashworthiness Testing on EVs

Over the course of several years, researchers have investigated the ability of vehicles to ensure the safety of occupants during accidents. This has been achieved through a combination of methods, including conducting real crash tests utilising vehicle prototypes, as well as simulating vehicle crashes using computer software and considering vehicle parameters retrieved from experiments [4].

Crash tests are intricate experiments that involve significant non-linear deformations and necessitate multiple design, prototyping, and testing iterations. Conducting a vehicle crash test requires substantial labour, specialised personnel, advanced facilities, prototype vehicles for testing, sensing and measurement systems, and so on. However, extremely accurate results can be obtained by this means [4].

Palvoelgyi et al. [27] studied the crashworthiness of an electric G-van through the conduction of a barrier impact test at 48 km/h. The detachment of the battery tray occurred, and uncontrolled g-loadings were transmitted to the vehicle.

A study on a newly developed Nissan body structure to assess occupant safety against battery pack deformation and direct contact was conducted by Uwai et al. [28]. The following tests were performed: frontal test with a deformable barrier at 64 km/h, side pole test at 32 km/h, and rear test at 80 km/h. No battery pack deformation or electrical conduction was observed after all tests, attesting to the protection provided by the layout and body structure of the vehicle.

The EVERSAFE project [29] aimed at investigating EVs in relation to expected crash loading, battery crash behaviour, potential compatibility issues with existing vehicles, and

post-crash handling procedures. Three testing activities were performed: a side pole impact test with a Mitsubishi i-MiEV and rear and frontal impact tests on a BMW i3. The aftermath of the side pole test indicated that there was no apparent damage to the battery pack, and the high voltage outside the battery pack dropped to below 60 V, as required by safety regulations. No evidence of electrical, thermal, or chemical hazards in the occupants' compartment was discovered. The rear impact to the BMW i3 was performed by a crash trolley, and in the observations, only mechanical damages were appreciable. The vehicle's passenger compartment exhibited little to no intrusion, opening the doors easily. No injury assessment was performed.

O'Malley et al. [30] analysed crash tests performed by the IIHS and Australasian New Car Assessment Program (ANCAP) to assess occupant safety and vehicle dynamics during frontal collisions. The carried-out tests corresponded to the moderate overlap of 40% offset into deformable barriers at a speed of 64 km/h and the small overlap of 25% offset into rigid barriers at the same speed. According to the IIHS report, the battery pack area of the vehicle remained unaffected in all test scenarios, with no electrical safety issues.

A. Żuchowski [31] reviewed the results of crash tests carried out with six EVs within the weight interval of 1200 to 2300 kg in the period of 2012 to 2013. The test corresponded to the vehicle's frontal impact travelling 56 km/h into a rigid barrier. The deformation on the frontal crumple zone and the loads acting on the dummies placed at the driver's and passenger's seats were evaluated. The obtained results were compared to the ones of similarly-configured ICEVs. It was found that the resultant deformation of the crumple zone is larger for the EV models, which consequently yields smaller dynamic loads on the occupants of the vehicle.

Polestar [32] conducted a small overlap frontal offset test on the Polestar 2. The reported observations were as follows: the front wheel was quickly detached, which minimised the likelihood of structural stack-up and deformation within the cabin; the Severe Partial Offset Crash (SPOC) block, which protects against metal intrusions during an impact, sustained severe damage, and the battery pack remained undamaged as was sought.

Lastly, it is worth mentioning that the growing interest in vehicle and occupant safety in crash scenarios has originated the necessity of assessing vehicle crashworthiness at the initial stages of vehicle development. For these, less laborious and faster methods than conducting a full-scale crash tests are needed, which explains the extension and importance of FEM for this particular role. This will be explored next.

2.3 Crashworthiness Analysis Using the Finite Element Method

2.3.1 The Origin of the Finite Element Method

FEM is a numerical technique that allows the obtainment of an approximate solution for problems encompassing Partial Differential Equations (PDEs) or formulated as functional minimisation. This is accomplished by dividing the domain into a collection of discrete parts, termed "finite elements". Therefore, the continuous physical problem is converted into a discretized one, used to attain and analyse relevant variables of the given problem [33].

FEM emerged in the twentieth century as a result of the work of many contributors. In fact, as early as 1906, the method that can be regarded as the forerunner of the Finite Element Analysis (FEA) approach was applied to solve problems involving elastic bars arranged in a regular pattern acting as an isotropic elastic body [34].

In 1909, W. Ritz [35] presented the first analysis of discrete direct variational calculus with trial functions within the whole domain of a system. The method was applied to

statically loaded clamped plates, modelled by the 4^{th} order Kirchhoff Two-Dimensional (2D) PDE. An important limitation of this approach is the fact that the selected shape functions need to satisfy the boundary conditions of the problem [36, 37].

B.G. Galerkin [38], in 1915, introduced a fundamental concept of the primal finite element method: the principle of direct variation by the orthogonality of the equilibrium residuum and the test functions. This approach can be viewed as a variation of the principle of virtual work [37].

A. Hrenikoff [39] introduces, in 1941, the framework method by which the solution domain was discretized into a mesh of lattice structure. This is considered one of the earliest forms of mesh discretisation. However, this particular version of a discrete element method did not find broader applications [37].

In 1943, R. Courant [40] proposed another basic concept of the FEM: the discretisation of the system's domain in finite subdomains that serve as the supports of the shape functions. Therefore, the above-mentioned limitation imposed by Ritz's and Galerkin's methods, where the test and trial functions within the whole domain are used as supports, is overcome, as all the trial functions are not required to satisfy the problem's boundary conditions. The method was applied to the St. Venant torsion of a prismatic bar modelled by the 2D-Poisson PDE, and linear triangular and quadrangular elements were employed. Around the same time, similar works of discretisation were done independently by other researchers, including McHenry and Newmark [41, 37].

J.H. Argyris et al. [42] published, in 1954, their research which aimed at the generalisation, extension, and unification of the energy principles on the analysis of elastic structures. These principles, examples of which are the principle of virtual work and the minimum potential energy principle, represent a vital basis for the application of FEM for solids. Two years later, the work of M.J. Turner et al. [43], which centred on the "stiffness and deflection of complex structures", was presented. FEM based on the principle of virtual work was introduced, and FEM interpolants for triangular elements were successfully derived. These works are commonly regarded as the formal presentation of the finite element method [36, 41, 44].

R.W. Clough [45] coined the name "finite element" for the first time in 1960, while the first book devoted to the extensive formulation and study of the FEM subject is attributed to Zienkiewicz [46] and was published in 1965.

The development of the FEM coincided with crucial advancements in digital computers and programming languages. Rapid improvements in the speed and capacity of computers enabled the instant success and evolution of the method, as well as its ramifications into other fields than the originally intended, through the decades [36, 37]. From its inception, the literature on FEM has experienced exponential growth, as have its industrial applications. Today, numerous journals are dedicated to the theory and application of the method, making knowledge on FEM readily accessible for professionals and academics alike [44].

FEM has been used in structural analysis for over 60 years. Currently, it constitutes a basic requirement for any type of engineering analysis, as it can routinely allow the solving of complex industrial problems. Nowadays, FEM is been extensively utilised in the analysis of structures manufactured in composites, as these materials have been gathering attention across many industries owing to their unique properties. Computational modelling is also used in other fields besides engineering, such as dentistry and orthopaedics [34, 47].

2.3.2 Finite Element Method in Dynamic Analysis

In the 1970s, there was much interest in the possibility of using the FEM to simulate and analyse the dynamic behaviour of structures, including crashworthiness, of great relevance

to the automotive industry [41].

FEM in structural dynamic problems numerically resolves a set of nonlinear PDEs of motion in the space-time domain, coupled with material stress-strain relationships and the specification of appropriate initial and boundary conditions. Firstly, the equations are discretized in the space domain by problem formulation in a weak variational form and assuming an admissible displacement field. A set of second-order differential equations in time are yielded. These are then solved by time discretisation [9].

At that point, many time integration schemes had been developed, including the Newmark-β method [48], Wilson-θ method [49], the Hilbert-Hughes-Taylor α method [50], the Houbolt integration algorithm [51], and the explicit time integration algorithm. Earlier developments in nonlinear finite element technology resorted to implicit time integration methods [52]. Explicit solvers were first introduced by T. Belytschko et al. [53] proposing the development of mixed explicit-implicit solutions. Important advancements resulted from using explicit, implicit-explicit, or implicit time integration with damping control to solve nonlinear structural dynamics problems by these personalities [9, 41].

Explicit time integration algorithms were then being utilised to solve numerous engineering problems in diverse areas such as dynamic contact, dynamics of solid structures, fluid mechanics, and particularly FEM Lagrangian hydrocodes [41]. Nevertheless, owing to the inherent properties of the explicit integration scheme, which will be detailed in the posterior Chapters of this work, it became extensively used in the automotive industry, establishing FEM technology as the main instrument of passenger vehicle design and crashworthiness analysis. In fact, by the 1980s, thousands of workstations were running explicit integration-based FEM codes in the three major automakers in the United States of America [41].

One of the earliest FEM analyses in computational contact mechanics emerged in 1976, with the publishing of work by T.J.R. Hughes et al. [54]. It marks the first work on FEM modelling of dynamic and impact problems, where interaction between different continuous objects occurs. Examples of the applications of these problems are the interaction between pavement and tires and target impact and penetration. This research topic remained popular until the late 1990s, with relevant contributions from many diverse personalities, particularly N. Kikuchi, J.T. Oden and J. Simo [41].

2.3.3 Recent Research on Crashworthiness FEM Simulation on EVs

In recent years, as the prevalence of EVs in the automotive market grows rapidly, crashworthiness studies using the FEM, both at component and vehicle levels, have equally gathered increased interest and relevance.

As already stated, due to its outstanding accuracy in predicting material behaviour, stresses, and deformation during impact, explicit non-linear FEA has undoubtedly emerged as the most widely recognised modelling approach for EV crashworthiness [4].

Typically, the main purpose of crashworthiness-focused research for EVs utilising FEM is to analyse and optimise current industry solutions, particularly in terms of crashworthiness properties and weight. This optimisation can be achieved through material changes, the inclusion of absorbing structures, thickness alterations and reinforcements, topological optimisation, and many other techniques. The ensuing damage to the battery packs as a consequence of the crash event is commonly the parameter of assessment since the mechanical abuse of the battery system can present a serious threat to the safety of the vehicle passengers.

Some of these studies, in addition to the structural analysis, also provide insight into the thermal and electrical performances of the battery in the event of a crash. This is of great

importance since multiple aspects contributing to vehicle occupant safety can be evaluated.

2.3.3.1 Crashworthiness Analysis in FEM at Vehicle Level

This subsection addresses examples of FEM studies developed to assess the crash behaviour of vehicles, with a later focus on EVs. The research will preferably be presented chronologically, as for the publication date.

Belingardi et al. [55] utilised the Altair HyperMesh® software to develop and evaluate, in the case of a frontal impact, the introduction of an impact attenuator in an EV Formula Student car body. The enhanced structure fulfilled the initial requirements stipulated in accordance with SAE 2008 regulation, presenting an average deceleration of approximately 14 g-force and improvements in the absorption of kinetic energy.

Zhang et al. [56] resorted to FEM to study the effect of the front wheels on the impact load transfer and load path, i.e., how the tire deformation influences the absorption of the crash energy in a Small Lightweight Electric Vehicle (SLEV) model. The model was subjected to multiple load cases representative of actual crash test parameters. The results yielded that the front wheels absorbed a considerable amount of kinetic energy equivalent to that of other frontal structural components.

Numerical simulations of crash events, both against a barrier and against other vehicles, for an electric four-wheel vehicle were performed by Berzi et al [57]. The main subject of study was the energy storage system and, in the end, it was concluded that the accelerations acting on the battery's Centre of Gravity (CG) were within acceptable limits for all of the case studies analysed.

Through their study on the multi-material design of a vehicle body, Chen et al. [58] concluded that composite materials are beneficial for applications in energy-absorption components, presenting advantages when considering crashworthiness and social effects simultaneously.

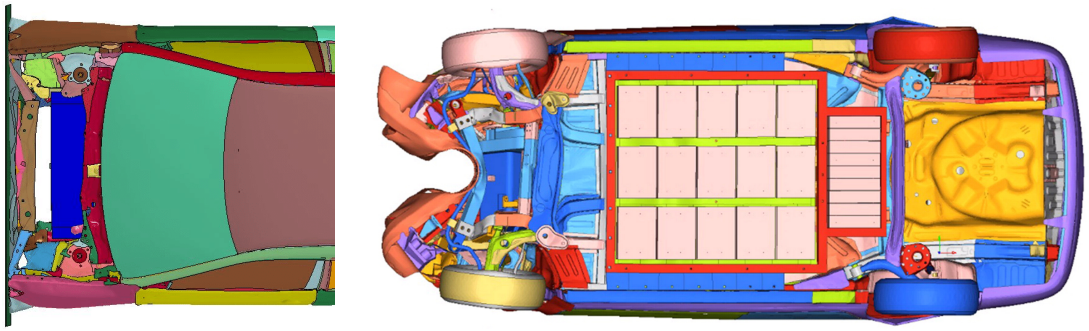
Li et al. [59] resorted to the Altair HyperWorks® software to model a SLEV and to the nonlinear FE code LS-DYNA to perform a numerical analysis which mimicked a full frontal test, with respect to Chinese national regulations. The study utilised a six-sigma design optimisation method and obtained enhancements in the performance and weight of the EV.

A novel procedure to convert a model of a conventional ICEV into that of an EV was suggested by Navale et al. [60]. The resulting structure was then checked against load conditions specified by Euro NCAP. LS-DYNA and ANSA, the latter as pre-processor, were used. The two versions of the vehicle were then compared in terms of deceleration, intrusion measurements, and overall factors affecting the crash behaviour, with the modified model achieving similar results to the donor one. Zhang et al. [61] also converted an ICEV model prototype into a BEV and subjected the resulting model to full-wrap frontal and side impacts. Topology and size optimisations were employed to redesign the front-end structures of the vehicle body. The results showed greater crashworthiness properties and reductions in the weight of the vehicle.

Lastly, it is relevant to point out that FEM has also found significant relevance in the development of simulation models to evaluate injuries to passengers in crash events [20]. For instance, Kirkpatrick et al. [62] published an article regarding developing and validating an LS-DYNA FE occupant model suitable for crash analyses of roadside safety features and useful for studying occupant kinematics. The occupant model was constructed from the weight and geometry specifications of ATDs, and modelled from rigid bodies connected by joints. Similarly, the flexible components of the model, such as the neck, were built from deformable elements. Putra et al. [63] used an optimisation strategy to present a head-neck

FE model for an average female occupant. To replicate human reactions during a whiplash-induced rear impact, the model incorporates an active neck muscle controller.

Two of the discussed examples of these analyses are illustrated in Figure 2.3, for illustration purposes.



(a) **(b)**

Figure 2.3: Examples of FEM models elaborated to evaluate the EV crash behaviour. **(a)** Full frontal barrier crash against a rigid impact wall at 50 km/h [64]. **(b)** Frontal pole test with rigid pole at 50 km/h [60]

2.3.3.2 Crashworthiness Analysis in FEM at Battery Pack Level

Given the key role played by the energy storage system in the performance and safety of an EV, as above-mentioned, the properties of the battery pack and BPE are of uttermost importance. In addition, the mass associated with the HV battery of a BEV is also an extremely relevant matter, since it directly impacts the autonomy of the vehicle. Indeed, the battery packs are one of the largest, if not the principal, contributors to the overall weight of the EV. As a result, in recent years, researchers have explored and proposed various methodologies for obtaining not only crash-resistant but also lightweight battery pack designs.

Kukreja et al. [64] studied the implications of placing a damage-tolerant battery pack in the secondary safe zone of a vehicle. The multifunctional battery pack, called Granular Battery Assembly (GBA), comprises cylindrical battery units and sacrificial metal tubes in a bimodal packing distribution. The pack presents functions of energy storage, stress control, and energy dissipation capabilities. Benefits in terms of space efficiency, weight, and simplification of vehicle design were found; however, additional investigation regarding the integration of thermal and electrical systems, GBA manufacturing methods, and experimental validation needs yet to be addressed.

The energy absorption and packing efficiency of the battery packs were assessed by Uerlich et al. [65]. The LS-DYNA solver was employed to conduct static and dynamic analyses based on NCAP standards, and the effect of the mass was evaluated. Alternative battery pack geometries were examined against commercially available structures, and the energy absorbed by the cells was studied with the use of simplified crushable foam material. It was concluded that a hexagonal pack is beneficial in both assessment parameters.

Pan et al. [66] performed a crush and crash analysis of an automotive BPE for lightweight design assessment. A modal test was conducted to validate the nonlinear dynamic FE model of the battery housing, and, posteriorly, the simulations within the scope of the work were performed with respect to test standards. The influence of the material and thickness was investigated, and the results displayed enhancements of the crashworthiness of the lightweight

design. The same authors also conducted a study on the use of advanced high-strength steels and the employment of size optimisation in the battery packs of EVs. Mechanical shock and fatigue life were analysed numerically, prior to the crash and crush simulations.

Using the LS-DYNA FE software, Qiao et al. [67] performed crash simulations in accordance with the Chinese NCAP, aiming to analyse the deformation and stress occurring on the battery box, as well as to evaluate the most dangerous battery monomer, during a frontal collision to a wall. Including Ethylene-Vinyl Acetate (EVA) foam on the front and rear sides of the battery monomer resulted in a 12.65% reduction in the maximum deformation of the battery housing.

Ruan et al. [68] concluded that the structural stresses were caused by acceleration loads in all directions on the battery, and the most stress occurred in the connection area between the battery pack ears and the box. Structural optimisation of the battery pack was performed, with the adoption of reinforcing ribs, and the resulting model was verified with the assistance of the Altair HyperMesh® solver. The battery toughness, weight, and minimum natural frequency were improved.

The employment of a sandwich structure, based on an inventive auxetic structure positioned in the structure's core, was done by Biharta et al. [69]. This structure was designed and analysed with the aim of protecting the energy storage system of an EV in the case of an impact of the load on the road.

Szabo et al. [1] researched the topographical optimisation of a battery module case that equips an EV. The results of the FEA show that the optimised model demonstrates a reduction in cell deformation and in the weight of the structures when subjected to a side impact.

To offer the reader an understanding of the model geometries commonly employed on these numerical studies, Figure 2.4 is presented.

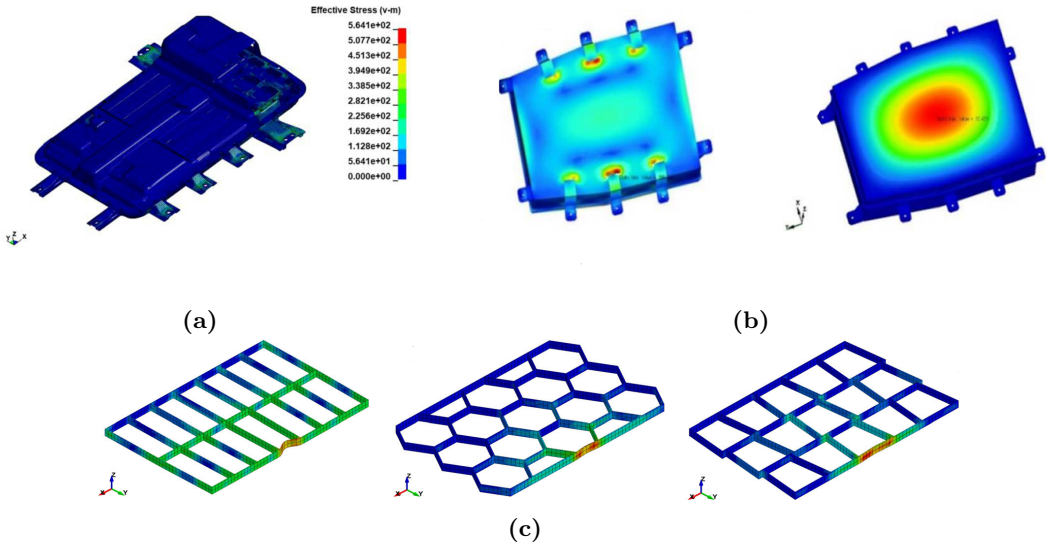


Figure 2.4: Examples of FEM models elaborated to evaluate the battery pack's and BPE's behaviour in crash situations. **(a)** Effective stress on the battery pack model after the crash simulation [66]. **(b)** Stress and displacement, respectively, distributions in the battery pack under bump, acceleration, deceleration, and turning conditions [68]. **(c)** Deformed models of empty packs (rectangular, hexagonal, and trapezoidal, respectively) under dynamic impacts [65].

Lastly, it is relevant to acknowledge that a significant number of other studies assessing the numerical simulation and design optimisation of the battery housing structure, it is on the electrical, thermal, and mechanical levels can be found in the literature. However, because one of the primary focuses of this work is the crash analysis, cases where this is not addressed were considered out of the scope of this work.

2.3.3.3 Research Gaps and Future Directions

Dhoke et al. [70] presented, in 2021, a critical review on the lightweight design of battery pack enclosures for EVs. In their work, the authors presented their findings on research gaps and future research directions for EV battery packs. In the course of the review performed in this section of the present work, it was concluded that many of the mentioned limit topics still hold significance two years later, although numerous additional studies have been conducted on this subject since then.

In Table 2.4, some of the common points found between these two investigations are showcases and explained.

Table 2.4: Research gaps and future research directions on the battery pack enclosure design, with focus on crashworthiness assessment (Adapted from [70])

Research Gaps/ Future Research Directions	**Description**
Battery Pack Design for Test Condition	Scarce evidence found on real test load cases and impact loads for design optimisation. More detailed studies need to be performed.
Battery Pack Housing Lightweight Design	Further investigation on the lightweight design of the battery enclosure with satisfactory shock-absorbing capacities are of considerable interest. The employment of composite and honeycomb has not found relevance in the consulted research, similarly to the use of topology optimisation.
Battery Pack Enclosure Placement in Vehicle	Little to no studies analysing the localisation of the battery pack on the EV, particularly in terms of crash, have been found. Potential research field in battery pack housing design optimisation.
Battery Pack Enclosure Manufacturing Feasilibily and Layout Space	Many of the research found in literature disregards, by the use of simple models, the effects of particular manufacturing process factors on the overall design and on the layout space, i.e., the systems in the interior of the housing, and interfacing it. More complex works addressing the manufacturability of the chosen enclosure design and material are necessary.
Battery Pack Enclosure Design for Recycling	Some studies have addressed the topic of recycling efficiency of the battery pack itself. However, with the proposal of innovative materials for usage in the battery pack enclosure, it would be interesting to assess their impact on the environment during their life cycle.
Battery Pack Design Test Setup	Validating the results of the constructed battery pack enclosure FE models with experimental tests under various loading conditions (for instance, random vibration, mechanical shock, and crashworthiness) would allow the definition of valuable simulation methodologies. More efforts should be employed in this sector.

Lastly, it must be noted that in some of these examples, very simplistic models are used for the studies, particularly in those regarding BPE crash analyses. Even though, oftentimes, the use of such models is justified by the novelty of the proposed method, serving solely to demonstrate the validity of the idea in an uncomplicated and efficient way to the reader, more complex models are necessary to address realistic scenarios and truly evaluate the mechanical behaviour of the structure, thereby examining accurate safety levels.

This serves to contextualise the present work in the spectrum of the already conducted BPE research and represents, in fact, one of the innovations of this work: the use of a significantly complex battery housing structure to be extensively numerically studied in a crash.

The utilised structure and procedure followed in this analysis will culminate in physically meaningful results and fill a major gap found in this research. Moreover, the care employed in the model and numerical analysis means that the proposed optimisation methodologies will provide realistic weight reductions. Moreover, care in terms of the manufacturability and recyclability of the BPE solutions addressed in this work was employed. This will evidently be the subject of later Chapters.

Chapter 3

Fundamentals of Solid Mechanics

This Chapter provides the reader with the fundamentals of Solid Mechanics behind the numerical analyses performed in this work. Therefore, basic concepts for the analysis of structures, such as the stress tensor, the strain field, the equilibrium equations, and the generalised Hooke's Law, are defined.

For a Three-Dimensional (3D) problem, the stress state at a given point is defined by three components on each of the three orthogonal axes. The stress components can be assembled into a matrix representation of the stress tensor (Equation 3.1) [71].

$$\boldsymbol{\sigma} = \begin{bmatrix} \sigma_{xx} & \sigma_{xy} & \sigma_{xz} \\ \sigma_{yx} & \sigma_{yy} & \sigma_{yz} \\ \sigma_{zx} & \sigma_{zy} & \sigma_{zz} \end{bmatrix} \tag{3.1}$$

It can be derived from the equilibrium conditions of an element that the stress tensor is symmetric, i.e., $\sigma_{ij} = \sigma_{ji}$ [71]. This property enables the utilisation of the Voigt notation, a mathematical technique that allows the reduction of the tensor's order. The simplicity and compactness of this representation make it particularly advantageous in the field of computational mechanics. Equation 3.2 illustrates the application of the aforesaid notation in Equation 3.1 [72].

$$\boldsymbol{\sigma} = \begin{Bmatrix} \sigma_{xx} & \sigma_{yy} & \sigma_{zz} & \sigma_{xy} & \sigma_{yz} & \sigma_{zx} \end{Bmatrix}^T \tag{3.2}$$

For a body subjected to the action of a system of arbitrary forces, the stress distribution must fulfil two requirements: the global equilibrium of the body as a whole and the local equilibrium of each infinitesimal element within the body. It can be shown that for the 3D case, the equations of equilibrium can be established as shown in the system of Equations 3.3 [73],

$$\begin{aligned} \frac{\partial \sigma_{xx}}{\partial x} + \frac{\partial \tau_{xy}}{\partial y} + \frac{\partial \sigma_{xz}}{\partial z} + X = 0 \\ \frac{\partial \tau_{xy}}{\partial x} + \frac{\partial \sigma_{yy}}{\partial y} + \frac{\partial \tau_{yz}}{\partial z} + Y = 0 \\ \frac{\partial \tau_{xz}}{\partial x} + \frac{\partial \tau_{yz}}{\partial y} + \frac{\partial \sigma_{zz}}{\partial z} + Z = 0 \end{aligned} \tag{3.3}$$

where X, Y, and Z represent the body forces along the Cartesian axis applied to the element.

For illustration purposes, the 2D representation of an infinitesimal element with stresses and body forces in equilibrium, is represented in Figure 3.1.

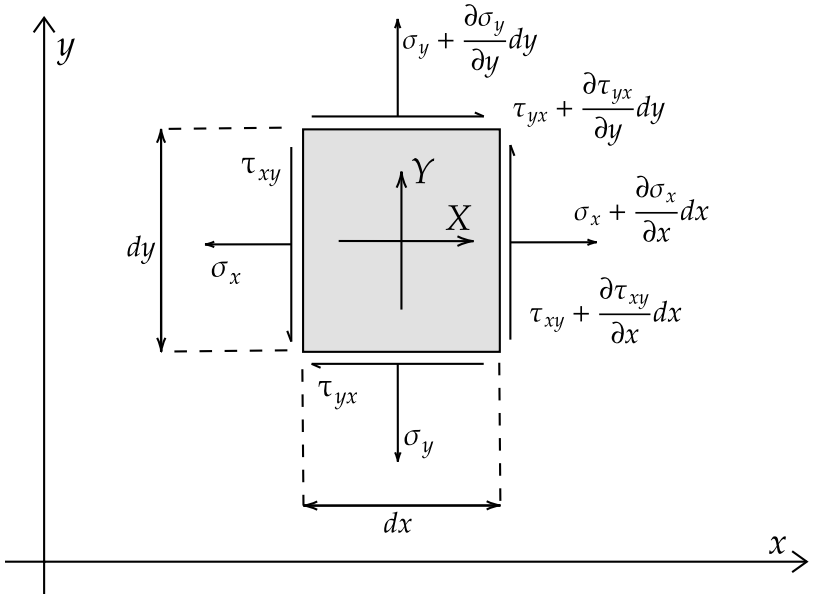


Figure 3.1: Two-dimensional representation of an infinitesimal element of a body, with stresses and body forces (Adapted from [71]).

Analogously to the stress tensor, the strain tensor of an infinitesimal element is defined by three normal and six shear strain components. As presented in Equation 3.4, these quantities can be determined from the displacement field, which comprises the displacements u, v, and w along the axes of the Cartesian coordinate system, x, y, and z, respectively [71].

$$\begin{aligned} \varepsilon_{xx} &= \frac{\partial u}{\partial x} \\ \varepsilon_{yy} &= \frac{\partial v}{\partial y} \\ \varepsilon_{zz} &= \frac{\partial w}{\partial z} \\ \gamma_{xy} &= \frac{\partial v}{\partial x} + \frac{\partial u}{\partial y} \\ \gamma_{xz} &= \frac{\partial w}{\partial x} + \frac{\partial u}{\partial z} \\ \gamma_{yz} &= \frac{\partial w}{\partial y} + \frac{\partial v}{\partial z} \end{aligned} \tag{3.4}$$

The matrix representation of the strain tensor is provided in Equation 3.5, while the corresponding Voigt notation is represented in Equation 3.6 [71],

$$\boldsymbol{\varepsilon} = \begin{bmatrix} \varepsilon_{xx} & \varepsilon_{xy} & \varepsilon_{xz} \\ \varepsilon_{yx} & \varepsilon_{yy} & \varepsilon_{yz} \\ \varepsilon_{zx} & \varepsilon_{zy} & \varepsilon_{zz} \end{bmatrix} \tag{3.5}$$

$$\boldsymbol{\varepsilon} = \begin{Bmatrix} \varepsilon_{xx} & \varepsilon_{yy} & \varepsilon_{zz} & \gamma_{xy} & \gamma_{yz} & \gamma_{zx} \end{Bmatrix}^T \tag{3.6}$$

where $\gamma_{ij} = 2\varepsilon_{ij}$.

The relation between the stress and the strain can be expressed by the generalised Hooke's Law (Equation 3.7). This law represents the most general linear relation among all the components of the stress and strain tensor [72],

$$\boldsymbol{\sigma} = \mathbf{C}\boldsymbol{\varepsilon} \tag{3.7}$$

where $\mathbf{C}$ is the stiffness tensor of material properties.

For a generic case, the stiffness tensor presents 81 and 16 components for 3D and 2D cases, respectively. However, making use of the minor symmetries of the aforesaid tensor, which result from the symmetry of the stress and strain conditions, it is possible to reduce the number of material constants to 21, in a 3D problem, for the most general anisotropic linear elastic material [72].

The constitutive law for an isotropic, linear elastic and homogeneous material is presented in Equation 3.8 [72],

$$\mathbf{C} = \lambda(\boldsymbol{I} \otimes \boldsymbol{I}) + 2\mu\mathbf{I} \tag{3.8}$$

in which: $\boldsymbol{I}$ is the second-order identity tensor, $\mathbf{I}$ is the symmetric fourth-order identity tensor and λ and μ correspond to the Lamé constants. Notice how for an isotropic material the constitutive matrix is expressed by only two independent constants.

The fourth-order stiffness tensor is often found in the literature in Voigt notation, expressed in terms of the engineering constants of E, Young's Modulus, ν, the Poisson's ratio, and G, the shear modulus. The relationship between these coefficients and the Lamé constants is established in Equation 3.9 [72].

$$G = \mu, \quad E = \frac{\mu(3\lambda + 2\mu)}{\lambda + \mu}, \quad \nu = \frac{\lambda}{2(\lambda + \mu)}, \quad \lambda = \frac{\nu E}{(1+\nu)(1-2\nu)} \tag{3.9}$$

These relationships illustrate that the engineering constants are intrinsically dependent on each other, enabling the derivation of the following expression that relates all three constants (Equation 3.10) [71].

$$G = \frac{E}{2(1+\nu)} \tag{3.10}$$

Finally, $\mathbf{C}$ can be established as shown in Equation 3.11 for isotropic materials.

$$\mathbf{C} = \frac{E}{(1-2\nu)(1+\nu)} \begin{bmatrix} 1-\nu & \nu & \nu & 0 & 0 & 0 \\ \nu & 1-\nu & \nu & 0 & 0 & 0 \\ \nu & \nu & 1-\nu & 0 & 0 & 0 \\ 0 & 0 & 0 & \frac{(1-2\nu)}{2} & 0 & 0 \\ 0 & 0 & 0 & 0 & \frac{(1-2\nu)}{2} & 0 \\ 0 & 0 & 0 & 0 & 0 & \frac{(1-2\nu)}{2} \end{bmatrix} \tag{3.11}$$

Chapter 4

Fundamentals of the Finite Element Method

In this Chapter, the FEM fundamentals, particularly those related to explicit dynamics, are explored. First, the relevance of the method is noted by its advantages over other (numerical) techniques, and its modelling approach is discussed. General concepts, such as the weak and strong form, the stiffness matrix, and element formulation, are addressed. Then, the subject of study becomes the dynamic analysis in FEM. Time integration techniques are discussed, with a focus on the explicit integration algorithm and how it differs from the implicit one. Concepts such as time step and mass scaling are explained.

4.1 Finite Element Method

The behaviour of most components and/or structures is governed by one or more partial differential equations, associated generally with intricate boundary conditions and complex geometries. The solution to these equations can be obtained by diverse approaches, for instance, analytical and numerical methods. In opposition to the former, the latter technique is capable of providing approximate solutions for complex problems of practical importance [74].

Out of all the existing numerical techniques, the finite element method is the most extensively used at academic and industrial levels. Importantly for this work, this method allows solving a wide spectrum of Solid and Structural Mechanics problems, in which the primary aim is to obtain the displacement, deformation, and stress fields. Therefore, terminology mostly related to this field will be utilised further to discuss FEM [36, 44, 74].

Resorting to FEM for computer-based simulations entails significant advantages over other methods for design engineers [36, 74]:

- Enablement of the analysis of bodies with arbitrary geometry, loads, and boundary conditions, allowing a close resemblance between the model and the actual object.
- Reductions in the number of iterations necessary to design new solutions mean less time and cost employed in their development and more time for quality assessment.
- Permits both the design and performance optimisation of the components and the entire system prior to the prototyping and manufacturing stages.
- Analysis of a vast range of problems, from quasi-static to time-dependent or eigenvalue, and the study of cases where material and geometric nonlinearities are present.

- Tool for solving problems from diverse physical fields, for instance, Fluid Mechanics, Heat Transfer, and Acoustic.

As stated in Chapter 2, FEM owns its name to its fundamental idea of representing the continuum or body of matter as an assembly of subdivisions, i.e., finite elements. These elements are interconnected at a discrete number of nodes, or nodal points, which are located on the finite element's boundaries. The variation of the field variable, in this case, the displacements of the nodes, corresponds to the unknown parameters of the problem.

It is assumed that the state of displacement within each element can be defined in terms of an approximating function (also termed "interpolation model") dependent on the nodal displacements. Likewise, the state of strain within an element is defined in terms of nodal displacements. The stress state of the element and its boundaries, in turn, is defined by the aforesaid strains, the initial ones, and the material's elastic properties. The determination of a system of forces concentrated on the nodal points that counterbalances the boundary stresses and any distribution loads takes place [46, 75].

An effective computational method must have a solid mathematical and physical basis, i.e., yield convergent solutions and be applicable to practical problems, as is the case of FEM. The FEM modelling approach is schematised in Figure 4.1.

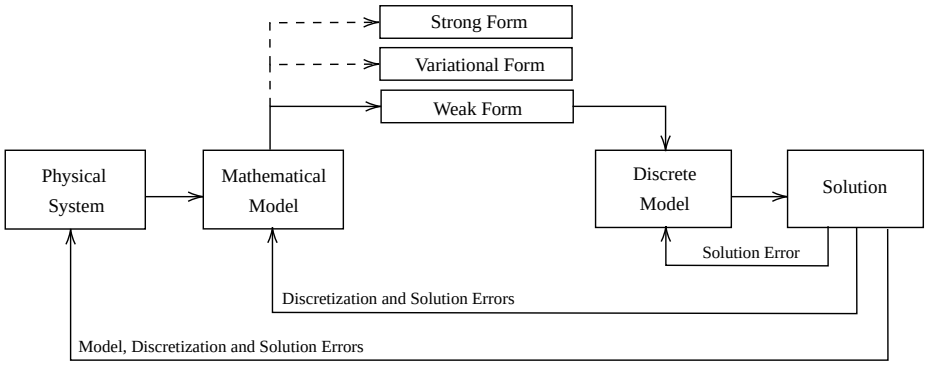


Figure 4.1: Iterative modelling approach based on numerical approximations of physical problems (Adapted from [74]).

The differential equations governing a physical system must obey the equilibrium equations or another type of equilibrium equations that directly results from simplifications of the former. Hence, the strong form consists of a system of ordinary or partial differential equations in space and/or time related to suitable boundary conditions and to be verified locally. Understandably, since the aforementioned equations must be met at any mathematical point of the domain, it is challenging to solve them if the physical problem is complex [74, 76].

The weak form formulation emerges as an answer to this concern. The weighted integral statement achieves the approximate solution to the problem through a discretized system of N algebraic equations instead of solving the differential equations that govern the system. At every integration point, the weak form is established, leading to an average domain equilibrium condition. This entails that the number of nodal points in which the problem domain is discretized influences the precision of the obtained solution. Generally, a higher nodal density yields more accurate results than a lower one. Furthermore, the task of imposing boundary conditions is also simplified by the weak form since they can be applied directly to the nodes [74, 76].

To explain the fundamental formulation of the finite element characteristics, two main approaches can be taken, a so-called "direct" formulation and an energy approach, equivalent

to each other. Considering the FEM as a variational approach contributed significantly to formulating and solving problems in different engineering fields in a unified manner. Hence, an energetic approach was chosen to address the FEM fundamentals in this manner.

4.1.1 Principal of Minimum Potential Energy

A functional can be interpreted as a function of various other functions. In simple terms, the fundamental problem in variational calculus is to find the function $\phi(x)$ that makes the functional in Equation 4.1 stationary,

$$I = \int_{x1}^{x2} F(x, \phi, \phi_x, \phi_{xx})\, dx \tag{4.1}$$

where x is the independent variable, $\phi_x = \frac{d\phi}{dx}$, $\phi_{xx} = \frac{d^2\phi}{dx^2}$, I and F are functionals [75].

The functional I often finds diverse physical meanings across most applications. In the case of Solids and Structural Mechanics, it corresponds to the potential energy, V, which is a function of the displacement vector $\boldsymbol{\phi}$, whose components (u, v and w) in turn depend on the coordinates x, y, z. In this field, the principle of minimum potential energy, a variational formulation method, can be used to solve the problem in question [75].

Since the above-mentioned energy principle will be utilised to derive the basic formulation of finite element equations, it is crucial to have a solid understanding of what it states. Therefore, let us consider the body represented in Figure 4.2, in which the domain Ω is bounded by Γ, where the surface forces, $\boldsymbol{t}$ act. $\boldsymbol{b}$ represents the known body forces.

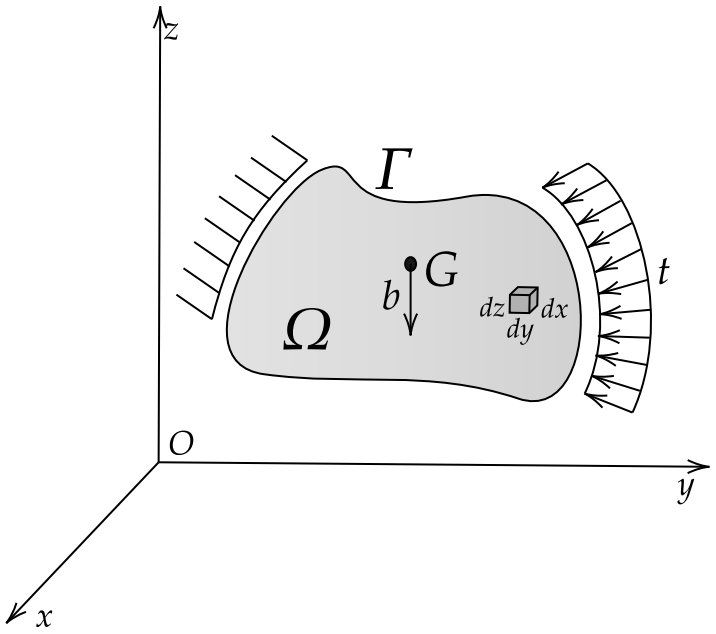


Figure 4.2: Continuous body subjected to body and surface forces (Adapted from [76]).

The potential energy of an elastic body, V, be defined as shown in Equation 4.2,

$$V = U - W_f \tag{4.2}$$

where U represents the strain energy and W_f is the external forces' work on the body.

The principle of minimum potential energy declares that, out of all possible displacement states a body can assume that simultaneously satisfy compatibility as well as the kinematic and displacement boundary conditions, that which makes the potential energy achieve a minimum value, satisfies the equilibrium conditions. Therefore, at the equilibrium state, the principle of minimum potential energy (expressed in terms of the displacements u, v, and w) yields the expression given in Equation 4.3 [75].

$$\delta V(u, v, w) = \delta U(u, v, w) - \delta W_f(u, v, w) = 0 \tag{4.3}$$

Note that the forces and stresses are hypothesised as constant, the variations are related to the displacements only.

Equation 4.4 defines the strain energy of a linear elastic body [75].

$$U = \frac{1}{2} \int_{\Omega} \boldsymbol{\varepsilon}^T \boldsymbol{\sigma} d\Omega \tag{4.4}$$

Recalling the stress-strain relations addressed in Chapter 3, by considering the presence of initial strains $\boldsymbol{\varepsilon_0}$, the strain energy is defined as shown in Equation 4.5 [75].

$$U = \frac{1}{2} \int_{\Omega} \boldsymbol{\varepsilon}^T \mathbf{C} \boldsymbol{\varepsilon} d\Omega - \int_{\Omega} \boldsymbol{\varepsilon}^T \mathbf{C} \boldsymbol{\varepsilon}_0 d\Omega \tag{4.5}$$

The work performed by external forces is given by Equation 4.6 [75],

$$W_f = \int_{\Omega} \boldsymbol{u}^T \boldsymbol{b} d\Omega + \int_{\Gamma} \boldsymbol{u}^T \boldsymbol{t} d\Gamma \tag{4.6}$$

where $\boldsymbol{u}$ represents the displacement vector.

Finally, from 4.5 and 4.6, the potential energy of the body can be expressed as shown in Equation 4.7 [75].

$$V(u, x, w) = \frac{1}{2} \int_{\Omega} \boldsymbol{\varepsilon}^T \mathbf{C} (\boldsymbol{\varepsilon} - 2\boldsymbol{\varepsilon}_0) - \int_{\Omega} \boldsymbol{u}^T \boldsymbol{b} d\Omega - \int_{\Gamma} \boldsymbol{u}^T \boldsymbol{t} d\Gamma \tag{4.7}$$

Having laid out the framework of the principle of minimum potential energy, it can now be used to derive the finite element equations. Thus, the displacement field within each element will be assumed by a simple form of variation, and the conditions for which the functional I (i.e., V) are minimised are derived, establishing the equivalence relation between the strong and the weak forms [75, 74].

The resulting approximate equilibrium equations safeguard the compatibility conditions and the natural boundary conditions, which are ensured by the formulation of a variational principle itself. Therefore, only the geometric boundary conditions must be enforced on the solution [75].

4.1.2 Formulation of Finite Element Equations

In this section, the equilibrium equations for a 3D static problem will be derived by resorting to the principle of minimum potential energy. The purpose of this is to gift the reader the crucial fundamentals of the currently assessed method in a brief and simple manner.

Having discretized the body in a number E of finite elements, given the fact that the nodal displacements are the unknowns of the present problem, it is necessary to express both the displacements and the potential energy by means of the nodal degrees of freedom [46].

Hence, within a typical element e, the state of displacement is assumed as provided in Equation 4.8 [75],

$$\boldsymbol{u} = \begin{Bmatrix} u(x,y,z) \\ v(x,y,z) \\ w(x,y,z) \end{Bmatrix} = \mathbf{N}\boldsymbol{d}^{(e)} \tag{4.8}$$

where $\mathbf{N}$ represents the matrix of shape functions and $\boldsymbol{d}^{(e)}$ the vector of the nodal displacements of the element.

The potential energy functional of the body is defined by the sum of the potential energies of individual elements, $V^{(e)}$, considering solely the body and surface forces. It can be written as given in Equation 4.9 [75].

$$V = \sum_{e=1}^{E} V^{(e)} \tag{4.9}$$

By manipulation of Equation 4.7, the potential energy of an element e is defined by Equation 4.10 [75].

$$V^{(e)} = \frac{1}{2}\int_{\Omega^{(e)}} \boldsymbol{\varepsilon}^T \mathbf{C}(\boldsymbol{\varepsilon} - 2\boldsymbol{\varepsilon}_0) - \int_{\Omega^{(e)}} \boldsymbol{u}^T \boldsymbol{b} d\Omega - \int_{\Gamma^{(e)}} \boldsymbol{u}^T \boldsymbol{t} d\Gamma \tag{4.10}$$

The strain vector, whose components were already presented in Equation 3.4 of the previous Chapter, can also be expressed as a function of the nodal displacement vector $\boldsymbol{d}^e$. This is provided in Equation 4.11 [75],

$$\boldsymbol{\varepsilon} = \mathbf{B}\,\boldsymbol{d}^{(e)} \tag{4.11}$$

where $\mathbf{B}$ represents the strain matrix, shown in Equation 4.12.

$$\mathbf{B} = \begin{bmatrix} \frac{\partial}{\partial x} & 0 & 0 \\ 0 & \frac{\partial}{\partial y} & 0 \\ 0 & 0 & \frac{\partial}{\partial z} \\ \frac{\partial}{\partial y} & \frac{\partial}{\partial x} & 0 \\ 0 & \frac{\partial}{\partial z} & \frac{\partial}{\partial y} \\ \frac{\partial}{\partial z} & 0 & \frac{\partial}{\partial x} \end{bmatrix} \mathbf{N} \tag{4.12}$$

Considering the stress-strain relations already explored, the stresses now can be obtained as showcased in Equation 4.13. Then, the potential energy of the element is calculated by Equation 4.14 [75].

$$\boldsymbol{\sigma} = \mathbf{C}(\boldsymbol{\varepsilon} - \boldsymbol{\varepsilon_0}) = \mathbf{C}\,\mathbf{B}\,\boldsymbol{d}^{(e)} - \mathbf{C}\,\boldsymbol{\varepsilon_0} \tag{4.13}$$

$$\begin{aligned} V^{(e)} = \frac{1}{2}\int_{\Omega^{(e)}} \boldsymbol{d}^{(e)T}\mathbf{B}^T\mathbf{C}\mathbf{B}\boldsymbol{d}^{(e)} d\Omega - \int_{\Omega^{(e)}} \boldsymbol{d}^{(e)T}\mathbf{B}^T\mathbf{C}\boldsymbol{\varepsilon_0} d\Omega - \\ \int_{\Gamma^{(e)}} \boldsymbol{d}^{(e)T}\mathbf{N}^T\boldsymbol{t} d\Gamma - \int_{\Omega^{(e)}} \boldsymbol{d}^{(e)T}\mathbf{N}^T\boldsymbol{b} d\Omega \end{aligned} \tag{4.14}$$

Although Equations 4.10 and 4.14 consider only body and surface forces, often the nodes are also subject to external concentrated forces. Let $\boldsymbol{F}$ represent the vector of nodal forces acting in the direction of the nodal displacement vector $\boldsymbol{d}$ of the entire body. Thus, the

total potential energy of the structure must account for this new term [75]. Equation 4.15 represents this new condition.

$$V = \sum_{e=1}^{E} V^{(e)} - \boldsymbol{d}^T \boldsymbol{F} \tag{4.15}$$

The summation in Equation 4.15 entails the expansion of the element matrices to body size ones, followed by the summation of overlapping terms. Therefore, the above-mentioned equations yield Equation 4.16, which represents the total energy of the body in terms of the nodal displacements, $\boldsymbol{d}$ [75].

$$\begin{aligned} V = \frac{1}{2}\boldsymbol{d}^T \left[\sum_{e=1}^{E} \int_{\Omega^{(e)}} \mathbf{B}^T \mathbf{C} \mathbf{B} d\Omega\right] \boldsymbol{d} - \boldsymbol{d}^T \sum_{e=1}^{E} \left(\int_{\Omega^{(e)}} \mathbf{B}^T \mathbf{C} \boldsymbol{\varepsilon_0} d\Omega + \right. \\ \left. \int_{\Gamma^{(e)}} \mathbf{N}^T \boldsymbol{t} d\Gamma + \int_{\Omega^{(e)}} \mathbf{N}^T \boldsymbol{b} d\Omega \right) \text{-} \boldsymbol{d}^T \boldsymbol{F} \end{aligned} \tag{4.16}$$

As discussed previously, the static equilibrium configuration of the body can be found by establishing and solving a system of equations that stipulates the necessary conditions for the minimisation of the potential energy. This is expressed in Equation 4.18 [46, 75].

$$\frac{\partial V}{\partial \boldsymbol{d}} = \mathbf{0} \tag{4.17}$$

Equation 4.19 is obtained from the previous equation, by considering Equation 4.16 [75],

$$\left(\sum_{e=1}^{E} \mathbf{K}^{(e)}\right) \boldsymbol{d} = \boldsymbol{F} + \sum_{e=1}^{E} \left(\boldsymbol{F}_i^{(e)} + \boldsymbol{F}_t^{(e)} + \boldsymbol{F}_b^{(e)}\right) = \boldsymbol{F}_t \tag{4.18}$$

where $\boldsymbol{F_t}$ denotes the vector of total nodal forces and Equations 4.19, 4.20, 4.21 and 4.22 represent, respectively, the element stiffness matrix, the element load vector due to initial strains, the element load vector due to surface reactions, and, lastly, the element load vector due to body forces [75].

$$\mathbf{K}^{(e)} = \int_{\Omega^{(e)}} \mathbf{B}^T \, \mathbf{C} \, \mathbf{B} \, d\Omega \tag{4.19}$$

$$\boldsymbol{F}_i^{(e)} = \int_{\Omega^{(e)}} \mathbf{B}^T \, \mathbf{C} \, \varepsilon_0 \, d\Omega \tag{4.20}$$

$$\boldsymbol{F}_t^{(e)} = \int_{\Gamma^{(e)}} \mathbf{N}^T \, \boldsymbol{t} \, d\Gamma \tag{4.21}$$

$$\boldsymbol{F}_b^{(e)} = \int_{\Omega^{(e)}} \mathbf{N}^T \, \boldsymbol{b} \, d\Omega \tag{4.22}$$

The equilibrium equations of the body can then be condensed into Equation 4.23 [75],

$$\mathbf{K}\boldsymbol{d} = \boldsymbol{F}_t \tag{4.23}$$

where the global (or assembled) stiffness matrix is given by Equation 4.24 and the global nodal load vector by Equation 4.25.

$$\mathbf{K} = \sum_{e=1}^{E} \mathbf{K}^{(e)} \tag{4.24}$$

$$\boldsymbol{F}_t = \boldsymbol{F} + \sum_{e=1}^{E} \left(\boldsymbol{F}_i^{(e)} + \sum_{e=1}^{E} \boldsymbol{F}_t^{(e)} + \sum_{e=1}^{E} \boldsymbol{F}_b^{(e)} \right) \tag{4.25}$$

From Equation 4.23, the solution for the nodal displacements and element stresses can be achieved after incorporating the suitable boundary conditions.

Finally, as end notes, it is important to mention four pertinent considerations [75]:

- Even though the formulae presented from Equations 4.19 to 4.22 does not change with the type of element being considered, the latter parameter does influence the orders of the stiffness matrix and load vector.
- Local coordinate systems are typically used to compute the element stiffness matrices and element load vectors as a way to reduce the computational effort. These must then be transformed to a global coordinate system before using Equations 4.24 and 4.25.
- In this derivation, both the element and the global stiffness matrices are always symmetric, as is the matrix $\mathbf{C}$ and the product $\mathbf{B}^T\,\mathbf{C}\,\mathbf{B}$;
- To solve the equilibrium equations, the non-singularity condition of the stiffness matrices must be verified.

4.1.3 Mesh Generation

To enrich the scope of the present Chapter, the diverse element types used in FEM, some of which will be resorted to in the posterior numerical analysis performed within this work, are presented. The derivations of the properties and formulations of each element will not be assessed; however, their definition and main characteristics are stated, providing the reader with an improved understanding of the rationale for several choices made in later Chapters.

As stated before, the core of the FEM consists of the discretisation of a continuum body or structure into finite elements. This discretisation can be done by resorting to diverse element types, whose selection depends on various factors. The generation of a finite element mesh should consider the following factors for a given problem: 1) the mesh must suitably reproduce the geometry of the computational domain and load; 2) Large gradients in the solution should be accurately represented; 3) Elements with unacceptable geometries should be avoided, particularly in zones of large gradients [44].

Adequate element selection and mesh generation are crucial to the obtainment of accurate results while simultaneously saving computational efforts. Choosing the employed element types and the mesh refinement levels are problem-dependent parameters. Selecting the best combination of these factors is therefore expected from the analyst. [44].

For 1D problems, truss (or rod), beam, or frame elements (Figure 4.3) can be utilised. The difference between these relies on the loads each is capable of enduring. Truss elements can only carry either tensile or compressive axial loads, deforming exclusively in the axial direction. Beam elements endure bending solicitations, such as the case of Euler-Bernoulli or Timoshenko beams. Frame elements represent a combination of the previous element types, carrying both mentioned solicitation conditions. Evidently, the allowed translational and rotational displacements of the nodes of each element vary depending on the element itself [75, 74].

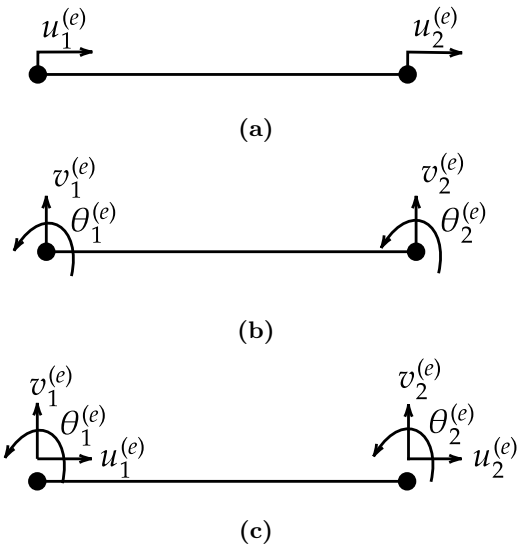


Figure 4.3: 1D elements and respective local degrees of freedom. **(a)** Two-noded generalised rod element. **(b)** Two-noded generalised beam element. **(c)** Two-noded generalised frame element.

For 2D problems, triangular or quadrilateral elements (Figure 4.4) can be utilised. Each may be linear or quadratic, depending on the number of nodes of the element being considered.

Triangular elements can be linear (i.e., of first order), possessing three nodes, or quadratic (second order elements), with six nodes, half of the nodal points in the corners, and the other in the midpoint of the sides. Linear triangular elements present a constant strain matrix, since **B** is independent of the position within the element. Therefore, this element is often termed a "Constant-Strain Triangle" or CST. Second-order triangular elements, in turn, present an improved stiffness behaviour in bending, and in spite of a relatively simple mesh generation, they are increasingly computationally expensive [75, 44].

In linear quadrilateral elements, contrary to the linear triangular element, the strain matrix is no longer constant. Quadratic quadrilateral elements evidently also represent the stiffness behaviour in bending more realistically and allow for a mesh with fewer elements to achieve satisfactory results. However, they are computationally expensive and entail a more complex mesh generation. The Lagrange quadratic quadrangular element has nine nodes: four on the corners of the element, four on the midpoints of the sides, and one in the centre of the element. As the internal nodal points of the higher-order elements of the Lagrange family do not contribute to interelement connectivity, they can often be disregarded in the name of reducing the element matrices. Serendipity elements are a representation of this condition, as all the nodes are positioned on the element boundary [44].

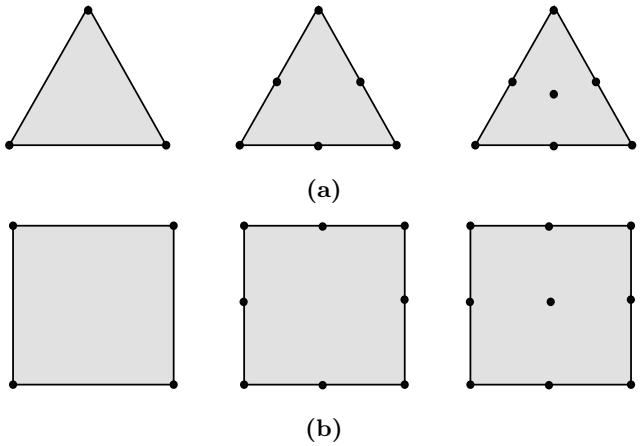


Figure 4.4: Linear and quadratic, Serendipity and Lagrange 2D elements (left, centre and right) **(a)** Triangular elements. **(b)** Quadrangular elements.

In 3D problems, a great number of elements is used to obtain reasonably accurate results, meaning that a significant amount of simultaneous equations is solved in static analyses.

Just like the triangular element is the basic element in 2D problems, the tetrahedron, with four nodal corners, is the basis for modelling 3D problems. As before, the linear variation of a quantity is defined by the now four nodal values. For a full quadratic expansion in a 3D case ten nodes are needed, placed in the corners and mid-sides of the tetrahedron. The corresponding 3D element to the 2D quadrangular one is the hexahedron: the simplest of which has eight corner nodes, and the second-order one which in this case presents twenty nodes. Figure 4.5 portrays the aforesaid solid elements [44, 46].

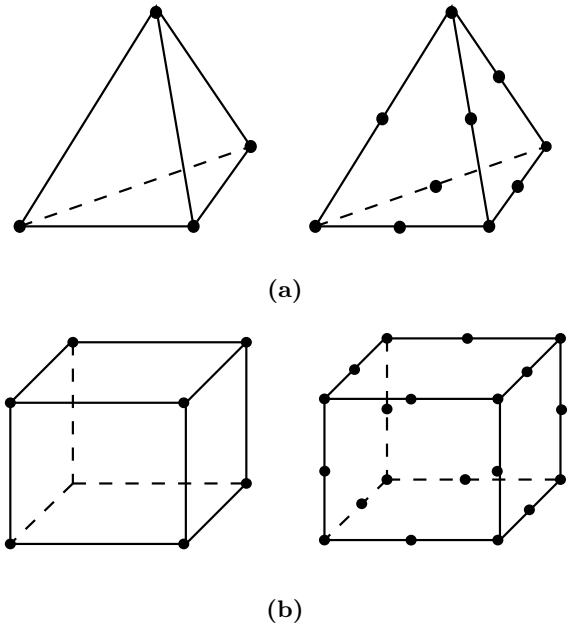


Figure 4.5: Linear and quadratic 3D elements (left and right). **(a)** Tetrahedron elements. **(b)** Hexahedron elements.

4.1.4 Numerical Integration

When possible, integration of a function is best conducted analytically to obtain the integral in closed form. However, it is frequently difficult, or even impossible, to achieve a result in this manner. In this scenario, the integral must be obtained numerically, with numerous methods being accessible for this purpose.

Recall that the numerical quadrature concept is the basis for automating the calculation of stiffness matrices and equivalent nodal force vectors in FEM [77]. Moreover, in FE applications, the Gauss method, particularly the Gauss-Legendre quadrature, has proven to be the most helpful out of the various schemes available for the numerical evaluation of definite integrals. This explains its extensive use in FEM, as well as its assessment in the theoretical portion of this work [75].

In general, the integral can be approximated by a quadrature formula, represented in Equation 4.26,

$$\int_a^b f(x)\,dx \approx \sum_{i=1}^{n} w_i f(x_i) \tag{4.26}$$

where f_i is the function value at the point where the function is evaluated, w_i is the weight associated with that i^{th} point and n is the number of integration points [78].

The Gauss quadrature is an open quadrature rule, as it resorts to function values evaluated at a number of interior points and corresponding weights to approximate the integral by means of a weighted sum. The location of the integration points, also designated "Gauss points", is the one that enables the obtainment of the greatest accuracy for a given number of them [75, 78].

Some of the fundamentals of the Gauss quadrature is that it addresses integration over a symmetrical range of $x \in [-1, 1]$. In addition, this quadrature yields exact values of integrals for polynomials of degrees up to $2n-1$. To respect the limits of the domain associated with the Gauss quadrature formulation, variable transformation is often employed, and the natural coordinate system is utilised [78].

Thus, to further develop the expression presented in Equation 4.26, consider Equation 4.27, in which a polynomial function $F(\xi)$ of degree p, in the domain $\xi \in [-1, 1]$ is portrayed. By numerical integration using the Gauss-Legendre quadrature, the exact integral of the aforesaid function, in the referred domain, can be achieved by summing the values of the function at the n specific quadrature points multiplied by the corresponding weights assuming, as stated above, that $p < 2n-1$ [78].

$$\int_{-1}^{1} F(\xi)\,dx \approx \sum_{i=1}^{n} w_i F(\xi_i) \tag{4.27}$$

Multidimensional integrals are computed by repeatedly applying 1D quadrature rules; however, the integrals associated with different elements differ in between themselves. For exemplification purposes, consider, for instance, a 2D quadrangular element. In this case, the Gauss quadrature formula is obtained by integrating first with respect to one coordinate, followed by the second one (Equation 4.28) [75, 79].

$$\int_{-1}^{1}\int_{-1}^{1} f(\xi,\eta)\,d\xi d\eta \approx \int_{-1}^{1}\left[\sum_{i=1}^{n} w_i f(\xi_i,\eta)\right] d\eta = \sum_{j=1}^{n} w_j \left[\sum_{i=1}^{n} w_i f(\xi_i,\eta_j)\right] \quad = \quad \sum_{i=1}^{n}\sum_{j=1}^{n} w_i w_j f(\xi_i,\eta_j) \tag{4.28}$$

Additionally, in Table 4.1 are represented the locations of the Gauss points, in the natural coordinate system, and the respective weights, taking into account values of n ranging from 1 to 5 in a 2D quadrangular element.

Table 4.1: Quadrature point's locations and weights for Gauss-Legendre quadrature [77]

Number of Gauss points (n)	**Coordinates (ξ_i)**	**Weights (w_i)**
1	0	2
2	$\pm\sqrt{\frac{1}{3}}$	1
3	0	$\frac{8}{9}$
	$\pm\sqrt{\frac{3}{5}}$	$\frac{5}{9}$
4	$\pm\sqrt{\frac{3}{7}-\frac{2}{7}\sqrt{\frac{6}{5}}}$	$\frac{18+\sqrt{30}}{36}$
	$\pm\sqrt{\frac{3}{7}+\frac{2}{7}\sqrt{\frac{6}{5}}}$	$\frac{18-\sqrt{30}}{36}$
5	0	$\frac{128}{225}$
	$\pm\frac{1}{3}\sqrt{5-2\sqrt{\frac{10}{7}}}$	$\frac{322+13\sqrt{70}}{900}$
	$\pm\frac{1}{3}\sqrt{5+2\sqrt{\frac{10}{7}}}$	$\frac{322-13\sqrt{70}}{900}$

Lastly, it is worth mentioning that hourglass strain modes can be found in the 2D elements discussed above for plane elasticity when the stiffness matrix is integrated using exclusively one Gauss point, i.e., in a reduced form. With reduced integration, the stiffness matrix characteristic decreases, thereby increasing the algebraic multiplicity of the null eigenvalues. This leads to the introduction of null energy strain modes that, for this element, can propagate throughout the entire mesh [77].

In addition, however, reduced integration can be useful for particular applications. For thin plates under bending, the transverse shear strains are negligible and, therefore, the element stiffness matrix yields inaccurate results, i.e., an overly stiff behaviour of the structure, consequent of the generalised displacements. In this problem, if using quadrangular elements, the one-point Gauss rule should be employed to evaluate the shear energy terms and, thus, improve the stiffness behaviour. Quadratic quadrangular elements, however, do not endure this phenomenon in full integration [77].

4.2 Dynamic Analysis in FEM

The analysis of systems or structures under time-varying loads or motion is referred to as a dynamic problem. This class of problems analyses the system's dynamic behaviour over time, including the effects of inertia, damping, and external forces. The primary purpose of dynamic analysis is, thus, to comprehend the response of the system to this time-dependent elements [74].

Structural Mechanics problems generally entail the solving of the generic differential system of equations of motion presented in Equation 4.29, as it describes the dynamic behaviour of a discrete linear system with n degrees of freedom [74].

$$\mathbf{M}\ddot{\boldsymbol{u}}(t) + \mathbf{D}\dot{\boldsymbol{u}}(t) + \mathbf{K}\boldsymbol{u}(t) = \boldsymbol{F}(t) \tag{4.29}$$

where, $\mathbf{M}$ represents a general mass matrix, $\mathbf{D}$ is a general damping matrix, $\mathbf{K}$ is a general stiffness matrix, $\boldsymbol{F}(t)$ is the external forces vector and $\boldsymbol{u}$ a general displacement vector [80, 74].

This equation is solved for the unknown time-dependent quantities, i.e., the displacement, velocity and acceleration, from which it is possible to derive other physical quantities, such as the strain, stress, and reaction forces [80].

To obtain the solution for this system of equations the initial conditions of the problem must be known. They are presented for a general case in Equation 4.30 [74].

$$\begin{aligned} \boldsymbol{u}(t=0) &= \boldsymbol{u}_0 \\ \dot{\boldsymbol{u}}(t=0) &= \dot{\boldsymbol{u}}_0 \end{aligned} \tag{4.30}$$

For certain problems, such as in harmonic analyses, the solution can be obtained following an analytical approach. However, as stated previously, typically numerical methods are required. This path involves a process of time discretisation with a given time step and a suitable time integration scheme to describe the approximation of the solution [80]. These will be discussed in the following subsections of this project.

Interpreting FEM once again as a variational approach and focusing on dynamic problems, particularly transient dynamic ones, there are two variational methods that may be used to formulate the general variational equation. These are Hamilton's principle and the Galerkin method, both of which yield equivalent expressions for Equation 4.31. This Equation corresponds to the principle of virtual work, i.e., the weak form of the momentum equation,

$$\int_{\Omega} [\rho \boldsymbol{a}\delta\boldsymbol{x} + \boldsymbol{\sigma} : \delta\boldsymbol{\varepsilon}] d\Omega = \int_{\Omega} \rho \boldsymbol{b}\delta\boldsymbol{x} + \int_{\Gamma} \boldsymbol{t}\delta\boldsymbol{x} d\Gamma \tag{4.31}$$

where $\delta\boldsymbol{x}$ is an arbitrary bounded vector that satisfies the constraint $\delta\boldsymbol{x} = 0$ on Γ_u, the portion of the boundary Γ where the system has a specified displacement [81, 82].

From this expression, dropping the arbitrary variable, the equations of motion in the discrete weak form can be obtained, as presented in Equation 4.32,

$$\begin{aligned} \mathbf{M}_c\boldsymbol{a} &= \boldsymbol{F}^{ext}(\boldsymbol{x}, \boldsymbol{v}, t) - \boldsymbol{F}^{int}(\boldsymbol{x}, \boldsymbol{v}, \boldsymbol{\sigma}, t) \\ \boldsymbol{F}^{ext}(\boldsymbol{x}, \boldsymbol{v}, t) &= \int_{\Omega} \rho \mathbf{N}^T \boldsymbol{b} d\Omega \\ \boldsymbol{F}^{int}(\boldsymbol{x}, \boldsymbol{v}, \boldsymbol{\sigma}, t) &= \int_{\Gamma} \mathbf{B}^T \boldsymbol{\sigma} d\Omega \\ \mathbf{M}_c &= \int_{\Omega} (\rho \mathbf{N}^T \mathbf{N}) d\Omega \\ \boldsymbol{a} &= \ddot{\boldsymbol{u}}(\boldsymbol{x}, t) \end{aligned} \tag{4.32}$$

where $\mathbf{M}_c$ is the consistent mass matrix, $\boldsymbol{x}$ the coordinate, $\boldsymbol{v}$ the velocity, $\boldsymbol{a}$ the acceleration, and $\boldsymbol{F}^{ext}$ and $\boldsymbol{F}^{int}$ are the external and internal forces, respectively [81].

The relations in Equation 4.33 were considered in the equation above [81].

$$\begin{aligned} \boldsymbol{v} &= \dot{\boldsymbol{u}}(t) \\ \boldsymbol{a} &= \ddot{\boldsymbol{u}}(t) \end{aligned} \tag{4.33}$$

4.2.1 Time discretisation

From a computational perspective, temporal discretisation is evidently sought instead of determining the solution at every instant in the interval $t \in [0, T]$. This discretisation entails approximating time at discrete points within this interval by dividing it into a number N of sub-intervals as described in Equation 4.34 [77].

$$[0, T] \approx \bigcup_{n=0}^{N} [t_n, t_{n+1}] \tag{4.34}$$

A suitable integration algorithm is required to obtain the variables of interest in each time step. However, selecting the appropriate integration scheme is no easy task, as each scheme has its advantages and disadvantages in terms of stability, accuracy, and efficiency [77] [83].

The explicit integration method refers to a numerical scheme employed for integrating a system of ordinary differential equations. These equations emerge from the spatial discretisation of a continuous system. In this context, the designation "explicit" arises from the fact that the equilibrium conditions are expressed at a specific moment in time when the displacements of all spatial points have already been determined [9].

Explicit integration methods advance the solution at t^n to t^{n+1} solely based on the solution values at at $t \leq t^n$. The forward Euler corresponds to the simplest explicit integration rule and is presented in Equation 4.35, in a general form, using the y coordinate [82],

$$y^{n+1} = y^n + \Delta t \, f(t^n, y^n) \tag{4.35}$$

where $\Delta t = t^{n+1} - t^n$ is the time step and $f(t, y)$ represents the function defining the time derivative of y.

For comparison purposes, the most straightforward implicit integration rule is the backward Euler, provided in Equation 4.36, that requires also the solving of Equation 4.37. The term "implicit" results from the fact that the solution at t_{n+1} is obtained accounting for the unknown value f_{n+1} [82] [77].

$$y^{n+1} = y^n + \Delta t \, f(t^{n+1}, y^{n+1}) \tag{4.36}$$

$$y^{n+1} - \Delta t \, f(t^{n+1}, y^{n+1}) = y^n \tag{4.37}$$

While the two-time integration rules may seem identical, in the explicit method the time step is limited by a stability condition and thus, this approach is conditionally stable. The backward Euler method, on the opposite, is unconditionally stable with no limitations on the time step, except those related to accuracy [82]. The accuracy of the two methods is formally the same. However, while the convergence of the explicit time integration method is guaranteed and therefore convergence checks are not required, on the implicit rule the same is not verified [82].

To compare the two integration rules, assume that function evaluation entails a considerable cost. The implicit equation must be solved via an iterative numerical method, with each iteration requiring at least one evaluation of $f(t, y)$. Then, if the backward Euler mandates m function evaluations to solve the implicit equation, the explicit integration rule can

take m steps of $\frac{\Delta t}{m}$ for an equivalent cost and improved accuracy. Nevertheless, the implicit formulation becomes more efficient when the ratio between the required time step size for accuracy and the stable time step of the forward Euler method is greater than the number of function evaluations needed to solve Equation 4.37 [82].

The computational cost of the iteration in implicit methods is primarily determined by the solution of the system of linear algebraic equations (by Newton or quasi-Newton methods), which often significantly outweighs the cost of evaluating the function $f(t, y)$ for a large number of equations. To be competitive in terms of computational cost with explicit methods, implicit methods should take larger time steps. However, even if the accuracy requirement allows for larger time steps, the convergence behaviour of the iterative solver can impose limitations on the latter, hindering the efficiency of the implicit method [82].

With solving a Solid Mechanics problem where wave propagation is of considerable relevance, the propagation of the wave across the elements must be resolved in time, requiring a time step less or equal to the length of time required for a wave to propagate across an element. Because this constraint is identical to the stable time step sizes characteristic of explicit methods (in the order of $10^{-5} \sim 10^{-8}$), explicit methods are the best option for addressing this class of problems [82].

For problems of considerable time magnitude, the implicit method is more advantageous. Due to the stability requirement of the explicit integration rule, smaller time steps, many more time increments, and therefore a significantly lengthier procedure would be necessary. In practical terms, creep and static or dynamic problems, ranging from duration of 1 s to years, are more efficiently assessed by an implicit analysis [80].

The nature of the explicit method limits its application to short transient problems, ranging from the time magnitude of 10^{-4} s to about 10 s, i.e., until the so-called quasi-static problems (limited to cases where the inertia effects can be assumed negligible). Thus, explicit methods are widely used for applications such as drop tests, impact, and penetration problems, detonation, and ballistics. Additionally, explicit time integration is more accurate and efficient for cases involving nonlinearities: large deformations and strains, nonlinear material behaviour with failure, complex contact, fragmentation, and nonlinear buckling [80].

4.2.2 Explicit Integration Method

This subsection particularly explores the explicit time integration scheme, as it constitutes one of the principal subjects of this work. Its fundamentals and principal characteristics will be investigated to reach a comprehensive understanding of this matter.

4.2.2.1 Central Difference Integration

The central difference method is the most vastly used explicit integration method in explicit finite element and finite difference methods. The explicit scheme utilises central difference to approximate the acceleration [81].

To simplify the analysis of this method, assume that the time domain $[0, T]$ is uniformly divided into N sub-intervals, $[t_n, t_{n+1}]$, with $t_{n+1} - t_n = \Delta t = \frac{T}{N}$, as stated earlier. The finite difference method approximates the velocity and acceleration as time derivatives, as shown in the system of Equations 4.38 and 4.39 [81].

$$\begin{cases} \partial_t \boldsymbol{u}_{n+\frac{1}{2}} = \dfrac{\boldsymbol{u}_{n+1} - \boldsymbol{u}_n}{\Delta t} \sim \dot{\boldsymbol{u}}_{n+\frac{1}{2}}, \\ \partial_{t^2} \boldsymbol{u}_n = \dfrac{\partial_t \boldsymbol{u}_{n+\frac{1}{2}} - \partial_t \boldsymbol{u}_{n-\frac{1}{2}}}{\Delta t} = \dfrac{\boldsymbol{u}_{n+1} - 2\boldsymbol{u}_n + \boldsymbol{u}_{n-1}}{\Delta t^2} \sim \ddot{\boldsymbol{u}}_n \sim \dfrac{\dot{\boldsymbol{u}}_{n+\frac{1}{2}} - \dot{\boldsymbol{u}}_{n-\frac{1}{2}}}{\Delta t}, \end{cases} \tag{4.38}$$

$$\begin{cases} \partial_t \boldsymbol{u}_{n+\frac{1}{2}} = \partial_t \boldsymbol{u}_{n-\frac{1}{2}} + \partial_{t^2} \boldsymbol{u}_n \, \Delta t \\ \boldsymbol{u}_{n+1} = \boldsymbol{u}_n + \partial_t \boldsymbol{u}_{n+\frac{1}{2}} \, \Delta t \end{cases} \tag{4.39}$$

Utilising this method, the acceleration is computed resorting to Newton's second law, as presented in Equation 4.40 [81].

$$\partial_{t^2} \boldsymbol{u}_n = \mathbf{M}^{-1} \, \boldsymbol{F}_n \tag{4.40}$$

Note that in the detailed procedure, contrary to the displacement and acceleration, calculated at the beginning and end of each time step, t_n and t_{n+1}, the velocity is located at the middle of the time step, $t_{n+\frac{1}{2}} = t_n + \frac{\Delta t_{n+1}}{2}$. This is evidenced in Figure 4.6 [81].

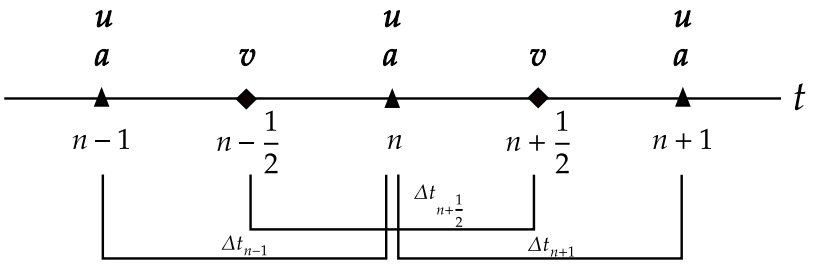


Figure 4.6: Time integration events (Adapted from [81]).

The fundamental algorithm of the explicit FEM is illustrated in Figure 4.7 for the case of an elastic material model, for simplicity purposes. The consideration of material nonlinearities would dictate the need for updates in the stress calculation process [81].

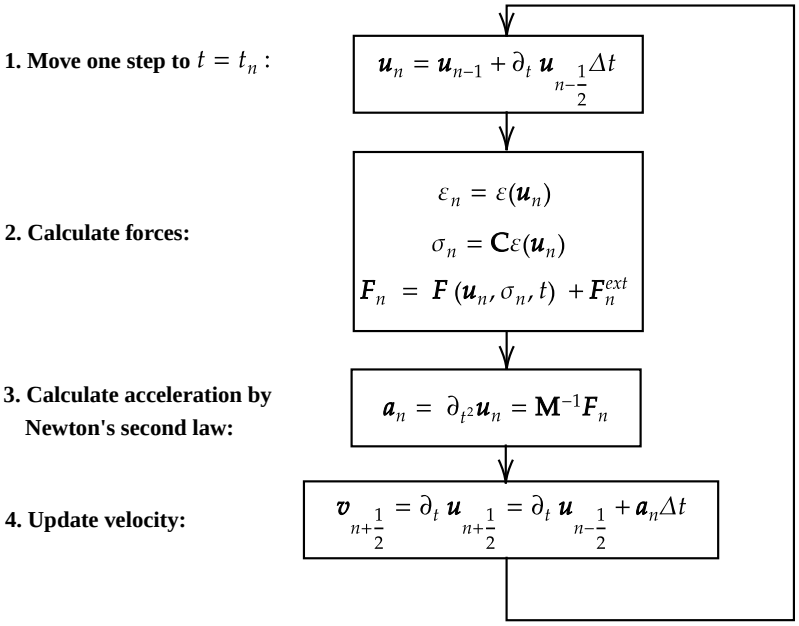


Figure 4.7: Explicit finite element algorithm (Adapted from [81]).

As is evidenced in Figure 4.7, the procedure of the explicit FEM is cyclic. Consider as the starting point for this brief exposition the direct computation of the external forces, originating from the given load conditions and the internal forces emerging from the stress, both computed following Equation 4.32. Employing the central difference method, the approximate acceleration is derived explicitly from Newton's second law with the available information at t_n (Equation 4.40). From Equation 4.39, the nodal velocities and displacements are computed. As a consequence of the incremental deformation, incremental changes in strain and stress occur. Consequently, the internal force is determined once again and, simultaneously, the external force at time t_{n+1} is evaluated in accordance with the specified loading conditions. Next, the acceleration at time t_{n+1} is computed, and so on [81].

It is noteworthy to mention also that the simple procedure portrayed in Figure 4.7 possesses the capability to generate a unique solution, provided that all the material models and constraint conditions are correctly defined. In fact, each individual step is devoid of any possibility of producing multiple solutions [81].

Finally, despite having already presented the formulation of the explicit time integration rule, as well as the basic steps of its application in FEM, there are still crucial characteristics of the explicit scheme left to be discussed. These characteristics, presented in the next subsections, justify both the limitations and the efficiency of the currently discussed method.

4.2.2.2 Stability Condition and Time Step Size

Contrary to the implicit time integration method, as stated before, the explicit approach must satisfy a stability requirement. The latter dictates that the integration method is stable only if the time step size, Δt, is smaller than that of a critical one. This condition, designated as the Courant–Friedrichs–Lewy (CFL) condition, is presented in Equation 4.41 [80, 81].

$$\Delta t \leq \Delta t^{crit} = \frac{2}{\omega_{max}} \tag{4.41}$$

where Δt^{crit} is the critical time step size and ω_{max} represents the highest natural frequency of the system, which is derived from the speed of sound of the system [80]. This states that if $\Delta t \geq \frac{2}{\omega^{max}}$ then $u_2(t_2) \leq -2u_2(t_1)$ and the system diverges quickly [81].

The stability condition of the explicit scheme requires evaluating the maximum frequency of the whole system, and that changes continuously during the analysis. This brings numerous issues, such as considerable computational cost, but also the fact that the explicit code lacks an eigen solver. The most common approach to tackle this issue is to rely on the fact that, as shown by Flanagan and Belytchko, $w_{max}^{sys} \leq w_{max}^{(e)}$, i.e., $\Delta t_{min}^{(e)} \leq \Delta t^{crit}$. Thus, the minimum element time step is considered for the system computation and the stability condition is conservatively fulfilled [80, 81].

In explicit analysis, stress waves propagate through the mesh, which changes the zones of stress concentration. This translates into the fact that the element size is not automatically dependent on the geometry, as it is in implicit analysis where static regions of stress concentration can be found and for which the stress gradients in that zone must be captured by a refined mesh (in the sense that smaller elements are necessary in those zones). In explicit FEA, the mesh refinement should bring smooth transitions, and not necessarily a smaller element size, to increase the accuracy and efficiency of the simulation [80].

As a matter of fact, note that the total solution time depends on the time step and on the number of elements in the manner expressed in Equation 4.42,

$$\begin{aligned} t^{sim} = t^{cycle}\, n^{cycle} \quad &= \left(n^{(e)}\, t^{(e)}\right) \frac{T}{\Delta t} \\ \Uparrow n^{(e)} \quad &\Longrightarrow \Uparrow t^{sim} \\ \Downarrow \Delta t \quad &\Longrightarrow \Uparrow t^{sim} \end{aligned} \tag{4.42}$$

in which T and Δt are, respectively, the simulation end time and time step size, $n^{(e)}$ and n^{cycle} correspond in turn to the number of elements and the number of cycles, and t^{sim}, t^{cycle} and $t^{(e)}$ are the computation time for simulation, for one cycle and for one element, respectively. Accordingly, the greater the number of elements and the smaller the time step established, the bigger the computer time for the simulation [80].

The time step can be easily computed by an expression equivalent to the one in Equation 4.41, presented in Equation 4.43,

$$\Delta t \leq SF\, \mathbf{min}\left(\frac{L}{c}\right) = 0.9\, \mathbf{min}\left(\frac{L}{c}\right) \tag{4.43}$$

where SF is the time step safety factor (often taken as 0.9, which corresponds to the default value in some commercial FEM software, such as in Ansys®), L is the characteristic element length and c is the speed of sound in the material of the body [80, 82].

The value of c can be computed by Equations 4.44, 4.45 and 4.46 for beam, shell, and solid elements, respectively,

$$c = \sqrt{\frac{E}{\rho}} \tag{4.44}$$

$$c = \sqrt{\frac{E}{\rho(1-\nu^2)}} \tag{4.45}$$

$$c = \sqrt{\frac{E(1-\nu)}{\rho(1+\nu)(1-2\nu)}} \tag{4.46}$$

where ρ represents the density [80].

It can be concluded that the value of c is greater for stiffer and less dense materials, leading to a smaller time step. A strategy to increase the latter and, subsequently, decrease the simulation time is to lower Young's modulus and/or increase the density (by process of mass scaling, as will be seen next). In addition, note that rigid elements (of infinite rigidity, theoretically) do not affect the time step of the analysis [80].

Regarding the characteristic length of the element, its calculation depends on the element type in question. See Figure 4.8 where the characteristic length of solid elements, shell elements, and beam elements is represented [80].

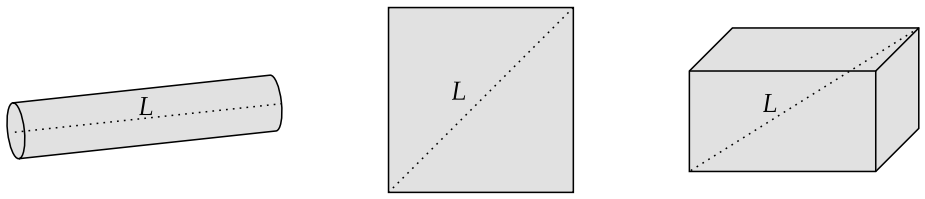


Figure 4.8: Characteristic length for critical time step calculation in beam element, shell element, and solid element (left, centre and right) (Adapted from [80]).

Hence, the analysis time step depends on the element size and should be such that, during a time step, a travelling wave should only pass through no more than one element. Hence, the smallest elements command the time step and uniform element size is desired. A non-uniform mesh, where only a small number of elements (linked with a reduced value of L) can dramatically impact the time step size, entails a bigger analysis time which is undesirable [80].

Lastly, it is fundamental to point out that the critical time step size is updated throughout the analysis as the elements deform: the presence of elements under tension tends to increase in the time step, while elements in compression create an opposite effect. Furthermore, the critical time step size primarily concerns stability; however, in order to achieve higher accuracy, it may be necessary to utilise even smaller time steps [80, 81].

4.2.2.3 Mass Scaling

In cases where achieving a uniform mesh is not possible, such as with complex geometries or when a mixture of different element types are being used, controlling the time step size and analysis time can be done by resorting to alternative strategies [80].

Mass scaling is a purely numerical method that involves scaling the mass matrix in order to increase the stable time step. This technique is relatively straightforward to implement and has become widely adopted in many applications [80, 82].

When the number of elements that control the time step, i.e., small elements, is reduced and isolated in groups, the uniform mass scaling method works quite well. It entails the scaling of the density of those elements so that the time step to them associated is equal to an established minimum, as seen in Equation 4.47, obtained from manipulation of Equation 4.43,

$$\frac{\rho^s}{\rho^0} = c^2 \left(\frac{\Delta t^s}{L} \right) = \left(\frac{\Delta t^s}{\Delta t^{(e)}} \right)^2 \tag{4.47}$$

where ρ^s corresponds to the scaled density, ρ^0 to the original density, and the parameters t^s and $t^{(e)}$ represent the specified minimum time step size and the element time step size using the original density, respectively [82].

Mass scaling increases the inertia forces, as can be derived from Newton's second law, but it does not influence body loads. This characteristic can be extremely useful for quasi-static and low-velocity or energy simulations [80].

Despite being a very effective technique for various applications, it should be noted that this approach is not suitable for particular cases in which wave propagation plays a significant role, for instance, high-speed ballistic impact and failure. In addition, mass scaling should be properly limited since it alters the physics of the problem [80, 82].

It is the job of the analyst to check the mass scaling in post-processing and infer the validity of the results. Some frequently used rules of thumb to assess the validity of the findings utilise the ratio established between the added mass and the total mass for the parts of interest. If this ratio is below 5% in dynamic analysis and 20% in quasi-static analysis (this can also be problem dependent), it is likely that the mass scaling technique did not impact significantly the physical significance of the results. The kinetic energy of the analysis should also be checked to validate the use of this technique [80].

4.2.2.4 Lumped Mass Matrix

The diagonal (or lumped) mass matrix is one key feature of the explicit time integration scheme and one that contributes majorly to the efficiency of the method and its overall success. The diagonalisation of the mass matrix in explicit FEM enables the obtainment of smaller simulation times and lower computational storage necessities. Furthermore, the diagonal mass matrix demonstrates favourable performance when employed in conjunction with the central difference method, mitigating the occurrence of undesired oscillations observed when applying a consistent mass matrix [82].

The consistent mass matrix (defined previously in Equation 4.32) of an element, represents a discretisation of the continuous mass distribution and captures the dynamic coupling between the elemental displacements. The elemental diagonal matrix, however, mitigates this dynamic coupling. Through a non-consistent formulation, different displacement models are associated with the stiffness and mass matrices. Furthermore, it assumes that the mass is concentrated at the nodes, as it does not consider the spatial distribution of mass within elements (thereby, simplifying the computations) [74].

Utilising the diagonal mass matrix transforms the calculation of acceleration, by the application of Newton's second law (as seen in Equation 4.40), into a simple division operation, eradicating the need for inversion of the mass matrix [81].

There are multiple methods to obtain the lumped mass matrix, the consistent mass matrix being the starting point for many of them. Some of these are [81, 82]:

- Simple lumping, i.e., distribution of the total mass of the element to its nodes;
- Nodal integration, using an integration rule that has integration points coincident with the nodal points;
- Row (or column) summing, of easy software implementation, consists of simply summing the entries in each row of a mass matrix and associating the resultant value to the diagonal.

Considering the consistent mass matrix presented in Equation 4.32, the lumped mass matrix is defined by the row summation method as presented in index notation in Equation 4.48,

$$\mathbf{M}_d = \boldsymbol{\delta}_{IJ} \sum_J \int_\Omega \rho \mathbf{N}_I \mathbf{N}_J d\Omega = \boldsymbol{m}_I \boldsymbol{\delta}_{IJ} \tag{4.48}$$

where $\boldsymbol{\delta}_{IJ}$ is the Kronecker delta (Equation 4.49), $\boldsymbol{m}_I$ can be defined as demonstrated in Equation 4.50, and there is no summation on index I [81].

$$\boldsymbol{\delta_{IJ}} = \begin{cases} 0 \textbf{ if } I \neq J \\ 1 \textbf{ if } I = J \end{cases} \tag{4.49}$$

$$\boldsymbol{m}_I = \int_\Omega \rho \mathbf{N}_I d\Omega \tag{4.50}$$

Chapter 5

Electric Vehicle and Battery Design

This Chapter presents relevant concepts regarding BEVs, battery packs and the principal subject of this work, the battery pack enclosure structure.

The first section of this Chapter overlooks the definition of a BEV and its emergence in the automotive market. The reasons that justify their recent commercial success, as well as the main hindrances for a consumer's intentions to acquire a fully-electric vehicle, are investigated. Then, the functions of a BPE are addressed with the aim of justifying the industry's state-of-the-art choices for design, position, and material selection for this component. Data retrieved from a benchmarking platform is used to provide insight into realistic industry solutions to the reader.

5.1 Battery Electric Vehicles

Battery electric vehicles are an electric vehicle type that runs solely on the electric energy stored in rechargeable batteries. The exclusive reliance on the battery packs differentiates it from other EV variants, since no optional source, for instance, gases, hydrogen energy unit, or ICE is utilised [5]. Even though BEVs incorporate different kinds of vehicles, from bikes to rail cars or skateboards [5], in this work mainly passenger cars will be assumed, studied, and addressed.

BEVs coexist in the market with other automotive electrical solutions, such as Fuel Cell Electric Vehicles (FCEVs), a hybridisation of two energy sources: hydrogen fuel and battery, Hybrid Electric Vehicles (HEVs), for which the energy sources are gasoline fuel and battery and Plug-In Hybrid Electric Vehicles (PHEV). HVEs can be classified as a micro-hybrid, mild hybrid, or full hybrid, the reliance of both the electric motor and battery increasing from the micro to the full versions [84]. HEV and PHEV are very similar, differing in the fact that the plug-in version has extra features, such as larger battery packs, and can be recharged from the distribution grid [85].

Figure 5.1 presents a simplified scheme for vehicle classification considering: the types of propulsion device (engine and motor), the energy source (gasoline, battery, and hydrogen fuel), as well as the corresponding levels of utilisation [84].

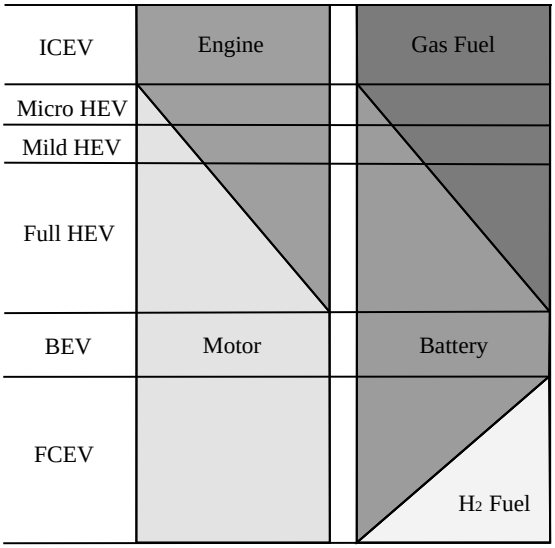


Figure 5.1: Vehicle spectrum with regards to propulsion device, energy source, and corresponding utilisation level (Adapted from [84]).

A simplified architecture of a BEV powertrain can be observed in Figure 5.2. As can be concluded, a BEV's powertrain consists of a battery system that is electrically linked to the electrical machine through power electronics for the propulsion of the EV [86].

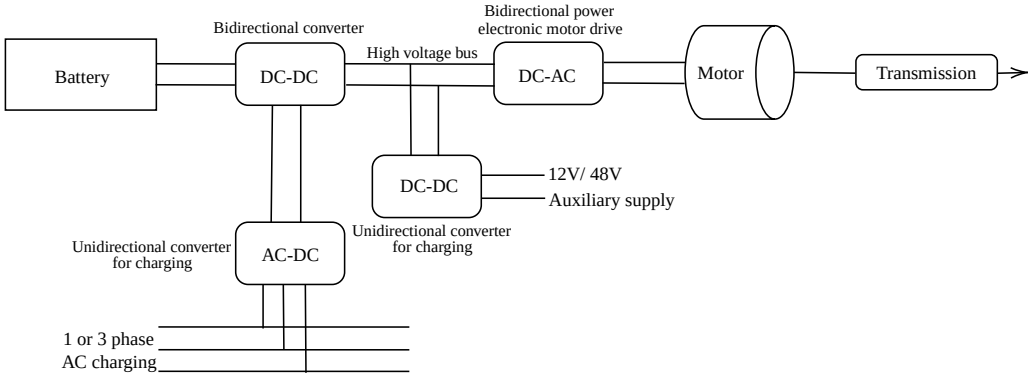


Figure 5.2: Diagram of a BEV's powertrain (Adapted from [87]).

Rechargeable batteries are the energy storage devices utilised in BEVs, whereas the electric motor constitutes the sole propulsion source. The electric motor is connected to the wheels of the vehicle and utilises the energy stored in the batteries to move it. The power electronics controller regulates the speed and torque of the motor, as well as the movement of electrical energy passed on by the battery. Typically, DC-DC converters, a DC-AC inverter, and an AC-DC rectifier are employed to adjust the voltage of the power flowing both in and out of the energy source to the motor [5, 87]. Noticeably, a BEV possesses an all-electric propulsion system and is always in charge-depleting mode. The large battery packs can be externally recharged when the vehicle comes to a stop or on drive, by regenerative braking, a process by which the vehicle is slowed by converting its kinetic energy into chemical energy [85].

In historical terms, the study and development of electric vehicles are not recent by any means; in fact, this dates back to the eighteenth century. Then, in the following century, more precisely in 1894, one of the first successful electric vehicles, the Electrobat, was created by Pedro Salom and Henry Morris [5]. From there, the interest in EVs has grown, particularly so in the last decade when it has reached significant heights.

At the end of the twentieth century, to respond to governments' regulatory actions to reduce air emissions and incentives for vehicle electrification, automakers directed efforts into producing hybrid vehicles. This resulted in the EV1 model, released in 1996 by General Motors, and in the Toyota Prius model, the world's first commercial HEV to be produced in series. BEVs and PHEVs made their way into the market starting from the year 2010 with models such as the Nissan Leaf, Mitsubishi i-MiEV, or Tesla Model S [88]. In the present, the sales of electric vehicles have spiked. In Figure 5.3 the increase in sales and registrations of EVs in China, the United States (US), Europe, and other regions, from 2016 to 2021, are illustrated.

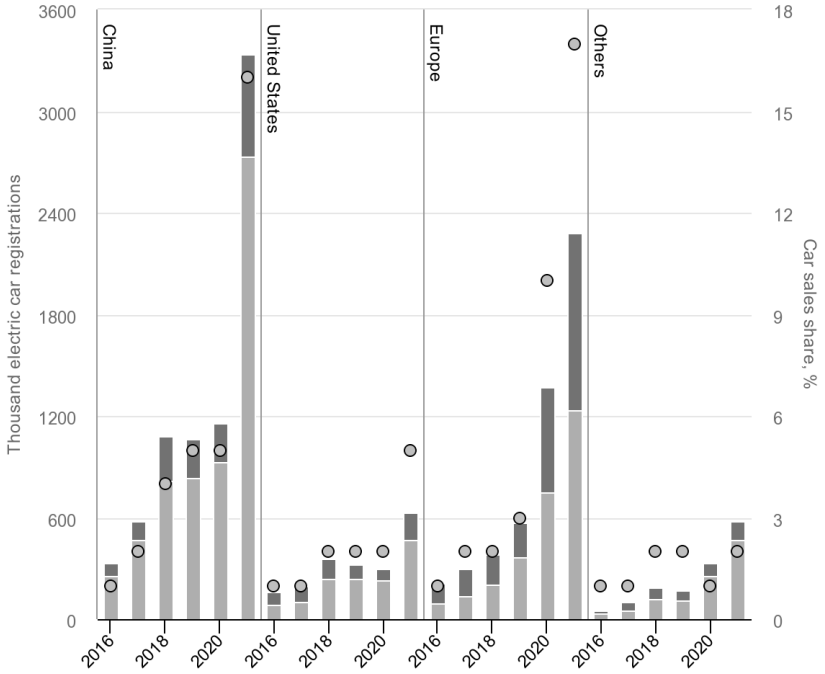


Figure 5.3: Sales and registrations of electric cars in China, US, Europe, and other regions, from 2016 to 2021 [88].

As can be concluded from Figure 5.3, 2021 represented a record year for electric vehicle sales. For perspective, approximately 120 000 electric cars were sold worldwide in 2012, while the same amount was sold per week in the above-mentioned year. Out of all EVs, BEVs presented the most increase in this timeframe, of about 70% [88]. The growth in EV sales was maintained throughout 2022, where, for instance, in the first quarter of the year, the sales in China more than doubled compared to the same period of 2021, while the US and Europe accounted for an increase of 60% and 25%, respectively [89].

Li et al. [90] performed a systematic overview of peer-reviewed articles aiming to identify and understand the factors that influence consumer intentions to purchase BEVs. The diverse factors were classified into three types: demographic, psychological, and situational, and it was suggested that consumers' motives resulted from a mixture of the three. Focusing particularly on the situational factors, it was concluded that the environmental benefits

linked to BEVs are important driving factors for consumer adoption of electric vehicles. On the contrary, the driving range, associated costs (particularly the high front purchasing cost), and issues related to charging times and infrastructure constitute the main barriers [90].

To reach a deeper understanding of the relevance of the given theme and contextualise the purpose of this work, the stated situational factors will be explored and supplemented by other pertinent characteristics of fully electric vehicles.

5.1.1 Environmental impact of the BEV

The transportation industry is one of the pillars of contemporary society and plays an important role in world economic growth [90].

Nowadays, the transport field encompasses mainly vehicles equipped with internal combustion engines. These vehicles are powered by fossil fuels, either diesel or petrol, emitting greenhouse gases such as carbon dioxide (CO_2). Once these gases are released, they can stay in the atmosphere for up to 100 years, forming a "blanket" around the earth which traps more heat and subsequently increases the temperature of the planet. Additionally, ICEVs also emit carbon monoxide (CO), non-methane organic gases, nitrogen oxides (NO_x), and Particulate Matter (PM), toxic releases that form smog. The colossal dependence on these vehicles entails significant issues: summing to the evident excessive oil consumption and reliance, toxicological and epidemiological studies have demonstrated that exposure to the resultant air pollution and greenhouse emissions can lead to damaging health consequences [87, 2].

Vehicle emission intensities have declined by factors of 2-100 over the past decades to meet regulatory standards. Examples of these regulations are the Tier 3 and the Euro 6, operative in the US and Europe, respectively, applicable for light-duty vehicles. These documents set emission standards with the aim of reducing emissions of pollutants, thus improving air quality through progressively more stringent sets of standards. Although an increase in vehicle population and travel demand has been experienced in these regions, even without considering electric vehicles, the trend is for future emissions of most pollutants to decline considerably. This is explained partly due to the stated regulations, but also owing to substantial technology improvements [2].

Nowadays, however, the transportation sector is still one of the biggest contributors to the issues above-mentioned, impacting directly and negatively the environment and human health. For instance, in 2017, the transport field was responsible for 27% of total GreenHouse Gas (GHG) emissions in Europe, almost 72% of which were related to road transport. In 2020, road transport emitted 77% of all EU transport GHGs.

Improvements in living standards, socioeconomic advancements, and an overall greater environmental awareness have made it evident that deep changes to the transport field needed to occur, particularly in the specified sector. Currently, most of the existing and prospective policies in the European Member States are, in fact, directed to this category, which is set to decarbonize faster than other transport modes. In Graph 5.4, the historical greenhouse gas emissions, as well as the projections With Existing Measures (WEM) and With Additional Measures (WAM), by transport mode, can be consulted. It can be verified that only road transport emissions are expected to decrease until 2030 [1, 2, 3].

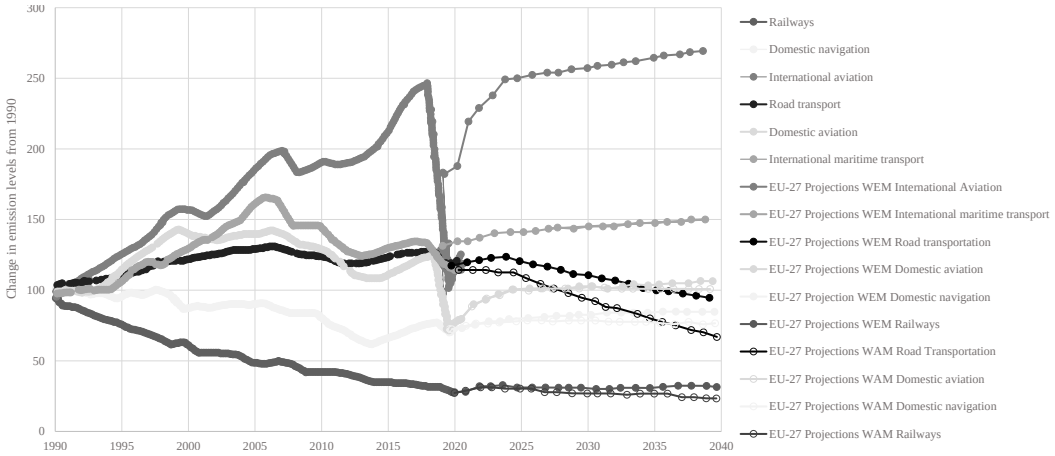


Figure 5.4: Greenhouse gas emissions from transport sectors in the EU, by transport mode and scenario (Adapted from [3]).

Following the ambitious objectives presented in the Green Deal in 2019, by which Europe strives to become the first climate-neutral continent, as a way to ensure that the established goal is met, the "Fit for 55" deal was published in 2021. As the name suggests, the purpose of the "Fit for 55" Package is to make European Union's (EU's) climate, energy, land use, transport, and taxation policies suitable for the reduction of net greenhouse gas emissions by at least 55% by 2030, relative to 1990 levels [91].

The Fit for 55 Package identifies electric mobility as a key component of transportation decarbonization. Indeed, with a growing number of EVs on the roads, their potential as viable solutions to the massive CO_2 and GHG tailpipe emissions caused by transportation is becoming increasingly clear in the automotive industry [1, 91]. Notwithstanding, it is necessary to address the fact that BEVs still need to overcome some environmental challenges themselves in the near future. Currently, there are mainly three issues gathering the attention of experts, as their solution would further enhance the positive impact of EVs on the environment [87]:

- The mining process of lithium (the key element in the production of LIBs for the BEVs currently in the market) leads to a considerable environmental footprint.
- The storage and recycling process for batteries is still in its beginning stages, constituting a rather inefficient, expensive, and unsafe procedure.
- The majority of power is still being produced in coal power plants. This entails that unless clean energy sources, such as solar, wind, and hydroelectricity are resorted to, the influence EVs will have on reducing emissions will not reach their full potential.

Despite the evident environmental benefits brought by BEVs, according to Axsen et al. [92], indeed, some consumers are still sceptical of their capabilities to provide environmental protection. The rationale for this relies heavily on the three motives explained above.

Furthermore, note that it takes a period from 6 months to 2 years for a standard EV to become more environmentally friendly than an ICEV. This is related to the fact that the manufacturing process of an ICEV is extremely efficient, as the result of continuous improvements over the last century, which significantly contrasts with the battery production process. In the long run, however, as seen in Figure 5.5, EVs compensate for the impact of their manufacturing process in terms of fuel consumption: while an ICEV produces 50

metric tonnes of CO_2 in its lifetime, an EV releases about 28 metric tonnes [87]. Carbon label implementation, as well as active efforts to the development of solutions for battery pollution, have the potential to successfully increase consumer acceptance and adoption [90].

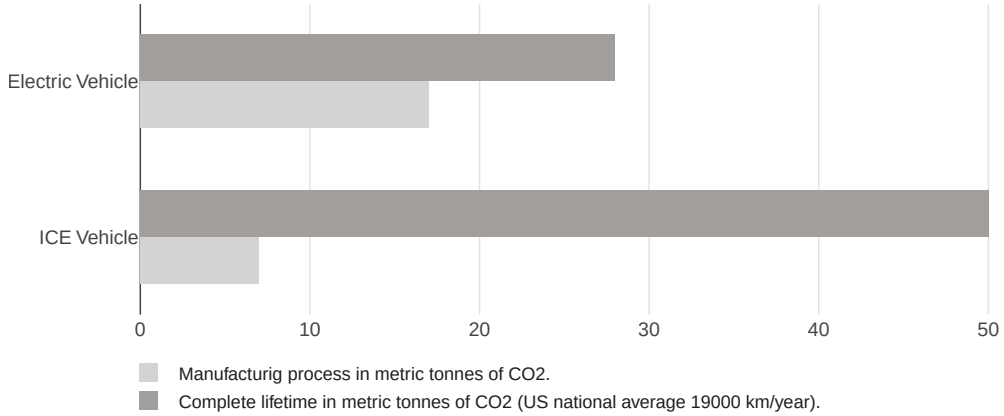


Figure 5.5: Comparison of the environmental footprint of an ICEV and an EV, based on CO_2 emissions during production and over the entire lifespan [87].

Lastly, it must be noted that an increasing number of electric vehicles on the roads will understandably entail additional electricity generation. The European Environment Agency (EEA) estimates that Europe's total electricity consumption by EVs will grow from about 0.03% in 2014 to a staggering 9.5% by 2050. Therefore, without coordinated investment, this extra demand will pressure the electricity infrastructure, particularly in countries with fluctuating renewable energy supplies, becoming a considerable challenge [93].

5.1.2 Cost Structure of the BEV

The electrification trend originates new challenges for automotive manufacturers, yielding new requirements for future vehicles and paving the way for previously unexplored mobility systems. While doing so, different cost structures are developed [94].

Profiting from new technology requires the identification of the optimal solutions for individual components and vehicle assemblies. Since the best technical solution is often the most expensive, the cost is an important parameter to assess the feasibility of a new vehicle concept. Evidently, the cost of the final product is a fundamental criterion for the consumer as well [90, 94].

When comparing BEVs to similarly-configured conventional ICEVs it is clear that the purchase cost of the EV is more significant which, according to literature, constitutes a relevant barrier to a more extensive diffusion of these vehicles in the market [90]. In opposition, the lower operational cost of a BEV (about six times smaller than that of an ICEV) acts in its favour. This difference in operating costs is mostly related to the low efficiency of the Internal Combustion Engine (ICE), of approximately 30 to 35%, in comparison to one of the electric motors, from 90 to 92%. The flow of cumulative mechanical and thermal losses in the thermal engine explains the disparity in efficiency between the two solutions [1]. In addition, electric machines present other remarkable characteristics regarding high service life, low maintenance costs, and reduced noise levels [87].

The cost structure of a BEV considerably differs from that of an ICEV, with the battery alone composing up to one-third of all vehicle-related costs. The cost of the battery is dependent on the components used in its manufacture, such as its materials, electrodes,

body shell, etc. While ICEVs are considerably cheaper than BEVs, this difference in price is decreasing and is set to reach only 9% by 2030 [94, 95]. This decay is illustrated in Figure 5.6, where the price of multiple individual components of the vehicle are discriminated.

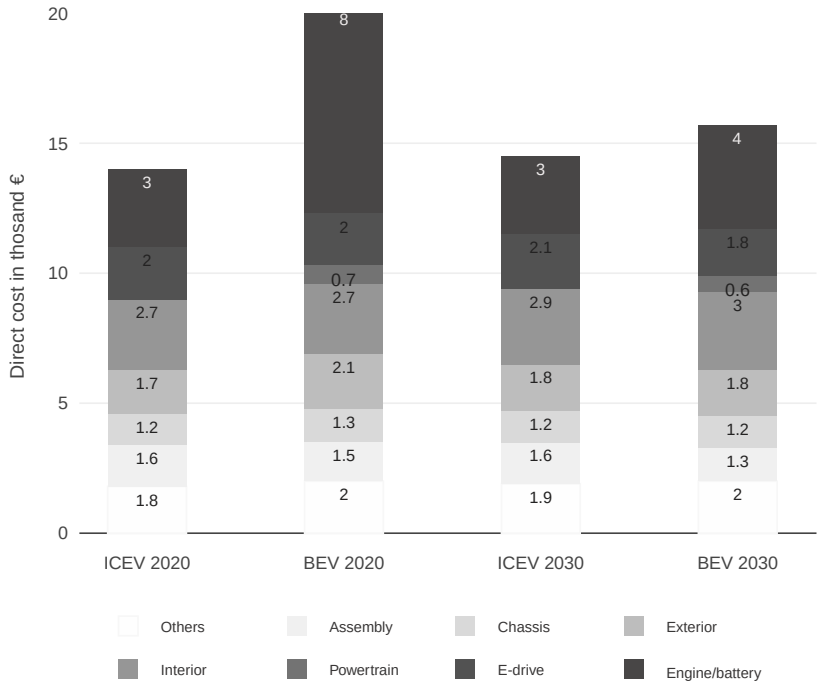


Figure 5.6: Cost structure of present-day and future BEVs, in comparison to ICEVs (Adapted from [94]).

Dumortier et al. [96] suggest that the long-term economic benefits of reduced energy consumption and low electricity prices associated with BEVs can offset much or all of their upfront cost. However, the authors also found that consumers tend to prioritise the immediate expenses of purchasing a vehicle rather than the long-term savings. Consequently, the cost advantages of BEVs may not be immediately apparent to consumers, hindering their widespread adoption. Short-term focused measures, for example, enhanced economic incentives, could increasingly encourage consumers to acquire BEVs, therefore accelerating its mainstream diffusion.

5.1.3 Charging times and infrastructure of the BEV

As defined previously, BEVs operate solely on the battery power and the battery packs can be externally recharged with a plug-in charger or through regenerative braking [87].

Issues related to long charging times and insufficient charging infrastructure are regarded as technical barriers to BEV adoption. Notorious improvements in this field are thus necessary to achieve safer, more reliable, and faster-charging infrastructure, which would contribute to end drivers' scepticism about electric mobility and allow BEVs to compete with ICEVs on a greater scale. However, investors in charging would expect quick and regular returns [87, 90]. Various technological advancements have been made to alleviate range anxiety. In Table 5.1 it is possible to find diverse charging solutions, complemented by its general description, which includes possible benefits and limitations [87].

Table 5.1: EV charging technologies (Adapted from [87])

EV charging technologies	Description
Conductive charging – AC/DC	The most vastly used charging method. The EV is charged by a cable plugged into its electric grid. Both AC and DC charging types are available: AC allows reduced costs and performance improvements, due to the fact that it is possible to charge the battery anywhere utilising the onboard charger and the AC grid. DC enables high-power charging, i.e., low charging times. As the charger is outside the vehicle, the charging rate can be altered according to the requirements.
Wireless power transfer (WPT)	The power transfer in non-radiative WPT technologies can be inductive (IPT) or capacitive (CPT). IPT is based on two magnetically linked coils: the primary connected to the electricity grid, laid on the road surface, and the second set on the top or bottom of the car. CPT uses electric field coupling. The couples may be unipolar or bipolar, this dictates the number of metal plates on both the transmitter and receiver sides. CPT is best suited for high voltage, low current batteries, whereas IPT is best suited for low voltage, high current batteries.
Battery swapping	This charging type entails switching the depleted battery for a full one by a fully manual or automated process. This model suggests that the EV driver is the owner of the vehicle, not the battery. After the swap, the battery then continues to be charged at the station, allowing for slow charging which can improve battery life. The limitations of this method include the necessity of standardisation of the battery interface, a much more complex infrastructure and faster battery degradation (due to recurring charging and discharging).
Smart charging and V2X	Smart charging entails the intelligent control of the EV charging power. This helps decrease the peak power demand on the distribution network and increases the efficiency of the power transfer. Vehicle-to-grid systems, for example, can give EV owners novel revenue paths. The power can travel from the battery to the grid, to a home or building, and to any load (V2G, V2B, and V2L, respectively). All these methods are included in the term V2X. V2X allows electricity storage inside the vehicle, which can be used to minimising the demand on the power grid. In fact, EVs may become a relevant system component in the power supply. Financial incentives and a regulatory structure for V2X introduction is still in the works.

5.1.4 Energy and power densities of the BEV

The battery electric storage system is the fundamental element of an all-electric propulsion system, due to the fact that its capacity defines the performance and the driving range

of the vehicle, i.e., the distance that a fully charged BEV can travel prior to the battery running out of electricity [95].

The batteries along with numerous mechanical and electrical components comprise the battery packs adopted by electric and hybrid vehicles [66]. In Figure 5.7, a black box-type model illustration of a battery pack and its main components is presented.

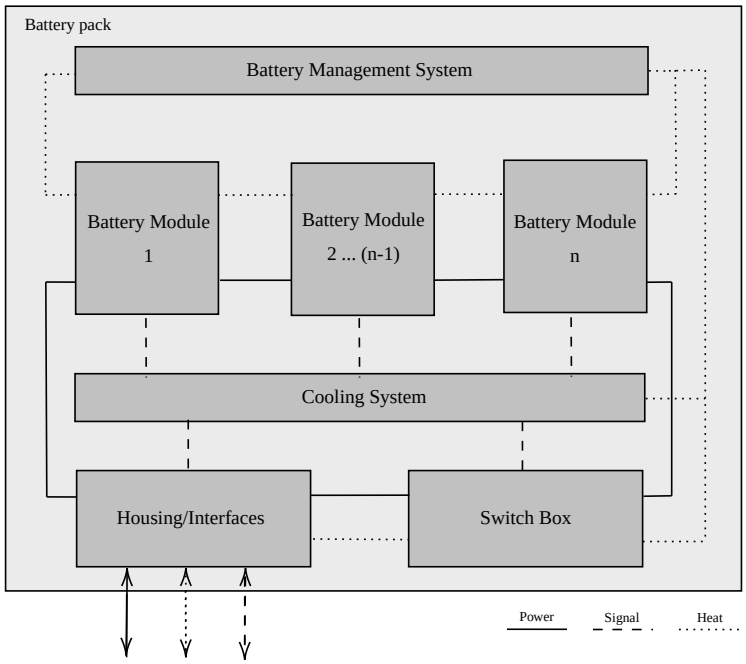


Figure 5.7: Schematic illustration of a battery pack and its main components [97].

Battery cells are the primary components of a battery pack. A cell is an electrochemical device that converts chemical energy into electrical energy. Cells are combined together in series or in parallel to form modules, which in turn are assembled to form the battery packs. Cell selection is vital for the determination of key attributes of the BEV, namely the design space, performance, costs, and safety [98, 99, 6].

It is possible to find many battery technologies in the market, each one with its benefits and limitations. The most prominent storage technologies are, for instance: lithium-ion, lead-acid, nickel-cadmium, nickel-metal, and sodium-nickel chloride batteries, as well as supercapacitors and lithium-carbon capacitors [7]. Through research in literature, it can easily be concluded that LIB technology is the most broadly used in electric vehicles. In fact, there are multiple lithium-ion chemistries available to the automotive industry [100].

Characteristics related to power, lifespan, low and high-temperature performances, as well as safety levels depend significantly on the material combination used in the manufacture of the battery cells, particularly on the lithium-ion donator in the cathode. Therefore, commercial batteries are designated after the latter. Lithium cobalt oxide (LCO), Lithium Manganese Oxide (LMO), Lithium Iron Phosphate (LFP), lithium Nickel Cobalt aluminium oxide (NCA), and lithium Nickel Manganese Cobalt oxide (NMC) are all used for this purpose [100].

In Table 5.2 various characteristics of state-of-the-art commercial BEVs can be consulted. These include the battery chemistry, vehicle and battery pack weight, capacity, and driving range.

Table 5.2: EV battery chemistry and relevant characteristics as of 2018 [100]

Vehicle	Battery Chemistry	Capacity [kWh]	Vehicle Weight [kg]	Battery Pack share in weight [%]	Driving Range [km]
BMW i3	NMC	33	1343	24	180
Nissan Leaf	NMC	30	1516	20	170
Ford Focus Electric	NMC	33.5	1651	20	180
Tesla Model S P100D	NCA	102	2234	26	505
BYD e6	LFP	82	2420	29	390
Fiat 500e	NMC	24	1352	19	135
Chevrolet Bolt EV	NMC	60	1624	27	350
Volkswagen e-Golf	NMC	35.8	1605	22	195
Mitsubishi i-MiEV	NMC	16	1170	19	95

As can be concluded from the Ragone plot of Figure 5.8, lithium-ion battery cells achieve the highest efficiency, energy density, and power density out of all other cell solutions available in the market, which explains its generalized use by the automotive manufacturers [6, 7].

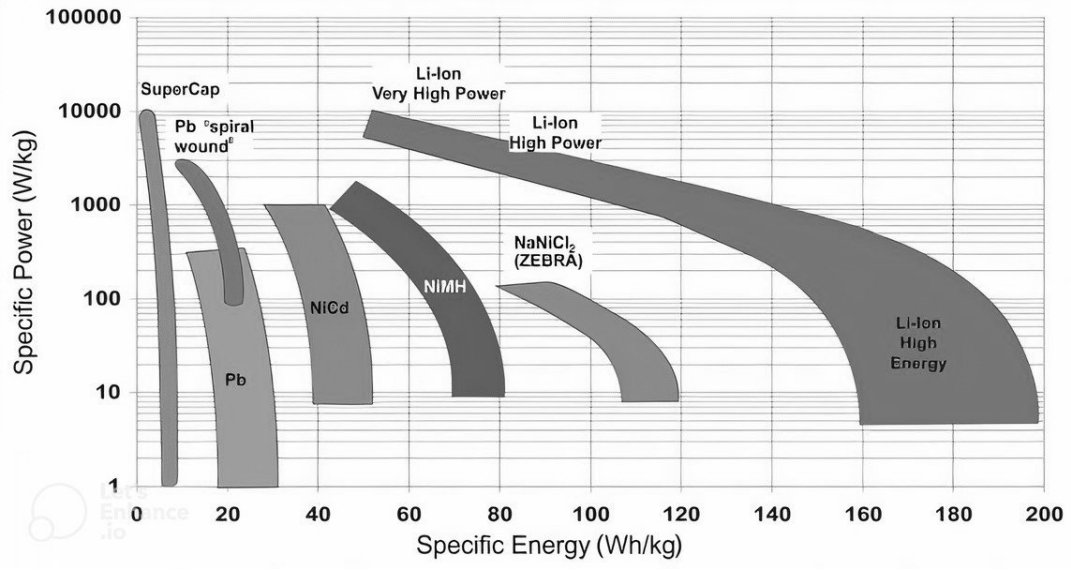


Figure 5.8: Ragone plot of various battery technologies with specification at the cell level for automotive applications without lithium-sulfur, and metal-air batteries [7].
SuperCap: supercapacitor; Pb: lead; Li-ion: lithium-ion; NiCd: nickel-cadmium; NiMH: nickel–metal hydride; NaNiCl2: sodium–nickel chloride; ZEBRA: Zero Emission Battery Research Activities.

In addition to chemistry, capacity, and safety, commercially available LIB cells can also differ in shape. The cell shape may be cylindrical, prismatic, or pouch-shaped (Figure 5.9), which influences the design of the modules and pack housing, cooling necessities and electrical design [6]. Owing to the low packing density of cylindrical geometries and to persistent issues related to the quality of welding of pouch designs, prismatic cells are preferred for automotive applications at present due, particularly in larger-sized BEVs [7].



Figure 5.9: Various cell shapes: cylindrical, prismatic and pouch (left, centre and right) [7].

While the energy density of LIBs cells has been increasing steadily in recent years, the gravimetric and volumetric energy densities of these batteries, i.e. the amount of energy stored per unit weight and volume, respectively, are still not comparable to the ones of other energy sources, such as gasoline. Moreover, the energy densities at the cell level are not representative of the densities of the pack, since the battery also encompasses other elements related to management systems, cooling, structural protection, wiring, etc. Accounting for this additional hardware reduces overall pack-level energy densities [94, 101].

This represents one of the biggest obstacles to the widespread adoption of EVs by the masses, as the relatively low energy storage capacity of the batteries is reflected in the driving range [101]. Consumers are already familiar with the high driving ranges enabled by ICEV. Indeed, their range preference overcomes their real demand [90]. Industry efforts are being employed to improve the energy efficiency of EVs, but this is not an easy task. An elevated battery capacity leads to increments in terms of cost and weight, thereby increasing energy consumption, which directly affects the vehicle's autonomy. Some of the current trends to surpass this issue entail [66, 1, 101]:

- Functional optimisation of the components of a battery cell and development of next-generation batteries, as the energy densities of LIBs approach saturation.
- Improvements in performance and energy-efficiency of Battery Management Systems (BMSs).
- Reduction of the number of components in the electric powertrain to decrease mechanical losses and development of energy flow management systems at the vehicle level.
- Perform enhancements and design of lightweight automotive battery packs and their enclosures.

Lastly, before delving into the discussion related to the main subject of this work, it is relevant to briefly address vital components of a battery pack, illustrated above in Figure 5.7. In fact, a highly sophisticated BMS, an efficient thermal system and a resistant BPE are crucial to the safe operation of lithium-ion batteries [7].

The BMS performs the functions of battery monitoring, diagnostics, electrical and thermal management, and cell balancing. The State-Of-Charge (SOC) and State-Of-Health (SOH) are constantly evaluated and the safety and long-lasting lifespan of the battery is secured [7]. The purpose of thermal management is to guarantee that the temperatures within the battery remain as constant as possible and close to a predefined level. Extreme temperatures have penalising effects on the lithium-ion battery, as low temperatures reduce

the power capability of the cells and high temperatures decrease the lifetime. Furthermore, issues related to overheating may arise, compromising the safety of the vehicle [7]. The battery pack enclosure, in turn, will be extensively discussed in the following Chapter, given its relevance in this work.

5.2 Battery Pack Enclosure

Either during operation or in an impact incident, various stress types may arise in the energy source of the BEV. As can be observed in Figure 5.10, these include: 1) Mechanical stresses, related to impact, deformation, penetration, free fall, mechanical shock, vibrations, and immersion; 2) Electrical stresses, due to overloading, forced download, and high C-rate; 3) Thermal stresses: originating from (over)heating and thermal runaway [1].

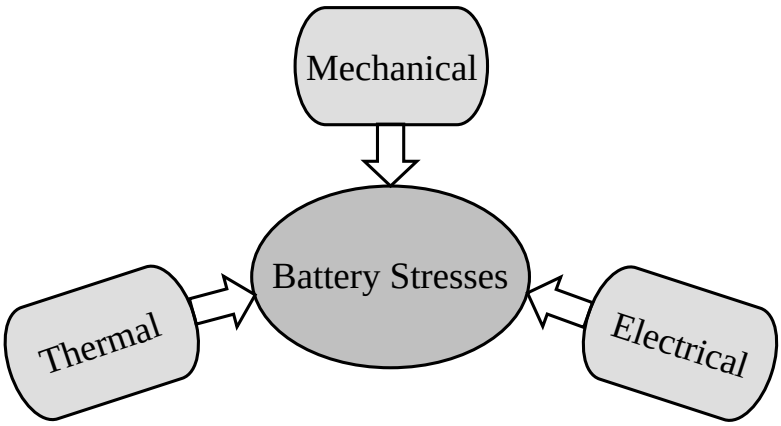


Figure 5.10: Stresses arising during LIB exploitation (Adapted from [1]).

As evidenced by relevant literature and already assessed, temperature can represent a major enemy of LIBs [102]. Owing to the fact that real-time temperature regulation and monitorisation of the battery packs constitute extremely challenging tasks, initially, numerical research related to battery safety in EVs was, for the most part, directed to battery modelling methods for the design of an efficient BMS (by incorporation of new heating/cooling systems). However, in recent years it has become clear that, for that same purpose, experts must also focus on the mechanical design of the battery pack, including the BPE and modules [99].

A priority that starts in the design phase of a BEV is the safe integration of the batteries into the powertrain and onto the vehicle, as to avoid later problems that may result in numerous safety issues [7]. When installed into a vehicle, the battery packs are constrained and supported by a case, referred to as a "battery pack enclosure" [66]. The function of this housing component is essentially the protection of the elements it shields, as well as representing the mechanical, thermal and electrical interface of the battery with the vehicle [97].

During the operation of an EV, the vehicle will likely be subject to sharp environments, such as external vibrations and shocks due to changing road slopes. The battery pack itself will endure those dynamic loadings and random vibrations, in addition to potential external impacts originating from the event of a traffic accident. The ensuing deformations and mechanical damage to the BPE may lead to short circuits, ignition, and fire hazards,

severely compromising the safety of the driver, vehicle, and road [99], as already assessed in Chapter 2 of this work.

The safety of a BEV greatly depends on the safety of the battery pack itself, which in turn is determined by the mechanical properties of the enclosure, particularly its crashworthiness, i.e., its ability to resist crash and large deformations [66]. Therefore, it is of vital importance that the BPE results from an engineering design that ensures, not only, its thermal stability, high strength, and crash resistance, but also, in accordance with what has been previously stated and constitutes one of the main objectives of this work, the low weight of the structure. According to what has been discussed, only then is it possible to increase the driving range of the BEV and the lifespan of the battery pack. Because it reduces energy consumption, more battery cells can be installed without increasing vehicle mass, which is critical and desired for the advancement of EVs [66, 102].

To succinctly outline the diverse roles performed by the battery housing, a functional tree diagram is presented in Figure 5.11. In the diagram, it is possible to consult the main functions and sub-functions coupled to this structure. Note that this tree is of great interest in the idea-generation phase of a design project and will be useful in further steps of this work.

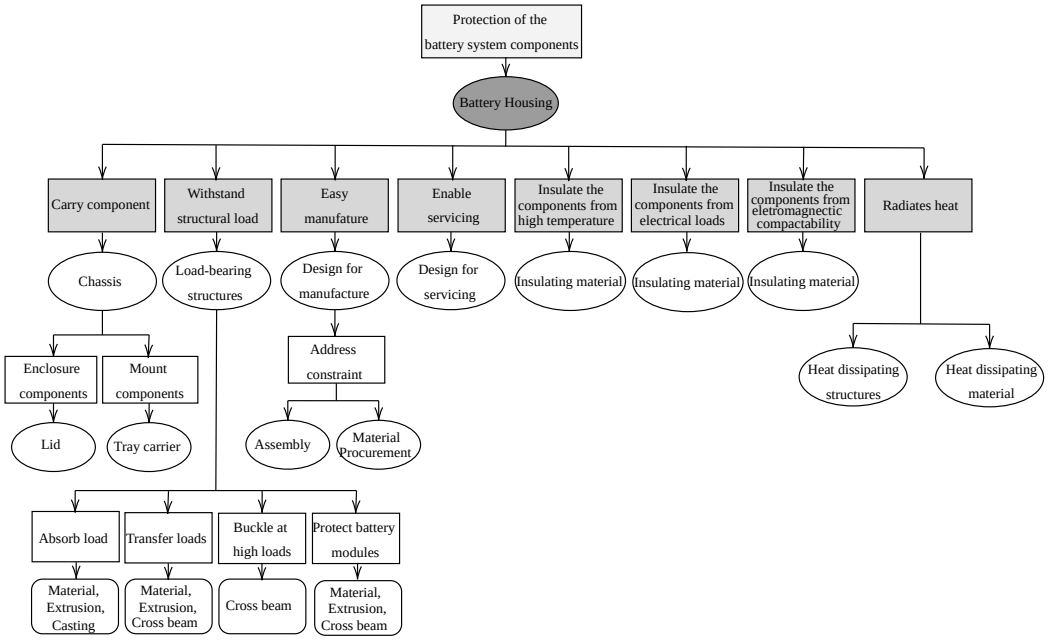


Figure 5.11: Functional tree diagram of the battery pack enclosure (Adapted from [103]).

It should be emphasised that, for the principal aim of this work, i.e., the crash and explicit dynamic analysis of protection structures for units of energy storage of BEVs, just as relevant as understanding current regulation standards and tests governing the design and performance of BEVs and battery packs (as explored on Chapter 2), is to be knowledgeable of the automotive industry's choices and rationale for the placement and fixation of the packs, as well as of the materials and geometry frequently used in the BPEs. The next subsections will focus on each of the referred parameters.

5.2.1 Design of the Battery Pack Enclosure

The battery pack housing is designed in strong interaction with the one of the vehicle body [97]. The incorrect architecture of the former will result in a variety of serious issues, such as cracking, noise and/or even battery damage. Thus, the design of the enclosure must be carefully performed with deep considerations regarding the mechanical, safety, service (and cost) requirements [97, 104].

Geometry-wise, the shape of the battery pack enclosure can vary from a fairly compact and parallelepipedic unit to an arbitrary shape, in order to fit into irregularly shaped cavities in EVs. In fact, the BPE is a highly customised component, tailored for its application [66, 97]. The shape and size of the housing are defined by two main factors: 1) the design space and mounting points available on the vehicle; and 2) the internal components that must fit in the housing. The enclosure's shape generally replicates the shape of the battery packs, which can be regular or irregular (i.e., presenting uniform or variable height). Furthermore, based on the loading and mounting requirements, the housing structure may present constant or varying thickness and strength. For illustration purposes, Figure 5.12 presents six examples of the BPEs of state-of-the-art commercial EVs.

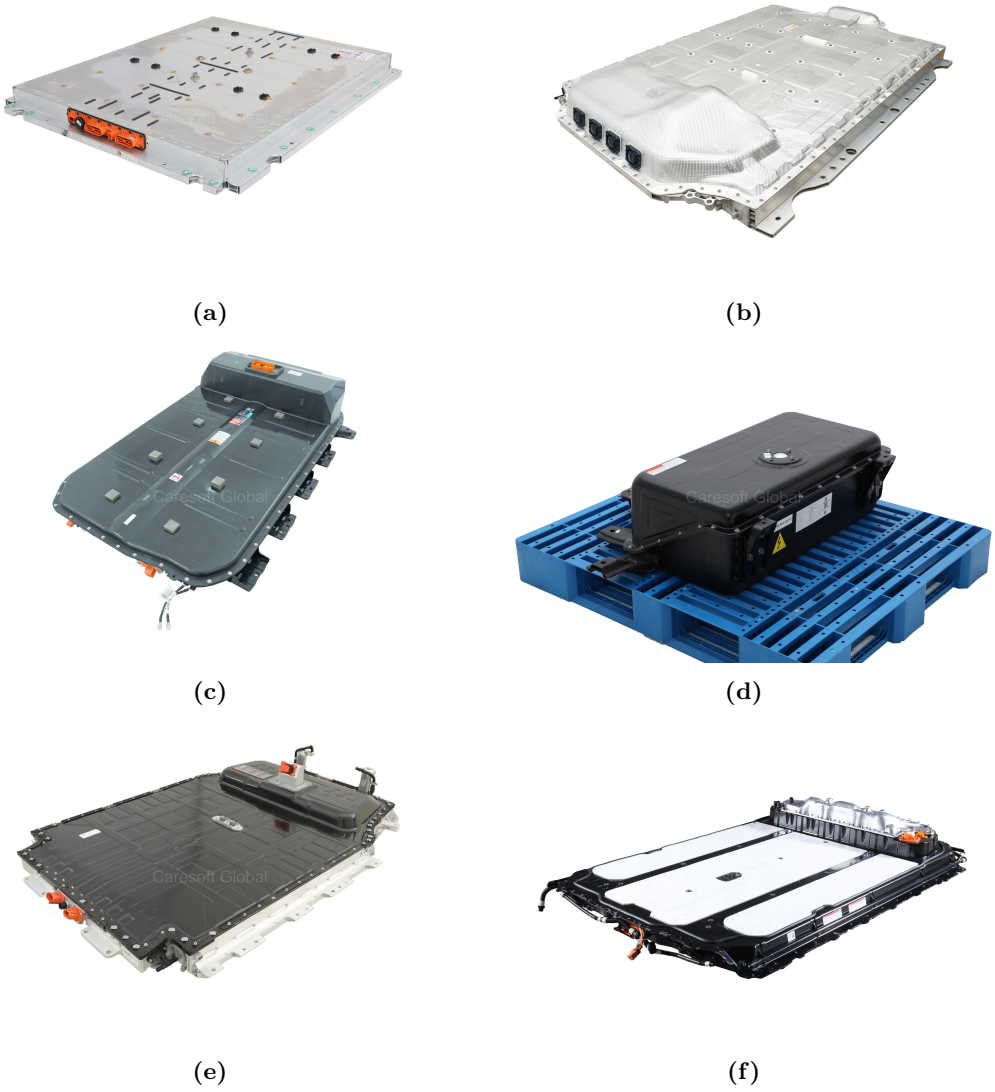


Figure 5.12: Battery packs of state-of-the-art of commercial EVs [105]. **(a)** Audi Q4 e-tron Quattro. **(b)** BMW iX xDrive40. **(c)** Chevrolet Bolt Premier. **(d)** Dacia Spring Comfort Plus. **(e)** Nissan Ariya B6 Variant. **(f)** Tesla Model 3 Long Range RWD.

As can be concluded by the consultation of the Figure above, typically, the battery pack housing resembles a closed box, comprised of upper and lower sections, connected by mechanical fasteners along a joint line and an elastomeric seal. The seal prevents particles and liquids from entering the battery pack and is tailored to a specific Ingress Protection (IP) class. In most cases, the components have a common plan view shape but with diverse shapes and heights. A flange can also often be found to add stiffness to the structure and serve mounting and sealing purposes. Including ribs and other similar design elements in the enclosure further increases its overall stiffness, strength, and crash performance without the weight penalty otherwise brought by conventional metal cases [66, 97].

For completeness purposes, the SAE standards regulating the mechanical design of automotive battery packs can be found in Table 5.3. Any BPE design should, thus, be designed considering the presented guidelines.

Table 5.3: SAE standards regulating the mechanical design of automotive battery packs (Adapted from [106])

Standard	Title	Scope
SAE J240	Life Test for Automotive Storage Batteries	Simulates automotive service when the battery acts in a voltage regulated charging system.
SAE J1766	Recommended Practice For Electric, Fuel Cell And Hybrid Electric Vehicle Crash Integrity Testing	Defines test methods and performance criteria to evaluate post-crash electrical safety, retention of electrical propulsion components and electrolyte spillage.
SAE J1797	Recommended Practice For Packaging Of Electric Vehicle Battery Modules	Provides common battery designs through the description of dimensions, termination, retention, venting system, and other features required in an EV.
SAE J1798	Recommended Practice For Performance Rating Of Electric Vehicle Battery Modules	Presents common test and verification methods to determine EV battery module performance.
SAE J2185	Life Test for Heavy-Duty Storage Batteries (Lead Acid Type only)	Applies to lead-acid 12V heavy duty storage batteries for uses in starting, lighting and ignition applications on motor vehicles and/or off-road machines.
SAE J2289	Electric-Drive Battery Pack System: Functional Guidelines	Common practices for the design of battery systems for vehicles that use a rechargeable battery to provide or recover all or some traction energy for an electric drive system.
SAE J2344	Guidelines For Electric Vehicle Safety	Defines the favoured technical guidelines relating to safety for vehicles that contain High Voltage (HV) during normal operation and charging.
SAE J2380	Vibration Testing Of Electric Vehicle Batteries	Describes the vibration durability testing of a single battery consisting of either an EV battery module or an EV battery pack.
SAE J2464	Electric And Hybrid Electric Vehicle Rechargeable Energy Storage System (RESS) Safety And Abuse Testing	Characterises a body of tests that may be used for abuse testing of these vehicles to determine the response of the electrical energy storage and control systems to conditions/events beyond their normal operating range.
SAE J2929	Safety Standard For Electric And Hybrid Vehicle Propulsion Battery Systems Utilising Lithium-Based Rechargeable Cells	Safety criteria for a lithium-based rechargeable battery system to be used for vehicle propulsion as an energy storage system connected to a high voltage powertrain.

Lastly, once more, it must be mentioned that BPE lightweight design is deemed as essential particularly to decrease the overall weight of the EV and, by that, minimise its energy consumption and improve the vehicle dynamics. A method oftentimes used by the automotive industry to reduce the weight associated with the energy storage component is to design the BPE as an integral part of the vehicle, thereby functioning as an EV structural component. An example of a commercial BEV where the housing is utilised as a load-bearing part of the vehicle structure is the Tesla Model X.

5.2.2 Battery Pack Placement and Fixation

The placement of the battery packs in the vehicle is a strategic task, aiming to: 1) fill unused space in the vehicle, contributing to effective space utilisation; 2) position the CG of the vehicle as low as possible, minimising the mechanical stresses and fatigue on the mounting frame and enhancing the driving dynamics; 3) maximise heat dissipation through suitable air circulation; 4) reduce the risk for passengers of contact with high voltage components; and, lastly, 5) place the packs away from common crash zones of the structure, i.e., the front and rear of the vehicle [66, 102].

Based on data from real-world accidents and laboratory crash tests in unibody-style vehicles, two safety zones can be defined (Figure 5.13). In most commercial cars, the battery pack is placed in the so-called "primary safe zone", which essentially corresponds to the passenger cabin, at the centre of the vehicle chassis, a reinforced area protected from external impact loads by the carefully designed vehicle structure [64].

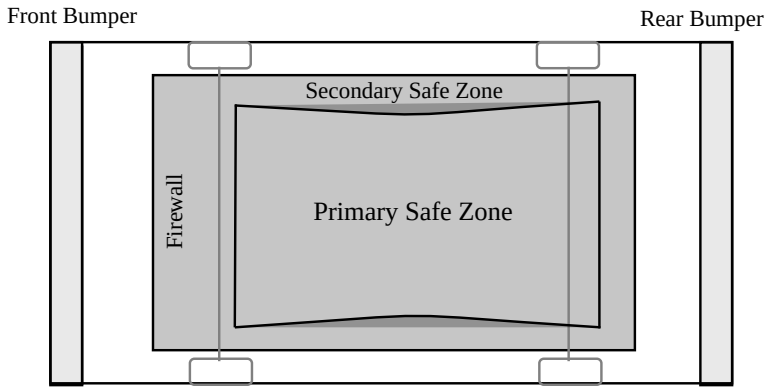


Figure 5.13: Safety zones based on data from vehicle intrusions from accidents and laboratory tests (Adapted from [107]).

With the aim of improving the battery pack safety in the case of vehicle impact while considering the fact that the cabin space is restricted, the battery pack is generally located on the inner cabin side of the floor panel, beneath the passenger seats. The described location is illustrated in Figure 5.14 for a Nissan Leaf model. Moreover, the position of the battery packs in various state-of-the-art commercial cars can be found in Table 5.4.

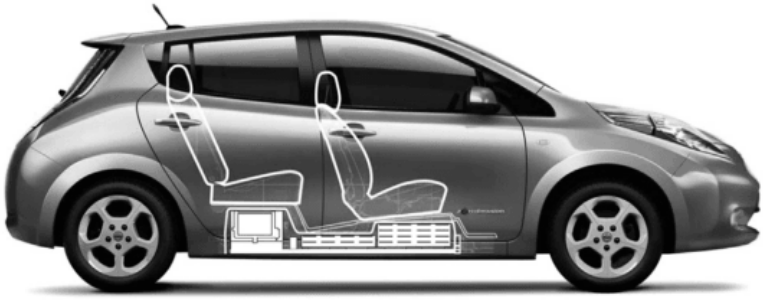


Figure 5.14: Battery pack positioning in a Nissan Leaf [102].

Table 5.4: Placement of battery pack in some state-of-the-art commercial cars (Adapted from [102])

Vehicle	Battery location
BMW i3	Center
Nissan Leaf	Center
Ford Focus Electric	Rear
Tesla Model S P100D	Center
BYD e6	Center
Fiat 500e	Rear
Chevrolet Bolt EV	Center
Volkswagen e-Golf	Rear
Mitsubishi i-MiEV	Center

Since the presented battery pack localisation limits considerably the battery volume and design, studies in which alternative pack designs and positions in the vehicle are proposed and analysed may find significant importance in future EV generations. However, currently, as was addressed in Chapter 2, this has yet to be researched on a large scale.

5.2.3 Materials of the Battery Pack Enclosure

Material selection plays a fundamental role to attenuate the mechanical, thermal, and electrical abuses that the battery pack endures during the ride conditions. Only with appropriate materials is it possible to achieve the functional requirements of a robust and reliable battery packaging design [102].

Commercial BPEs are mostly manufactured in aluminium, steel, and composites. In addition, different materials are preferred for diverse components of the housing, depending on their function in the assembly [97]. Hence, a brief discussion regarding the roles of the main elements of the enclosure and material types commonly utilised in them is presented.

Regarding the upper battery pack housing, it can often be found that this element only deals with relatively small external forces and shocks, i.e., the main loads are absorbed by the bottom casing. This explains the fact that, in numerous EVs, the top cover is oftentimes manufactured in lightweight composites or characterised by considerably thin thicknesses. In the former case, the component is typically made via an integrated injection moulding process. It must be noted, however, that the usage of these materials entails the solution of potential issues related to the Electro-Magnetic Compatibility (EMC) of the battery pack, as

well as the low melting point of the material, which can originate a safety risk. Deep-drawn aluminium may also be a solution for this component [66, 97].

As for the battery pack side parts and bottom members, an optimal choice for their construction is the utilisation of lightweight metals such as aluminium or aluminium alloys. This selection enables the attainment of desired properties in terms of rigidity and strength necessary for sustaining the weight of a cell assembly. A frequent solution, particularly for the bottom battery housing, is deep-drawn steel, a material that offers a high to very high stiffness and allows the design of considerably large battery packs. Alternatively, casted aluminium enables a flexible design of the shape and wall thickness, which may facilitate the integration of mounting interfaces and other elements. The inclusion of ribs and other design elements is utilised to improve the strength, stiffness and crash properties of the system, while avoiding the weight penalty linked with traditional steel casings. The maximum size of casted aluminium casings is, however, limited. Lastly, another common option is the employment of aluminium extrusion profiles, which offers benefits in terms of industrialisation and, consequently, costs. Extrusion profiles are inexpensive, and casings built of this material have a high mechanical strength and are typically associated with reduced weight. The difficult bonding process and the achievable tolerances are challenges for adopting this technology.

Overall, resorting to metal solutions for the BPE has been considered as advantageous as they are capable of, additionally, withstanding the severe temperature and pressure conditions to which a battery pack may be subjected. Note, however, that these metals have exceptional thermal conductivity, which can complicate the thermal management of the batteries [7, 97]. Another key requirement for the battery pack bottom and upper case and assured by these materials is that they must be chemically stable and not react with the battery components [102].

In relation to the gaskets or sealing portion, materials that possess high deformability and moisture resistance, such as elastic members, are desired. O-rings should be fabricated from materials that exhibit excellent temperature resistance, such as fluoroelastomers, silicones, or Teflon. Polymers (for instance, a plastic such as nylon) are typical solutions to manufacture battery mounting brackets [7].

To shed some light on the present trends of the automotive industry, in Figure 5.15, some of the most prominent models of commercial EVs are represented, in an orderly manner, in terms of range, with the principal material being utilised in the manufacture of their BPE being appointed. It can be deduced that aluminium is the preferred solution for EV battery housings, particularly in long-range BEVs [108].

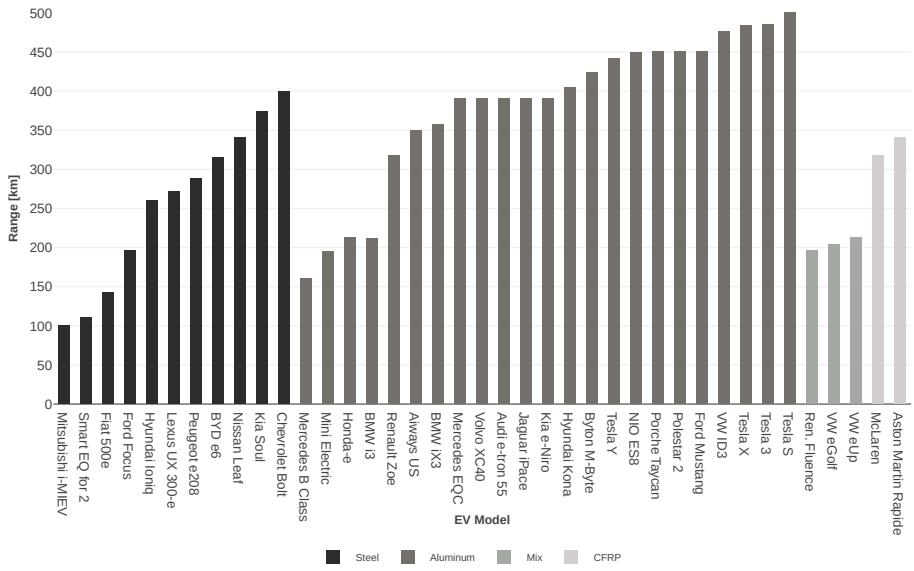


Figure 5.15: Materials used in battery pack enclosure of state-of-the-art commercial car and their range (Adapted from [108]).

As shown in Figure 5.16, the current three main drivers for material selection and lightweight design. They are the following [108]:

- Cost - Important aspect for both the manufactures and consumers. Note that the cost of the raw materials does not equate to the value of a lightweight design, which considers battery and elements re-sizing, cost savings of body structure, etc.
- Performance - As was also already explored, a lighter design translates into improved performance results. Impacts on the driving range, driving dynamics, energy consumption, and towing capacity are verified.
- Sustainability - Manufacturing and recycling procedures must be considered. The effect of design choices and material selection, and comparison between different options, can be analysed by Life Cycle Assessment taking into account ISO 14040/44 guidelines.

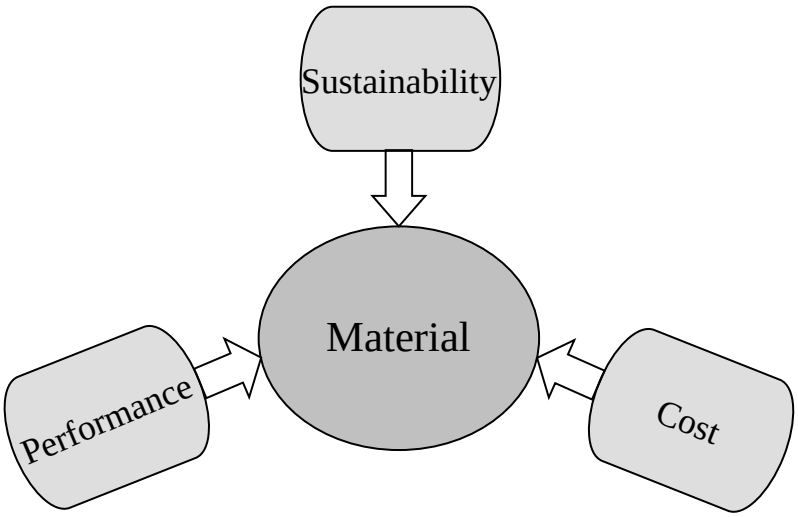


Figure 5.16: Drivers for material selection and lightweight design (Adapted from [108]).

Given the fact that further steps of this work will entail the selection of one or more materials for the construction of numerical models to be studied and optimised, the three material classes presented in Figure 5.15 will be examined in terms of their qualities and limitations for application in BPEs. The three drivers of Figure 5.16 will for that be considered. Moreover, specific examples of potential materials to use will be addressed, based on extensive literature research. Recall that obtaining the precise materials utilised in the manufacture of automotive components is an extremely challenging task, due to confidentiality conflicts. Therefore, the following subsections of this work are of significant interest.

5.2.3.1 Aluminium in Battery Pack Enclosure Manufacturing

Aluminium, particularly aluminium alloys, are being extensively used in manufacturing BEVs and are set to play an even more important role in the coming years. In fact, the use of aluminium alloys in vehicles as a lightweight material is expected to increase by 260 kg over the next ten years, with applications both in extruded body parts and battery enclosures [109, 110]

Aluminium alloys are perhaps the most relevant design material for this application when their wide range of mechanical and technological properties is being considered. These materials present key properties for production such as good formability (for deep-drawing and extrusion), machinability, weldability, and corrosion resistance, which make it desirable for lightweight design [109]. Moreover, other relevant fundamental characteristics of these materials, which can be explained by the three discussed drivers, complete the reasoning for their widespread use in extruded body parts and battery cases.

Firstly, the cost of a lightweight aluminium design is attractive for large and performance-oriented EVs [108]. This is meaningful since, according to the data retrieved by [111], a market shift is occurring, where the rising trend is towards larger vehicles that contain an increased aluminium content and premium models with an above-average aluminium percentage. Furthermore, aluminium is the material with the highest growth rate in automotive applications, mainly due to the substitution of steel in platform parts and substantially higher aluminium content in BEVs, which are, in turn, increasing significantly in market share. Therefore, the gap between the cost of aluminium and disputing materials is set to

decrease in the future, further enhancing the competitiveness of the former.

Performance-wise, in light of the fact that an optimised aluminium design is 40% lighter than an equivalent-sized optimised steel design, benefits can easily be found with the application of the aforesaid material. An aluminium case safeguards this component's lightness, shock resistance, and high thermal conductivity. Recall that by using a heavier material for the body, such as steel, it is necessary to add more batteries to the design and use more powerful electric motors to achieve the same levels of range and acceleration. This leads to a secondary weight gain [108, 109].

In terms of sustainability, it is crucial to note that at the end-of-life of a vehicle, approximately 96% of the aluminium can be recycled and reused for automotive parts. This enables a smaller demand and dependence on virgin materials, contributing to a circular economy [108]. Actually, because the melting temperature of the recycled material is lower than that of the pure aluminium, a 95% reduction of the GHGs emission during production is possible [112].

The research carried out with respect to the numerical simulation of BPEs revealed that aluminium alloys were the preferred option for assigning to the components of the numerical models of the casings [60, 68, 99, 113, 114, 115]. Three series of aluminium alloys, in particular, were repeatedly used by authors: the 5000, 6000, and 7000. Hence, it is useful to succinctly explore the main characteristics of each of those.

The 5000 series (Al-Mg) corresponds to the aluminium alloy group for which magnesium corresponds to the main alloying element [116]. The principle aspects and properties of the aluminium alloys of this series for the discussed application are the following [108]:

- Non-heat treatable aluminium alloys.
- Extremely good cold formability in O-temper.
- Cold work in H-tempers may be used to strengthen the material.
- High corrosion-resistant alloys.

The main alloying elements of 6000 series aluminium alloys (Al-Mg-Si) are magnesium and silicon [116]. The following characteristics contribute to the fact that this series is the major automotive alloy family [108]:

- Heat treatable, with the formation of Mg_2Al_3 and Mg_2Si precipitates.
- Remarkable cold formability in T4 temper.
- Paint-bake or post-forming heat treatment strengthens the material.
- Exceptional corrosion resistance.
- Acceptable associated cost.

Copper and zinc are the main alloying components of the 7000 series aluminium alloys (Al–Cu–Zn), the content of the latter being three to four times greater than the one of the former. Magnesium also plays an important role [116]. The most relevant characteristics of this series are [108]:

- Heat treatable, being the highest strength alloy family.
- Constrained cold formability.

- Hot stamp plus press quenchable.
- Stress corrosion cracking may constitute an issue.
- Not in volume in the automotive industry, particularly due to its higher cost.

A material property chart where the three discussed aluminium alloy series are represented in terms of their yield strength (in MPa) and elongation (%) can be found in Figure 5.17. The strength and formability attributes discussed for each of the aluminium alloy series are, thus, evidenced in the plot.

Although not represented in the aforesaid illustration, it is worth noting that the termed "standard" materials can be found until about the 250 MPa mark, which corresponds to where the high-strength materials start to emerge. This family of materials ranges to approximately 400 MPa. From then on, the materials in question, mainly the 7000 series in this case, are considered ultra-high-strength materials.

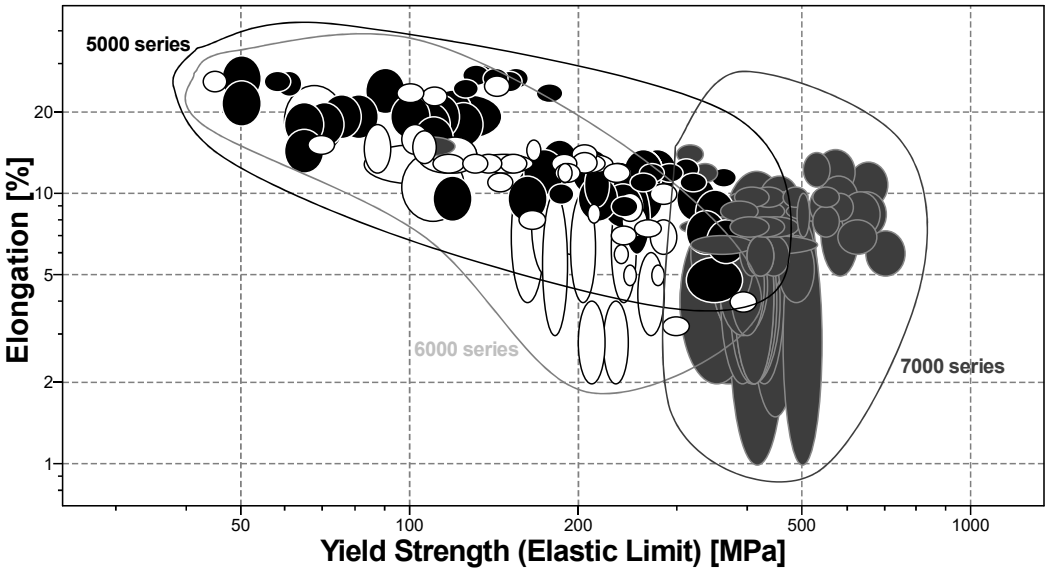


Figure 5.17: Material plot of aluminium alloys used in the automotive industry, in terms of tensile yield strength and elongation (Adapted from [117]).

Despite being challenging to obtain the specific materials utilised in commercial vehicles, [108] and [118], the formal corresponding to a document of a global leader in the aluminium industry, and the latter a work discriminating three aluminium alloys currently being employed in the latest models and prototypes of Aston Martin Lagonda® (although not necessarily in battery housings), were considered. In addition, recurring materials surfacing during the conducted research were taken into account. These findings are presented in Table 5.5.

Table 5.5: Realistic examples of aluminium alloys utilised in the automotive industry

Recurring materials surfacing on research	Constellium [108]	Machado et al. [118]
Al 5052 O-Temper Al 5083-H323 Al 6061-T6 Al 7037-T742	Al 5182 O-Temper Al 5754-H24 Al 5754 O-Temper Al 6111-T6 Al 7075-T6	Al 5754-H22 Al 6016-T4 Al 6060-T6

5.2.3.2 Steel in Battery Pack Enclosure Manufacturing

High Strength Steels (HSS) and Advanced High Strength Steels (AHSS), in particular, contain various interesting characteristics for their application in battery pack enclosures.

Advanced high-strength steels developed and commercialised in the last decade are intended to assist automotive businesses in meeting lightweight criteria without sacrificing occupant safety requirements. These steels are formable due to their exceptional mix of high strength and ductility [119].

For comparison purposes, an HSS-intensive body structure achieves a 20-30% mass reduction in comparison to a conventional steel structure, which contributes to greater dynamic performance. However, an even more interesting approach is an integrated multi-material one, where the mass and the functional properties of aluminium, magnesium, polymer matrix composites, and AHSS can be exploited [120].

The use of advanced high-strength steels has also been on the rise due to the reduction of total costs this material class allows, in comparison to other materials such as aluminium alloys and Carbon fibre Reinforced Polymers (CFRPs) [121].

In terms of sustainability, metals such as steel are relatively easy to recycle. It has been calculated that resorting to recycled steel instead of steel from primary sources can realistically conduct to 80% saving of CO_2 emissions [112]. The CO_2 emissions associated with the production of virgin steel are smaller than those generated by virgin aluminium, the latter being a highly energy-intensive process [122].

Like aluminium alloys, AHSS has been extensively utilised in numerical studies conducted in battery housing models, with a focus on elements of the enclosure with load-bearing functions and the necessity of crashworthiness resistance, such as structural frames or in the bottom case [66, 22].

5.2.3.3 Composites in Battery Pack Enclosure Manufacturing

Despite the expected aluminium boost in EV manufacturing, there are factors that may affect the rate of growth of this material in the long term. The proliferation of composites, particularly for closures and battery housings in EVs, is one of the principal ones [111].

There are many advantages associated with the employment of a composite battery enclosure. The most palpable is, evidently, the weight saving. In fact, a composite battery housing design with identical properties to an equivalent-sized aluminium one is 40% lighter. This allows the obtainment of unusually high energy-density battery packs, which undoubtedly affects the driving dynamics, driving range, and overall performance of the EV in a positive way [66, 123].

To fulfil the structural functions of the battery enclosure, an interesting composite solution would entail a sandwich core, for instance, composed of PolyEthylene Terephthalate

(PET), aluminium foam, or similar materials, with multiple layers of carbon fibre and/or glass fibre fabrics. Diverse textiles, from mats to fibre webs can be utilised, dependent on demands and the materials can be chosen according to the requirements of the particular application, which constitutes another advantage of composites. The stiffness of the enclosure is crucial and is highly dependent on the sandwich structure employed. With a suitable integration of the composite battery housing in the EV and perhaps the use of aluminium hollow chamber profiles, the conventional crash test requirements are ensured and the levels of safety are equivalent to those typical of metal-based solutions [123].

In Figure 5.18, the density, tensile strength, and specific tensile strength of fibre-reinforced polymers, in this case, CFRP, and Glass fibre Reinforced Polymer (GFRP), are compared against those of steel, aluminium alloys, and pine wood. As can be seen, it is in the last properties that GFRP, and particularly CFRP, shine.

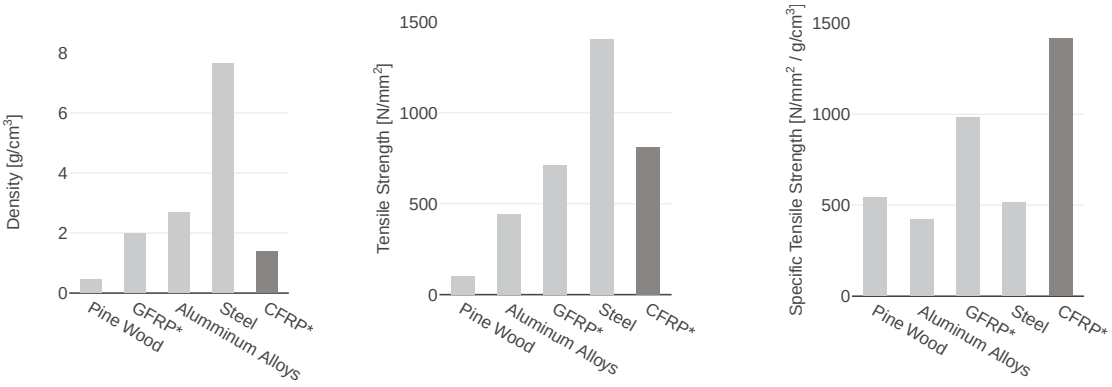


Figure 5.18: Properties of fibre-reinforced polymers set side by side with those of steel, aluminium, and wood (*for a fibre orientation of $0/\pm 45 = 1/1$) (Adapted from [123]).

In comparison to state-of-the-art metal-based solutions, composite housings present enhanced corrosion resistance and thermal management [124]. The low levels of thermal conductivity inherent to these materials, about 200 times lower than those of aluminium, are remarkable prerequisites for competent fire safety. Additionally, owing to the composites insulation effect, less energy is employed for thermal regulation which contributes to the vehicle's efficiency and consumption cutbacks [123].

Other relevant characteristics have also been assessed. For instance, electromagnetic shielding for critical areas is possible using a carbon fibre web, an adequate number of layers, and assessing their fibre volume content. Finally, the high specific stiffness of fibre-reinforced components, adding to the reduced weight and good damping properties, has a positive influence on the vehicle's Noise, Vibration, and Harshness (NVH) behaviour [123].

In terms of costs, by resorting to composite materials there is often a trade-off established between the related weight savings and the high costs of production. Therefore, this expensive material is often solely implemented substantially only when equally high returns are anticipated. The downsizing powered by the use of composites, however, secondarily allows reductions in battery costs of about 5%, according to Trautwein et al. [125]. Finally, the last thing to be mentioned on the cost driver with regards to composites, is that efforts are actively being employed to reduce the cost of these materials as their inherent characteristics are of great interest to crossfield applications and have gathered attention in recent decades.

With respect to the sustainability driver, it can be considered that some of these materials are not easily recyclable, as is the case of GFRP [126], for example. Reusing or recycling the reinforcing fibres at the end of life is challenging, remoulding the thermoset matrices is

not performable, and due to the complex composition of these materials and frequent contamination between their constituents, their reusing is often limited. CRRPs, for instance, have mainly been disposed of by landfilling in the past. However, as polymer matrix composites are increasingly finding their way into more mainstream vehicles, particularly EVs, the sustainability aspect related to these materials has gathered the attention of scholars and industrials alike [112].

Carbon fibre Sheet Molding Compounds (CF-SMC) is a material class constituted by prepreg chips or bundles of cut carbon fibres dispersed in a matrix. Epoxy and vinylester resins represent the most used materials in the matrix constituent. According to [124] and [126], this class presents tremendous potential for battery enclosures applications in EVs. The crashworthiness of CF-SMC in a structural battery case was numerically analysed in the last reference and positive outcomes were obtained, proving the validity (and linked advantages) of employing this solution to lightweight structural parts of EVs.

5.2.4 Summary of State-of-the-art Battery Pack Enclosure Solutions

To conclude this Chapter and to provide concrete information about state-of-art commercial vehicles, in Table 5.6 are presented the used material types, the weight, and the dimensions of the battery packs of several EVs in the market. The Iceberg by Caresoft Global vehicle benchmarking data platform [105], a resource available to the author of this work for a limited time by CES, was utilised for retrieving this comprehensive data.

Because most of the models assessed transversely across this Chapter, in Tables 5.2 and 5.4, for instance, are not available in this database they are not represented in the following table. However, there was care in choosing EV models similar to the ones addressed previously.

Table 5.6: Summary of materials, weight, and dimensions of commercial (Adapted from EVs [105])

Electric Vehicle	Battery pack enclosure			
	Material		Weight [kg]	Dimensions [mm]
	Top Cover	Bottom Case		
Audi Q4 e-tron 50 Quattro 2022	Aluminium	Mix of Aluminium Alloys	490.5	1833 x 1444 x 325
BMW iX xDrive40 2022	Thermosets, Aluminium, Magnesium, Foam	Aluminium, Steel	521.5	2410 x 1680 x 340
BYD Han AWD High Performance Flagship 2022	Plastic	Aluminium	581.4	2414 x 1229 x 255
Chevrolet Bolt Premier 2017	Plastic	Steel	426.9	1810 x 1275 x 380
Citroen E-C4 Feel Pack 2021	Steel	Steel	317.1	2140 x 1340 x 295
Dacia Spring Comfort Plus 2021	Steel, Foam	Steel	189.1	788 x 1179 x 308
Ford Mustang Mach-E First Edition 2021	Synthetic Rubber	Steel, Sealants	595.5	2270 x 1515 x 335
Hyundai Ioniq 5 Ultimate 2021	Steel	Aluminium, Adhesive, Steel	455.4q	2190 x 1465 x 150
KIA EV6 Air Active 2021	Steel	Aluminium, Sealants, Steel	474.5	2180 x 1459 x 215
Mercedes-Benz EQS 580 4Matic Edition 1 2022	Steel, Sealants	Aluminium, Steel, Sealants	701.7	2307 x 1546 x 253
Nissan Ariya B6 Variant 2022	Steel, Plastics	Aluminium, Steel	443.0	2017 x 1456 x 335
NIO ET7 75KWH 2022	Plastics, Steel, Foam	Aluminium, Foam, Steel, Sealants	542.5	2064 x 1540 x 185
Renault Zoe RIVIERA R135 ZE 50 2020	Steel	Aluminium, Steel	273.8	1645 X 1280 X 350
Tesla Model 3 Long Range RWD 2017	Steel, Aluminium, Synthetic Rubber	Steel	455.9	2155 x 1485 x 336
Tesla Model Y Long Range AWD 5-Seater 2021	Steel	Aluminium, Material Mix	444.7	2158 x 1470 x 341
Toyota bZ4X Limited AWD 2023	Steel, Plastics, Sealants, Foam	Steel and Aluminium	448.5	1781 x 1622 x 183
Volkswagen ID.4 First Edition 2021	Aluminium	Aluminium, Steel	488.0	1827 x 1443 x 170

Chapter 6

Numerical Analysis Procedure

This brief Chapter plays two fundamental roles in this work. Firstly, it represents a partition between the end of this thesis's theoretical and mathematical review portion and the start of the numerical part of it. In addition, it lays down the methodology followed for the numerical analysis.

Having acquired all the knowledge capacitated by the comprehensive scientific review, the reader is now in a condition to fully understand the steps and choices performed in the numerical analyses conducted to achieve the established goal for this work.

Prior to the exposition of the work performed in the following Chapters, it is necessary to mention the utilised software:

- For the purpose of developing the geometry for the main case of study, the 3D computer-aided design (CAD) modelling software NX® was utilised. Given the inherent simplicity of the geometry of the problem chosen for the convergence study, SpaceClaim, a 3D direct modelling software tool developed by, and within, Ansys®, was employed. It was also used to design an alternative BPE component, as will be seen next;

- The software utilised for all the numerical simulations performed within the scope of this work was Ansys®. The commercial FEM software was used for all pre-processing, calculation, and post-processing. Material and geometry assignment, mesh creation, and imposition of all-natural and essential boundary conditions, including load conditions, were imposed within the software's domain. The analysis systems of Static Structural, Explicit Dynamics, Modal, and Transient Structural were explored.

The numerical roadmap followed in this work is illustrated in Figure 6.1.

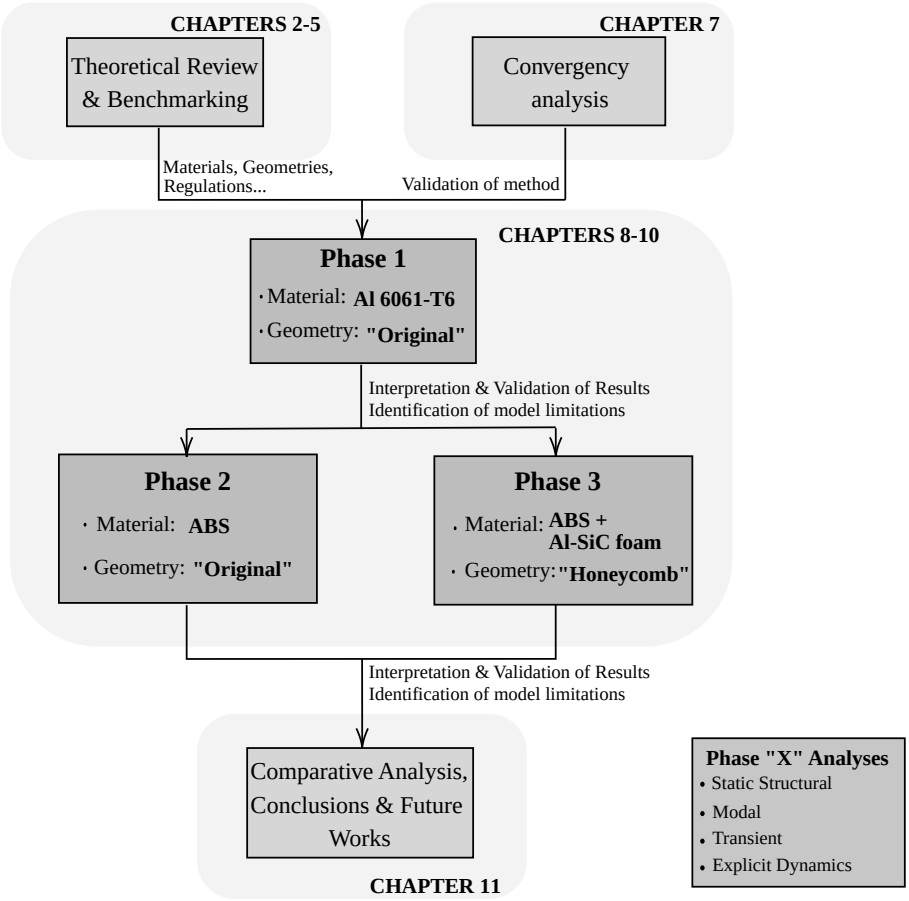


Figure 6.1: Structure of the numerical portion of the work being performed.

The mathematical, theoretical, and social review, as well as the benchmarking performed resorting to the Iceberg [105] platform, provided the fundamentals to the definition of essential parameters, such as the material and geometry design, crucial for the starting point of the numerical analysis of the main subject of this study. This initial point corresponds to Phase 1, where the so-called "Original model" of a battery pack enclosure was designed and set up as realistically as possible (by similarity to a current industry solution) and later studied. Phases 2 and 3 involve the analysis of models resulting from two distinct optimisations of the "Original model".

The numerical analysis of this work is essentially composed of Phases 1 through 3, which are preceded by a convergence study to validate the method employed in the explicit dynamic analysis. Each of the Phases is constituted by four analysis types for each of the above-mentioned Ansys® analysis systems. Five simulations are performed for each phase, one for each analysis type, except for the explicit dynamic analysis. In the latter, two simulations were performed at different velocities to better understand the structure's behaviour to the impact and the influence of velocity on the damage to the BPE. Each of the analysis types and their relevance in this work will be presented in the following subsections of this Chapter.

Preferably, a similar mesh and the same analysis parameters will be established for a given analysis type across all of the Phases unless the opposite is mentioned and justified. This means that while it will be possible to find diverse meshes and analysis parameters in distinct analysis types, these will oftentimes be identical for all of the simulations performed for a given kind (either in the same phase or not) unless otherwise stated. This was done

to truly compare the findings related to each of the different BPE solutions in the multiple analyses conducted, based solely on their performance without any other possible influence.

Therefore, the differences between each of the Phases rely essentially on the materials and on the geometry chosen for the various models. The disparity in these "variables" leads, of course, to differences between the results found in identical analysis types; it is not only on the resistance of the structure to crash and impact events but also on its overall weight. Since the primary objective of this work is to propose improvements in the crashworthiness and weight of battery pack enclosures, the best combination between lightweight materials and geometry design is sought.

It may be thought that the mechanical resistance of a structure and its weight are more often than not opposite characteristics, in the sense that the success of one does not occur without the detriment of the other; however, that is not always the case. In fact, for a structure like a battery pack enclosure, the equilibrium between both properties is of major importance, as was addressed before, since it defines the essential balance of a BEV regarding safety and performance requirements. Recall that these requirements are some of the buyer's main concerns when acquiring an EV. This validates the purpose of this work as of great interest for the field it is inserted in.

After numerically analysing the aforesaid characteristics in the "Original model" of Phase 1, alternatives were searched to optimise them. Although the optimisation routes were immense, the rationale between the selected paths, besides the established objectives for this work, was to provide the reader with solutions consistent with the industry's demands and knowledge while bringing a degree of innovation to the problem being treated. Therefore, typical solutions, such as utilising a CFRP structure, a material that has already been extensively studied for similar structures and whose properties and characteristics are already well-established, were not considered.

In the rest of this Chapter, the original structure, obtained from a relevant industry solution, is presented and contextualised. Next, the multiple analyses and respective relevant parameters are explored. Prior to that, however, it is relevant to mention that the numerical simulations were performed in an HP Z8 G4 Tower Workstation with 193 GB installed RAM, associated with two Intel Xeon Gold 6136 CPU @ 3.00GHz processors. Twenty-four cores were utilised in all of the simulations. This resource was made available by CES.

6.1 Industry Inspiration for the Study

As could be concluded from Figure 5.12 presented in the last Chapter, although the precise design of the battery packs, and therefore, battery pack housing, is not the same for each EV, in most cases, a degree of resemblance can be found. Oftentimes, a rectangular, box-like flattened structure is the solution for this component.

One of the research gaps that emerged in the first stages of this work was that often very simplistic models and load cases were used to investigate the crashworthiness of structures of protection of the packs. Although coherent with the study and of some interest, the yielded results are of limited application and overall physical meaning. Hence, part of the novelty that characterises this work is grounded on using a realistic base model, resulting from similarity, by reverse engineering process, from a real-life industry solution. The CAD of this structure is then associated with materials used currently in the industry. After the employment of a suitable mesh, the model would be subjected to various analyses. These, in turn, should be established based on present automotive regulations or programs that dictate crash testing parameters. The regulations themselves are already established based

on real-life events (and worst-case scenarios), so the level of sensibility of the load cases set up in FEM is assured. This knowledge is, once again, the outcome of the research provided in the first Chapters of this work.

6.1.1 Battery Pack Enclosure Structure

The process of selecting a battery pack enclosure was based on two principal requirements:

- The BPE must be employed in a well-positioned commercial BEV to provide a degree of realism and sensibility to the present study;
- A sufficient level of the available information regarding the BPE to enable the obtainment of a precise model must be verified.

Since the manufacturer of the assessed BPE does not maintain any link to the institution or organisation in which this work is inserted, for legal reasons, it is impossible to disclose the exact model being replicated. However, what can be said is that the inspiration for the starting geometry, i.e., for the model of Phase 1, is an example of a battery pack enclosure that fulfils each of the above conditions.

The BEV in which the BPE is inserted corresponds to an evolution of a former model of the corresponding automotive manufacturer. According to Pall Kornmayer [127], a former engineer responsible for the design of the centre underbody of this BEV's structure, the purpose of this commercial model was to achieve a more robust structure than its predecessor, capable of withstanding increased vehicle loads, meanwhile diminishing body costs and simplifying the body assembly of the former. The answer to these objectives relied on an almost entirely aluminium structure that utilised large cast nodes and extruded profiles with stamped panels.

The BPE's geometry and the vehicle's battery pack's location can be consulted in Figure 6.2.

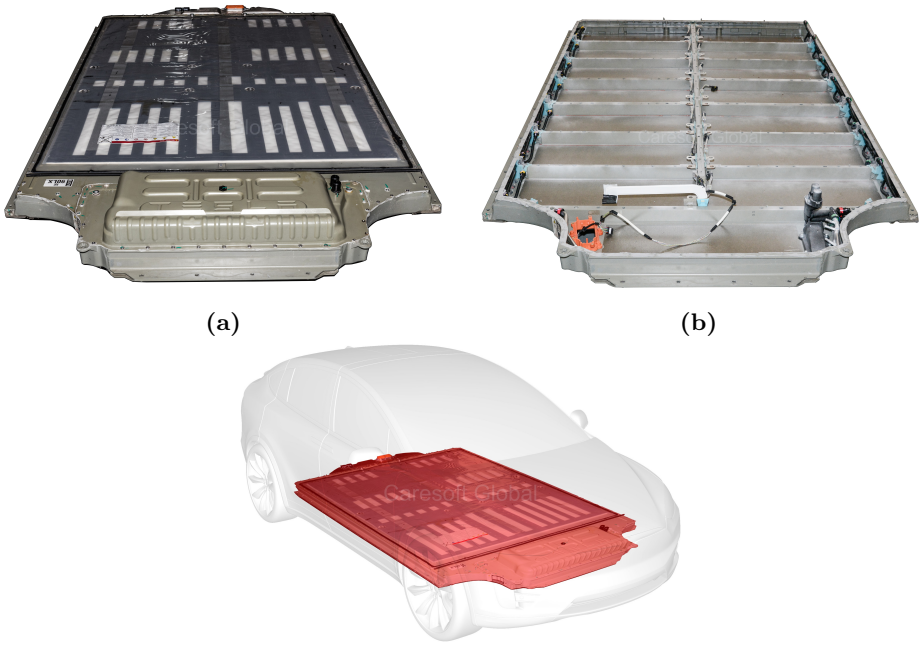


Figure 6.2: Industry inspiration for the battery pack enclosure in this study [105]. **(a)** Battery protection structure fully closed. **(b)** Battery protection structure without the top cover. **(c)** Position of the battery pack (enclosure) in the vehicle.

The battery pack enclosure of this model presents more functions than the shielding and protection of the battery modules. In fact, the battery pack is integrated into the vehicle's structural frame, allowing the BPE's inherent rigidity and strength to improve overall vehicle performance and impact resistance [128]. As was seen in Figure 6.6, the battery pack is located on the centre underbody of the vehicle, between the passenger cabin floor panel and the driving surface. The battery pack spans the width of the car, from rocker panel to rocker panel, and the majority of the space between the front and rear suspensions. This extension of the battery pack (enclosure) enables the mentioned enhancements in the vehicle structure and performance [128].

The BPE is mounted on the rocker panels, vehicle structural members that correspond to aluminium or aluminium alloy extrusions, on each side. This integration is possible as the BPE comprises lateral members that include a mounting flange positioned beneath the rocker. The battery housing and the rocker are then mechanically coupled by a combination of bolts and nuts [128]. Considering the integration of the battery pack in the vehicle and the side crash test that will be simulated (a matter that will be discussed in the next sections), it was concluded that the rocker panels should be included in the studied BPE models. The representation of this component, which does not belong to the enclosure assembly, is justified by the fact that when the vehicle endures a side impact, the panels absorb most of the impact energy. Indeed, in this case, the rocker panels are part of the deformable zone, while the battery pack can be interpreted as a backup structure to impact [127]. Thus, it would be incorrect to simulate a direct side impact on the BPE, which would lead to the obtainment of unrealistic results. Furthermore, the lateral components' presence is relevant to understanding how the rocker's deformations and stresses are transmitted to the battery pack.

In Figure 6.3, the illustration of the cross-section of one rocker panel and its attachment

to the battery pack housing, retrieved from the US Patent 8,833,499 B2 [128] (assigned to the automotive manufacturer in question) can be consulted. Although it was not possible to have access to the specific rocker cross-section of this model to verify if this was, in fact, the exact employed solution, if the represented geometry is not it, the commercial solution is something extremely similar to equivalent properties and manufacturing processes. Therefore, this cross-section was replicated in the CAD of the structure, with only slight variations originating from the inputs of other sources.

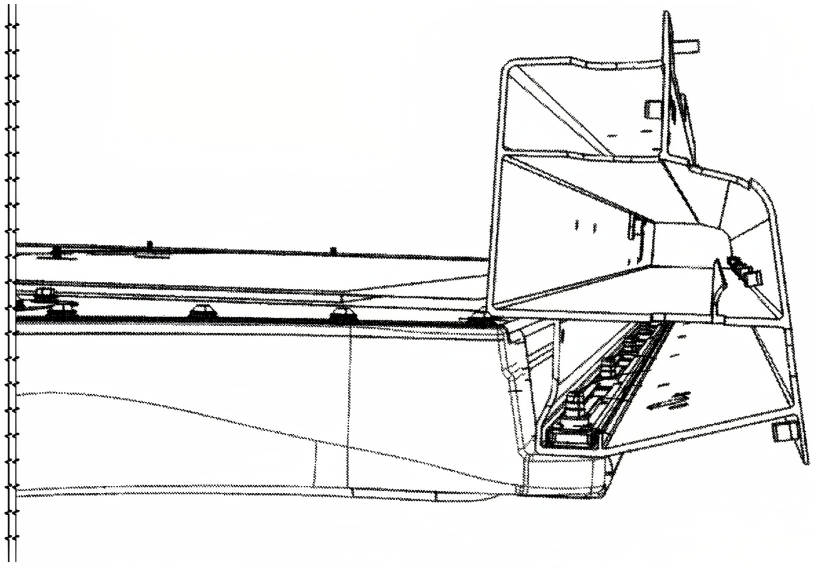


Figure 6.3: Attachment of the battery pack enclosure to the rocker panel (and cross-section of the latter) [128].

Evidently, just as incorrect would be to simulate a direct frontal impact to the battery pack. Given the fact that the vehicle presents frontal (and rear) deformation zones that, as explained before, absorb impact energy during a crash, most of the energy is dissipated across these regions. The "primary safe zone" is where the passenger compartment and the battery pack are located and, therefore, protected. Hence, the frontal crash event will be simulated by resorting to a transient analysis without direct impact, which will be explored in the following subsection.

By now, it is well established that a battery pack is composed of a variety of elements related to a multitude of functions. For completeness purposes and to provide knowledge of how the different battery pack components are integrated into each other, a tier down of the battery pack assembly, consisting of its main elements, is provided in Figure 6.4.

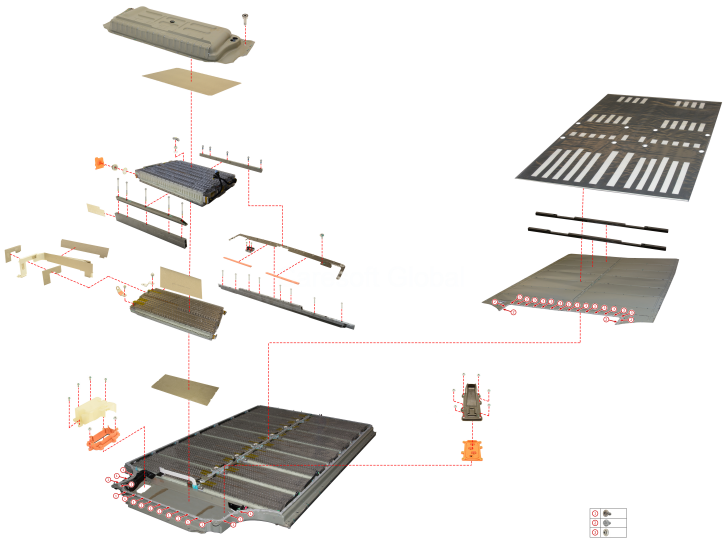
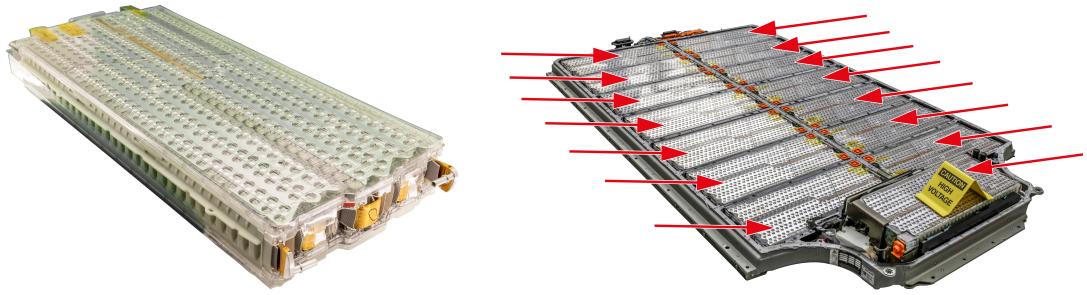


Figure 6.4: Battery pack tier-down, considering its main components [105].

In the Figure above, its possible to visualise, in addition to the BPE components themselves, elements such as support bars, battery modules, corresponding brackets, seals, holding plates, foams and insulators, connectors, vent plugs, and others. The majority of these will not be represented in the studied model. Still, it may be relevant for the reader to understand how these elements are included in the battery pack, their positions, and their relations to each other to grasp a bigger picture of the HV battery assembly.

Regarding the BPE, only the components with load-bearing functions (i.e., those identical to the ones presented in Figure 6.2, without the top foam evidently) will be explicitly built in the model inspired by this industry solution. Therefore, the BMS and all the other electrical and thermal elements that interface this component were considered out of the scope of this study. In fact, the only electrical component to be represented in the model and the only exception to this rule are the battery modules. Although they will not be truly represented in the CAD made of the structure, the modules will be accounted for in the analysis in physically-equivalent ways, given the relevance of their presence in the battery pack to the overall results of the simulations. This matter will be discussed next.

In Figure 6.5, for illustration purposes, one module unit and the position of the fifteen modules that are included in the addressed battery pack can be found.



(a) **(b)**

Figure 6.5: Battery modules used in the industry inspiration for this study [105]. **(a)** A module unit. **(b)** Positioning of the fifteen modules within the BPE.

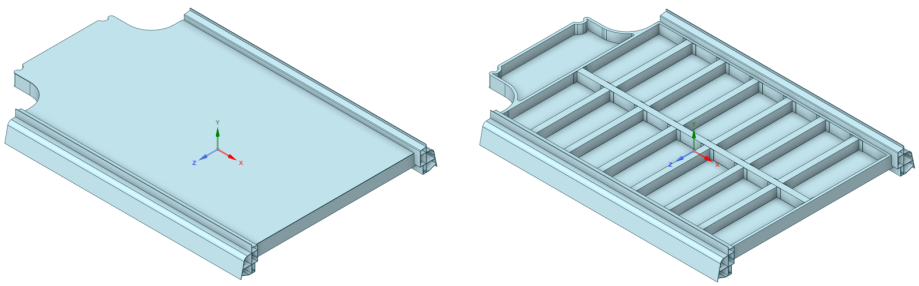
6.1.2 Battery Pack Enclosure Model

6.1.2.1 Model Geometry: Design Parameters

As previously disclaimed, most data regarding the manufacture of an automotive structure, from its specific dimensions, materials, characteristics, and others, is confidential. This lack of public information can significantly impact the degree of realism of independent studies conducted with the purpose of evaluating state-of-the-art automotive components and possible optimisation paths for them.

Due to this, of course, no realistic 3D CAD model of the assessed BPE, with the precise dimensions and geometry, can be found available in any database for applications similar to those of this work. Therefore, the only solution to this issue was to draw the desired structure geometry from scratch by a process of reverse engineering. The design was then achieved by similarity resorting to multiple sources of information. The main reference was the available data in the Iceberg benchmarking platform [105] regarding the studied vehicle, structure, and its integration in the Body-In-White (BIW). Furthermore, knowledge found in the US Patent 8,833,499 B2 [128] and typical dimensions for the different components of the enclosure assembly emerging from representative models in the conducted research were all considered since the aforesaid exact values are unknown.

Despite being, evidently, simplified to some extent, as necessary for reaching a reasonable computational cost in the posterior numerical study and made with approximated dimensions, it can, nevertheless, be stated that the adapted CAD is representative of the real complex BPE structure, i.e., made with sensible geometry and dimensions. The CAD obtained at the end of this reverse engineering process can be found in Figure 6.6.



(a) **(b)**

Figure 6.6: CAD of the BPE structure. **(a)** Battery protection structure fully closed. **(b)** Battery protection structure without the top cover.

The CAD that was input as the geometry of the "Original model" of Phase 1 is composed of:

- The rocker panels, connected to the BPE by a flange of the bottom case of the latter on each side, with the already discussed aim.
- A thin top cover whose main purpose is to shield the battery pack from other vehicle components and the entrance of any possible substances. This element does not present a strong structural function, as is often the case in real battery pack housings. It is bonded to the bottom case.
- A bottom case, which in comparison to the top cover, is a much thicker and more robust element whose main function is to contribute to the structural integrity of the BPE (and the vehicle too).
- Internal reinforcements, the biggest one crossing the longitudinal span of the BPE almost entirely, and twelve smaller ones crossing it orthogonally in a symmetric manner to the former (six on each side). These reinforcements act as separators to the module units and, very importantly, transfer the loads actuating on the structure, dissipating them across the whole assembly and thereby contributing to its structural integrity. They are fixed by their extremities on the lateral internal surfaces of the bottom case.

The relevant dimensions of the CAD are indicated in Figure 6.7, where additional views of the BPE and rocker panel's geometry can be found, and in the corresponding Table 6.1. The thicknesses, not represented in the aforesaid Figure due to the difficulty of their graphic representation, range from 3 mm, for instance, in the rocker panels and top cover, to 20 mm on the bottom case, to 50 mm on the reinforcements of the structure.

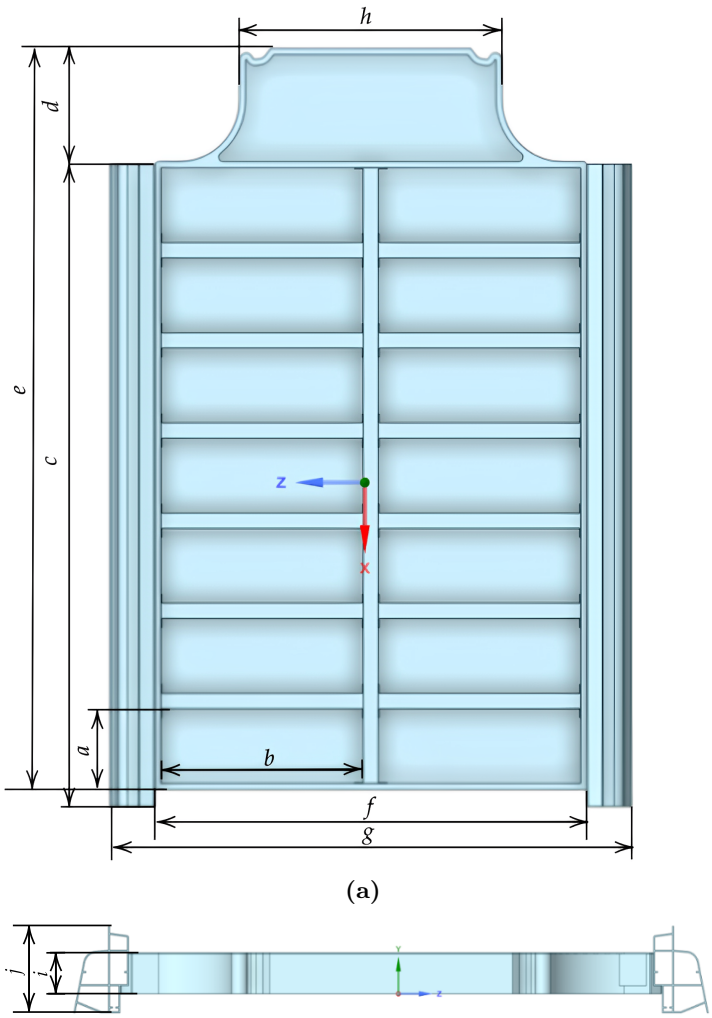


Figure 6.7: Dimensions of the CAD of the battery pack enclosure. **(a)** Top view. **(b)** Frontal view.

Table 6.1: Dimensions of the battery pack enclosure CAD

Dimension	**Value [mm]**
a	244.2
b	675.5
c	2049
d	472
e	2418
f	1441
g	1741
h	876
i	100
j	214

Despite the noticeable symmetry of the BPE and rocker panels in the $x - y$ plane and, thus, the fact that only half of the structure could be analysed to decrease the inherent computational effort brought by the model geometry, the complete geometry was assessed. This is justified by the fact that it is extremely relevant to analyse the stress and strain distribution, and their propagation, across the whole model and to study deformation in the same manner.

As a starting point, it is also relevant to address the considered unit system chosen, not only in the utilised CAD software but also in Ansys®, to define and analyse the relevant simulations. Hence, the relevant quantities to this study and corresponding units are provided in Table 6.2. Evidently, the units in which the density and pressure are expressed in result from the units of the associated metrics to these quantities, such as length, mass, and force.

Table 6.2: Analysis unit system in Ansys®

Quantities	**Unit**
Length	mm
Mass	kg
Force	N
Time	s
Density	kg/m^3
Pressure	MPa

6.1.2.2 Assumptions and Limitations

In this subsection, the assumptions, differences, and limitations of the obtained CAD with respect to the real BPE structure are assessed.

As was briefly stated above, the thermal and electrical stresses in the battery pack will not be considered in this study, only the mechanical ones. It is known that in the event of an impact, multiple coupled processes such as material fracture, short-circuit occurrence, thermal propagation, and current flow may take place. However, the scope of this work is mostly related to the evaluation, through explicit dynamic analysis, of the crashworthiness of realistic and improved BPEs. Therefore, it was assumed that the referred thermal and electrical processes are a by-product of the stress and deformation levels in the module cavities, i.e., they would only take place after the observation of the latter.

As noted by Deng et al. [101], there is a difference of four to five orders of magnitude between the individual layers in a battery cell and the battery pack. To represent each layer, or even cell, in a module or pack-level simulation entails a colossal computational cost. Even though a battery failure event usually occurs locally and the behaviour of each component should be taken into account, considering the above reason and the immense level of computational effort necessary for the deep analysis, this matter will be disregarded.

Next, it was weighted if a simple alternative could be chosen to represent the modules in the CAD geometry physically. Given the time established for the course of this work, it was found that, once again, the computational effort brought by including these components in the BPE model would not be compatible with the deadline of the work itself. Even if the modules were represented by simple box-like structures without any other geometric complexity in their respective cavities, to assess the intrusion of the BPE into those elements simply, the analysis time would increase substantially. Therefore, an equivalent way to

evaluate the mentioned parameter needed to be found to assess the matter, preserving the essential physics of the problem.

The reached solution was to represent each of the fifteen modules in the structure by means of distributed loads, resulting from their individual mass, in each cavity. By doing this, examining their influence in the enclosure was possible. It was assumed that any motion of the modules within the cavities is negligible (as is often the case in real life) and, therefore, the selected approach can be utilised in static and dynamic problems. The procedure for the calculation of the distributed mass resulting from the presence of the modules in the BPE will be discussed next.

According to the Iceberg benchmarking platform [105], the weight of the fifteen modules in the BPE structure serving as inspiration for this study is 375.6 kg. Therefore, the mass of each module unit can be calculated by simply dividing this total value by fifteen, as shown in Equation 6.1, where a value of 25.04 kg was yielded.

$$m_{module} = \frac{375.6}{15} = 25.04 \ \mathbf{kg} \tag{6.1}$$

In the Static, Transient, and Modal analyses, this value will be attributed as a distributed mass by simply selecting the surface where the mass is employed and input of its value. Thus, in this case, a distributed mass of 25.04 kg was employed on the bottom surface of each module cavity, just as portrayed in Figure 6.8. In the Explicit analyses, a physically equivalent approach will be taken, as will be explained in subsection 6.5, due to the intrinsic characteristics of the method.

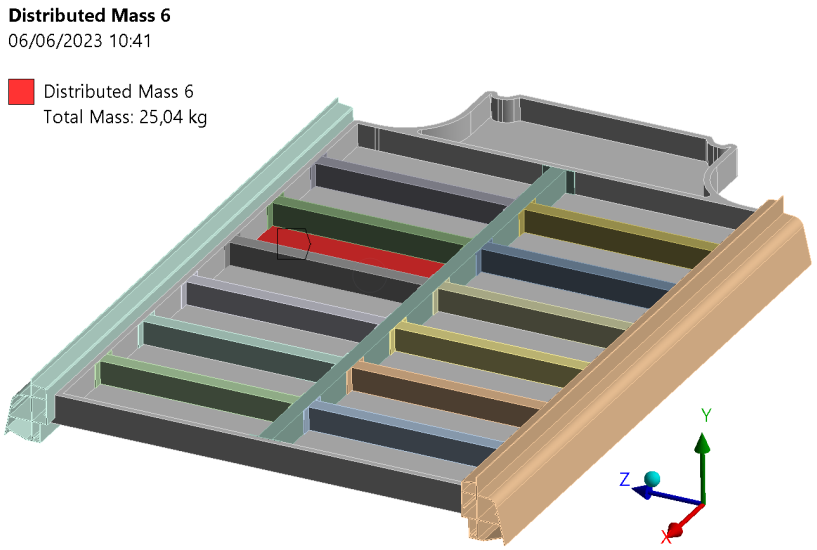


Figure 6.8: Attribution of a distributed mass in the bottom surface of the module cavities to represent their presence in the BPE.

In addition, note that this computed mass value will only be significant, and therefore employed, in the "Original model" and in those where this geometry does not change, i.e., where fifteen modules remain present in the BPE. A restriction was not made to accommodate the fifteen modules across all designs, as will be seen in Chapter 10 of this work. In models with alternative geometries where these are no longer relevant, and the battery cells are arranged in a different manner, the total mass of 375.6 kg will be divided by the pertinent number of units for that case. This was done since the potential difference in mass associated, for instance, with the employment of differing cell technologies, is likely minimal.

Finally, the intrusion within the cavities will be quantified by comparison of the undeformed and deformed structure configurations before and after the crash event, respectively. From this, along with other extremely valuable assessment parameters, conclusions regarding the health of the battery modules can be extracted.

Note, however, that no approach is done to simulate the weight of the EV itself, which, considering the fact that the industry inspiration for this BPE model constitutes a structural member of the EV, could have been considered to some degree. However, it is important to note that the weight of an EV is mostly supported by the suspension and the A and B pillars of a vehicle. Thus, it would be extremely challenging to accurately approximate the portion of the vehicle's weight that effectively relies on the rocker panels and BPE themselves. This explains the decision to leave this unknown load out of the scope of this study, which also enables, understandably, simplifications on the constructed models and the necessity of less computational power in the simulations to be performed.

6.1.2.3 Battery Pack Enclosure Model Materials

As discussed in subsection 5.2.3.1, aluminium and aluminium alloys constitute materials vastly utilised in the automotive industry. Their use has been growing rapidly, particularly in EVs, where their mechanical properties and density are essential.

Considering the information retrieved from both the US Patent 8,833,499 B2 [128] and the Iceberg data platform [105], the battery pack enclosure of the present BEV is mostly manufactured from an aluminium or aluminium alloy. Because the specific materials utilised in the BEV are not disclosed by the automotive manufacturer, the reasoning for the material to be employed in the model of the structure came from the research presented in that section, and material from Table 5.5 was selected.

6000 series aluminium alloys are the most widely used series for automotive solutions, owing to a balance established between its cost and its mechanical properties. In the research performed in the scope of this work, two 6000 series aluminium alloys stood out as the most heavily used in studies where the assessment of similar automotive structures is performed: the Al 6060-T6 and the Al 6061-T6.

In the Ansys® material database, a complete material characterisation of the Al 6061-T6 alloy for an explicit analysis was found. Since the obtainment of these particular curves is, oftentimes, extremely challenging, this material was chosen for employment in the BPE geometry of Phase 1. This material was also assigned to the rocker panels, given the fact that the BEV's BIW is equally manufactured in aluminium and aluminium alloys for the most part.

Relevant material properties of the Al 6061-T6 alloy and associated curves can be found in Table 6.3, Figure 6.9, related to the Steinberg-Guinan strength, and Figure 6.10, for the case of the shock Equation Of State (EOS).

Table 6.3: Al 6061-T6 material properties (Adapted from [129])

Property	Value
Isotropic Elasticity	
Young's Module [GPa]	68.9
Poisson's Ratio [-]	0.33
Shear Modulus [Pa]	$2.76e10$
Density [kg/m^3]	2703
Steinberg Guinan Strength	
Initial Yield Stress, Y [Pa]	$2.9e8$
Maximum Yield Stress, Ymax [Pa]	$6.8e8$
Hardening Constant, B [-]	125
Hardening Exponent, n [-]	0.1
Derivative dG/dP, G'P [-]	1.8
Derivative dG/dT, G'T [Pa/C]	-1.7e7
Derivative dY/dP, Y'P [-]	0.018908
Melting Temperature, Tmelt [C]	$2.76e10$
Shock EOS Linear	
Gruneisen Coefficient [-]	1.97
Parameter C1 [m/s]	5240
Parameter S1 [-]	1.4
Parameter Quadratic S2 [s/m]	0

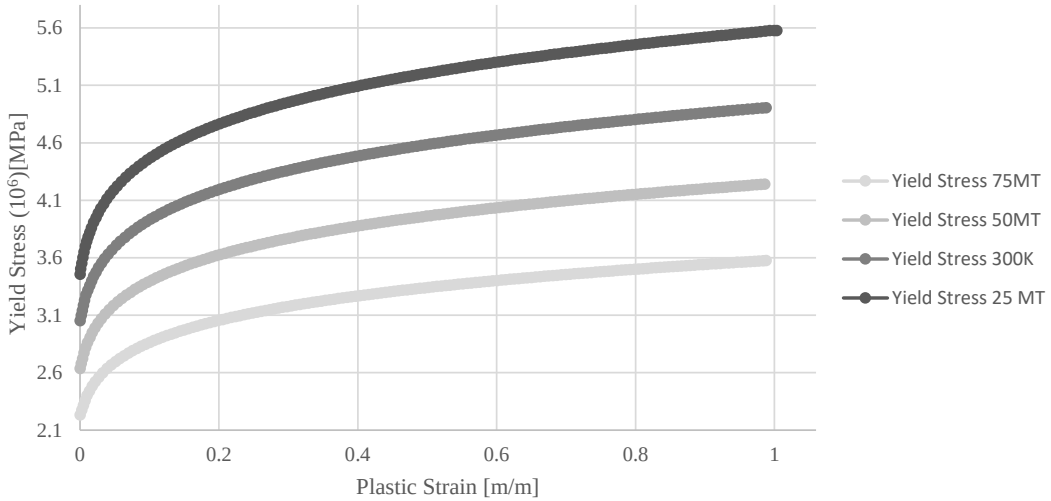


Figure 6.9: Al 6061-T6: Steinberg-Guinan strength (Adapted from [129]).

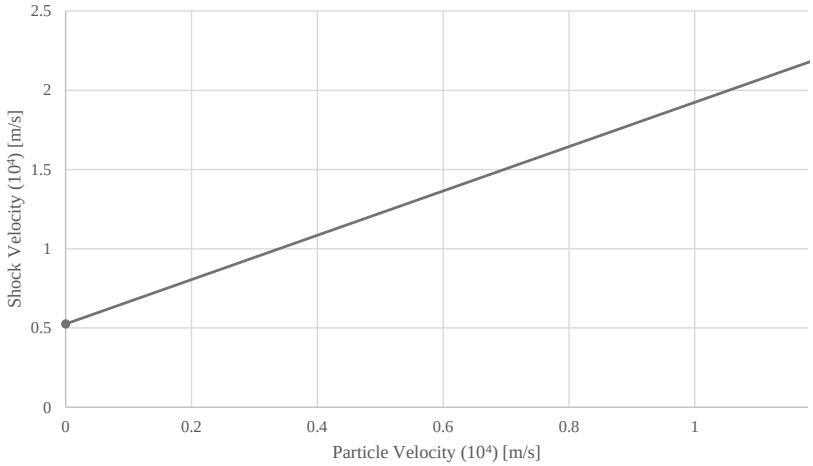


Figure 6.10: Al 6061-T6: shock EOS linear (Adapted from [129]).

Vehicle impacts are highly nonlinear transient dynamic phenomena. In fact, a nonlinear employed force-displacement relation is often characteristic of these events. This reality emerges from geometrical nonlinearities, material nonlinearities, and combinations of both. Thus, it is pertinent to replicate the presented nonlinearities to some extent in FEM when modelling a crash situation [20].

For some of the problems where the explicit scheme is mostly utilised, i.e., impacts, drop tests, problems dealing with large strains and nonlinearities, and others mentioned in Chapter 4, an EOS may be useful to model the material behaviour suitably [130].

An EOS is utilised to determine a material's hydrostatic or bulk response by establishing a relationship between pressure, density, and potentially, energy and/or temperature. The need for an EOS arises in situations characterised by extremely high rates of strain, material pressures significantly surpassing the yield stress, and the propagation of shock waves, all of which can very well occur in vehicle crashes. Naturally, these phenomena are closely interconnected. The Steinberg-Guinan strength model is a constitutive equation suitable to be employed in problems characterised by that same phenomena [130]. Additionally, it is relevant to note that linear EOS are the most commonly used EOS forms for non-gaseous materials, as is the case of Al 6061-T6 [130].

As will be seen in future steps of this work, the obtainment of these curves will not be possible for some of the materials employed in the BPE structures of the optimisations of the "Original model". However, given the fact that the explicit simulations will be run for low to moderate velocities, the influence of the definition of this parameter will not be substantial to the results obtained. Furthermore, in the explicit analyses (which replicate a side impact to the structure), most of the damage will likely occur in the rocker panel being impacted by the pole, with much smaller loads being transmitted to the BPE components themselves. These lateral vehicle elements will always be assigned the mentioned aluminium alloy; thus, it is possible to achieve a considerably accurate representation of the overall structure under impact and subsequent behaviour, even if the materials employed on the BPE components are not as deeply characterised.

6.1.2.4 Body Connections

To simulate an accurate assembly model, it is essential to define how the different bodies interact with each other. In Ansys®, this can be defined in the Connections settings, particularly in the Contacts' details.

As discussed in the presentation of the selected industry inspiration for this study, the attachment between the different load-bearing components of the BPE assembly is done by mechanically fastening. Thus, in the real automotive structure, mechanical fasteners, such as nuts and bolts, link the BPE to the rocker panels.

One possible option to simulate the attachment of the BPE to the rocker panels in the model would be to simulate the bolts themselves with a suitable pre-stress. This would correspond, of course, to the most realistic approach to the problem, enabling observations of the local stress concentrations resulting from the mechanical fastening, possible effects from bolt tightening, and how this same joining method behaves to impact. A good impact behaviour on the joint would be expected, as the bolted regions would work as "barriers" to this mechanical abuse [131]. Notwithstanding, simulating the exact performance of the fasteners and their interactions with the components of the joints is challenging, owing to the complexity of their real behaviour and also to the computational effort their representation (especially in great numbers) demands.

In all the presented models, all the defined surface contacts were assumed and set to bonded. This means the contact between the bodies was modelled as if they were joined with perfect adhesion. Thus, no separation or relative motion was assumed between the components at their interface. This definition aimed to physically represent the real constraints of this automotive structure in a simplified manner. Nevertheless, a so-called Tolerance value must be defined, which represents the maximum admissible distance between the surfaces for them to be interpreted as in contact. This means the bonded contact is broken if this value is surpassed. Simulating bonded surfaces enables the achievement of accurate approximations for the overall performance of the fasteners in cases where the above-mentioned considerations to them related can be disregarded in exchange for a less expensive computational solution. This justifies the chosen path, given the time limitations associated with this study.

Therefore, the pertinent Contacts settings across all analysis types are evidenced in Table 6.4. The definitions relative to the Body Interactions are related exclusively to the explicit simulations.

Table 6.4: Connections setting definition

Connections Settings	
Connection Type	Contact
Contacts Definition	
Contact Type	Bonded
Tolerance Type	Value
Tolerance Value [mm]	$5e-2$
Face/Face	Yes
Body Interactions	
Contact Definition	Trajectory
Formulation	Penalty

6.1.2.5 Mesh Metrics

The remaining model inputs to a full definition, in terms of mesh, loads, and boundary conditions, will be specified for each of the analysis types in the following subsections and

Chapters, along with any other relevant settings. This is justified by the fact that different analysis settings were defined based on the specific analysis formulations and requirements. Nevertheless, the quality of all of the meshes employed in the different models and analyses will always be assessed according to three out of four mesh metrics. Therefore, their meaning will be discussed in this preliminary Chapter.

To achieve a mesh that will enable the capturing of an accurate structure behaviour, the analyst should strive to use the highest quality elements enabled by its available computational power. Typically, high-quality elements are characterised by properties of uniformity and symmetry. To quantitatively assess particular geometric aspects of the elements of a certain mesh, mesh metrics are utilised. In this study, the mesh metrics used to evaluate the quality of the mesh are the Element Quality, Aspect Ratio, Skewness, and Characteristic Length. The latter parameter will only be used in the explicit dynamics analyses to the detriment of the skewness, which will only be featured in the static, modal, and transient analyses.

According to the Ansys documentation [132], the element quality metric is based on the ratio established between the volume and the sum of the square of the edge lengths, for 2D elements, and of the square root of the cube of the sum of the square of the edge lengths, for example, in the case of 3D elements. This parameter ranges from 0 to 1, with the maximum value representing an ideal square or cube.

The Aspect Ratio corresponds to the ratio between the "height" and "width" or between the "length" and "width" of triangular and quadrangular elements, respectively. Evidently, the range of this metric is from 1 to an infinite value, with the first value being sought, as it represents an equilateral triangular or a square shape [132].

Skewness describes the proximity or deviation of an element to an ideal well-shaped one, i.e., an equilateral element, once more. The values of this parameter range from 0 to 1, with 0 representing an ideal element and 1 a degenerate one. A value within the 0.25 to 0.5 interval is considered excellent, and one ranging between 0.5 to 0.75 is considered fair since it generally allows for a reasonable compromise between accuracy and computational costs [132].

As was discussed in Chapter 4, the minimum characteristic length of the mesh employed in an explicit simulation is an essential parameter, as it defines the stability condition of the explicit scheme, influencing the time the solver will need to solve the problem by means of the corresponding maximum time step size. This parameter is, for this reason, utilised as a relevant mesh metric for explicit dynamic analysis. Of course, a relatively high value for the minimum characteristic length is desired, adding to very close values of the minimum and maximum characteristic length, which indicates a uniform mesh. Thus, for the to be conducted explicit analyses, this mesh quality indicator will be used to replace the skewness, which is not as relevant for this analysis as for the other ones and not directly provided to be used as a metric by the explicit dynamics module in Ansys® [132].

6.2 Static Structural Analysis

Oftentimes, prior to conducting a dynamic analysis, it is pertinent to perform a static one, particularly when it is not possible to resort to a practical laboratory test to understand the fundamental behaviour of the structure. In fact, there are several reasons for this sequence of analysis.

A preliminary static analysis can help the analyst understand if the structure is mechanically capable of withstanding the anticipated static loads without excessive deformation or

failure. Therefore, it enables the validation of the structural design and integrity. In addition, an initial static analysis allows the identification of potential critical areas within the body, characterised by stress concentrations or excessive displacement, for example. Moreover, conducting this analysis can help the analyst find possible errors in the model's applied boundary conditions.

These factors justify the performance of this analysis type for each of the Phases within the numerical part of this work. In the conducted static analyses, all of the models were discretised with meshes identical to those then used in the corresponding explicit simulations and subjected to the suitable loads and boundary conditions:

- The only static input to all the bodies in the BPE model was the standard Earth gravity (a value of 9.8066 m/s^2 was considered, the default value in Ansys®) applied in the negative y axis in the given coordinate system.
- Although the definition of the boundary conditions for this case may be complex, the clamping of the bodies corresponding to the rocker panels were defined. This means that the inertia of the rocker panels was considered much greater than that of the battery pack and, given the connection of the BPE to the rest of the vehicle's BIW, in which the rocker panels are an integral part, this is the most realistic constraint for the present simulation.

Thus, by analysing the behaviour of the model when the only applied load corresponds to its own weight (including, evidently, the weight of the modules as well), it is possible to validate the model in terms of its fundamental integrity. This means that if excessive deformations or pre-stresses, for instance, are found in the structure in this preliminary analysis, the model must be redesigned. If, on the contrary, the structure solely presents significantly low values of these quantities, the model is well-built and ready for dynamic analysis.

The essential setup for the conducted static analyses, where the employed loads and boundary conditions can be observed, is represented in Figure 6.11 for the "Original model". Recall that the red zones represent the areas where the distributed loads corresponding to the modules' weight were applied, as discussed above.

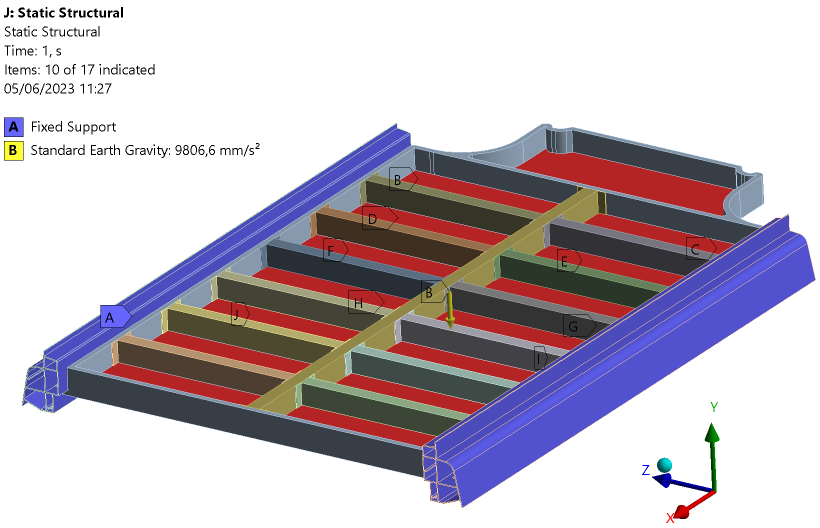


Figure 6.11: Loads and boundary conditions defined for the static analyses.

Regarding the analysis settings, they were left in their default definitions.

6.3 Modal Analysis

6.3.1 Modal analysis: Theoretical Context

In free vibration of a system, i.e., when the external solicitations actuating on it are null, the differential equation of motion is a second-order ordinary linear differential equation in the time variable and homogeneous. For a system with one Degree of Freedom (DoF), for instance, this corresponds to Equation 6.2,

$$m\ddot{x}(t) + c\dot{x}(t) + kx(t) = 0 \tag{6.2}$$

where m is the mass of the system, k is the stiffness constant, c is the viscous damping coefficient, and x, $\dot{x}$ and $\ddot{x}$ are, respectively, the displacement, velocity, and acceleration of the system [133].

Along with the initial conditions of displacement and velocity (as was already seen in Chapter 4, in the context of the FEM), the equation of motion fully describes the behaviour of a system undergoing free vibration [133].

After manipulation of Equation 6.2, it is possible to obtain the characteristic equation of the differential equation of motion (Equation 6.3) that allows, generally, two distinct roots (Equation 6.4) [133].

$$ms^2 + cs + k = 0 \tag{6.3}$$

$$s_{1,2} = \frac{-c \pm \sqrt{c^2 - 4mk}}{2m} = -\frac{c}{2m} \pm \sqrt{\left(\frac{c}{2m}\right)^2 - \frac{k}{m}} \tag{6.4}$$

Resorting to the basic concept of damping ratio, also termed ξ in this context, which characterises, in an adimensional manner, the damping of a system and corresponds to the quotient between the effective damping and the critical damping, Equation 6.4 can be rewritten as shown in Equation 6.5,

$$s_{1,2} = -\xi\omega_n \pm \omega_n \sqrt{\xi^2 - 1} \tag{6.5}$$

which, for an undamped system, $\xi = 0$, is equivalent to Equation 6.6

$$s_{1,2} = \pm j\sqrt{\frac{k}{m}} = \pm j w_n \tag{6.6}$$

where $j = \sqrt{-1}$ and w_n is the natural undamped frequency of free vibration of the system, defined by Equation 6.7 [133].

$$w_n = \sqrt{\frac{k}{m}} \tag{6.7}$$

From the inclusion of the roots in the differential equation of motion, after computing the initial condition of displacement and velocity and suitable manipulation, the expression portrayed in Equation 6.8 characterises the response of the given system in a natural regime [133].

$$x(t) = A\cos(w_n t - \phi) \tag{6.8}$$

Thus, the response of this system in a natural regime corresponds to an oscillatory movement around the static equilibrium position. Harmonic motion with a determined amplitude A, phase angle ϕ, and frequency w_n are verified. While the former parameters

depend on the initial conditions, the latter depends exclusively on the mechanical properties of the system, as was concluded from Equation 6.7. Thus, the natural (undamped) frequency of vibration represents the frequency at which the system naturally oscillates in response to an initial perturbation [133].

In Figure 6.12, the time evolution of the undamped system's free or natural response is depicted.

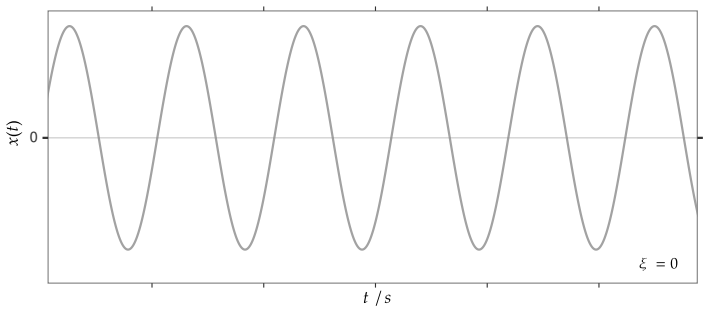


Figure 6.12: Natural response of an undamped system (Adapted from [133]).

Generalising for a system of n DoF, the system of n homogeneous differential equations of motion admits n non-trivial solutions of the form portrayed in Equation 6.9. Thereby, the system's natural frequencies are retrieved from the fact that the characteristic determinant must be null (Equation 6.10) [133].

$$\{x(t)\}_i = \{u\}_i \cos(w_i\, t - \phi_i) \qquad i = 1, ..., n. \tag{6.9}$$

$$\Delta(\omega) = |[k] - \omega^2[m]| = 0 \tag{6.10}$$

Each of the n distinct solutions $(w_i^2;\, \{u\}_i)\ i = 1, ..., n$ corresponds to a natural mode of vibration of the system, for which the harmonic and synchronous motion of the system is possible. Thus, the natural modes of vibration are the synchronous movements $\{x(t)\}_i$ characterised by the natural frequencies $w_i\ (i = 1, ..., n)$ and the modal vectors $\{u\}_i\ (i = 1, .., n)$. These define the shape, i.e., the spatial configuration assumed by the system during the synchronous movement [133].

The natural modes of vibration are an intrinsic property of the system and are unique to it. Although the amplitudes of the modal vectors are not unique, the ratio of their components is, and therefore, although the amplitudes of the modal forms are not unique, the modal forms themselves are [133].

Because the natural modes of vibration are independent, their linear combination is also a solution to the differential equations of motion. Accordingly, the response of a system under natural regime conditions is a result of the superposition of the n natural modes of vibration, suitably multiplied by a constant representative of the degree of participation of each mode to the natural mode of vibration (Equation 6.11) [133].

$$\{x(t)\} = \sum_{i=1}^{n} c_i\, \{x(t)\}_i \qquad i = 1, ..., n. \tag{6.11}$$

6.3.2 Modal analysis: Analysis Settings

Given the fact that a transient analysis was chosen to simulate the event of a frontal crash, it was deemed essential to run a modal analysis prior to the former. An undamped system

was considered, and the initial conditions for the transient analysis were then extracted from this modal analysis.

A modal analysis enables the obtainment of the structure's natural mode shapes and natural frequencies. As was discussed, these correspond to the spatial patterns of motion that the structure exhibits at specific frequencies and to the frequencies at which the structure vibrates without any external excitation. As the natural mode shapes are an intrinsic and unique property of the system, knowledge of these provides a valuable level of insight into the dynamic behaviour and response of a given structure.

Moreover, information regarding the mode participation factors, i.e., the contribution of each mode to the dynamic response of a structure, is provided to the analyst. This enables the obtainment of the dominant modes that contribute the most to the behaviour of the structure.

Regarding the loads and boundary conditions of the analysis, like in the static analysis, the following definitions apply (Figure 6.13):

- In terms of boundary conditions, the system presents full clamping of the rocker panels.
- No other load or input, except, for the distributed mass associated with the modules, was applied in the structure.

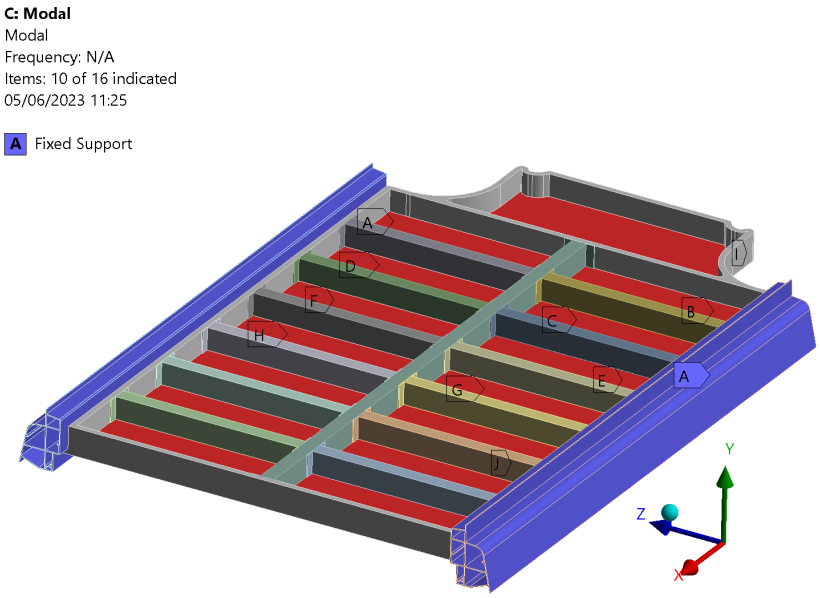


Figure 6.13: Loads and boundary conditions defined for the modal analyses.

Next, in terms of the defined analysis settings, these are presented in Table 6.5.

Table 6.5: Modal analysis: basic input analysis settings

Analysis Options	
Maximum Modes to Find	400
Limit Search to Range	Yes
Range Minimum [Hz]	0
Range Maximum [Hz]	3000
Solver Controls	
Damped	No

In complex problems, with thousands or even millions of DoF, understandably, it is not feasible to capture every corresponding mode of vibration and natural frequency of the system. However, owing to the fact that not every mode of vibration participates to the same extent in the deformation of a structure, as well due to the fact that oftentimes the higher frequency modes can be considered negligible, not every mode and frequency needs, in fact, to be obtained. Hence, the issue relies on how many of these should be considered for the modal analysis of a given problem.

To address this problem, two scalars can be consulted on Ansys®: the Mode Participation Factor and the Effective Mass [134]. The Mode Participation Factor measures the amount of mass moving in each direction for each vibration mode. A higher value of this parameter for a certain direction means that modes will be increasingly excited by forces or excitations in that direction. This Effective mass corresponds to the value of the latter factor squared, and both parameters are automatically calculated and presented by the program in the Solver Output after the modal analysis finishes [134].

Another extremely relevant scalar to analyse if one desires to infer if the most significant modes of vibration are being extracted in a given modal simulation is the ratio established between the effective mass and the total mass. This value ranges from 0 to 1, and the latter value can only be reached if every mode has been retrieved in the analysis. This, however, is not practical and thus, in most cases, depending on the specific problem and potential engineering guidelines, a value relatively close to the unit is satisfactory [134].

Concluding, the reasoning for setting 400 as the number of modes for the program to find was a trial-and-error approach. In a primary analysis, a lower number of modes was defined. However, when consulting the "Participation Factor Summary" solution output, particularly the summation of the ratio of effective mass to total mass of all the considered modes of vibration, it was verified that this value was still very far from the value of 1 for specific DoFs of the system. Hence, the input number of modes of vibration was increased to improve this statistic and achieve a result closer to the desired theoretical value.

The upper limit of the range of frequencies being considered, in turn, resulted from a balance established between computational effort and a value deemed by common-industry practice as "sufficient" to evaluate the frequencies characteristic of these types of problems. In addition, if a suitable number of natural modes of vibration of the structure and corresponding frequencies were not being captured in the simulation, an intrinsic tool of the FEM software itself produces a warning to the user. Hence, it can be concluded that the input settings are suitable.

6.4 Transient Structural Analysis

6.4.1 Transient structural analysis: theoretical context

A transient excitation refers to the application of a high-intensity force that occurs within a relatively short time compared to the natural period of the system. This excitation type is also commonly called a "shock" [133].

Consider a system with one DoF. A transient solicitation $f(t)$ can be interpreted as a series of impulsive forces $f(\tau)$ acting in time intervals of $d\tau$. The latter, in turn, are described by large impulse amplitudes acting on a very short time interval [133]. Thus, assuming that the generic impulsive force $f(\tau)$ originates the impulsive incremental response $dx(t)$, described in Equation 6.12, to $t > \tau$,

$$dx(t) = f(\tau)\, d\tau h\,(t-\tau) \tag{6.12}$$

$t-\tau$ is the argument of the impulse response function and corresponds to the time since the application of the impulse to the instant t [133].

The response in that instant t corresponds to the sum of the responses of each elemental impulse. The expression presented in Equation 6.13 is termed the Duhamel integral, representative of the principle of superposition of effects [133].

$$x(t) = \int_0^t f(\tau)\, h\,(t-\tau) d\tau \tag{6.13}$$

By substitution of the impulsive response function, considering the sum of both the transient response due to initial conditions and the forced response due to the transient excitation, the total response of the system is described by Equation 6.14,

$$\begin{aligned} x(t) = e^{-\xi w_n t} \left[x_0 \cos w_d\, t \; + \; \frac{\dot{x}_0 + \xi w_n x_0}{w_d} \sin w_d\, t \right] \\ + \frac{1}{m w_d} \int_0^t f(\tau)\, e^{-\xi w_n (t-\tau)} \sin w_d\,(t-\tau) d\tau \end{aligned} \tag{6.14}$$

where $w_d = w_n \sqrt{1-\xi^2}$ is the damped natural frequency of the system, and x and $\dot{x}$ correspond to the initial conditions of displacement and velocity, respectively [133].

A transient excitation in the form of a half-sine wave with a duration of t_c is illustrated in Figure 6.14 and is defined by Equation 6.15 [133].

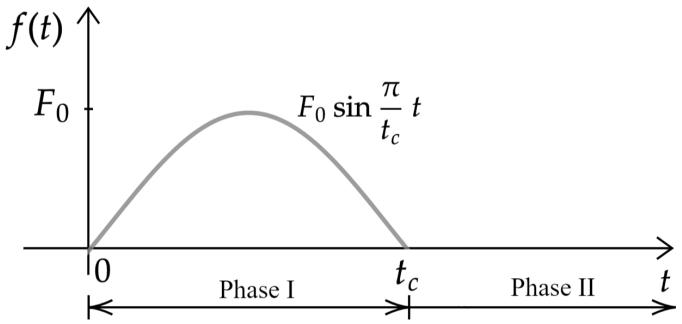


Figure 6.14: Half-sine wave transient solicitation (Adapted from [133]).

$$f(t) = \begin{cases} F_0 \sin \dfrac{\pi}{t_c} t & 0 \leq t \leq t_c \\ 0 & t > t_c \end{cases} \tag{6.15}$$

In engineering, the severity of a shock affecting a system is assessed by examining the maximum response of the system, which is influenced by both the nature of the shock and the characteristics of the system. The shock spectrum represents the maximum adimensional response of a system with one DoF to a transient excitation in the function of an adimensional parameter of the excitation (time or frequency). Therefore, each point in this spectrum corresponds to the maximum response of a single DoF system, with a specific natural period (frequency), to a particular type of shock [133].

The shock spectrum is, for a multitude of values of ξ, a family of curves. However, since the transient response is oftentimes not as sensible to damping as the harmonic stationary response in a harmonic regime, the response spectrums of undamped one DoF systems are often used as reference models [133].

The response of an undamped system to a transient excitation in the form of a half-sine wave is obtained using the Duhamel integral [133]. (Equation 6.16) [133].

$$\begin{aligned} x(t) &= \frac{F_0}{m\omega_n} \int_0^t \sin \omega\tau \sin \omega_n (t-\tau) \mathrm{d}\tau \\ &= \frac{F_0}{2m\omega_n} \left\{ \frac{\sin\left[(\omega+\omega_n)\tau - \omega_n t\right]}{\omega+\omega_n} - \frac{\sin\left[(\omega-\omega_n)\tau + \omega_n t\right]}{\omega-\omega_n} \right\} \Bigg|_0^t \end{aligned} \tag{6.16}$$

By inclusion of the corresponding limits of integration in Equation 6.16, the response of the system to each of the two phases showcased in Figure 6.14 is presented in Equations 6.17 and 6.18,

$$x(t) = \frac{F_0}{k} \frac{1}{\left(1 - \frac{1}{4}\left(\frac{T_n}{t_c}\right)^2\right)} \left(\sin \frac{\pi}{t_c} t - \frac{T_\mathrm{n}}{2t_c} \sin \frac{2\pi}{T_n} t \right) \quad 0 \leq t \leq t_c \tag{6.17}$$

$$x(t) = \frac{F_0}{k} \frac{\left(\frac{t_c}{T_n}\right)}{\left(\frac{1}{2} - 2\left(\frac{t_c}{T_n}\right)^2\right)} \left(\sin \frac{2\pi}{T_n} t + \sin \frac{2\pi}{T_n} (t - t_c) \right) \quad t > t_c \tag{6.18}$$

where $T_n = \frac{2\pi}{w_n}$ is the natural period of vibration of the system and the quotient $\frac{F_0}{k}$ corresponds to the static displacement.

6.4.2 Transient Structural Analysis: Analysis Settings

The transient structural analysis was the selected approach to evaluate the damage to the BPE in the case of a frontal impact on the vehicle.

As was briefly voiced in subsection 6.1.1, it would be incorrect to simulate a direct frontal impact to the BPE structure since its location was specifically chosen to maximise its shielding in these incidents. Indeed, this protection is achieved by employing strategically placed and engineered zones which deform and crumple in a controlled way to reduce the transfer of frontal and rear impact loads to the vehicle occupants and, in the case of EVs, to the battery pack. This concern in EVs is easily explained, resorting to the diversity of dangerous phenomena that may occur in the energy storage component of the vehicle, further threatening the safety of the passengers (Chapter 2). Hence, this controlled deformation

process extends the time interval in which the impact loads actuate and, therefore, helps slow down the vehicle's deceleration rate, which consequently is translated into the reduction of impact forces experienced by the passengers and the battery pack.

Due to this, an alternative way to simulate the "Full-Width Rigid Barrier" Euro NCAP crash test [135] was evaluated. The found solution to this issue was to perform a transient structural analysis, in which the whole BPE structure and rocker panels would endure a mechanical shock characterised by an acceleration pulse defined by a suitable regulation. Thus, instead of defining a velocity for the vehicle, as established in the Euro NCAP crash tests, a sudden (des)acceleration would be employed to the BPE, as it realistically takes place in the case of a vehicle crash.

Moreover, it is relevant to mention that each combination of geometry and material has an intrinsic damping ratio. For this analysis, an equivalent damping ratio was specified to the model system, with a value of 0.022. This industry-standard value has an empirical foundation and was based on industry knowledge acquired at CES.

6.4.2.1 Acceleration Pulse

The international standard IEC 60068-2-27 [136] was used to define the acceleration pulse applied to the structure. The utilisation of this specific norm to the detriment of those presented, for instance, in Table 2.1, is justified by the frequent use of the first regulation for similar applications in CES and, consequently, the open access to it.

This norm pertains to components, equipment, and other electrotechnical products, which may encounter non-repetitive or repetitive shocks. To infer the structural integrity of the components, they are subjected to standardised pulse-shaped shocks with predetermined peak acceleration and duration. This is what will be simulated in the model [136].

The half-sine pulse shape, one of the three basic pulse shapes specified in this normative, was considered for this analysis. In Figure 6.15, this pulse shape is presented.

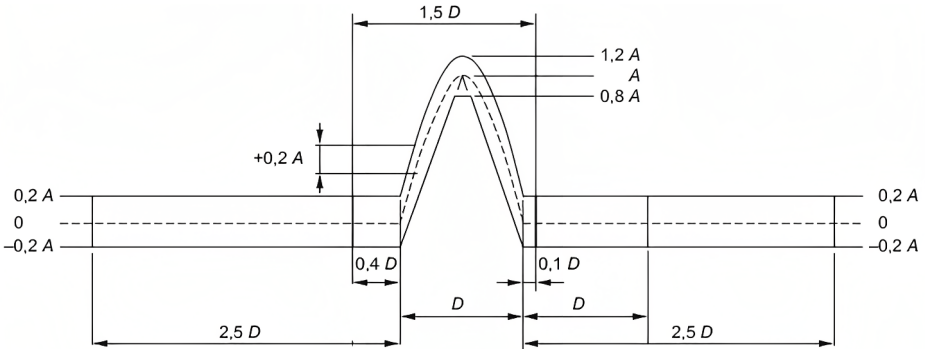


Figure 6.15: Pulse shape and limits of tolerance for a half-sine pulse [136].

The nominal pulse is presented in a dashed line, and the limits of tolerance are in a full line. In addition, A is the peak acceleration of the nominal pulse, and D is the duration of the nominal pulse. Nevertheless, note that since a numerical simulation with clear settings will be conducted, not a practical test with its inherent systematic deviations, the tolerance limits can be negligible and simply the nominal pulse characteristics will be assumed.

A "worst-case scenario" analysis was sought, and a peak acceleration value of $A = 500$ m/s^2, i.e., 50 G was chosen, as well as a corresponding duration of the nominal pulse of $D = 11$ ms, established by the consulted regulation. Note that the peak acceleration value is immense and was set to analyse the behaviour of the BPE structure in severe vehicle crashes.

The two phases of solicitation observed in Figure 6.15 (and Figure 6.14) must, then, be input into the Transient Structural module in Ansys®. Thus, two steps were created, one for each phase. Step 1 corresponds to the half-sine pulse shape, while Step 2 is described by a null value of acceleration in every direction of the structure during its duration. The aim of representing Step 2 is to observe the vibratory behaviour of the (damped) system when the transient excitation no longer acts on the structure, i.e., the system is in free oscillation.

To obtain the acceleration profile stipulated by the mentioned normative, an expression that described the amplitude, phase, and duration of this half-sine wave needed to be found. Firstly, 110-time steps of duration 0.1 ms, whose limits are numbered from $n = 1$ to 110 were considered in Step 1 to discretise the duration of the pulse suitably. To each, a value of acceleration is attributed in a way that it is possible to obtain the desired half-sine shape. The achieved expression is presented in Equation 6.19 and yields an acceleration in $\mathrm{m/s^2}$. The expression is then provided in $\mathrm{mm/s^2}$ in Ansys®, given the unit system being utilised.

It can be attested that this expression is correct, noting that: for values of $n = 0$ and $n = 110$, a null value of acceleration is achieved, while for $n = 55$ the peak acceleration is computed.

$$A = 500 \sin\left(\frac{\pi}{110} n\right) \ \mathbf{m/s^2} \qquad n = 0, ..., 110 \tag{6.19}$$

The plot obtained by this expression is portrayed in Figure 6.16.

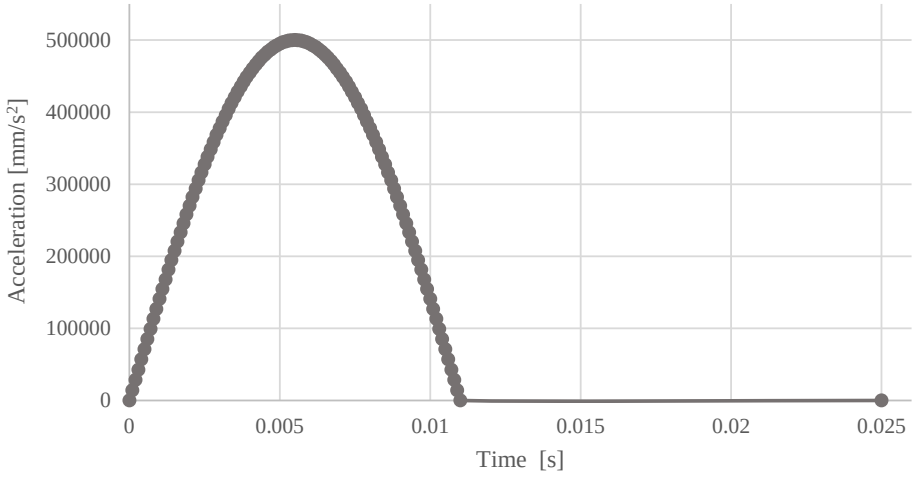


Figure 6.16: Acceleration profile applied in the model.

Step 2 is simply computed by attributing null accelerations in the three Cartesian axes during the entire duration of this step, for which a value of 14 ms was defined. This slightly bigger value than D was set to observe more of the post-crash behaviour.

This pulse was input as acting on the positive x axis. Recall that the "Full-Width Rigid Barrier" Euro NCAP test [135] is being simulated in this analysis. Many phases can be found in a real-life crash event where the vehicle collides with a rigid barrier or wall. In an idealised model, the first phase consists of the vehicle travelling at a certain velocity. Then, the vehicle collides with the wall, and the velocity reaches a null value. The situation is characterised by a force defined by Newton's second law of motion being exerted by the car into the wall. Assuming that the barrier is static and unbreakable, per Newton's third law, this force is equally applied by the wall to the car on the contrary direction. The latter is the force that causes the deformation of the vehicle's crumple zones and the oftentimes "accordion" configuration these deformation zones assume after the crash [137]. The chosen

direction for the application of the acceleration profile in the studied automotive components is, thus, justified.

Lastly, the loads and boundary conditions defined in the structure and illustrated in Figure 6.17 are, then:

- An acceleration pulse of peak acceleration of approximately 50 G, acting for 11 ms acting in the whole model, in the positive x axis, followed by free vibration of the (damped) system for 14 s.
- No further constraints were applied in the system in any DoF. Recall, nevertheless, that the boundary condition of clamping of the rocker panels, introduced in the modal analysis (that defined the initial conditions to this one), is transmitted for this case.

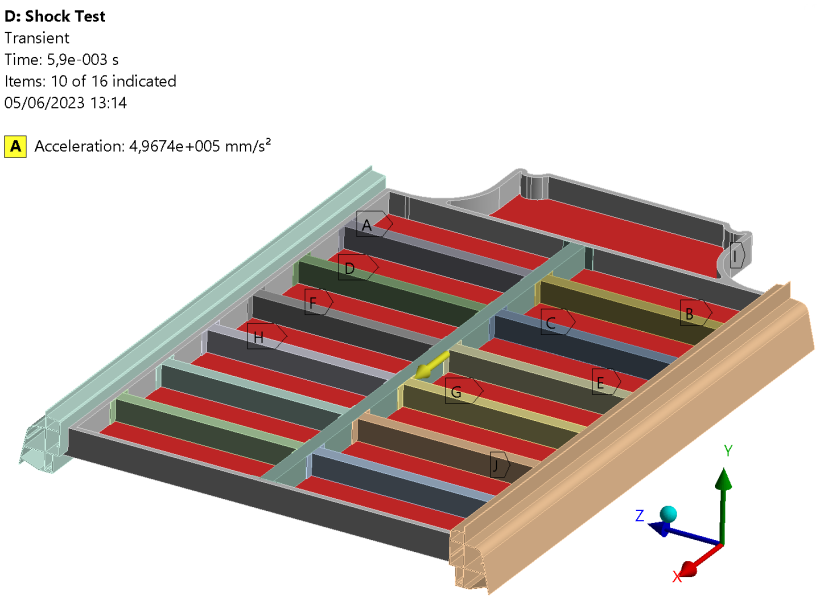


Figure 6.17: Loads and boundary conditions defined for the transient analyses.

Lastly, it is worth mentioning that for the majority of vehicle frontal impacts occurring on the roads, particularly those similar to the Euro NCAP'S "Full-Width Rigid Barrier" crash test, at 50 km/h, the rocker panels do not present significant damage to their integrity (see Figures 2.1 and 2.3). Consulting the outcomes of the performance of the above-mentioned real-life test to about any vehicle, something that can be generally found is that, while the frontal region of the vehicle presents evident deformation (resulting from its carefully engineered design for the purpose of energy absorption) the rocker panels of the vehicle remain intact, not presenting substantial energy absorption and, thus, deformation or compression. This validates the selected boundary condition applied to the vehicle's integral component.

Other relevant input analysis settings are presented in Table 6.6.

Table 6.6: Transient analysis: basic input analysis settings

Step Controls	
Number of Steps	2
Current Step Number	1 or 2
Step End Time [s]	0.011 or 0.025
Time Step [s]	$1e-4$
Damping Controls	
Damping ratio	0.022

6.5 Explicit Dynamic Analysis

6.5.1 Explicit Dynamics Analysis: analysis settings

Given the extensive review already conducted regarding the theoretical background and FEM application of the explicit method, unlike the previous sections, in which the theory behind the corresponding analysis types was presented, these matters will not be discussed once again. Refer to Chapter 4 for the fundamentals and principal characteristics of the explicit scheme and explicit FEM.

An explicit analysis was the chosen path to evaluate the consequences to the BPE originating from the occurrence of a side impact. It is well understood by now that the BPE will very likely not endure a direct impact in a side vehicle crash, however, the presence of the rocker panels on each side of this structure permits the simulation of a realistic impact case. These lateral components, just like they would do in a real-life crash event, will deform and absorb most part of the impact energy in the explicit simulation, prior to the energy transference to the BPE.

6.5.1.1 Side Pole Test

The inspiration for this simulation was the Euro NCAP "Side Pole" crash test [138]. As was explored and can be consulted in Table 2.3, this test entails the striking of the vehicle on the driver's side by a rigid narrow pole.

This rigid pole is specifically defined as a "vertical metal structure beginning no more than 102 mm above the lowest point of the tires on the striking side of the test vehicle when the vehicle is loaded and extending at least 100 mm above the highest point of the roof of the test vehicle" [138]. This pole is localised at 75° in relation to the longitudinal direction of the car and has a diameter equal to (254 ± 3) mm [138].

Thus, a body representative of the described pole was added to the explicit simulation model to simulate the impact between the BPE and rocker panels assembly and this structure. The straightforward geometry of the pole in the model of the explicit dynamics simulation can be observed in Figure 6.18 in conjunction with the BPE model and in Figure 6.19, where the extremely small distance between the pole and the rocker panels is evidenced.

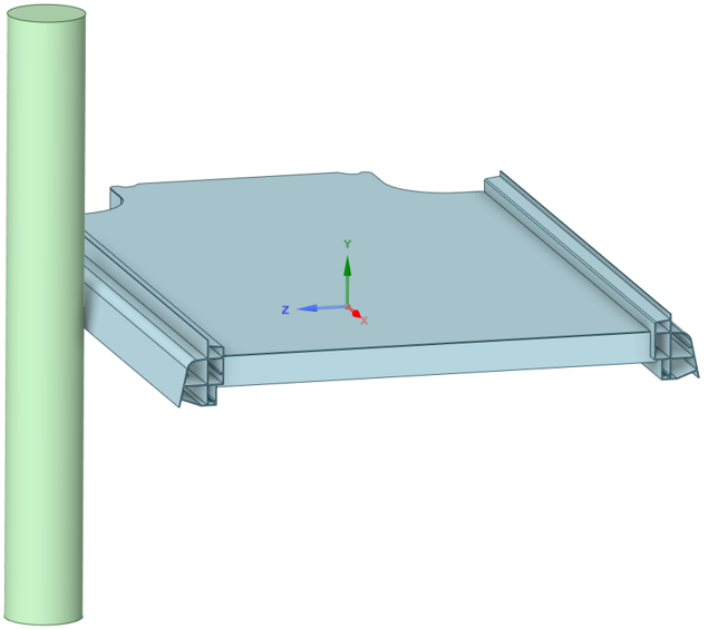


Figure 6.18: Rigid pole configuration and positioning.

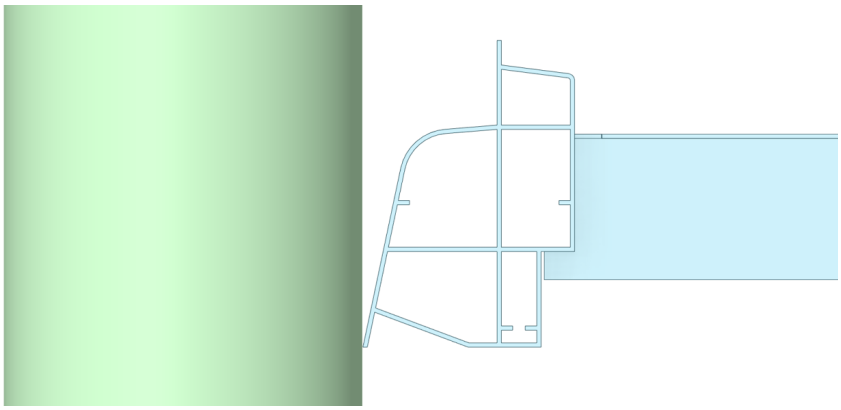


Figure 6.19: Distance in between the rocker panel and the rigid pole.

The close proximity of the rigid pole to the rocker panel of the automotive assembly in the simulation was set as the minimum possible value to reduce the computational effort required for the displacement of the automotive structure towards the pole. By reducing the distance between these bodies, the focus of the simulation could be directed towards the impact of the structures and the subsequent behaviour of the BPE immediately after the crash, without the unnecessary computational overhead.

The material chosen to model this additional body was a structural steel, retrieved, from Ansys® engineering data sources. The relevant properties of this material are provided in Table 6.7.

Table 6.7: Mechanical properties of the utilised structural steel in the rigid pole [129]

Mechanical Property	**Value**
Young's Modulus, E [GPa]	200
Poisson's Coefficient, ν [-]	0.3
Density [kg/m^3]	7850

Furthermore, it is relevant to mention that the pole was set as a rigid body. This brings advantages in simplification and computational efficiency since there is no need to model and compute the deformations, stresses, and strains within that body, as this is not of interest to this study: the distribution of these quantities in the automotive structure of interest is.

Another vital point to note is that the diagonal mass matrix, an essential property of the explicit integration scheme, is achieved by the discretisation of the mass of the system by lumping to the nodal points [81]. This explains the fact that in an explicit dynamics analysis, only concentrated masses can be applied. Hence, the first challenge found in simulating a BEV crash by an explicit dynamic analysis in FEM was how to represent the presence of the modules in the BPS, since they are not physically modelled, and in this analysis type, distributed masses cannot be applied onto a surface.

The found alternative to this issue consists of representing the loads acting on the BPE structure emerging from the presence of the modules by means of equivalent pressures to each cavity. Considering that the mass of each of the fifteen modules is the 25.04 kg found in Equation 6.1, by Newton's second law, the force originating from a module unit subjected, evidently, to the standard earth gravity (9.8066 m/s^2, the default value in Ansys®) is given by Equation 6.20.

$$F_{module} = m_{module} * \ G = 25.04 * 9.8066 = 245.557 \ \mathbf{N} \tag{6.20}$$

Given the dimensions of the module cavities described in Table 6.1, the area of the bottom surface of each cavity is given by the multiplication of the length by the width (Equation 6.21). Then, given the fact that the pressure consists of the force divided by the area in which it acts, the pressure that will be defined as acting on the aforesaid surface is computed by Equation 6.22.

$$A_{bottom\ surf} = a * b = 0.6755 * 0.2442 = 0.165 \ \mathbf{m^2} \tag{6.21}$$

$$P_{module} = \frac{F_{module}}{A_{bottom\ surf}} = \frac{245.557}{0.165} = 1488.23 \ \mathbf{Pa} \ \simeq 1.488e-3 \ \mathbf{MPa} \tag{6.22}$$

This pressure magnitude is then applied to the bottom surface of each module cavity to simulate their effect in the BPE as was done in the preceding analyses (Figure 6.20).

In addition to the definition of the modules, based on the test sheet of this Euro NCAP side impact crash test [138], the following loads and boundary conditions are prescribed in the explicit analysis (Figure 6.20):

- The rigid pole will be constrained in all its DoF, as it is assumed as fixed and indestructible;
- A constant velocity of 32 km/h (or 100 km/h) will be attributed to all the components of the BPE and rocker panel assembly in the positive z axis, i.e., in the direction of the pole, in the initial conditions settings.

In parallel to this explicit simulation inspired by the Euro NCAP's "Side Pole" test [138], an additional simulation will be performed. This new simulation will only differ from the above-mentioned in only one aspect: the velocity attributed to the automotive components. As was stated in Chapter 2, vehicle speed plays a crucial role in a crash's effect on the car's safety. Thus, by running a second simulation at the increased velocity of 100 km/h, more damage to the BPE and rocker panels will be observed and a more complete analysis of the structure's behaviour to impact will be achieved.

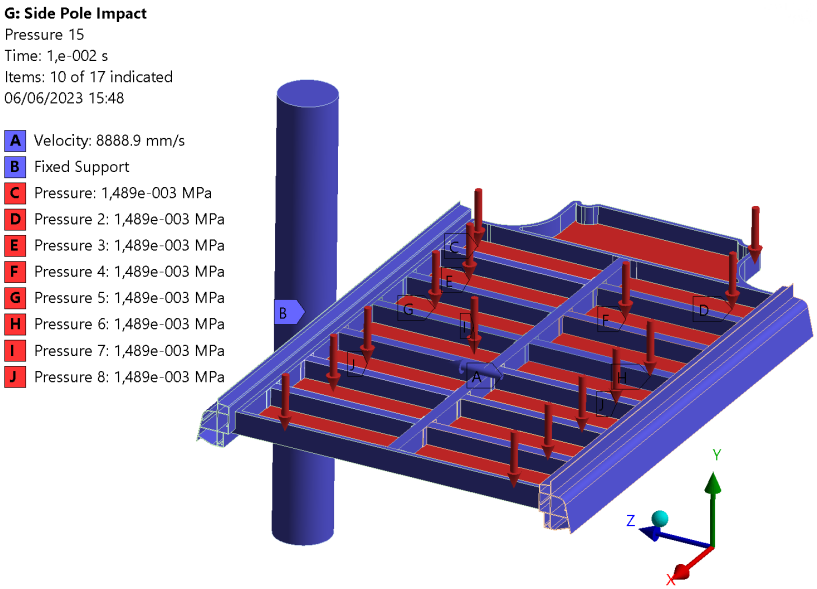


Figure 6.20: Loads and boundary conditions defined for the explicit dynamic analyses.

Moreover, the fundamental analysis settings defined for the explicit simulations are presented in Table 6.8.

Table 6.8: Explicit dynamics analysis: basic input parameters

Analysis Settings Preference	
Analysis Type	Low Velocity
Step Controls	
Number of Steps	1
Load Step Type	Explicit Time Integration
End Time [s]	0.01
Maximum Number of Cycles	$1e7$
Time Step Safety Factor	0.9
Minimum CFL Time Step [s]	Calculated, dependent on the mesh
Minimum Time Step [s]	$1e-9$
Maximum Time Step [s]	Program Controlled
Automatic Mass Scaling	Yes
Maximum Element Scaling	100
Maximum Part Scaling	5
Damping Controls	
Hourglass Damping	Flanagan Belytschko

Both explicit simulations, in which velocities of 32 km/h and 100 km/h were attributed to the automotive structures, were changed from Program Controlled to Low-Velocity analyses, as suggested by Ansys® support documentation [139].

The end time of an explicit dynamic analysis must then be entered by the user and selected as the most appropriate value for the problem under consideration. For this case, it is fundamental to observe the impact of the BPE and rocker panels with the pole, as well as to get a glimpse of the post-crash behaviour of the flexible structure. To be able to establish a comparison between the two explicit simulations, in each of the Phases that constitute the numerical portion of this work, the same end time was set across all the performed explicit analyses. The value for this parameter resulted from a trial-and-error process. In preliminary explicit analyses conducted for the "Original model", values like 0.005 s and 0.1 s were set as the end time of the analysis; however, it was 0.01 s that resulted as the most pertinent one. This end-time value provided the desired insights into the crash behaviour of the BPE while ensuring the highest computational efficiency.

Then, the maximum number of cycles was left as its default value in Ansys®, as was the time step safety factor (Equation 6.23). The minimum time step value was set as $1e-9$ and not Program Controlled to, once again, impede the solver to stop the simulation due to reaching a certain value of the time step. The validity of this definition will be explored after the obtainment of the solution.

Next, the minimum CFL time step needs to be inserted into the analysis settings by the user. For each simulation, this value was computed as the result of Equation 4.43 (expressed here once again, through Equation 6.23).

$$\Delta t = 0.9\,\mathbf{min}\left(\frac{L}{c}\right) \tag{6.23}$$

The value of the minimum characteristic length, L, of an element in the model can be directly retrieved from Ansys® for a given simulation. This can be found in the Quality section of the model's Mesh Details, by choosing the "Characteristic Length" as the mesh

metric. If the input mesh parameters or the geometry itself changes, it is likely that a different value of L will be found.

The value of c, the speed of sound in a particular material, however, needs to be calculated analytically by the user. Since solid elements were utilised in this analysis type, the relevant expression to the obtainment of this value corresponds to Equation 4.46.

It must be noted that, contrary to what is verified in the "Original model", in the models used for the other Phases of this work, more than one material is assigned to the BPE and rocker panels components. Nevertheless, as can be concluded from Equation 4.43, between two general bodies, each one made from a different material, the greatest speed of sound is reached in the stiffer one (i.e., where the greater value of E is found, for similar values of density and Poisson's ratio). Then, given the fact that Al 6061-T6 is the stiffer material utilised across all the Phases of this numerical portion of the work, the value of c will be always calculated with respect to this material to later compute the minimum time step size for stability. Finally, this value is computed as illustrated in Equation 6.24, resulting from Equation 4.46.

$$c_{Al\,6061-T6} = \sqrt{\frac{68.9e9\,(1-0.33)}{2703\,(1+0.33)(1-2*0.33)}} = 6145.52\ \mathbf{m/s} \tag{6.24}$$

The mass scaling tools were also left in their default definitions. The automatic mass scaling option was left as "yes" since the maximum part scaling definition was consistent with what was discussed in Chapter 4 in relation to this value in dynamic simulations. Hence, there was a certain level of safety related to these initial settings.

Lastly, the selection of Flanagan Belytschko hourglass damping resulted from the consultation of the Ansys® support documentation [139]. In practice, it was concluded that this parameter was oftentimes deemed essential to the obtainment of accurate results in some of the performed explicit dynamics simulations.

Chapter 7

Convergence Study

As discussed in Chapter 2, explicit FEM has been extensively utilised for the study of problems characterised by large deformation (i.e., large displacements and rotations) transient dynamics, such as crashworthiness analysis in the automotive industry. In spite of the notorious advancements in Computer-Aided Engineering (CAE), there are still considerable challenges in accurately predicting crash performance, which explains the fact that calibration-based engineering practices are still mandatory for this assessment [140].

The validation and verification concept has emerged in contemporary times as a vital approach in computational engineering. Indeed, empirical evidence has shown that without proper verification and validation of the model, its acceptance and practical application in real-world settings is unlikely to be accepted. This process aims at rigorously assessing and assuring the reliability and predictive capability of numerical methods as a tool for engineering analysis [66]. The two fundamental parts of the evaluation procedure are schematically represented in Figure 7.1 [140].

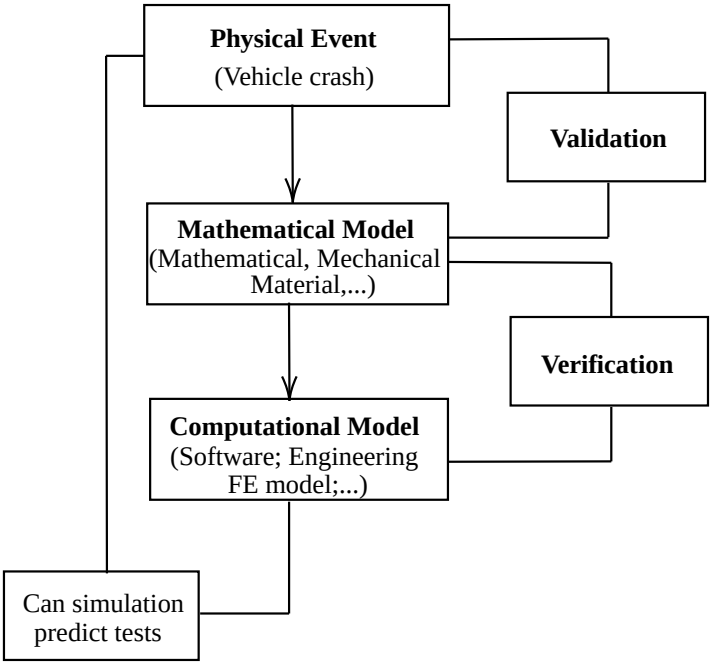


Figure 7.1: Validation and verification concept (Adapted from [140]).

The purpose of the validation process is to ensure that the mathematical model employed to replicate a physical event does so with acceptable accuracy. In turn, the verification stage ensures that the code and the computational model represent the mathematical model with satisfactory accuracy. The numerical model can be verified partly through a theoretical analysis utilising analytical solutions or established numerical results from simple examples [140].

Recalling the contents of Chapter 4, by the nature of the finite element method, the numerical results are, in fact, approximate solutions. Thus, it is of great relevance to investigate the accuracy and robustness of the method being employed. From a mathematical standpoint, the accuracy assessment entails a convergence study of the FE solution to the analytical solution when the mesh is refined. This is performed by progressively decreasing the element size of the mesh, therefore increasing the number of nodes as well as the number of unknowns. When the element size tends to zero, the numerical solution is expected to converge to the analytical solution in a determined sense of measurement [140]. Then, the analyst will also evaluate the results obtained in the progressive mesh refinement stages in light of their required computational power and time, i.e., the robustness of the method. Thus, when it is evident that the numerical results reach a level of mesh-size insensitiveness, it is counter-productive to continue to work on a model where a finer than necessary mesh is utilised since this will likely be translated into an increased computational cost, sometimes highly significant.

Hence, to attest to the validity and accuracy of the method, as well as to examine the influence of the mesh on the numerical results emerging from a physical problem in explicit FEM, the following presented convergence study was performed. The knowledge extracted from this case was then employed in the main numerical analyses of the next Chapters.

7.1 Partial Penetration of a Bullet to a Wall

The study case for the convergence analysis entails the high-speed impact and partial penetration of a generic bullet through a metal wall. The damage to the wall resulting from this event will then be assessed.

The rationale for this matter of study was to simulate a high-velocity impact, at a speed significantly higher than that addressed in the principal numerical study of this work. Evidently, the analytical solution of this analysis is not available and, therefore, the convergence behaviour will be examined considering the solution from a refined mesh.

7.1.1 Geometry, Boundary and Load Conditions

The geometry of the bullet and wall are illustrated in Figure 7.2, from frontal and lateral views. The dimensions are also illustrated in the same Figure.

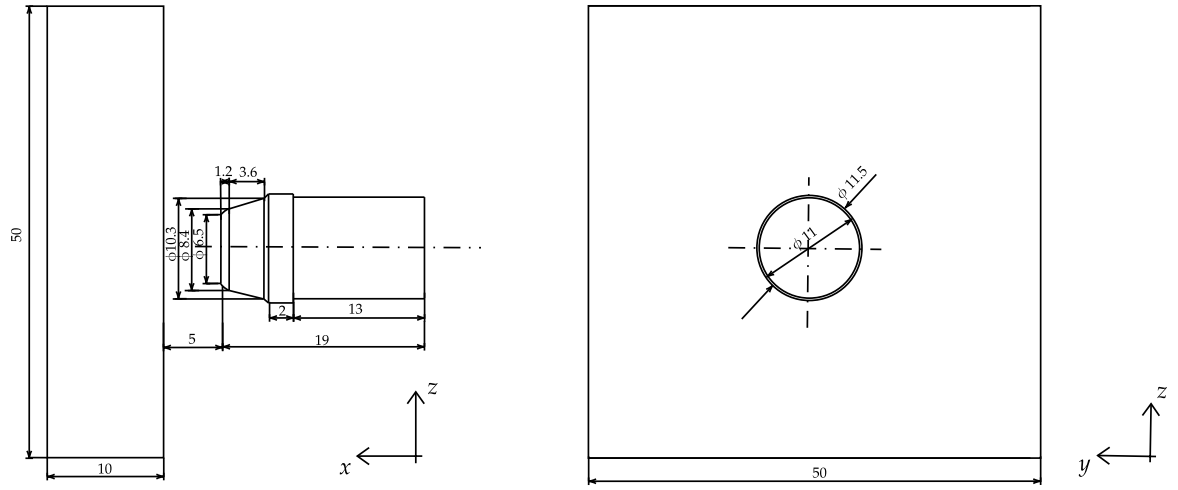


Figure 7.2: Geometry of the studied problem [140]).

Note the presence of two evident symmetry axes both in the bullet and in the wall: in y and in z. Nevertheless, given the fact that this is a simple geometry, it will be analysed in its entirety, instead of only a quarter of it (which would entail an even reduced computational power need).

A partial penetration of the wall by the bullet was chosen for this study, not a full penetration where the bullet enters and leaves the wall on the other side. This significantly simplifies the posterior evaluation of the pertinent physical quantities chosen for the convergence analysis.

To allow solely a partial impact, two strategies were employed:

- Wall thickness selection: set as 10 mm. It was observed that a thickness of 5 mm, for instance, allowed the full penetration of the bullet.
- Initial velocity definition: the velocity of 300 m/s ($v_0 = 300$ m/s) was introduced in the bullet. A higher value could evidently be opted for.

The initial distance between the bullet and the wall was set as 5 mm. Note that the selection of this dimension should take into account numerical considerations. In fact, since in most cases, the analyst is not interested in evaluating the displacement of the bullet towards the wall, but instead the contact between the bodies and the damage that emerges from this event, the first phenomenon is associated with an unnecessary computational expense. Given the fact that this is an extremely simple problem and, as will be seen next, characterised by significantly low solution times, the 5 mm distance remained between the bodies.

Lastly, it is necessary to mention that the exclusive boundary condition employed in the problem, was the fixation of the wall on each of its four lateral surfaces.

7.1.2 Mechanical Properties

Two metallic materials were employed for this analysis, that correspond to those used in the BPE explicit dynamics studies that follow.

To the bullet body was assigned structural steel. This corresponds to the material solution provided by Ansys® engineering data, already presented in Table 6.7.

The Al 6061-T6 aluminium alloy was introduced in the wall. The properties of this explicitly-defined material were found in the same material database as the steel and can be consulted in subsection 6.1.2.3, of the previous Chapter.

7.1.3 Mesh Discretisation

A high-quality mesh is a crucial requirement for efficient and accurate explicit analysis. To investigate the influence of the mesh in this problem type, four progressively refined spatial discretisations of the wall, the main subject of evaluation, were performed. The mesh of the bullet, however, was left in its default configuration.

Since the analysis being conducted is an explicit dynamics one, the mesh settings Physics Preference corresponds to explicit, while the Element Order is linear, as per default.

Tet4 and Hex8 3D solid elements were employed in this study. With regards to the integration scheme, its importance is understood; however, owing to the fact that the Autodyn solver automatically optimises this parameter for the specific case being addressed, no further care was employed in this matter.

As stated above, the bullet discretisation was performed according to its mesh default definitions. The default element size used was 1.967 mm.

Focusing now on the metal wall and on the four discretisations performed to evaluate the effect of the mesh on the accuracy of the emerging results, it is relevant to state that efforts to achieve uniform meshes were employed for the reasons discussed in Chapter 4.

A discretisation rule that allowed the obtainment of well-shaped elements, without significant distortion was selected. Considering that the mesh discretisations, noted i, are numbered from 1 to 4, with 1 being the coarsest mesh and 4 the more refined one, the expression in Equation 7.1 was computed to calculate the number of elements, n, in the thickness of the wall.

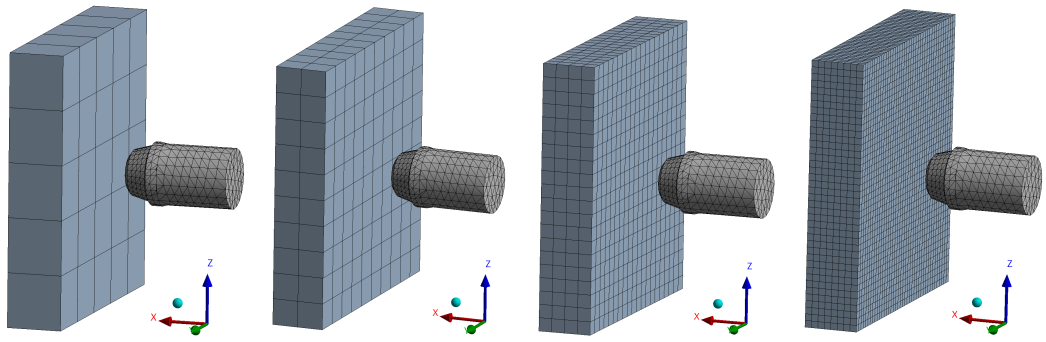
$$n = 2^{i-1} \tag{7.1}$$

From the coarsest to the finest mesh, respectively, 1, 2, 4 and 8 elements "split" the thickness dimension of the wall. These values, as well as the total number of elements and nodes for each of the four models (keep in mind, including those of the bullet), are presented in Table 7.1.

Table 7.1: Number of elements along the thickness of the wall and total number of elements and nodes for the whole model

Mesh discretisation number (i)	**Number of elements along the thickness**	**Total number of elements**	**Total number of nodes**
1	1	3453	886
2	2	3628	1177
3	4	5028	5028
4	8	16228	15943

The mesh discretisations of each of the four models are represented in Figure 7.3.



(a) **(b)** **(c)** **(d)**

Figure 7.3: Addressed mesh discretisations in the impacted wall. **(a)** Mesh discretisation 1 (coarsest mesh used). **(b)** Mesh discretisation 2. **(c)** Mesh discretisation 3. **(d)** Mesh discretisation 4 (more refined mesh).

This discretisation rule allowed, as desired, the achievement of well-shaped elements in all of the models. This was evidenced by the mesh metrics, for instance, with the obtainment of values ranging from 0.8 to 0.96 in the element quality indicator, across the four meshes. The most elevated value was, of course, achieved in the mesh discretisation 4.

7.1.4 Explicit Analysis Settings Definition

Given the simplicity of the study case, many of the program's default settings were maintained, as were found accurate for the given problem.

Firstly, it is relevant to mention that the bullet was set as a rigid body. This was done since the behaviour of the bullet to impact was not of interest to this study. As only the wall will be evaluated, this contributed to the reduction of the computational cost inherent to the model.

Regarding the body interactions, the contact detection type was defined as "trajectory" with the penalty formulation. A frictionless contact type was chosen to simplify the analysis. Of course, in the real event, the friction between the bodies would be present.

Having already defined both the boundary and initial conditions of the problem, the only parameter left to input was the end time of the analysis. This parameter must be input by the user. The most suitable end time for the analysis was chosen following a trial-and-error approach, resulting in a value of 0.001 s. Lastly, all the remaining analysis settings were left as the program's default definitions.

For completeness purposes, the most pertinent analysis settings for the conducted explicit analysis are presented in Table 7.2.

Table 7.2: Convergence study's explicit analysis settings

Analysis Settings Preference Type	Programme Controlled
Number of Steps	1
Load Step Type	Explicit Time Integration
End Time [s]	0.001
Maximum Number of Cycles	$1 * 10^7$

7.1.5 Convergence Results

In this section, the results obtained for the investigated problem are shown and discussed. The maximum directional deformation in the x direction, the maximum equivalent von Mises stress, the internal and hourglass energies of the wall during the simulations, as well as the computational times will be discussed.

7.1.5.1 Directional Deformation in x axis

The starting point of the results' assessment was the evaluation of the values of maximum directional deformation of the wall, along the x direction, through time. This particular directional deformation was selected as an evaluation parameter, instead of the total deformation, for instance, since it corresponds to the direction of the velocity vector of the bullet.

To simplify the analysis, the deformation presented by the back face of the wall will be evaluated. Figure 7.4 represents, both from lateral and frontal views, the distribution of this quantity on the aforesaid surface in the instant of maximum magnitude.

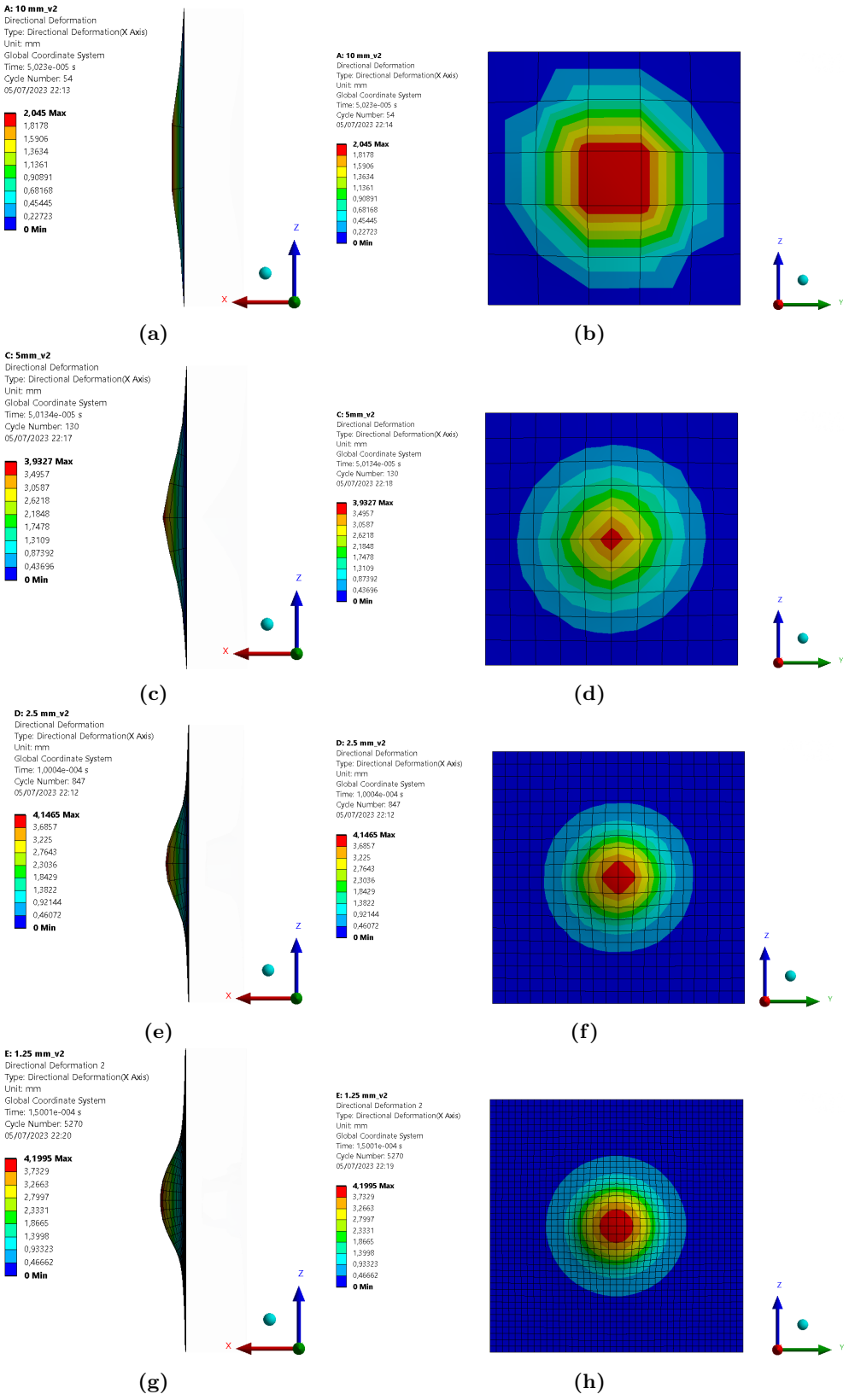


Figure 7.4: Directional deformation in the x axis found in the back face of the impacted wall: lateral (on the left) and frontal (on the right) view. **(a)** Mesh discretisation 1 (coarsest mesh used). **(b)** Mesh discretisation 2. **(c)** Mesh discretisation 3. **(d)** Mesh discretisation 4.

As anticipated, the location of the maximum deformation corresponds to the centre of the wall, longitudinally to the location of the bullet impact.

As can be observed, particularly in the lateral views, the first two discretisations fail to capture the realistic deflection of the centre of the wall, leading to: reduced deformation values in the discretisation 1; artificial curvatures that do not correspond to the realistic outcomes emerging from the impact of this bullet, in the discretisations 1 and 2. In addition, it is clear that the colour map is evidently smoother and more tangible, the more the mesh is refined.

Given the fact that the wall is clamped in its four lateral surfaces, a vibratory behaviour of the wall is to be expected from the bullet partial penetration. Thus, in Figure 7.5, the maximum directional deformations in the back face can be found, through the analysis type.

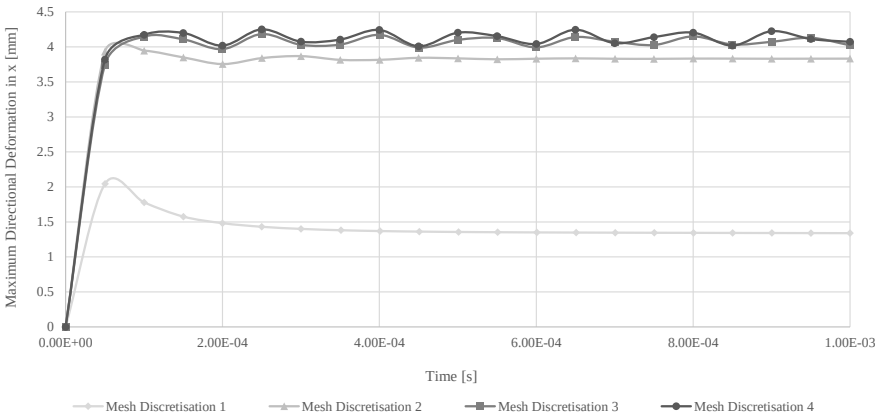


Figure 7.5: Maximum directional deformation, on the x axis, in the impacted wall (central node) through time.

The first information that can be extracted from the Figure above is that mesh discretisation 1 fails to capture the vibratory behaviour of the wall. Once more, this attests to the fact that this spatial discretisation is invalid to the study case, leading to inaccurate results.

Next, in the following three discretisations, from 2 to 4, they are significantly close in value and similar to each other. In each, an aspect that can be observed is the fact that there is a stabilisation of the maximum directional deformation in time. This attenuation is a realistic behaviour that emerges from the permanent deformation (i.e., plastic deformation) of the wall to the partial penetration of the bullet. This stabilisation occurs much earlier in the second discretisation than in the more refined models, which better represent the vibratory behaviour of the wall.

Lastly, it is noteworthy how the variation of the maximum values of this physical quantity is bigger from the mesh discretisation 1 to 2, followed by that of mesh discretisation 2 to 3 and then from the third to the fourth mesh discretisations, the latter being already extremely similar.

7.1.5.2 Equivalent von Mises Stress

The next quantity to evaluate was the maximum value of equivalent von Misses Stress found in the back face of the wall, for each of the performed discretisations. This is illustrated in Figure 7.7, at the instant where this maximum stress value is present in the surface.

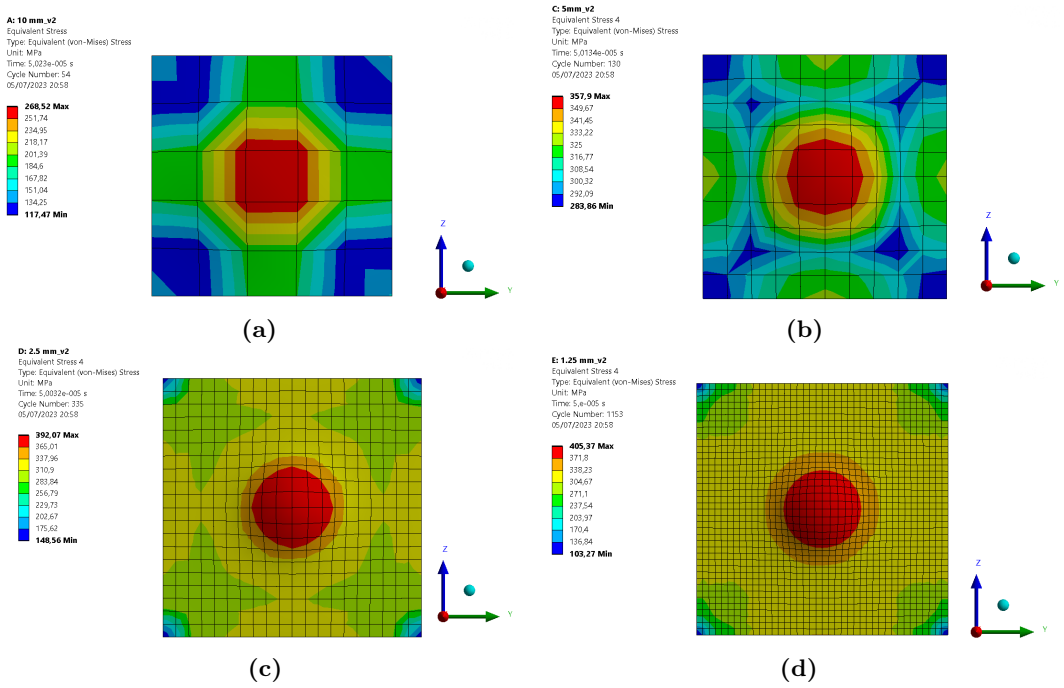


Figure 7.6: Equivalent von Mises stress found in the back face of the impacted wall. **(a)** Mesh discretisation 1 (coarsest mesh used). **(b)** Mesh discretisation 2. **(c)** Mesh discretisation 3. **(d)** Mesh discretisation 4.

As expected, once more, this maximum stress value occurs in the centre of the face, in the position where the bullet partially penetrates the wall. Additionally, given the latter location and the symmetry of the model, a symmetric distribution of this quantity is observed.

To schematically represent the maximum stress value found in the back face in each of the spatial discretisations, the graph represented in Figure 7.7 was established.

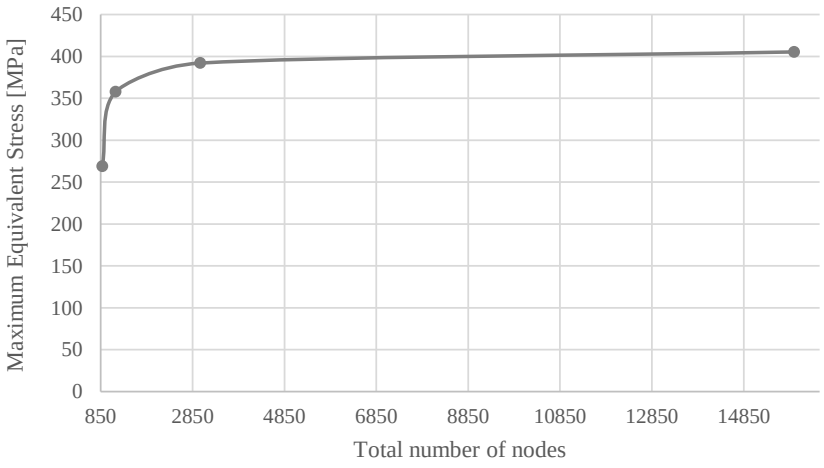


Figure 7.7: Maximum equivalent stress in the back face of the impacted wall (central node), for each of the four discretisations.

Notoriously, the mesh discretisation characterised by the minimum number of nodes, i.e., mesh discretisation 1, presents a maximum value of stress that differs about 140 MPa from that of mesh discretisation 4 (with the maximum number of nodes). This was to be expected since, as was already concluded, mesh discretisation 1 is unfit for use in this problem.

In addition, the interval of values found for the different meshes tends to be smaller the more the mesh is refined, as was also addressed in the directional deformation discussion. Note that the maximum value of stress found in mesh discretisation 4, 405.37 MPa, is much closer to that of mesh discretisation 3, 392.07 MPa, than the latter is of the second discretisation value (357.9 MPa).

This convergence behaviour was sought and shows that mesh-insensitiveness is gaining relevance in the last simulations. Were the refinement to continue, it is anticipated that the variation found between the maximum stress values is set to reduce in "adjacent" mesh discretisations.

7.1.5.3 Internal Energy

A parameter that is always pertinent to examine in impact cases is the internal energy of the impacted object, in this case, the metal wall.

This quantity will be evaluated through time, as was done for the directional deformation and is illustrated in Figure 7.8.

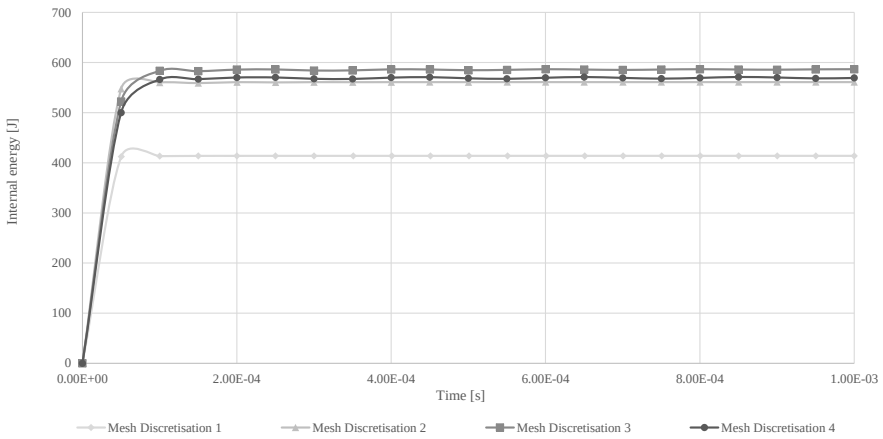


Figure 7.8: Internal energy of the impacted wall through time.

When the impact occurs, in this case, very close to the initial timeframe, energy conversion occurs: the internal energy of the impacted object increases, while the kinetic energy of the impacting body decreases. Since the analysis time being evaluated is extremely reduced, of about 0.001 s, after the initial abrupt increase of the internal energy of the wall a stabilisation of this value is expected.

Observing the Figure above, it is notorious that the mesh discretisation 1 fails to capture the expected energy boost presented by the wall. The other three discretisations, in turn, particularly the third and fourth present close resemblance. Mesh inventiveness can therefore begin to be verified.

7.1.5.4 Hourglass energy

As briefly addressed in Chapter 4, hourglass strain modes are undesired in FE simulation. A strategy to evaluate the influence of this numerical error in a certain analysis is to monitor the hourglass energy added to the system. The presence of significant hourglass energy indicates the occurrence of severe hourglass behaviour and, therefore, the obtainment of unreliable results.

The hourglass energy vs time plot is presented in Figure 7.9, for each of the four performed discretisations.

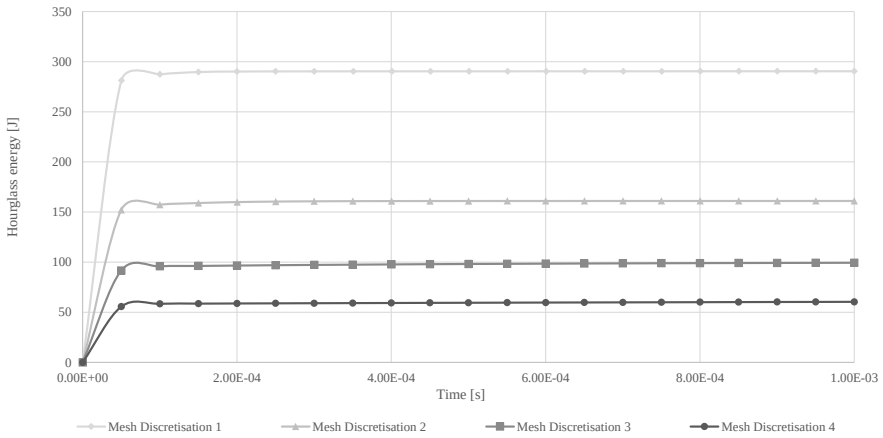


Figure 7.9: Hourglass energy of the impacted wall through time.

A rule of thumb commonly used in computational mechanics is to use as validation for this numerical phenomenon is to check if the percentage of hourglass energy is less than 10% of the total energy of the system [141]. This examination will be performed, assuming the average total energy of the system, considering the fact that for each discretisation this value remained nearly constant throughout the simulation in the extremely small time interval being evaluated (as is expected from a correctly set up explicit analysis).

Thus, in Table 7.3 are presented the average values of total energy and the percentage of hourglass energy in relation to the latter (utilising the maximum value of the hourglass energy through time).

Table 7.3: Percentage of hourglass energy present in the simulation with regards to the total energy of the system

	Average total energy of the system [J]	**Maximum value of hourglass energy [J]**	**Share of hourglass energy [%]**
Mesh Discretisation 1	413.8	290.4	70.1
Mesh Discretisation 2	560.7	161.0	28.7
Mesh Discretisation 3	584.3	99.3	17.0
Mesh Discretisation 4	568.4	60.4	10.6

By consultation of the Table above, it is evident that the selected indicator reduces significantly from the coarsest mesh to the finest mesh. In fact, considering the 10% often used as a validation criterion, only mesh discretisation 4 comes close to this indicator.

Once more, the variation of the percentage of the hourglass error from mesh discretisation 3 to 4 is much smaller than that between the two more coarse mesh discretisations. It is expected of the percentage of hourglass energy to be increasingly smaller the more refined a mesh is, tending to a stabilised value in a slower manner each time.

7.1.5.5 Simulation Elapsed Time

The time a simulation takes to run is an important parameter to analyse in computational mechanics, as it gives a clue of the computational efforts being employed in a certain application.

In Figure 7.10, a scatter plot illustrating the total elapsed run time associated with each of the conducted explicit simulations is presented. A logarithmic scale was employed in this graph.

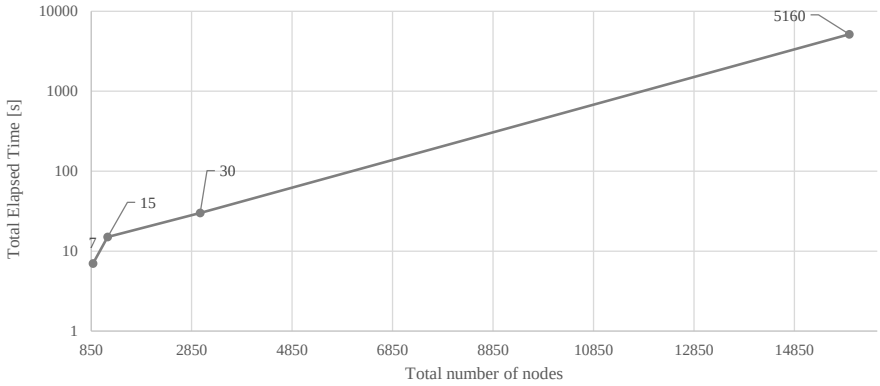


Figure 7.10: Total elapsed run time for each simulation.

It is notorious that while the models where the first three mesh discretisations were employed took less than 1 minute to run, that with the most refined mesh lead to a much lengthier time to yield the solution (about 86 minutes, about 170 times that of the previous discretisation). This is representative of the fact that the model with the finest mesh entails a more pronounced computational cost, in comparison to the other models.

Lastly, recall that the model spatially discretised with the third mesh conducted to the obtainment of identical results than those of the most computationally-expensive model. Thus, it appears sensible to resort to the former if the available computational power is limited, since a compromise between the validity of the results and the computational efforts is achieved.

Chapter 8

Phase 1: Original Geometry in Al 6061-T6

This Chapter concerns the particular specifications of the so-called "Original model" and the exposition of numerical results emerging from the multiple simulations associated with it.

The "Original model", as the name indicates, constitutes the starting point of this work's numerical study, having resulted from a well-positioned real-life industry solution of a BPE. Recall that the presentation and reasoning for the geometry of the obtained model and the material assigned to it (the Al 6061-T6 alloy) have already been explored in Chapter 6.

Contrary to what will be done in the following Chapters, which will also address the geometry and material alterations associated with the improved models, the only matters related to Phase 1 left to address correspond to: the discrimination of the weight of the model structure (detailed individually and globally); the discussion of the input mesh parameters and the achieved quality of the meshed models for the various analysis types; the exposition and assessment of the analyses' results.

In Table 8.1, the weight of the structure can be consulted, both at component and structure levels. This Table is of colossal importance since it will be used to assess one of the principal subjects of this work: the lightweight design of all BPE solutions. Since the weight values associated with the "Original model" correspond roughly to those of the industry inspiration for its design, the presented numbers will be used to calculate the weight reductions associated with the improved models.

Recall that the weight associated with the rocker panels and battery modules is the same in all of the Phases: the same aluminium alloy is assigned to the former part for each of the analyses, and the battery modules are represented in the structure by means of distributed loads, always of the same value. Thus, the weight associated with the mentioned components will not be accounted for in the weight reduction computations. In addition, these components are not part of the battery housing itself; therefore, including them in the calculations would not be correct, even if they do not influence the relative results.

Moreover, the mass corresponding to each component of the BPE was obtained indirectly from the program by resorting to the density of the Al 6061-T6 and the volume of each component. The latter can, in turn, be directly retrieved from Ansys' SpaceClaim®.

Table 8.1: Mass associated with the BPE model of Phase 1

Part	**Material**	**Density [kg/mm^3]**	**Volume [mm^3]**	**Mass [kg]**
Top Cover	Al 6061-T6	$2.703e-6$	9864525	26.66
Bottom Cover	Al 6061-T6	$2.703e-6$	81358780	219.91
Longitudinal Reinforcement	Al 6061-T6	$2.703e-6$	2439721	6.59
Transversal Reinforcement (6x)	Al 6061-T6	$2.703e-6$	5036321	13.61
			Total	≈ 266.78

Regarding the discussion of the numerical results, not only in this Phase but in all, they will be presented first in a global light, where the entire structure will be evaluated for a particular quantity and then, individually, for each of the components by which it is composed by. This will be done, preferably, on the transient and explicit dynamics analyses given their enhanced relevance to this work, for instance, to the static and modal analyses.

8.1 Phase 1: Static Analysis

As mentioned in the introductory Chapter to the numerical analyses, it is pertinent to evaluate the behaviour of the structure through a static analysis prior to performing a dynamic study.

The clamping of the rocker panels was the only constraint applied in the system, and the force resulting from the standard earth gravity constitutes the only load acting in the system. With this analysis, the evaluation of the deformations, stresses and strains emerging on the BPE due to the weight of the structure filled with the modules is sought. Moreover, if any, zones with stress gradients will be assessed.

To capture an accurate behaviour of the structure, the employment of a suitable mesh is essential. The employed mesh for this static analysis can be consulted in Figure 8.1.

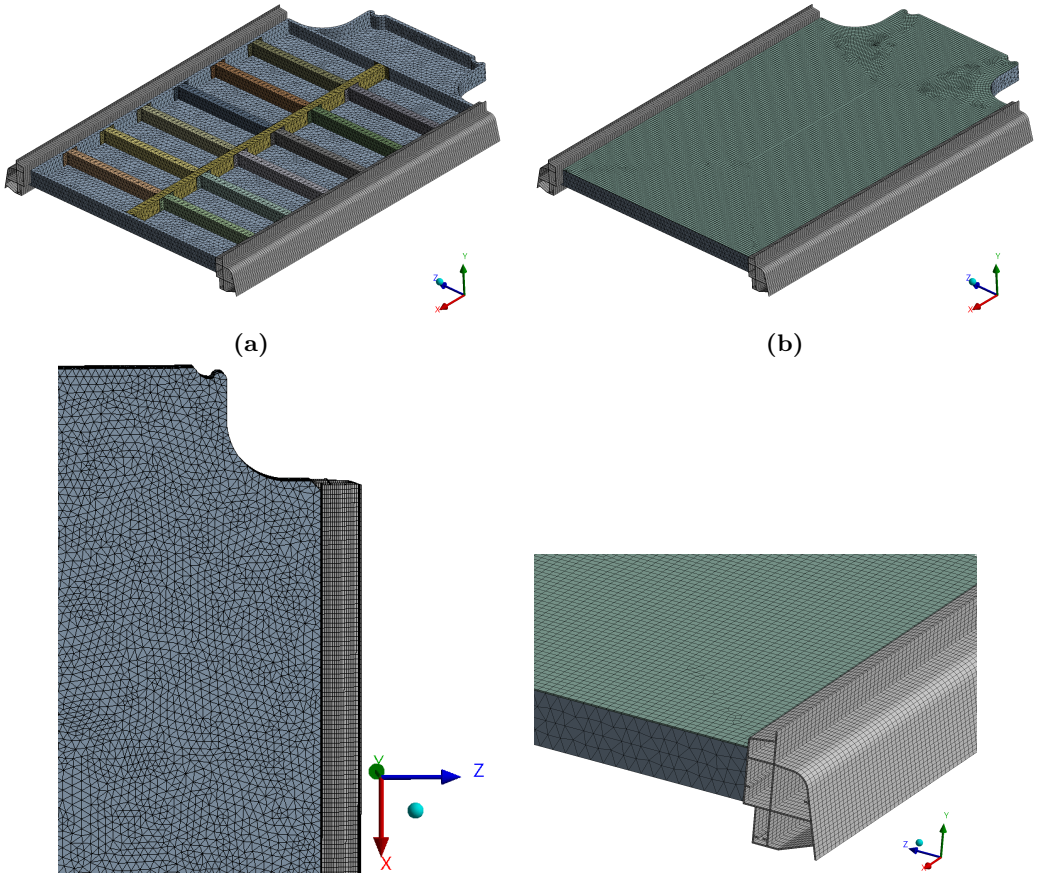


Figure 8.1: Static analysis of Phase 1: mesh applied in the model. **(a)** BPE with cover. **(b)** BPE without cover. **(c)** Bottom case detail. **(d)** Rock panel and top cover detail.

As can be observed, an extremely mapped mash can be found throughout the model, where mostly hexagonal elements were employed. The detail found in **(c)**, however, evidences the presence of some tetrahedral elements in a more complex region of the BPE geometry, which is consistent given the fact that these elements are the most qualified for usage in intricate regions.

This mesh resulted from the employment of the following parameters:

- In the mesh details, the Physics Preference and the Element Order were left in their default definitions: mechanical and program-controlled, respectively. The global element size was set as 15 mm, which applies to the surfaces or bodies to which no other individual sizing has been applied.

- After trying the employment of other methods, such as the Sweep (in the sweepable bodies evidenced by Ansys® itself) and Hex Dominant, to name a few, the Automatic method was applied to the bodies of the model. This corresponds to the method that yielded the best results in the mesh metrics, which will be addressed next.

- A body sizing was applied to the bottom case, where the element size was set as 25 mm. The increase in this parameter regarding the global mesh sizing resulted from the program's ease of meshing this component, characterised by a relatively simple geometry, where a more refined mesh would be translated into computational inefficiency.

This resulted in a mesh with 600655 nodes and 147778 elements. Tet10, Hex20, and Wed15 elements, i.e., second-order tetrahedron, hexahedron, and prismatic, respectively, 3D elements, can be found in the defined mesh.

To provide an even deeper insight to the reader of all element types employed in the spatial discretisation of the model, their technical designations are the following: SOLID186, SOLID187, CONTA174, TARGE170 and SURF154. The first types two correspond, respectively, to 3D second-order twenty-noded hexahedrons and 3D second-order ten-noded tetrahedrons solid elements. Both possess three degrees of freedom per node, them being translations in the nodal x, y and z direction. Uniform reduced integration, which corresponds to the default setting, was utilised. Then, TARGE170 and CONTA174 are used to represent 3D target surfaces and contact elements. Lastly, SURF154 is utilised in 3D structural analyses to serve load and surface applications [142]. Understandably, the solid elements compose the greater portion of the elements utilised in the mesh. As will be verified in the next stages of this work, these elements will be utilised for each simulation.

The quality of the mesh is assessed by the metrics discussed in Chapter 6, whose values are presented in Table 8.2.

Table 8.2: Phase 1: Static analysis mesh metrics

	Element Quality	**Aspect Ratio**	**Skewness**
Minimum	$5.4631e-2$	1.1787	$1.3057e-10$
Maximum	0.9998	39.068	0.99967
Average	0.46861	4.3288	0.3875
Standard Deviation	0.23181	2.0939	0.32161

Thus, an average element quality of approximately 0.50 was obtained, which was considered enough to the obtainment of significant results in the static analysis. However, as can be seen, for instance, by the minimum value of skewness and maximum value of aspect ratio, some elements are quite distorted, which could potentially lead to local inaccuracies.

After defining all evaluated static analysis parameters in the corresponding Ansys® module, it only took 28 seconds for the MAPDL solver to produce the results presented in the following subsections.

8.1.1 Total and Directional Deformation

The first step in the analysis of results is to examine the deformed configuration of the structure. Thus, in Figure 8.2, the deformed configuration of the BPE can be observed. To aid with the understanding of this quantity, a scale of 3600 was utilised.

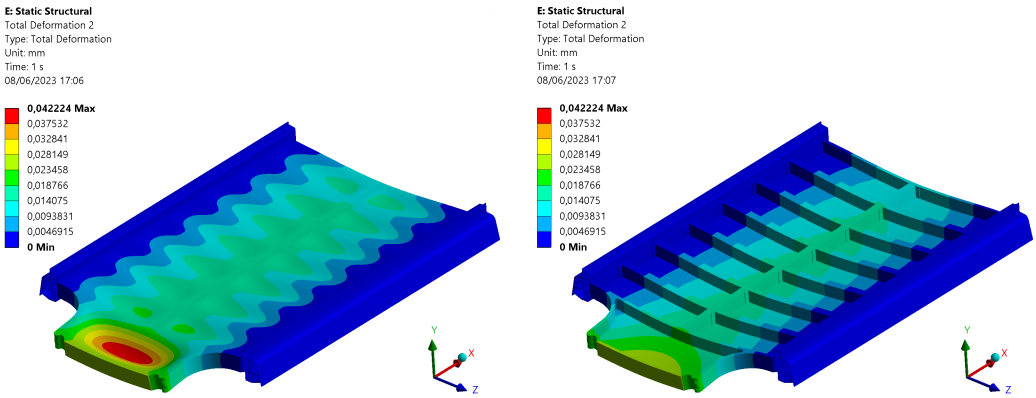


Figure 8.2: Static analysis of Phase 1: total deformation of the BPE (scale of 3600). **(a)** BPE with cover. **(b)** BPE without cover.

As can be concluded from the fact that the only load actuating on the model (and battery modules) was its own weight in y, most of the deformation occurs in that direction. Therefore, this directional deformation, which can be consulted in Figure 8.3, is the most pertinent to examine.

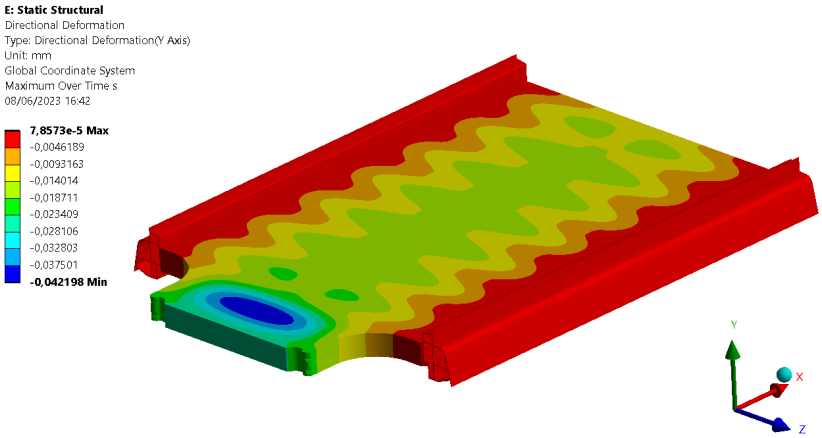


Figure 8.3: Static Analysis of Phase 1: directional deformation in y (true scale).

The distribution of deformations in the structure is symmetric on the x axis as a consequence of the symmetry of the model and of the boundary conditions in it employed about that same direction.

From the observation of both Figures, it is evident that the maximum deformations occur in the region of the frontal modal cavity of the BPE, both in the top cover and on the bottom case. This zone deflects downwards, as does the whole structure along its symmetry axis, where the bigger reinforcement meets the smaller transversal ones. The magnitude of this deformation increases longitudinally throughout the structure until the frontal cavity.

The most deformed component is the top cover due to its thickness being much smaller than those found in the remaining BPE. Moreover, the fact that the frontal region is the most deformed in the structure is correct since there are no additional reinforcements in this zone for a module cavity of a bigger surface area, contrary to what occurs in the most central zone of the BPE.

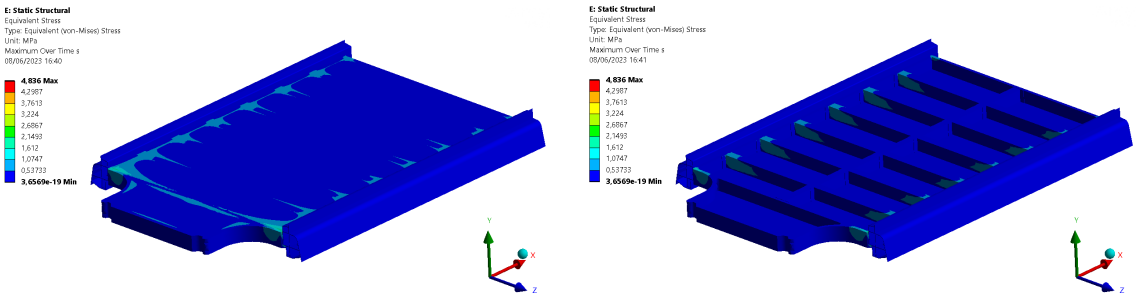
Resorting to the applied scale of 3600, it can be yielded that the structure bends slightly in the middle. There is compression in the top surface and traction in the bottom one. Nevertheless, it is extremely important to keep in mind that the deformations found in the structure are extremely small. This deformation would be imperceptible without the implication of this scaling factor in FEM, as it would be in real life.

Note that the maximum deformation the BPE endures due to its own weight is around 0.04 mm. The obtainment of this extremely reduced value verifies that the own weight of the structure does not inflict significant deformation in itself. This is, of course, essential for the application of a component in a vehicle since if a structure deforms significantly due to its own weight, it will not be able to withstand the portion of the weight of the vehicle that relies on it, as well as the many other external loads it is subjected to.

8.1.2 Equivalent von Mises Stress

It is equivalently pertinent to assess the stresses brought to the structure by its own weight. Understandably, like the deformations, and for the same reasons, the obtained values are anticipated to be extremely small.

The stress distributions across the BPE model can be consulted in Figure 8.4, in true scale.



(a) **(b)**

Figure 8.4: Static analysis of Phase 1: equivalent von Mises stress (true scale). **(a)** BPE with cover. **(b)** BPE without cover.

The results of the static simulation yielded that the most stressed zones, with a value of 4.8 MPa, correspond to the contact regions of the rocker panels and the corners of the BPE (Figure 8.5).

Oftentimes, it is incorrect to evaluate physical quantities in the proximity of the zones of application of concentrated loads and rigid boundary conditions. This is justified by the fact that, typically, these zones present contaminated values with no physical significance that emerge from numerical artefacts.

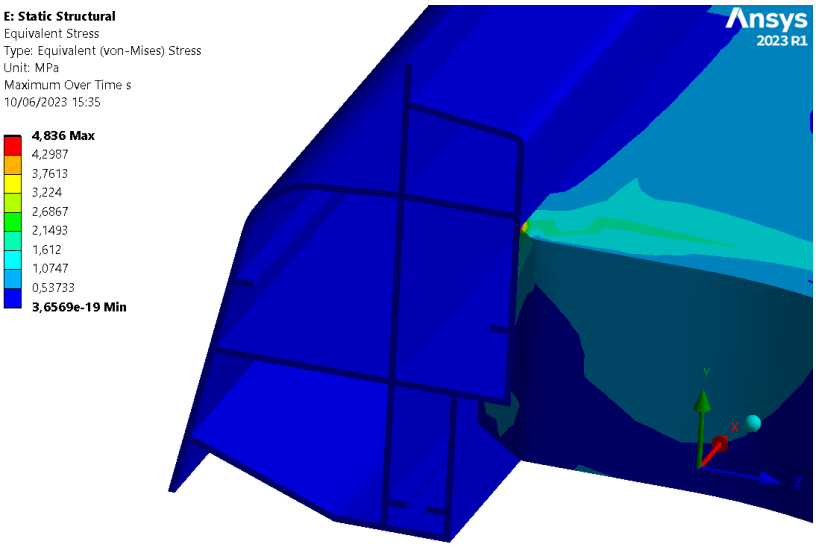


Figure 8.5: Static analysis of Phase 1: the most stressed region (true scale).

In this case, it can be easily concluded that these maximum stresses result from the applied rigid boundary conditions and possibly from the mesh employed in the model. Thus, these zones' stress concentrations have no true physical meaning and will be disregarded. As expected, the analysis of stress acting in further zones from this region yielded extremely small values for this quantity. Thus, this model, similar to the structure that inspired it, ensures that the structure's integrity is not slightly threatened when it is subjected solely to its own weight. In summation, it is possible to validate this model as capable of representing the structure for the dynamic analyses that follow.

8.2 Phase 1: Modal Analysis

As discussed in Chapter 6, the purpose of conducting a modal analysis was to retrieve the modes of vibration that participate the most in the deformation of the structure under dynamic loads. The obtainment of the coupled natural frequencies and natural mode shapes is often extremely valuable prior to transient analysis as it enables a preliminary insight into the structure's dynamic behaviour.

The only necessary matter left to discuss with respect to the modal analysis prior to the discussion of results is the mesh employed in the model. Like was done in the previous section, illustrations of the meshed model will be provided, along with the utilised mesh details and, subsequently, the achieved mesh quality values.

The following parameters were used to mesh the model:

- In the mesh details, the Physics Preference and Element Order were left, once again, in their default definitions that correspond once more to mechanical and program-controlled. A global element sizing of 12 mm was set, which is applicable for all of the components since no individual sizing was applied in this case.
- There was care in applying the Sweep method in the rocker panels components after seeing that these were sweepable bodies.
- The Patch Conforming method was employed in the bottom case and in the biggest internal reinforcement of the structure that lies longitudinally in the BPE.

A more refined mesh was used for this analysis compared to the one employed in the static one due to the fact that this analysis is significantly more complex. After trying several combinations of potential mesh parameters, the one defined above presented the best results in the mesh quality indicators. The input definitions were chosen considering the geometries of each component and with the aim of producing a mesh that will contribute to the balance between the accuracy of the solution and the computational cost associated with it.

The meshed structure is illustrated in Figure 8.6. The same element types of those employed in the preceding analysis were once again used to discretise the model.

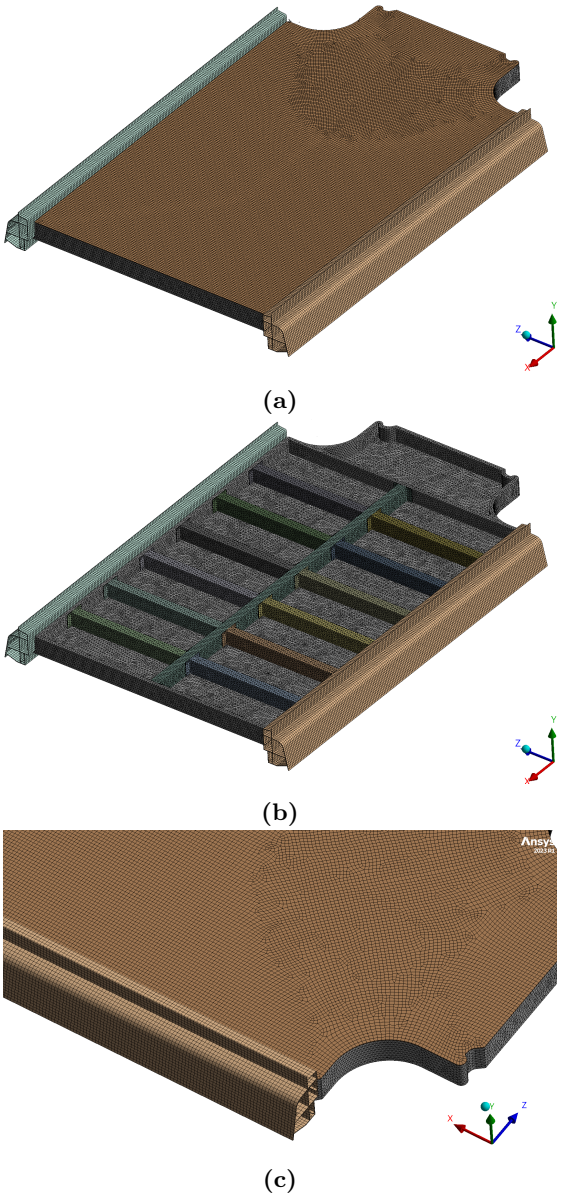


Figure 8.6: Modal analysis of Phase 1: mesh applied in the model. **(a)** BPE with cover. **(b)** BPE without cover. **(c)** Top cover and rocker panels detail.

The obtained mesh is visually similar to that achieved in the static analysis, where the same element types can be found in the same BPE regions, more or less. Nevertheless,

the currently assessed spatial discretisation comprises 1232719 nodes and 544926 elements, constituting a more refined mesh. In Table 8.3, the values associated with the metrics used to evaluate the quality of the employed mesh are provided.

Table 8.3: Phase 1: Modal and transient analyses mesh metrics

	Element Quality	**Aspect Ratio**	**Skewness**
Minimum	$2.9606e-2$	1.1576	$1.3057e-10$
Maximum	0.99999	65.68	1
Average	0.75515	2.2457	0.282
Standard Deviation	0.16464	1.0292	0.18029

As seen by the average values of the chosen mesh quality indicators, the mesh applied to the model appears suitable to be used for the following simulations to be performed. These metrics' maximum and minimum values result from distorted elements whose presence is rare in this case.

The model was then in a condition to be run. The time the program took to yield the solution was 100 minutes, not a lot for significantly complex analyses, as is often the case for this analysis type.

8.2.1 Natural Mode Shapes: Deformation

The modal analysis conducted in Phase 1 retrieved a number of 400 natural modes as input in the settings, whose natural frequencies' values ranged from 113.85 Hz, on the fundamental natural frequency, to 1593.6 Hz, on the frequency associated with the last extracted mode. Recall that the natural frequencies should be ordered ascendingly, i.e., $w_1 < w_2 < ... < w_n$, with w_1 being the fundamental natural frequency [133].

For illustration purposes, in Figure 8.7, the natural mode shapes associated with the first six natural frequencies are presented with regard to total deformation.

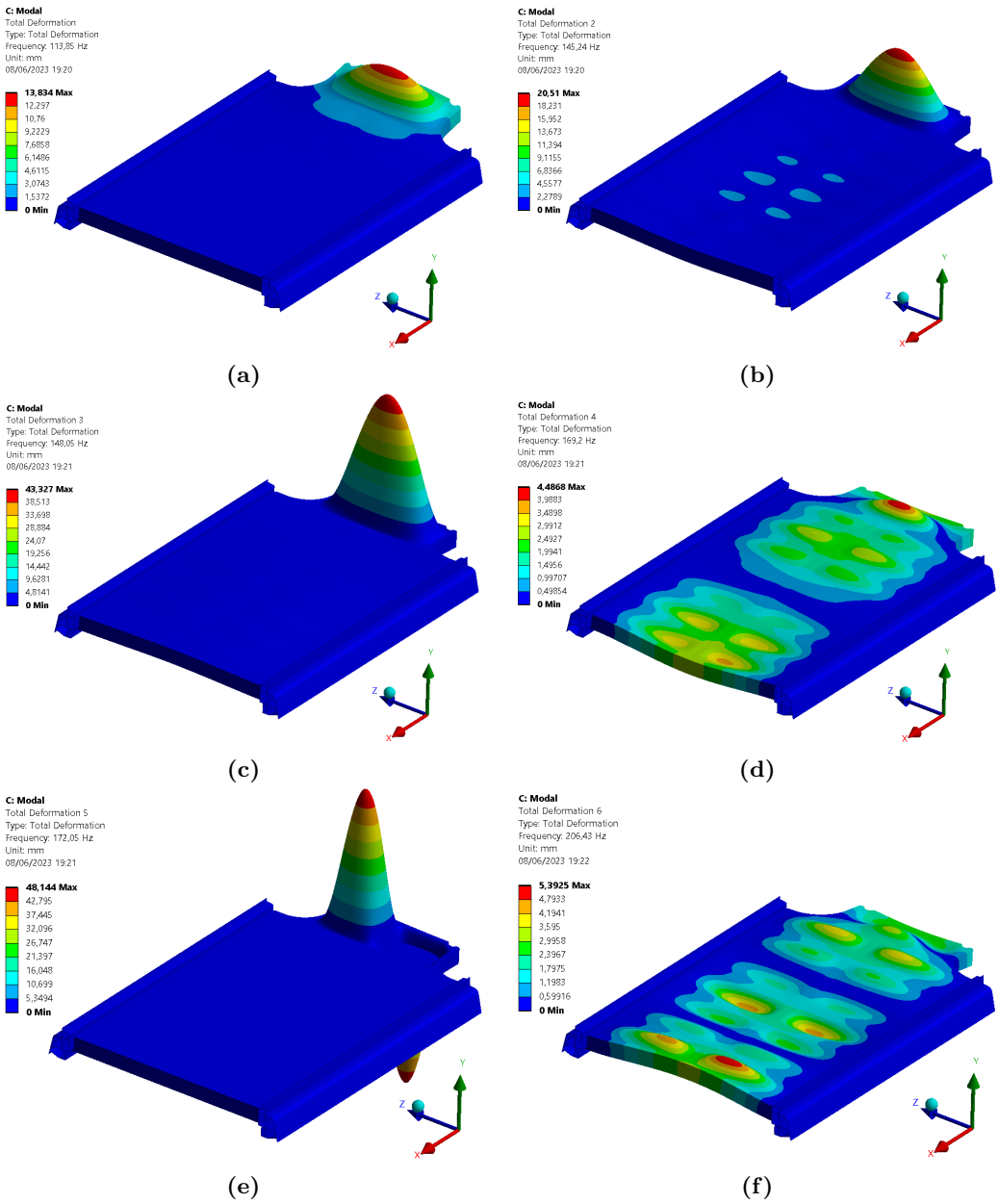


Figure 8.7: Modal analysis of Phase 1: natural mode shapes coupled with the first six natural frequencies (scale of 20). **(a)** 113.85 Hz. **(b)** 145.24 Hz. **(c)** 148.05 Hz. **(d)** 169.2 Hz. **(e)** 172.05 Hz. **(f)** 172.05 Hz.

From Figure 8.7, it is possible first to notice the symmetry in the presented vibration patterns. This motif originates, once again, from the symmetry of the structure and of the employed boundary conditions about the x axis.

Next, the dominant patterns of vibration exhibited by the structure are examined. The first three natural vibration modes concern the top cover's displacement above the frontal module cavity. For instance, the fourth and sixth modes are related to the deformation of the same component, but now in the central region of the BPE, above the zone where the transversal and longitudinal reinforcements meet. Therefore, it is possible to anticipate that these two zones, particularly the former (as was also found in the static analysis), may constitute the areas of highest deformation within the structure, even in damped systems, as

is oftentimes the case with automotive components. Furthermore, attention should be paid to these zones in the subsequent analyses to ascertain if they can possibly be identified as vulnerable regions of the structure.

Recall, however, that the purpose of conducting this analysis, more than evaluating the quantities of deformation corresponding to each of the modes of vibration under natural vibration, is to get a grasp of the overall dynamic response of the structure. Moreover, when alterations to the BPE's geometry and materials are to be performed, it will be interesting to understand how that affects the solution's vulnerability to vibration in the next Phases.

8.3 Phase 1: Transient Analysis

As stated in Chapter 6, the results of the modal analyses serve as initial conditions for the transient analyses. This entails transferring the geometry, material, and every setting input in the modal model, including the applied mesh, to the transient one.

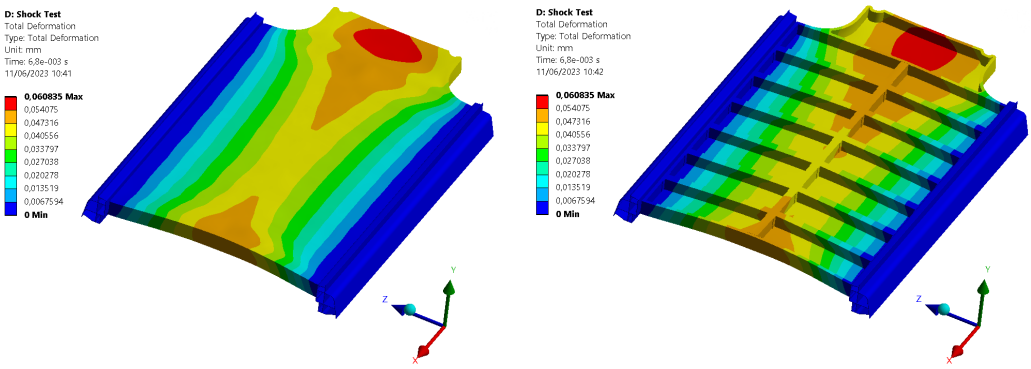
Hence, since all the relevant parameters for the transient analysis have been extensively discussed in the previous Chapter and in the previous section (the latter focusing on the mesh inputs and quality indicators), the conducted transient analysis has already been thoroughly explained.

The model was, then, in condition to be solved. The Ansys® solver Mechanical APDL yielded the solution after 152 minutes, approximately two and a half hours, of elapsed time.

8.3.1 Total and Directional Deformation

As per usual, the total and directional deformations of the structure will be the starting point of this evaluation of results.

The total deformation distribution in the structure is illustrated in Figure 8.8, where a scaling factor of 1000 was employed to enable the grasping of a more comprehensive understanding of the BPE's global behaviour.



(a) **(b)**

Figure 8.8: Transient analysis of Phase 1: total deformation distribution in the BPE and rocker panels (scale of 1000). **(a)** BPE with cover. **(b)** BPE without cover.

The first conclusion one can retrieve from the Figure above is that, even though a scaling of 1000 was applied to the structure, barely any deformation can be observed, contrary to what was expected.

Regarding the colour map related to the deformations occurring in the structure, a symmetric distribution was again found due to the same reasons. The furthest lateral compo-

nents, the rocker panels, do not present any deformation, owing to the applied boundary conditions, while the more internal parts present the highest values for this quantity. In fact, resorting to this extreme scale, it is observed that the BPE undergoes a slight upward bending towards the middle.

The most evident zone of maximum displacement corresponds to the one discriminated in the modal analysis of the structure, in the top cover, above the frontal module cavity. This further justifies the pertinence of conducting this type of preliminary simulation. Moreover, it seems consistent that this zone presents higher deformation, as a frontal crash was simulated.

Another zone of high displacement is found on the top cover, but now on the opposite end of the structure. Although a frontal impact was simulated, this second peak of vertical deflection in the back of the structure can be interpreted as resulting from the fact that the "impact forces" were absorbed and distributed throughout the structure, as explained before. Thus, there is a transfer of energy towards the rear of the structure, leading to this redistribution of loads which, in turn, causes a greater vertical deflection in that region.

Lastly, it is noteworthy to reflect on the fact that subjecting the BPE model to an extremely high peak (des)acceleration of 50 G-forces corresponds to a worst-case scenario. In fact, it seems unlikely that a BPE will be impacted to this extent in the event of a frontal impact, as an EV is provided with a deformation zone in its frontal region for that energy absorption purposes. In spite of the severity of the peak desacceleration introduced in the model, the maximum total deflection observed on the BPE model is merely 0.061 mm, of course, deemed negligible. Recall that the structure is rigid and extremely well fixated, owing to the boundary conditions introduced, which justify the aforesaid finding.

By gaining a more detailed understanding of the total deformation that occurs at the component level, this is illustrated in Figure 8.9. Note that an arbitrary rocker panel can be evaluated for the analysis where the assessed quantities present a symmetric distribution. This is the case now; however, in the explicit analyses, the most pertinent rocker panel for evaluation at the component level is, evidently, the one that is impacted.

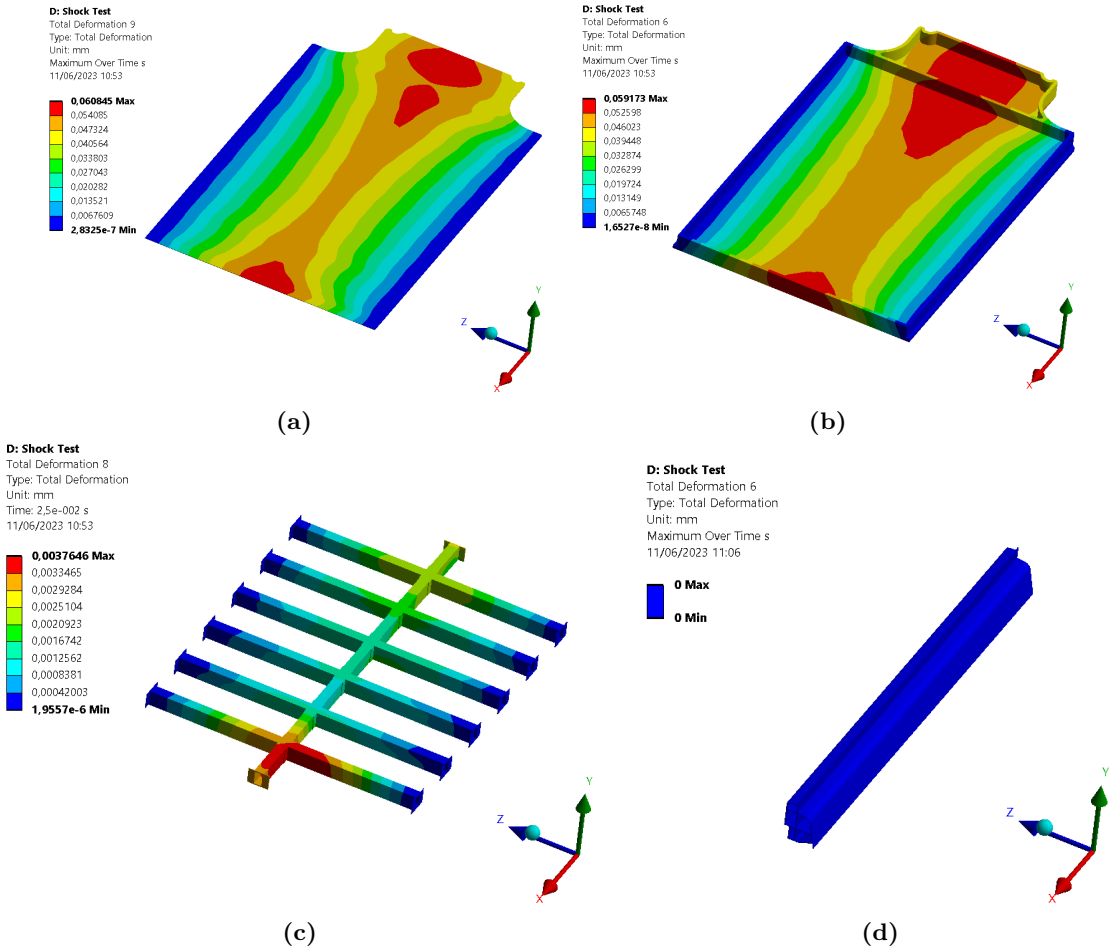


Figure 8.9: Transient analysis of Phase 1: total deformation distribution at the component level (true scale). **(a)** Bottom case **(b)** Top cover. **(c)** Reinforcements. **(d)** Rocker panel.

As verified, now on an individual scale, the maximum deformations to the structure subject occur in the top cover. This can be explained by the fact that this component is characterised by a thickness of 3 mm, an extremely small value compared to the same quantity in the other components of the BPE.

The bottom case endures a similar deformation to the top cover of 0.059 mm. This can be justified by the fact that, as was discussed in Chapter 5, it is fulfilling its purpose as the main structural component of the BPE. Moreover, it was validated that the rocker panels endure no total deformation, and the reinforcements present an even smaller value of maximum deformation compared to those of the top cover and bottom case.

As could be concluded from Figure 8.8, the most relevant component of deformation is on the y direction. Therefore, for completeness purposes, the distribution of this directional deformation is illustrated in Figure 8.10, both for the whole structure and for each individual component. No scaling was applied in this case since the behaviour of the structure was already assessed.

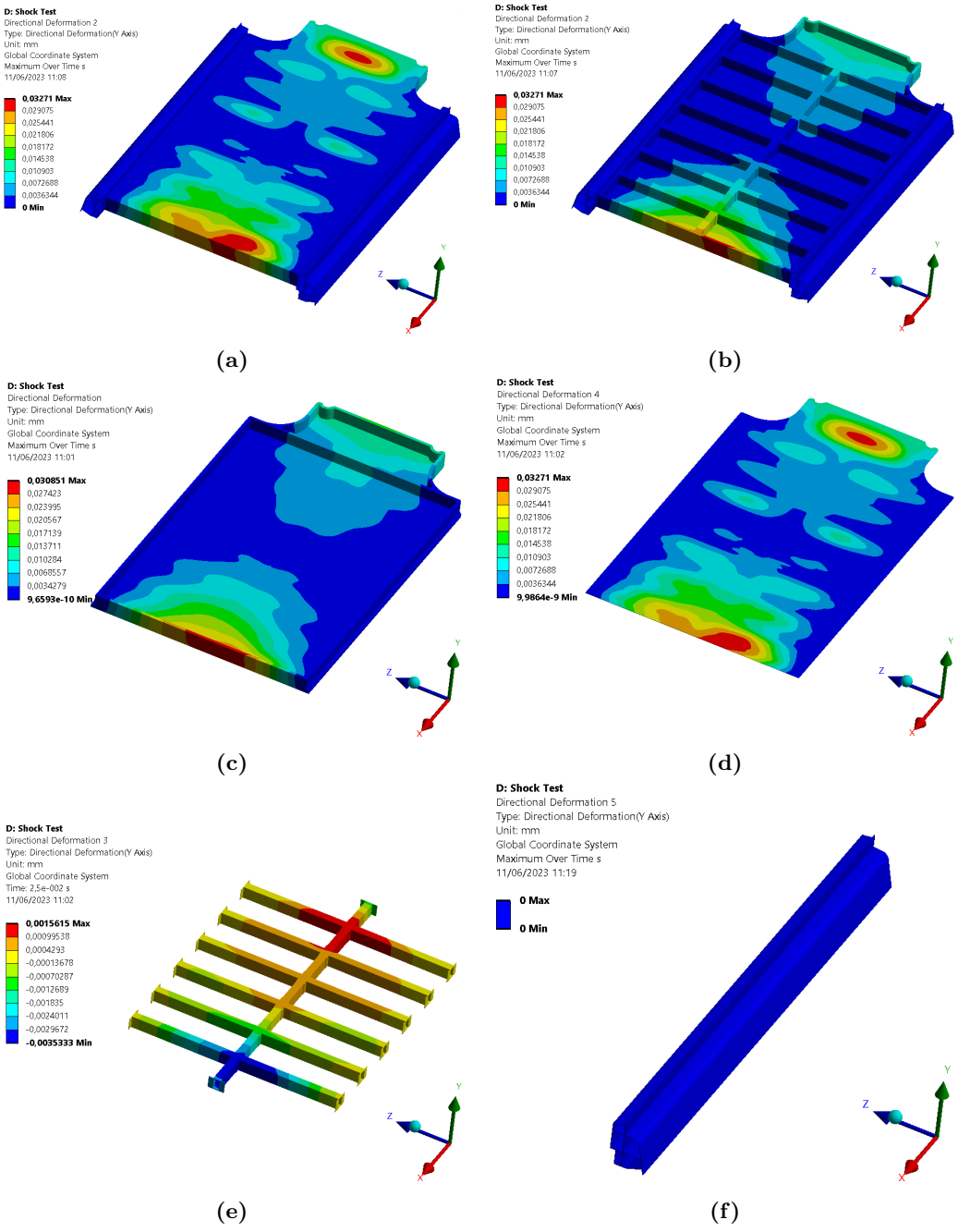


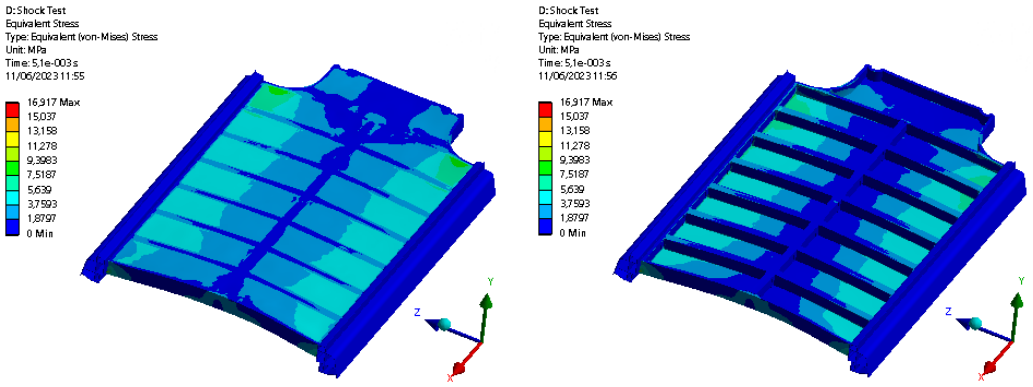
Figure 8.10: Transient analysis of Phase 1: directional deformation distribution in y, at the global and component levels (true scale). **(a)** BPE with cover. **(b)** BPE without cover. **(c)** Bottom case. **(d)** Top cover. **(e)** Reinforcements. **(f)** Rocker panel.

As can be concluded, the highest value of deformation the structure endures in y is about 0.033 mm in the top cover, closely followed by a similar value in the bottom case. The reinforcements, as expected, suffer little to no deflection, and the rocker panels are undeformed. This is consistent with what was already discussed above for the total deformation.

Note that the maximum deflection in y of the BPE also occurs not only in its frontal region but also on the rear. This is related, once more, to the energy distribution throughout the BPE.

8.3.2 Equivalent von Mises Stress

Regarding the equivalent von Mises stress, the overview of the distribution of this quantity in the structure is presented in Figure 8.11, at its instant of the maximum value for this quantity. Once more, a scaling factor of 1000 was applied.



(a) **(b)**

Figure 8.11: Transient analysis of Phase 1: equivalent von Mises stress distribution in the BPE and rocker panels (scale of 1000). **(a)** BPE with cover. **(b)** BPE without cover.

The stress is distributed symmetrically in the structure, with the greatest values of stress occurring in the contact zones of the BPE and rocker panels, towards the corner of the model. The internal zone of the BPE is apparently unstressed.

The maximum value of stress within the structure is approximately 16.9 MPa, considered significantly small. As occurred for the static analysis, this maximum value resulted from stress concentrations in the corner regions where the rocker panels meet the battery pack housing. Therefore, once again, it is possible to state that this gradient originates from the stiff boundary conditions applied in the model and, perhaps, from a mesh more coarse than it should be for this particular zone. Therefore, this stress peak has no real meaning and can be disregarded in the rest of the discussion.

In Figure 8.12, the distribution of equivalent von Misses stress is presented for each component of the model to further investigate the stress distribution in the BPE.

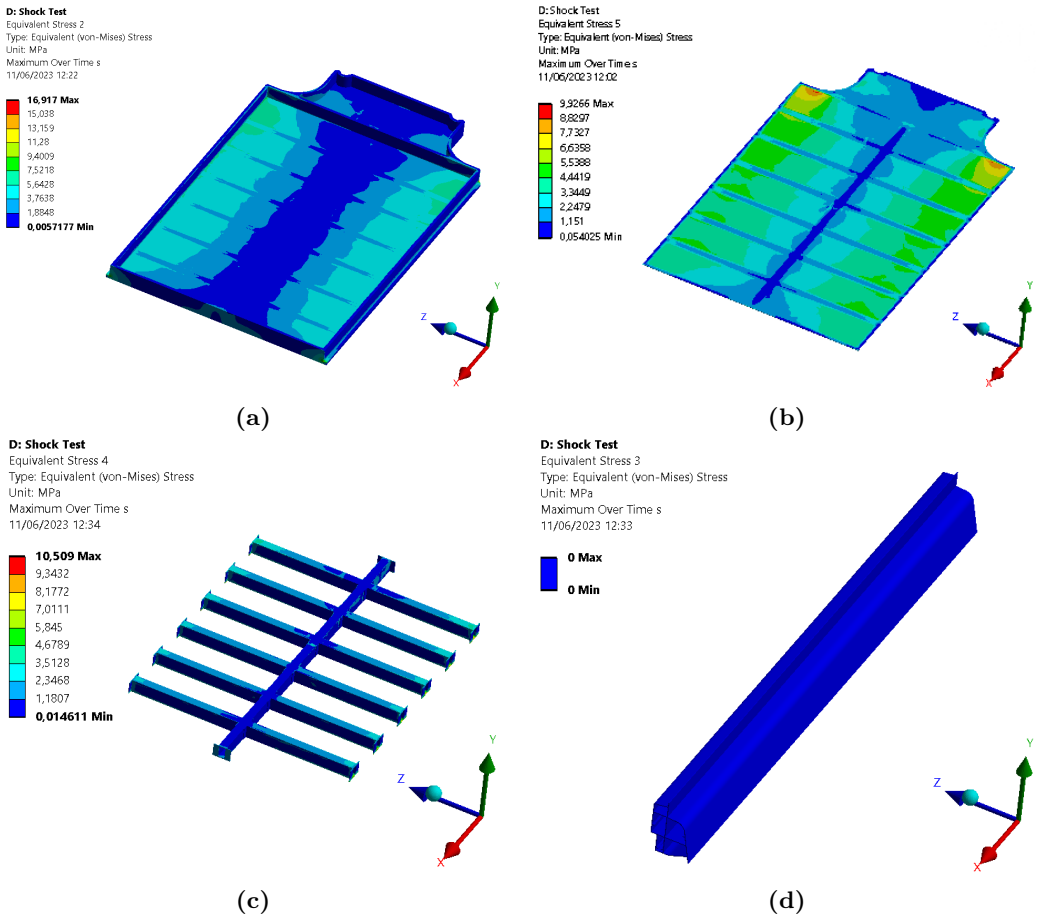


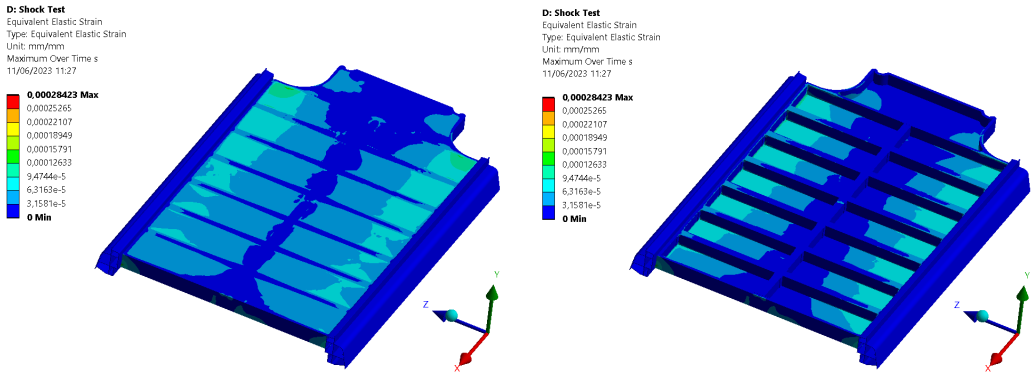
Figure 8.12: Transient analysis of Phase 1: equivalent von Mises stress at the component level (true scale). **(a)** Bottom case **(b)** Top cover. **(c)** Reinforcements. **(d)** Rocker panel.

It is now possible to identify the bottom case as the BPE component that endures the most stress, as expected for the principal structural member of the battery housing. On the contrary, it is possible to state that the rocker panels present a null value of stress, which is explained by the applied boundary conditions that aim to present the real behaviour of the structure. As was seen, for the Euro NCAP crash test that served as inspiration for this simulation, the rocker panels were found to maintain their overall structural integrity.

The maximum values of stress in the reinforcements also originate from numerical considerations and can, therefore, be disregarded.

8.3.3 Equivalent von Mises Strain

For completeness purposes, the equivalent von Mises strain was also examined. The plastic strain, on the opposite, will not be addressed since it is nonexistent in the model. The distribution of this quantity in the BPE can be consulted in Figure 8.13 without the employment of any scaling factor.



(a) **(b)**

Figure 8.13: Transient analysis of Phase 1: equivalent von Mises strain distribution in the BPE and rocker panels (true scale). **(a)** BPE with cover. **(b)** BPE without cover.

The maximum value of elastic strain yielded from the simulation's results is 0.00028, an extremely reduced value that can be interpreted as insignificant.

As can be concluded, the strain distribution in the structure is identical to the stress distribution. Once more, it can also be considered that the maximum value of strain value emerges from the addressed numerical considerations. Thus, the structure presents values of strain that can, evidently, be disregarded, and no further analysis of this quantity is justified.

In summation, no potentially problematic zones were found in the BPE under this analysis' conditions. It can then be stated that for a severe frontal impact, the modelled BPE structure presents no significant deformations, stresses, or strains. Hence, the structure ensures the health of the battery components, and it is possible to validate the model for this Euro NCAP-inspired crash event. Evidently, if the same conclusion is reached in the following explicit simulations, the geometry, materials, and input analysis settings in the model were correctly selected and employed; after all, a behaviour consistent with what is expected from the industry solution that inspired this model was achieved.

8.4 Phase 1: Explicit Dynamics Analysis

As defined in Chapter 6, the purpose of the explicit dynamics analyses to be conducted is to simulate a side-impact event to a BEV and investigate the resulting damage to the BPE. These will be performed for two distinct velocities applied in the automotive assembly to provide a deeper understanding of the behaviour of the structure.

Regarding the analysis settings associated with this analysis type, it is important to note that the mesh applied for each of the explicit analyses of each Phase is equal, as a way for it not to constitute a potential influencing factor to the obtained results. Furthermore, the mesh utilised for the explicit simulations resulted from similar inputs to those of the static analysis, such as the employment of the same sizing and method. However, some fundamental mesh parameters, such as the Physics Preference and Element Order, are altered due to intrinsic differences in the analysis formulations. Once again in their default definitions, these settings were now "explicit" and "linear". This physical preference represents the most suitable option for the given analysis, enabling the obtainment of a mesh composed exclusively of corner-noded elements characterised by smooth transitions and high smoothing, as desired [80].

These intrinsic differences lead to differences in the order of the elements used and the

values obtained for the mesh quality indicators. Given the Physics Preference used in this analysis, the model was meshed using Tet4, Hex8, and Wed6 elements, i.e., linear elements. Statistically, 123928 nodes and 171583 elements were used to discretise the BPE structure.

For the current analysis type, as explained in Chapter 6, the element quality, aspect ratio, and, most importantly, the characteristic length is used to investigate the quality of the mesh. The values obtained for each of these metrics are presented in Table 8.4.

Table 8.4: Phase 1: Explicit analysis mesh metrics

	Element Quality	**Aspect Ratio**	**Characteristic Length [mm]**
Minimum	$8.8008e-2$	1.0115	0.9609
Maximum	0.99989	62.017	23.666
Average	0.61285	2.7601	8.4498
Standard Deviation	0.21029	1.3773	5.9631

Overall, the consulted metrics yielded satisfactory values of mesh quality. The minimum characteristic length of an element that dictates the time step, according to the CFL stability condition and, consequently, the global simulation time, is of around 1 mm. In addition, an average element quality of 0.61 and an average aspect ratio of 2.76, suitable for the current analysis, were achieved.

The meshed model was then validated and was ready to be solved explicitly under 32 km/h and 100 km/h.

8.4.1 Side Impact at 32 km/h

The explicit simulation for which a constant velocity of 32 km/h (8.889 m/s) was assigned to the model, in the z direction, ran for 236 minutes, approximately 4 hours, utilising the Autodyn solver within Ansys®. This time length was expected and is acceptable for this analysis type and for this relatively complex geometry. Were a more complex geometry employed in this case, it is likely that the simulation would need an increased total elapsed run time to be solved.

The obtained solution will be evaluated with regard to a different number of parameters, such as the equivalent von Misses stress and strain, total and directional deformations, and total energy of the system.

The starting point for the discussion of results is the consultation of the energy summary of the simulation provided by the program. This plot provides immensely relevant information for a given explicit analysis. For the impact event being simulated, it is not only possible to retrieve the constant value of the total energy of the system (during the extremely reduced time interval that captures the impact instant and some post-crash behaviour) but also to visualise the energy conversion from kinetic to internal, that takes place when the contact of the two impacted surfaces is established. Furthermore, suppose the energy graph does not correspond to the anticipated one. In that case, it is possible to identify the potential occurrence of errors during the simulation's run time that has affected the problem's physics. In addition, the energy summary plot can be utilised to evaluate if excessive mass scaling was employed for the given problem and to conclude if the hourglass energy exceeded the limits of expert knowledge.

The plot of the retrieved energy summary is portrayed in Figure 8.14.

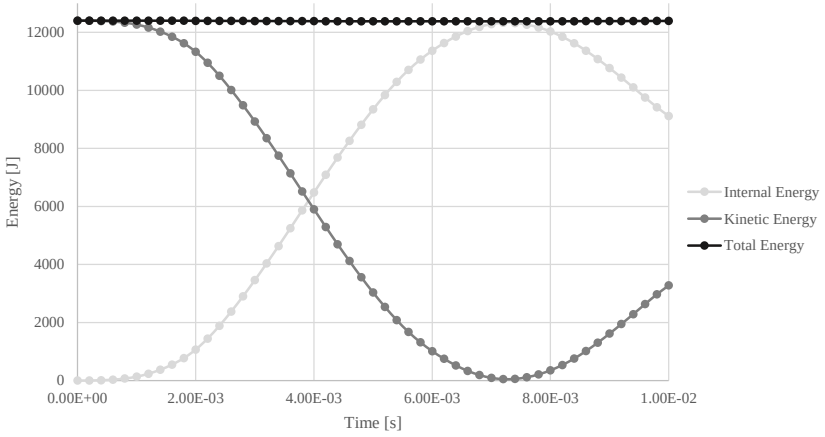


Figure 8.14: Explicit analysis of Phase 1, at 32 km/h: energy summary.

The presented graph corresponds to what was expected from the energy summary of the impact event being simulated. As can be observed, at the instant $t = 0$ s, the plot starts with all the energy quantities at their minimum value, except for the kinetic energy, at its maximum value. This is consistent with reality since, at that moment, the automotive assembly is simply moving towards the pole, and no impact has occurred yet. Right after this moment, the impact of the two bodies has occurred, which is evidenced by the initialisation of the conversion of kinetic energy to strain energy, termed internal energy in Ansys®.

At the instant $t = 7.4$ ms, the maximum contact between the two bodies is established. As such, the kinetic energy reaches its minimum magnitude while the system's internal energy presents a peak of its absolute value.

The total energy of the system is, for this particular analysis, about $1.2402e4$ J and is maintained throughout the assessed time interval. It can, thus, be concluded that the law of energy conservation is verified in the system for the aforesaid time range. This corresponds to what is expected in a correctly set-up explicit dynamics analysis [141].

Notwithstanding, something that must be reflected is that the solution's end time was set as 0.1 s, and therefore, only an extremely small time interval is being evaluated (to safeguard also the computational efficiency of the simulation). Although a real crash event is characterised by energy dissipation to the outside (by heat caused by friction, for instance), assuming that in these analyses, the total energy of the system remains constant and, therefore, this phenomenon has not taken place yet in a significant manner can be considered correct. Only the very initial moment of impact is being assessed.

From the time step where the maximum compression of the rocker panel takes place, the BPE starts to "bounce back" from the pole, causing the kinetic energy to increase and the internal energy to do the opposite. In fact, the peaks of both energy types start to stabilise until the equilibrium of the system is reached, something that evidently is not achieved in this small time range.

It is worth mentioning that the order of magnitude of the total energy itself is consistent with what was anticipated, considering the values found in identical works to this one, dealing with similar velocities.

8.4.1.1 Total and Directional Deformations

The pole, which was simulated as a rigid body, does not play a significant role in assessing the damage. Therefore, it will be excluded from the majority of the illustrations depicting the results obtained from the explicit analyses.

Prior to the consultation of the deformation distribution occurring on the structure as a result of the side impact, it is relevant to provide the reader with means to understand the structure's dynamic behaviour to the side impact. Hence, in Figures 8.15 and 8.16, some frames that capture the evolution of the structure's deformation are presented: the first capturing an above overview of the structure, and the second provided to visualise the deflection of the structure in the y direction. These frames will be provided for all of the explicit dynamic analyses performed during this work to assess how each model's assigned materials and geometry influence its crash behaviour. In addition, within the same Phase, these will also be utilised to analyse how the speed of the BEV influences the extent of observed damage to the BPE. A scale factor of 2 will be constantly employed to provide a more direct and meaningful comparison between all the explored cases. The colour map resulting from the program's scale for each of the time instants can, however, be disregarded, as it is relative to the magnitude of the quantity only at that specific instant.

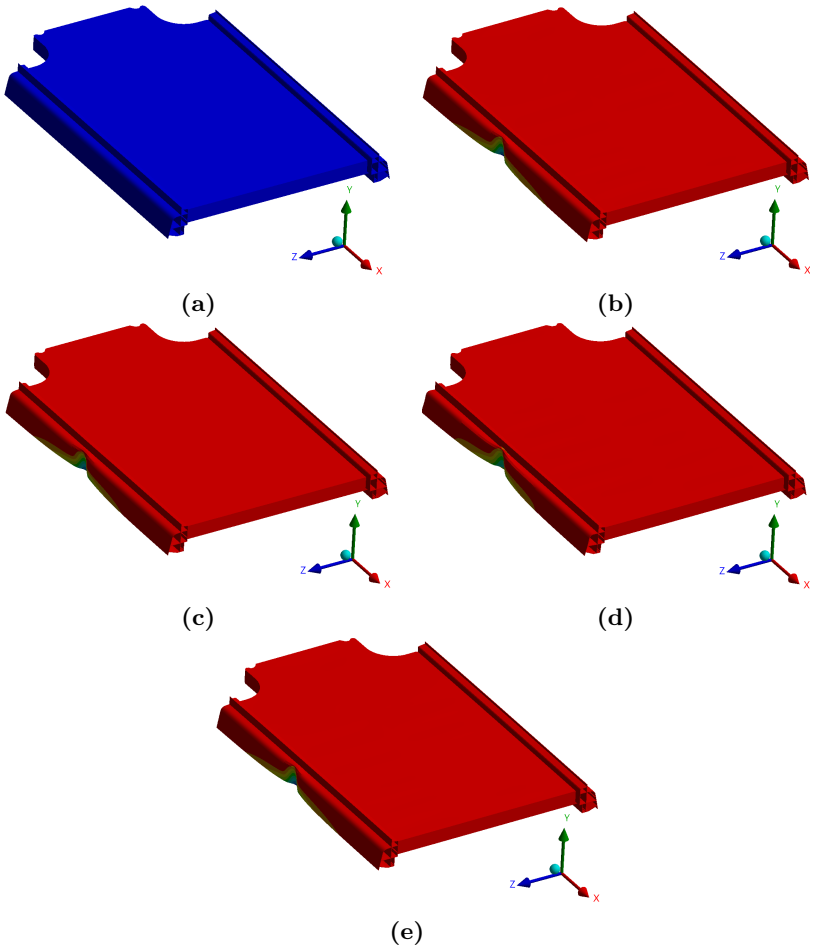


Figure 8.15: Explicit dynamic analysis of Phase 1, at 32 km/h: an overview of the deformation of the BPE in time frames (scale of 2). **(a)** $t = 0$ s. **(b)** $t = 2.5e-3$ s. **(c)** $t = 5e-3$ s. **(d)** $t = 7.5e-3$ s. **(e)** $t = 1e-2$ s.

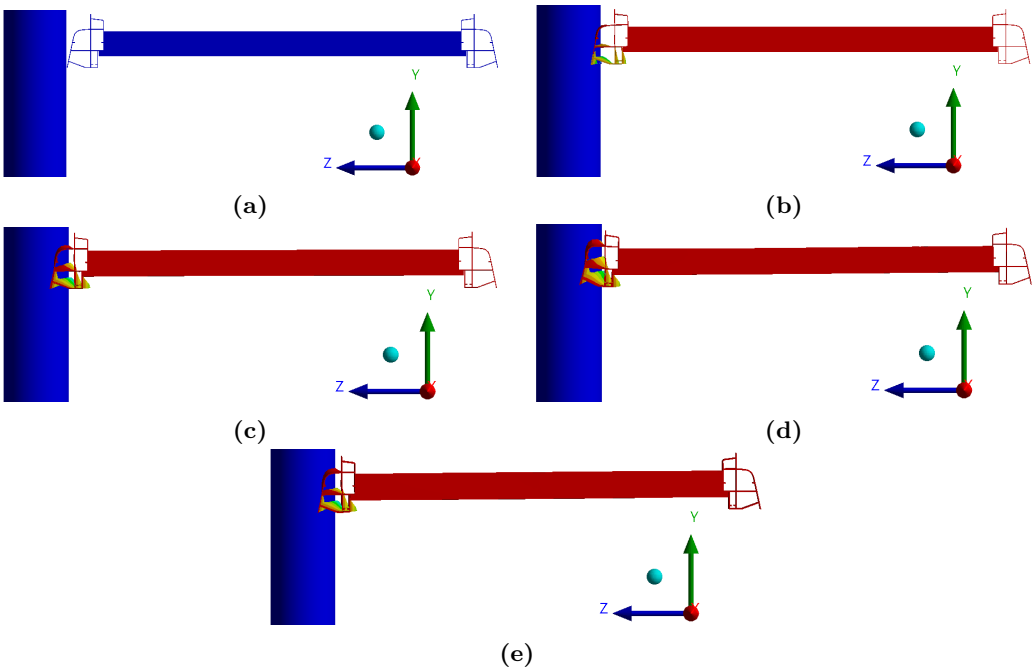
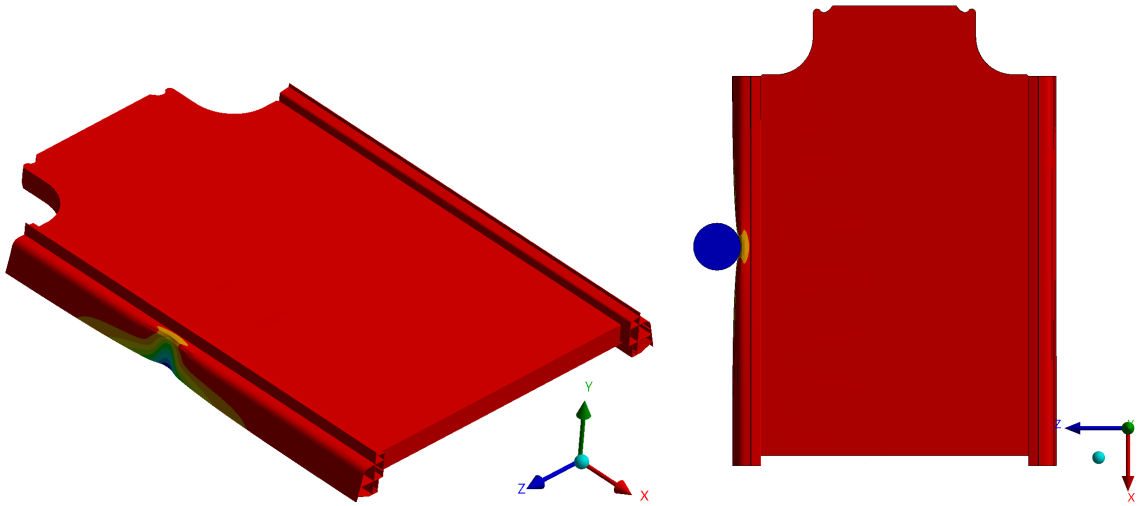


Figure 8.16: Explicit dynamic analysis of Phase 1, at 32 km/h: a frontal view of the deformation of the BPE, in the $z-y$ plane, in time frames (scale of 2). **(a)** $t = 0$ s. **(b)** $t = 2.5e-3$ s. **(c)** $t = 5e-3$ s. **(d)** $t = 7.5e-3$ s. **(e)** $t = 1e-2$ s.

In the presented Figures, it is possible to visualise the structure without any deformation, prior to impact, in frame 1. The contact between the pole and the rocker panel starts close to the instant $t = 2.5e-3$ s since some intrusion to the automotive component can already be observed. This deformation increases in the following time stamps, and the structure's small "bounce back" can already be observed in the last frame.

The deformation of the BPE in the y axis is practically nonexistent to the naked eye in the presented scale, aside from capturing a small upwards bending. The almost imperceptible deformation in y is likely due to the stiffness and lack of flexibility of the Al 6061-T6, assigned to the whole structure. In the posterior Phases of this work, this behaviour will be compared to the ones of the optimised BPEs models, where distinct, less rigid materials were employed.

To provide an insight into the real intrusion and deflections found in the model, both of these are represented in Figure 8.17, where the deformation of the structure in z can also be qualitatively assessed, in true scale, in relation to the initial position and configuration of the BPE represented by the wireframe. Noticeably, these deflections are minimal for the given velocity impact.



(a) **(b)**

Figure 8.17: Explicit dynamics analysis of Phase 1, at 32 km/h: the intrusion of the pole into the automotive structure (true scale). **(a)** Global view. **(b)** Deformation in the z direction.

Regarding the total deformations originating in the structure, its distribution in the BPE is represented in Figure 8.18 for its maximum value over time, globally and for each component.

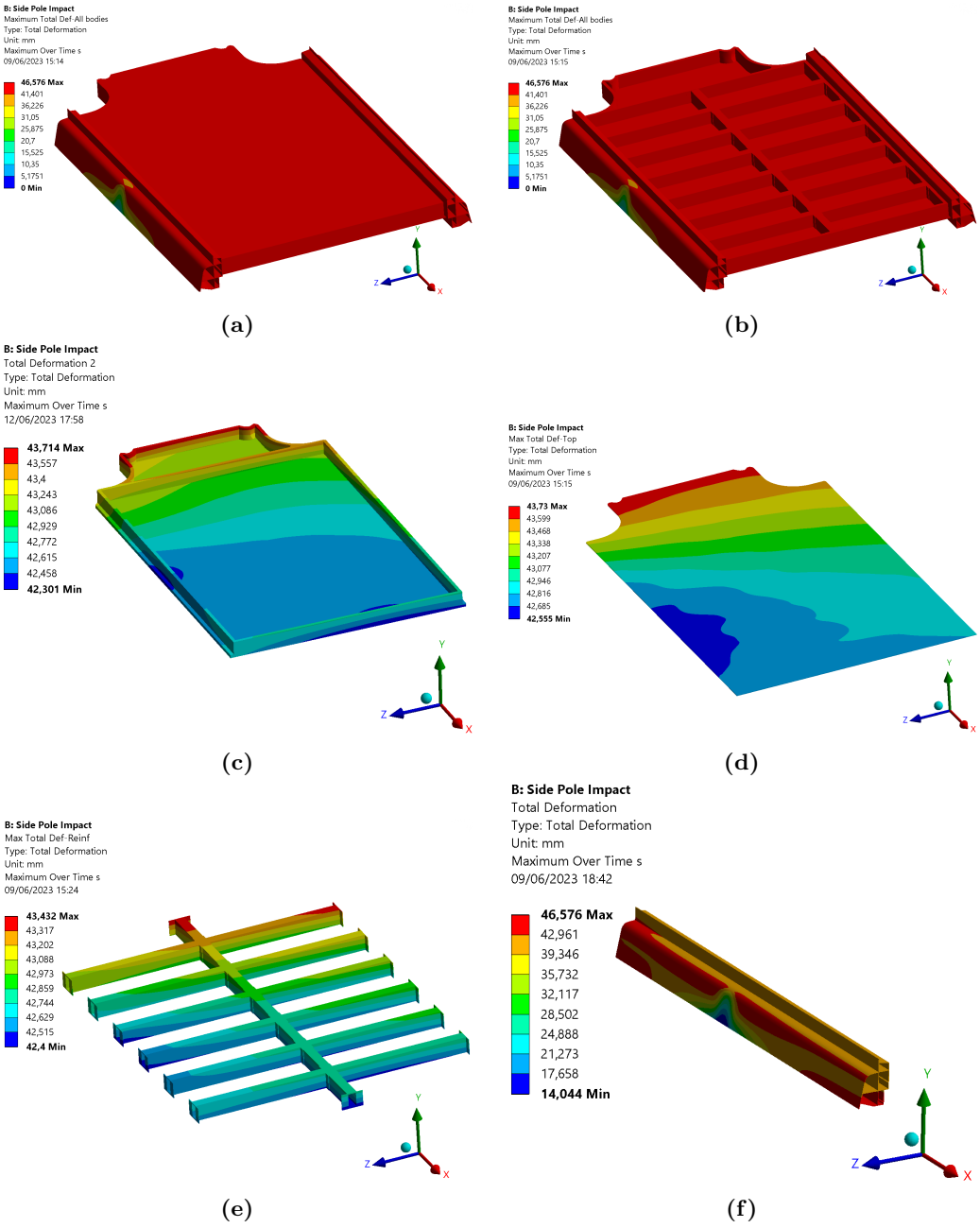


Figure 8.18: Explicit dynamics analysis of Phase 1, at 32 km/h: total deformation distribution at global and component levels (true scale). **(a)** BPE with top cover. **(b)** BPE without top cover. **(c)** Bottom case. **(d)** Top cover. **(e)** Reinforcements. **(f)** Rocker panel.

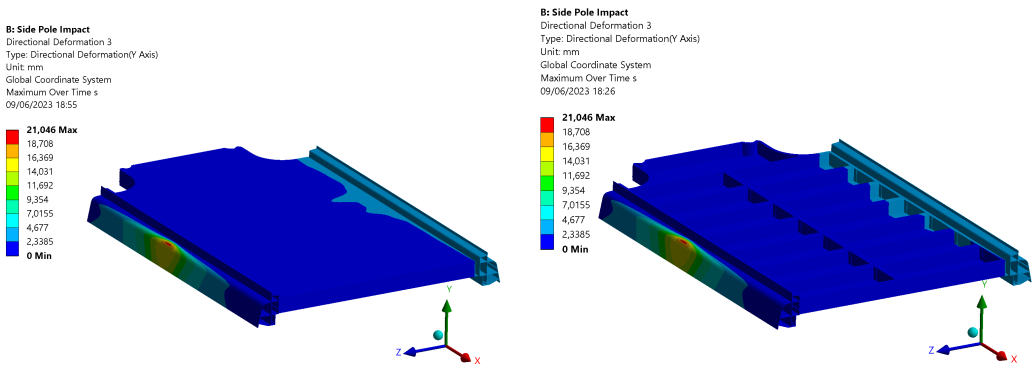
The program yielded a maximum deformation value of approximately 47 mm in the automotive assembly, in the zone of impact of the rocker panel and the pole, as anticipated. Evidently, if the impact took place at a different point of the BPE model, the zone characterised by the highest deflections would change its location accordingly.

In a first look at the problem, this deformation magnitude could potentially discredit this structure for application in a BEV. Thus, it is extremely relevant to note that this value accounts for the rigid body motion of the BPE and rocker panel assembly towards and outwards the pole in the z axis. If this translation were to be excluded, the deformations

would be much smaller in x. Therefore, while the assessment of the total deformation in the structure contributes to a qualitative interpretation of the distribution of this quantity, the quantitative values must be carefully evaluated.

The directional deformation in y will be evaluated for all the conducted explicit dynamic analyses, as it provides more precise information regarding the behaviour of the structure, particularly that related to bending. The directional deformation in x is less significant for this particular problem, so it will not be assessed.

Figure 8.19 displays the directional deformations on the structure on the y direction for the entire structure.



(a) **(b)**

Figure 8.19: Explicit dynamics analysis of Phase 1, at 32 km/h: directional deformation distribution in the y direction at a global level (true scale). **(a)** BPE with top cover. **(b)** BPE without top cover.

From the Figure above, it can be concluded that the zone of maximum deformation of the assembly in the y direction is present in the rocker panels in the immediate zone of impact. The magnitude of this deformation is about 21 mm.

A second peak of this directional deformation occurs at the opposite extremity of the structure, which is consistent with the "bending" presented in Figure 8.16 and with what was expected from a structure suffering an impact. As explained earlier, the location of the second zone of highest deformation in the structure is most likely justified by the energy transfer within the structure when the impact occurs and the associated load propagation. Moreover, evidently, the material properties of the structure themselves, such as the stiffness of the aluminium, contribute to the profile of deformations found in the structure. It can, thus, be concluded that these deformations result from the complex interaction between the impact forces and the capacity of deformation of the structure, defined significantly by its material properties, in addition to the intrinsic dynamic response of the body.

The distribution of the aforementioned deformation component is illustrated again in Figure 8.20, now regarding the individual parts of the automotive assembly.

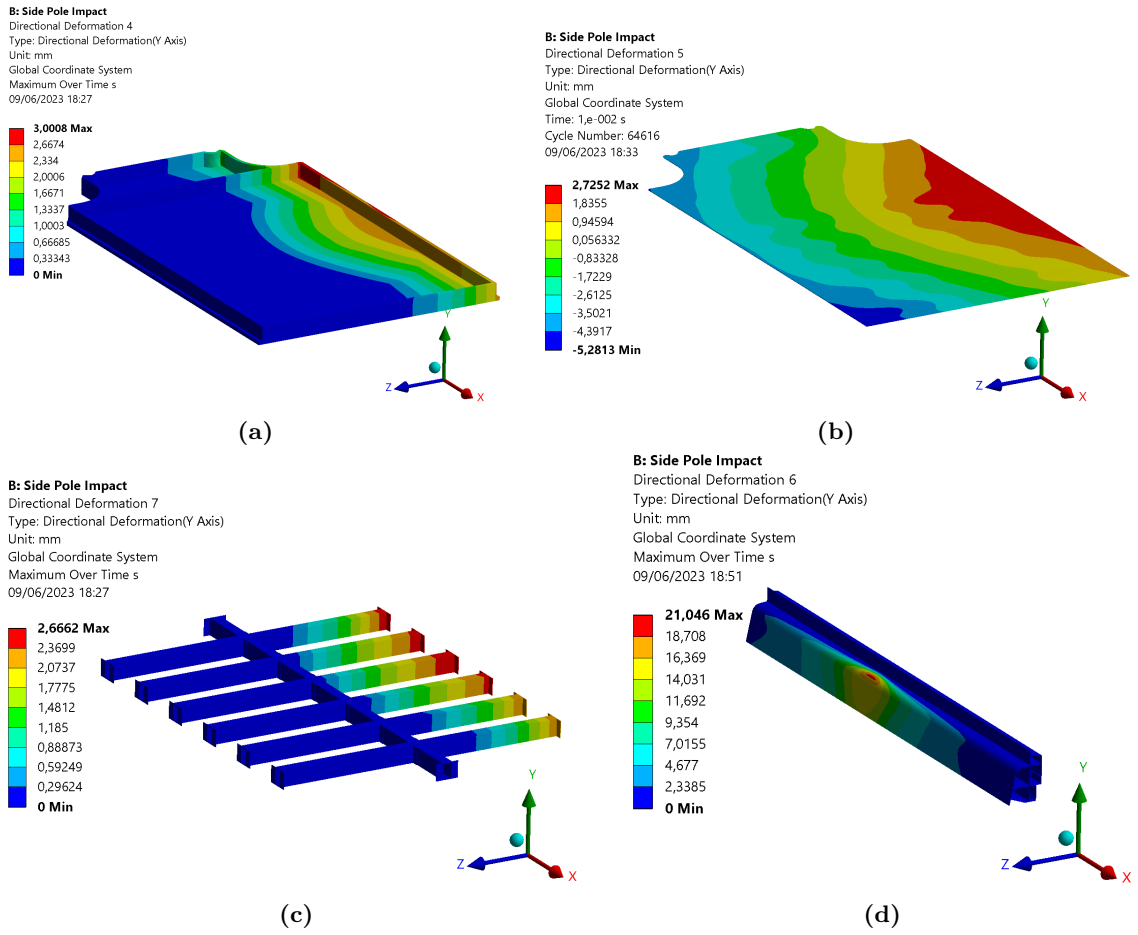


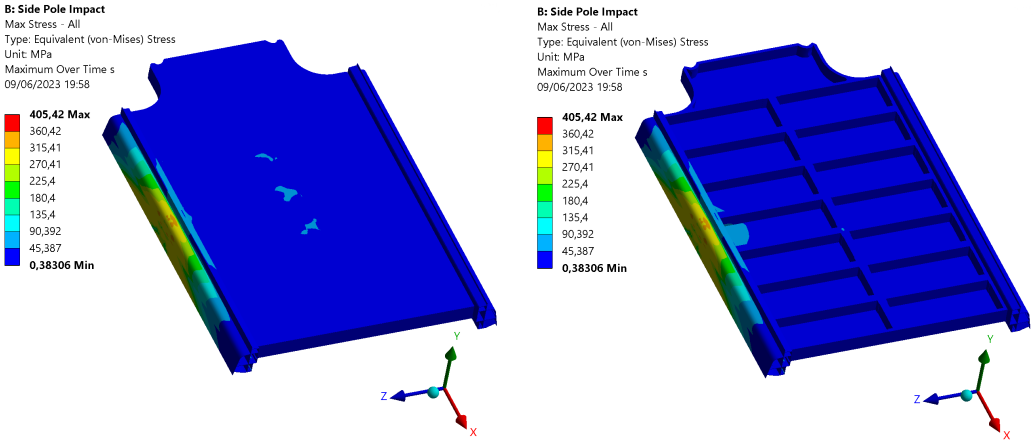
Figure 8.20: Explicit dynamics analysis of Phase 1, at 32 km/h: directional deformation distribution in the y direction at the component level (true scale). **(a)** Bottom case. **(b)** Top cover. **(c)** Reinforcements. **(d)** Rocker panel.

This Figure provides a deeper insight into the deformations of the structure. As can be concluded, from the point of view of the Figures above, the left side of the BPE suffers no deformation in y, with the exception only on the top cover, likely due to its smaller thickness. On the contrary, the right side of the structure presents the zone with the highest deformation within the BPE. The most deformed component of the BPE is the bottom case, presenting a deformation of 3 mm on the right side of the structure. This is correct, given the slight upwards deflection of the BPE, found for the most part on the opposite side to that being impacted.

While there is no information regarding the maximum deformation a BPE can endure without putting the well-being of the battery modules and cells at risk, the highest value of deformation presented by the BPE in y is insignificant. As such, exclusively from the assessment of this quantity, the zone where the above-mentioned deformations are found does not constitute a problematic region in the structure for the Euro NCAP-inspired side impact.

8.4.1.2 Equivalent von Mises Stress

Another quantity to be evaluated in the structure is, once again, the von Mises stress. The global-level distribution of this physical quantity can be consulted in Figure 8.21.



(a) **(b)**

Figure 8.21: Explicit dynamics analysis of Phase 1, at 32 km/h: equivalent von Mises stress (true scale). **(a)** BPE with top cover. **(b)** BPE without top cover.

As anticipated, the most stressed component of the BPE and rocker panels assembly is, without a doubt, the rocker panel being impacted. The most stressed region is where the panel and the pole meet during the impact. A maximum value of 406 MPa is obtained in this region.

Outside of the vicinity of the impact zone, however, the magnitude of the stresses descends rapidly, presenting, for instance, a value of 0.4 MPa in the opposite rocker panel, devoid of impact.

From a global perspective, very little stress propagation can be observed from the rocker panel to the BPE and within the battery housing components themselves. In Figure 8.22, the equivalent von Mises stress distribution is provided at an individual level for each relevant component to gather a deeper understanding of the stress distribution within each component and how it is transmitted across the automotive assembly.

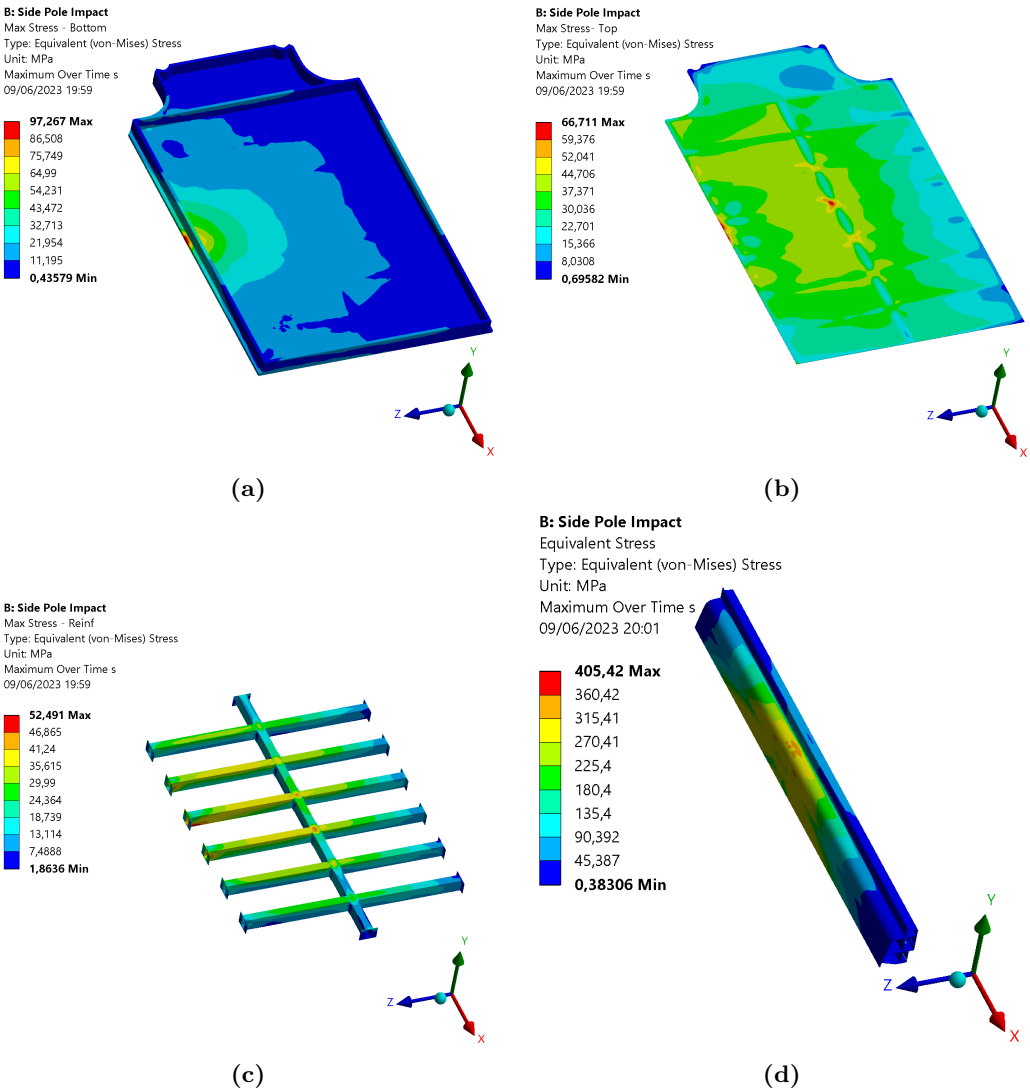


Figure 8.22: Explicit dynamics analysis of Phase 1, at 32 km/h: equivalent von Mises stress (true scale). **(a)** Bottom case. **(b)** Top cover. **(c)** Reinforcements. **(d)** Rocker panel that endures the impact.

At the component level, it is possible to observe the stress propagation in the structure in greater detail. From the Figure above, an almost symmetry about the z axis, crossing the region of the impact, can be observed in every component. Recall that this results from the position of the pole with regard to that of the car. This would not be observed if the pole were localised near one of the ends of the rocker panels.

The bottom case is identified as the most stressed component of the BPE, with a maximum stress value of 98 MPa in the proximity of the impact region. This makes sense since it is the principal structural member of the BPE. Furthermore, in the load path characteristic of the automotive structure, the impact loads are transferred from the vehicle's integral component to the BPE bottom case. From there, they are dissipated to the internal reinforcements and top cover, which justifies their smaller values of stress. The previously discussed load propagation, resulting from the energy of the impact being transferred throughout the structure, is now easily visible within each component.

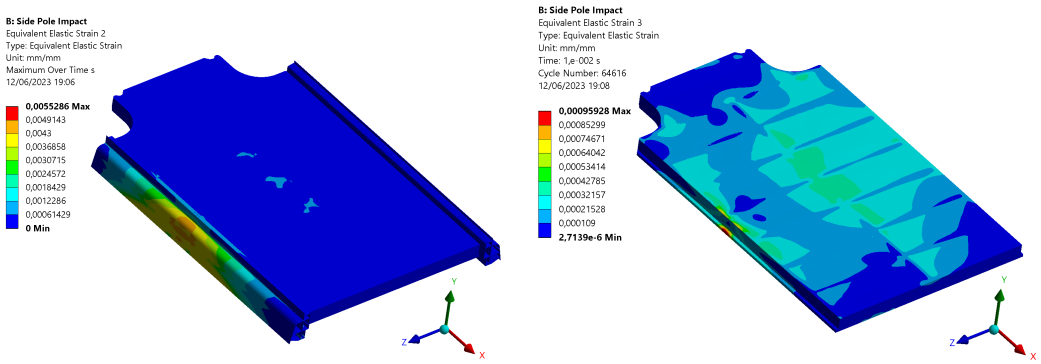
In summation, most of the stresses arising from the impact event are absorbed by the

rocker panels, components of the vehicle's body structure, and much smaller values are transferred to the BPE. This is consistent with what occurs in real-life side-crash scenarios.

8.4.1.3 Equivalent Elastic Strain and Equivalent Plastic Strain

Lastly, it is interesting to assess both the elastic and plastic strains originating in the structure due to the side-impact event.

Starting from the evaluation of the equivalent von Mises strain, its distribution in the automotive assembly and, then, exclusively on the BPE components is presented in Figure 8.23.

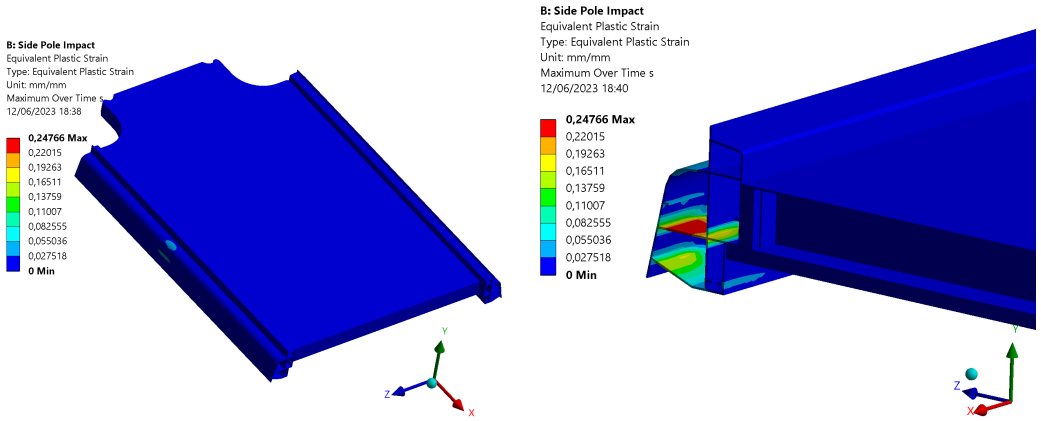


(a) **(b)**

Figure 8.23: Explicit dynamics analysis of Phase 1, at 32 km/h: equivalent von Mises strain (true scale). **(a)** Rocker panels and BPE. **(b)** Exclusively the BPE structure.

Understandably, it is possible to conclude that most of the elastic strain occurs in the impacted rocker panel component, with a maximum value of 0.005. Smaller values of strain can then be observed in the BPE structure itself, particularly in the neighbouring zones to the impact region, with a maximum value of 0.0009. These represent, of course, extremely low values of this physical quantity

Regarding the equivalent plastic strain, the permanent deformation occurring on the structure is illustrated in Figure 8.24, first for the whole assembly model and then for the cross-section where the maximum value of this quantity can be found.



(a) **(b)**

Figure 8.24: Explicit dynamics analysis of Phase 1, at 32 km/h: plastic strain (true scale). **(a)** Rocker panels and BPE. **(b)** Rocker panel cross-section.

From the Figure above, it can be concluded that the plastic strain is much more localised than the elastic strain. In fact, the highest value of strain, 0.24766, is found in the immediate impact region of the rocker panel.

Contrary to what was done for the equivalent elastic strain, the distribution of this quantity was not also presented exclusively for the BPE components. This was done purposefully since the BPE structure does not present yielding at any point. Since plastic strains entail the permanent deformation that occurs in a structure or material when subjected to high stress or impact loads, it is extremely satisfactory that this is not observed in the BPE structure.

Based on this analysis, it is possible to validate the BPE structure to the simulated Euro NCAP side-impact test. This means that the design and material selection processes were performed correctly, and a model that is representative of the real industry solution was achieved. In fact, the model yielded the desired results across the various analyses it was subjected to.

Despite the fact that the main purpose of this Phase was already fulfilled by the validation of the model to one prominent crash test regulation, it was deemed interesting to go a little further and evaluate the behaviour of the model to an impact of 100 km/h, a speed higher than this one by a factor of 3. This analysis is addressed in this Phase's next and last subsection.

8.4.2 Side Impact at 100 km/h

This second explicit analysis is in almost everything identical to the first. The differing parameter between the two was simply the alteration of the value of constant velocity from 32 km/h to 100 km/h, i.e., 27.778 m/s, in the initial conditions. Then, the model was ready to be solved, and a solution resulted after 246 minutes, about four hours, which is identical to the preceding simulation.

Once more, the discussion of the results of the explicit analysis will initiate with the consultation of the energy summary plot of the system provided by the program. It is presented in Figure 8.25.

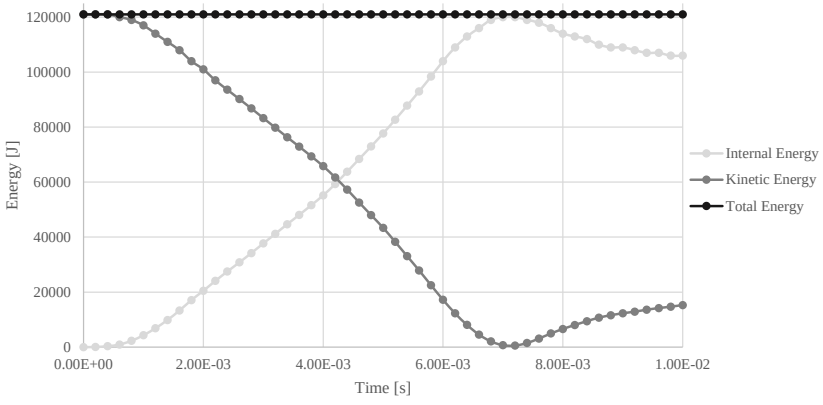


Figure 8.25: Explicit analysis of Phase 1, at 100 km/h: energy summary.

As anticipated, an identical plot to the one portrayed in Figure 8.14 of the explicit simulation at 32 km/h was obtained. As was already addressed, the obtained energy plot characterises the impact situation: firstly, when the impact initiates, the absorption of kinetic energy by the automotive assembly which is then converted into strain energy; then, the moment of maximum compression of the impacting bodies, where the two energy types

reach their minimum and maximum values, respectively; and, finally, then the opposite energy conversion takes place, evidencing the "bounce back" of the structure.

Through the observation of this plot, two relevant values can be extracted: the total energy of the system, of $1.2e5$ J, and the instant at which the maximum contact of the bodies is established, at $t = 7.2$ ms.

With respect to the value of the total energy of the system, it is now one order of magnitude higher than that of the previous explicit analysis. This difference in intensity can be directly related to the increase of velocity introduced in the BPE and rocker panels assembly. In fact, considering the initial kinetic energy of the system, which at that moment corresponds roughly to the total energy of the system, given that the mass associated with the BPE and rocker panels is the same in the two explicit analyses of this Phase, the only quantity influencing the kinetic energy of the translating component is its velocity. Thus, since the velocity is squared in the kinetic energy formula, this slightly more than triple improvement in the value of velocity entails an increase of kinetic energy, which now reaches a value approximately ten times higher than the one found in the previous explicit analysis.

Regarding the instant of maximum compression of the rocker panel experiencing impact, it can be stated that it is extremely similar to that of the explicit simulation conducted at 32 km/h. Given the fact that the impact took place first in this situation, as the assembly took less time to reach the pole, the identical value of this time parameter in both analyses indicates that for the impact at 100 km/h, more time was spent in the deformation of the structure.

Lastly, it is relevant to investigate the rate of energy conversion that characterises the "bounce back" phenomenon in the two explicit analyses of this Phase. It can be found that the slope that represents this velocity of conversion is much more pronounced in the preceding analysis than in this one. This can be explained by the fact that in the former analysis, much less kinetic energy was absorbed by the structure and converted into strain energy, which caused a more rapid "rebouncer". At 100 km/h, much more energy is absorbed by the rocker panels and posteriorly distributed to the BPE, which causes more extensive contact and, thus, deformation to the vehicle. This is translated into a slower energy conversion rate after the time step of $t = 7.2e - 3$ ms for the same analysis' end time.

8.4.2.1 Total and Directional Deformations

For the discussion of the relevant quantities in this analysis, similar illustrations with equivalent scaling factors to the previous one will be presented.

In Figures 8.26 and 8.27, representations of the structure's behaviour at five different time frames can be consulted. The first regards an overview from above of the entire structure. At the same timestamps, the latter focuses on the deflection of the structure in the y direction and facilitates the visualisation of the contact established between the pole and the rocker panel.

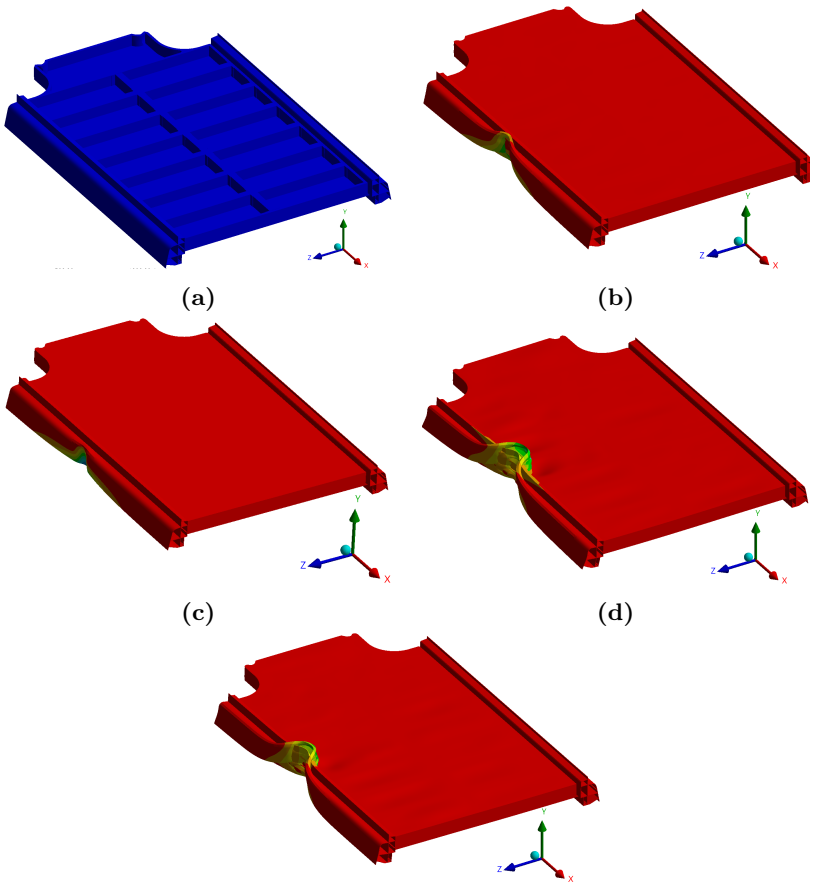


Figure 8.26: Explicit dynamic analysis of Phase 1, at 100 km/h: overview of the deformation of the BPE in time frames (scale of 2). **(a)** $t = 0$ s. **(b)** $t = 2.5e-3$ s. **(c)** $t = 5e-3$ s. **(d)** $t = 7.5e-3$ s. **(e)** $t = 1e-2$ s.

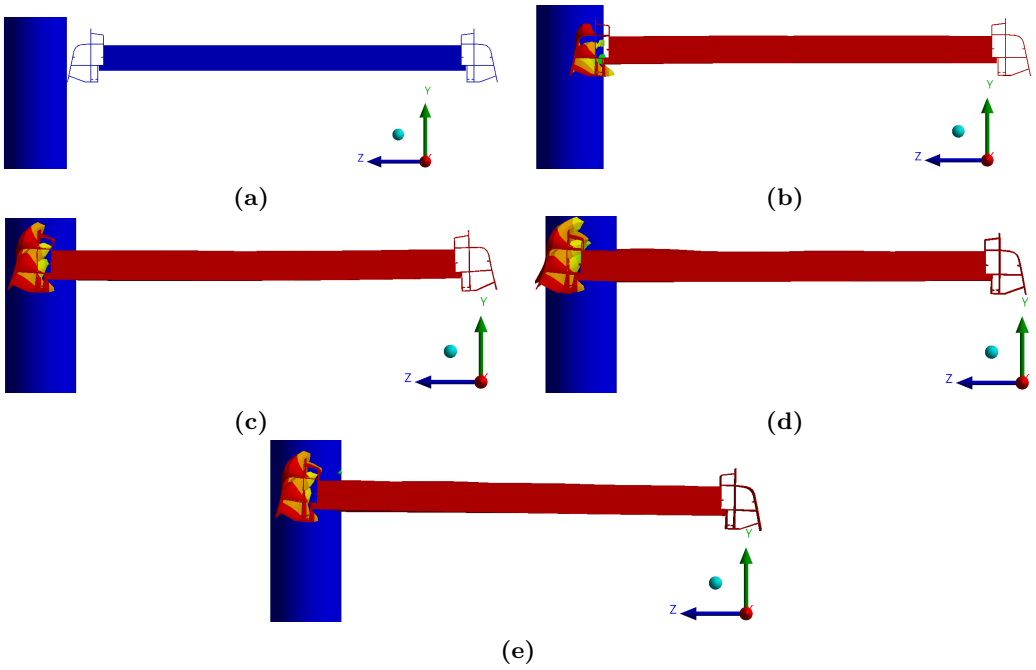
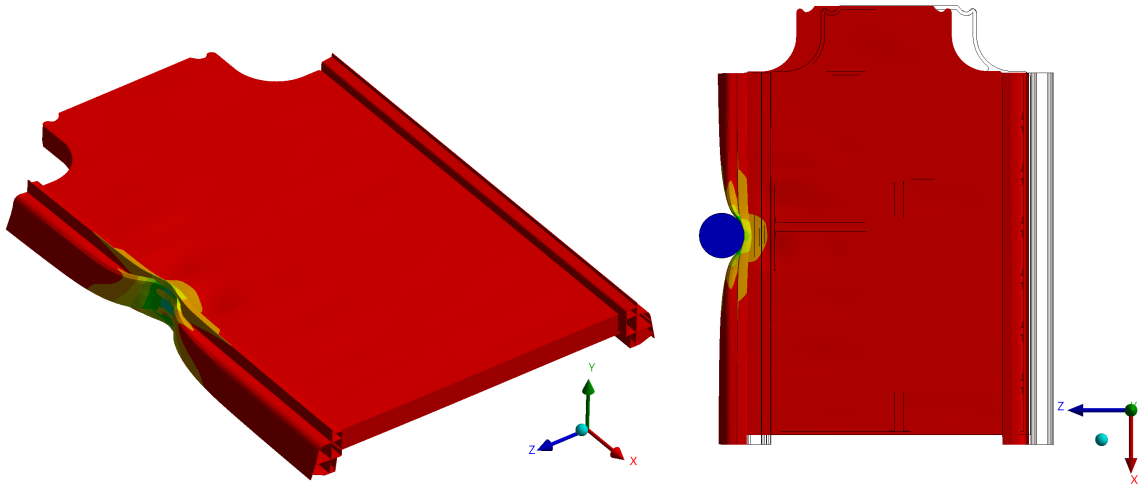


Figure 8.27: Explicit dynamic analysis of Phase 1, at 100 km/h: overview of the deformation of the BPE, in the $z-y$ plane, in time frames (scale of 2). **(a)** $t = 0$ s. **(b)** $t = 2.5e-3$ s. **(c)** $t = 5e-3$ s. **(d)** $t = 7.5e-3$ s. **(e)** $t = 1e-2$ s.

Although a scaling factor of 2 was employed, and therefore the deformation of the structure was visually magnified to allow for a deeper understanding, it is evident that the automotive assembly deforms to a much greater extent in this higher-velocity explicit simulation. This was expected, as early on in this work, the speed of a vehicle was identified as a major influencing factor to the damage occurring on it in a crash incident.

Focusing on Figure 8.27, although the intrusion of the pole into the automotive structure is much more prominent in this simulation than in the previous (although, in reality, less severe than that illustrated through scaling of 2), such a difference is not observed in the vertical deflection of the BPE. This serves, once more, to assess the stiffness associated with the current solution.

To visualise the real damage emerging in the automotive assembly due to the impact event, it is illustrated in true scale in Figure 8.28, accompanied by the representation of the deflection (and displacement) of the structure in z. Although the resulting deformation of the automotive structure is less serious than that represented in the Figures above, where a scaling factor was employed, it is much more significant than that originating from an impact at 32 km/h.



(a) **(b)**

Figure 8.28: Explicit dynamics analysis of Phase 1, at 100 km/h: intrusion of the pole into the automotive structure (true scale). **(a)** Global view. **(b)** Deformation in the z direction.

The distributions of the total deformation and directional deformations in y, these are provided, respectively, in Figures 8.29 and 8.30, at both the global and component levels.

Once again, it is possible to state that the maximum values of total deformation are present in the rocker panel being impacted, particularly in the contact region to the pole. This maximum value of deformation corresponds now to a magnitude of 150 mm instead of the 47 mm of the previous explicit simulation at, sensibly, one-third of the velocity. The change of the mentioned parameter justifies this difference.

Observing Figure 8.30, a maximum directional deformation value is found in the same zone of the maximum total deformation, now yielding a value of 67 mm. In the explicit analysis of this Phase, where a 32 km/h velocity was applied to the BPE and rocker panels, the value obtained is about three times smaller.

The maximum magnitude of this quantity in BPE components corresponds to a much smaller value, approximately 5 mm, found in the bottom case. In fact, the deformations endured by the BPE components themselves are not much different from those felt in the simulation at 32 km/h. Therefore, for now, this shows that the BPE model is capable of withstanding impact incidents occurring at a wide range of velocities.

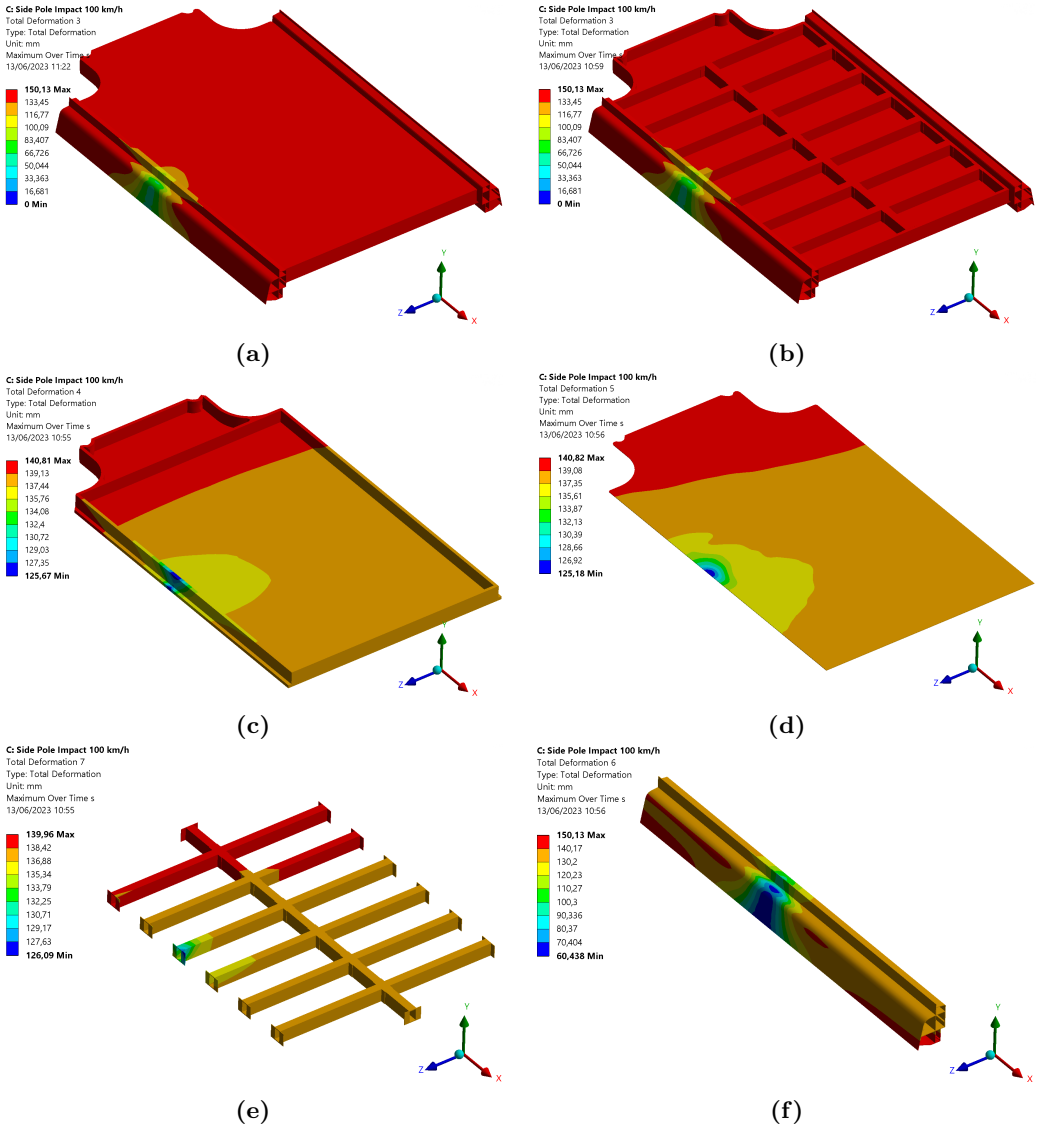


Figure 8.29: Explicit dynamics analysis of Phase 1, at 100 km/h: total deformation distribution at global and component levels (true scale). **(a)** BPE with top cover. **(b)** BPE without top cover. **(c)** Bottom case. **(d)** Top cover. **(e)** Reinforcements. **(f)** Rocker panel.

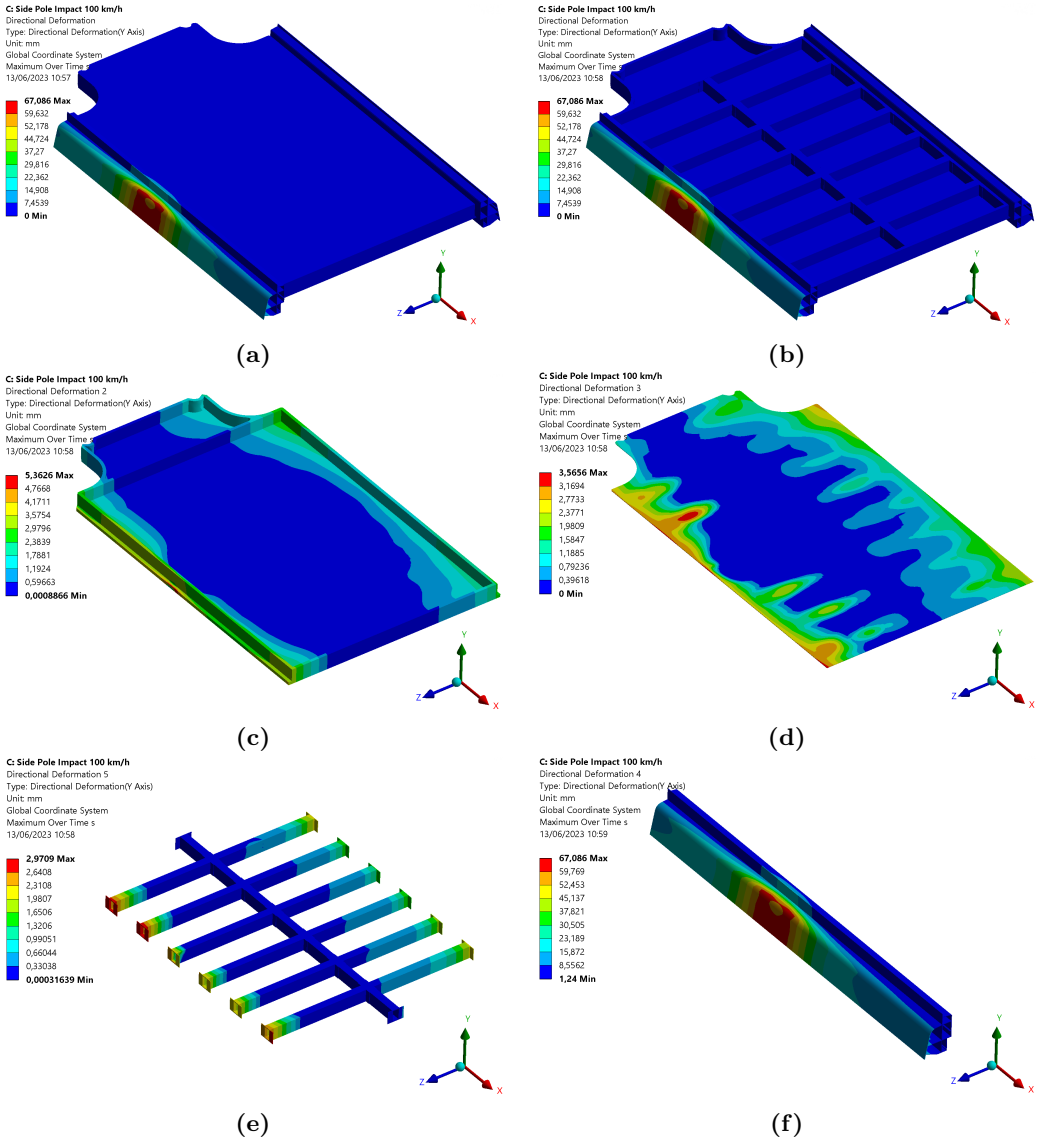
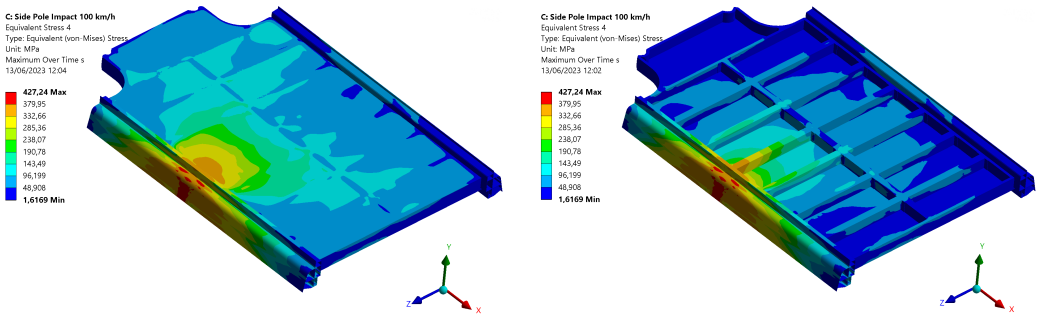


Figure 8.30: Explicit dynamics analysis of Phase 1, at 100 km/h: directional deformation distribution in the y direction at the global and component levels (true scale). **(a)** BPE with top cover. **(b)** BPE without top cover. **(c)** Bottom case. **(d)** Top cover. **(e)** Reinforcements. **(f)** Rocker panel.

8.4.2.2 Equivalent von Mises Stress

To assess the von Mises stress distribution and maximum magnitude present in the automotive assembly, consult Figure 8.31.



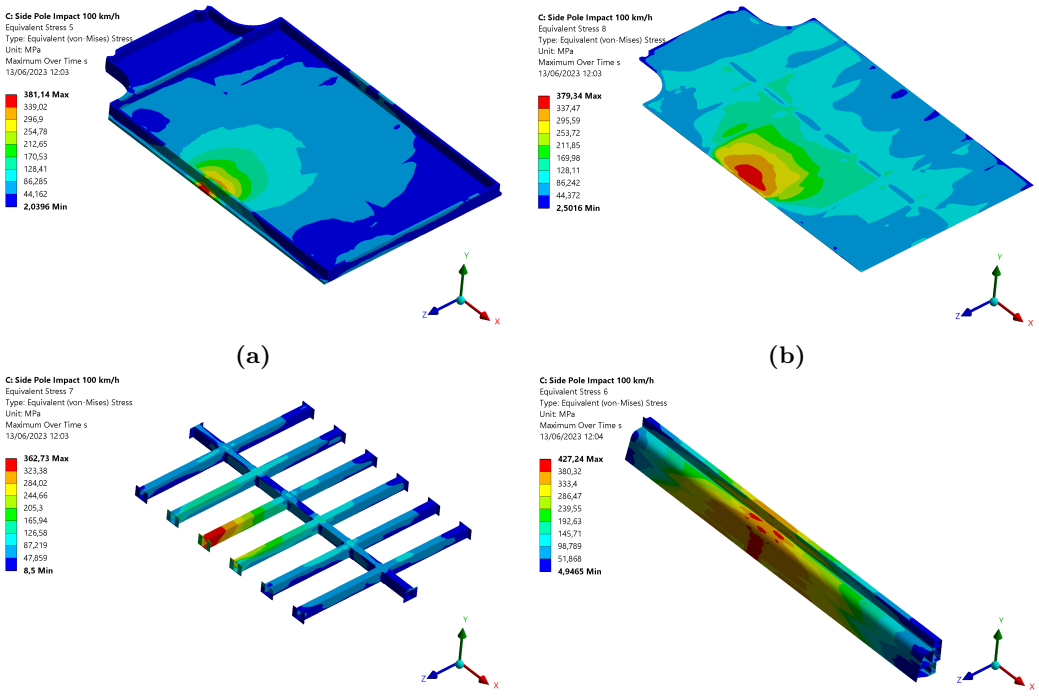
(a) **(b)**

Figure 8.31: Explicit dynamics analysis of Phase 1, at 100 km/h: equivalent von Mises stress (true scale). **(a)** BPE with top cover. **(b)** BPE without top cover.

The maximum stress within the model is found in the expected zone of the impacted rocker panel, presenting now a maximum intensity of 427 MPa, as opposed to the 406 MPa in the preceding analysis. Note how a change in velocity from 32 km/h to 100 km/h resulted in a stress increment to the model of only 21 MPa.

In comparison to Figure 8.21, a much more diffused distribution of stress throughout the structure is observed at the instant of maximum value over time.

To understand how this physical quantity is present at particular components, particularly in those composing this BPE solution, observe Figure 8.32.



(a) **(b)**

(c) **(d)**

Figure 8.32: Explicit dynamics analysis of Phase 1, at 100 km/h: equivalent von Mises stress (true scale). **(a)** Bottom case. **(b)** Top cover. **(c)** Reinforcements. **(d)** Rocker panel that endures the impact.

The main structural element of the BPE remains the most stressed one in this higher-velocity analysis, although the other components of the battery housing show similar stress

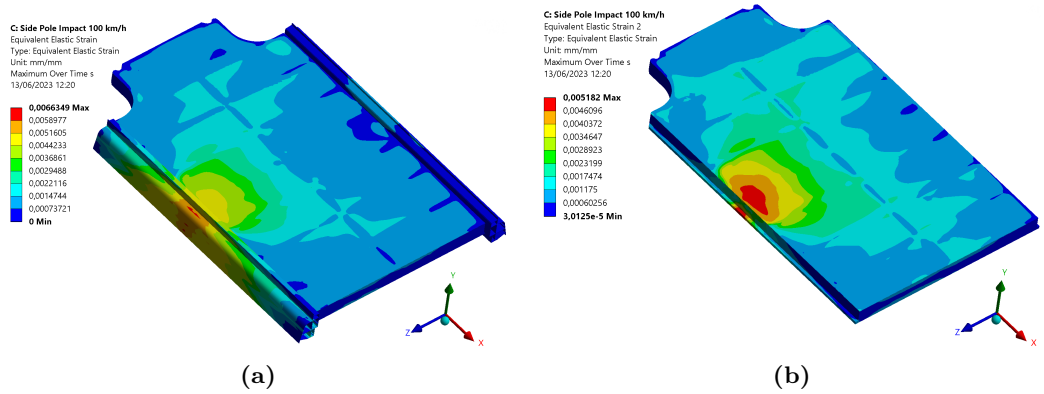
levels ranging from approximately 362 MPa to 381 MPa. This is consistent with the load path of the structure to the studied impact conditions. It is important to note that the maximum stress values in the battery housing are significantly higher in this analysis compared to the previous one, where they reached only 97 MPa. This is attributed to the model's definition of a higher velocity, resulting in more prominent stresses near the impact zone and more extensive transmission of loads to the BPE.

Recall, however, that these values of stress in the BPE components were associated with relatively small numbers of deformation, particularly in the assessed direction.

8.4.2.3 Equivalent Elastic Strain and Equivalent Plastic Strain

Lastly, it is interesting to assess the distribution of strains within the structure, both related to the elastic and plastic regimes. For that, Figure 8.33, regarding the elastic strain, and Figure 8.34, for the plastic strain, are presented.

Figure 8.33 illustrates the distribution of elastic strain, which exhibits a broader dispersion throughout the structure than that found in the previous analysis, especially in the BPE components. The maximum intensity of elastic strain in the BPE has increased to 0.006, compared to the previous value of 0.001, and it is now dispersed over a larger area of the BPE structure, including both the bottom case and top cover. This expanded distribution is a consequence of the heightened impact severity that characterised the currently assessed analysis.



(a) **(b)**

Figure 8.33: Explicit dynamics analysis of Phase 1, at 100 km/h: equivalent von Mises strain (true scale). **(a)** Rocker panels and BPE. **(b)** Exclusively the BPE structure.

With respect to the plastic strain showcased in Figure 8.34, it remains extremely localised in the impact region. Notwithstanding, it is now possible to observe some yielding of the BPE structure in the neighbouring regions where the rocker panel was hit.

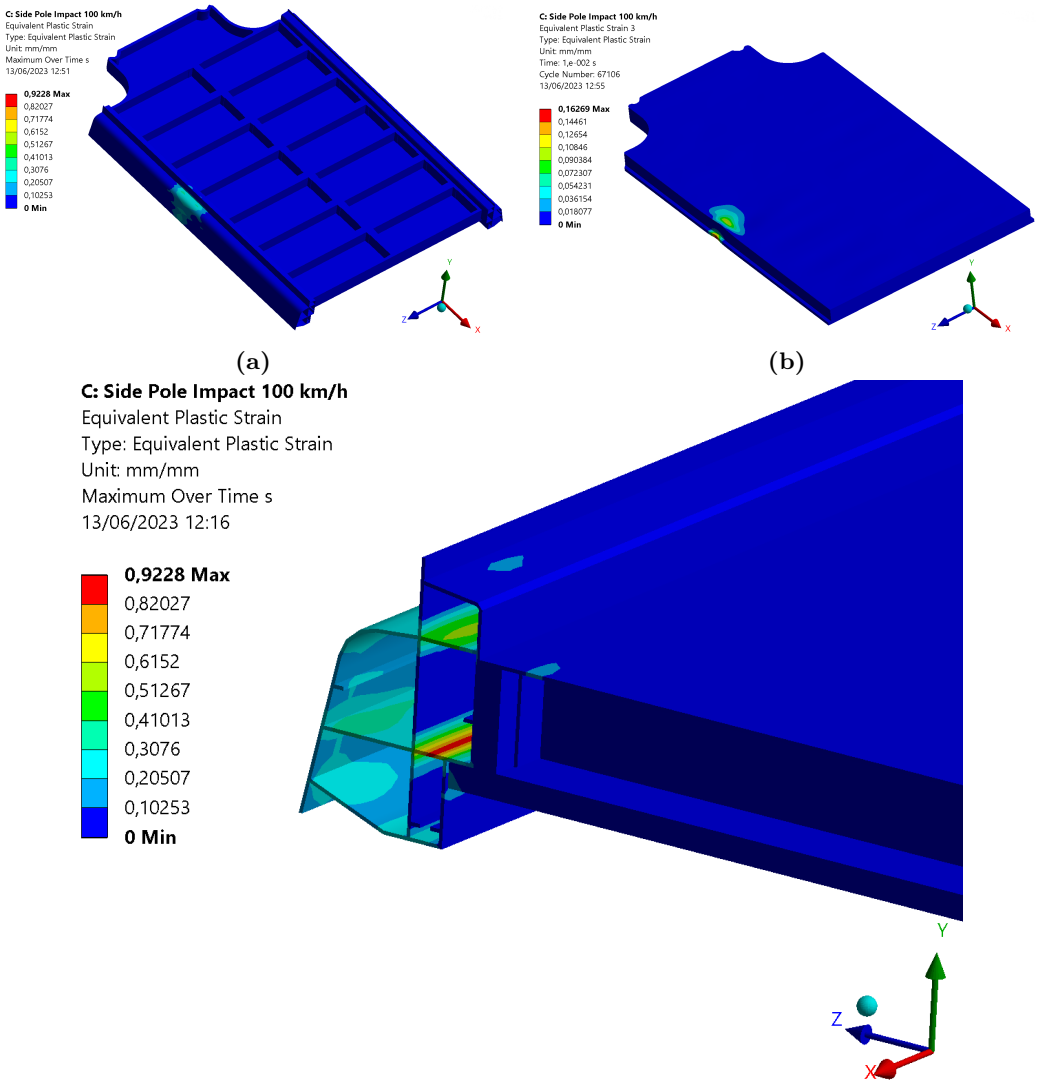


Figure 8.34: Explicit dynamics analysis of Phase 1, at 100 km/h: plastic strain (true scale). **(a)** Exterior region of the impacted rocker panel. **(b)** Exclusively the BPE structure. **(c)** Rocker panel cross-section.

In the BPE, a maximum plastic strain of 0.17 is achieved. However, this value can only be found in the extremity of the bottom case connected to the rocker panel. The top case, for instance, presents a maximum plastic strain value of 0.11, resulting from the energy absorption of the battery housing.

Given the fact that now the BPE undergoes extremely localised permanent deformation, it would be necessary to evaluate if this zone constitutes a potential weak point in the structure for these impact conditions, affecting the functioning of the battery modules in the close proximity of that region. This cannot be stated with certainty and would require additional numerical investigation and access to confidential industry information regarding the mechanical limits of the BPE solution that inspired this case. However, since it is inconclusive whether these factors lead to or not weak points of the structure, in Chapter 11, where the conclusions of this work are discussed, potential modifications or enhancements to the design or material of the BPE will be suggested. These proposals will specifically target

the identified areas of concern in the structure throughout all Phases of the study, aiming to improve the crashworthiness and overall structural integrity.

Chapter 9

Phase 2: Original Geometry with ABS

This Chapter regards all matters related to the first selected optimisation route: the obtainment of a model with the same geometry as the "Original model"; however, in this case, with the BPE completely manufactured in ABS. This constitutes Phase 2 of this work.

For this case, in addition to the mesh definition and analysis results, the rationale behind the material selection for the BPE is explained first. The enabled weight reduction from the change of material is consequently showcased. Next, the numerical results obtained from this comprehensive analysis group will determine whether the weight reduction was achieved without significantly compromising the crash resistance of the original model, as is sought.

9.1 Phase 2: ABS Material Properties

The objective for this optimisation path was to, by resorting to a polymeric material with some degree of current industry use and knowledge, obtain a lighter yet equally crashworthy BPE, capable of enduring identical impact loads. These reasons would contribute to validating its applicability in a BPE.

To aid in this search, the Granta® [117] material database was utilised. To filter the polymeric materials, the following restraints were input into the program:

- Satisfactory mechanical properties, particularly those related to impact.
- In terms of durability, the material must be self-extinguishing or non-flammable.
- The material should be recyclable.
- Good properties for injection moulding, a process that enables the obtainment of high volume series of identical and complex polymeric parts with good tolerances at a low cost per piece.

These constraints yielded a limited number of polymers. From those, a literature search was conducted to find a material already used in the industry that would be adequate for this application. This resulted in the chosen Acrylonitrile Butadiene Styrene, or ABS, as its typically designated.

According to Ruiz et al. [143], ABS is one of the most common engineering plastics in vehicles. Currently, it is utilised in components such as body parts, seating, bumpers, wheel

covers, etc. Thus, this material family fulfils the requirement of being already known in the automotive industry.

Given the fact that all the relevant properties are already guaranteed from the limits imposed in Granta® [117] search, the ABS selected to be assigned in the BPE model is now in condition to be presented. This thermoplastic can be found in the material database by the designation "ABS (flame retarded, moulding and extrusion)". The most relevant material properties for this study were extracted from Granta® [117] and are provided in Table 9.1. Although, in the material database, the material properties are presented in intervals and not in a precise value, the middle value of these ranges was considered. Finally, in Table 9.1, the most relevant properties of this study are provided. The mechanical properties were introduced in [144] to the obtainment of the approximate stress-strain curve that characterises the material, presented in Figure 9.1.

Table 9.1: ABS mechanical properties (Adapted from [117])

Mechanical Property	**Value**
Young's Modulus, E [GPa]	2.31
Poisson's Coefficient, [-]	0.4
Density [kg/m^3]	1185
Yield Strength [MPa]	39.3
Ultimate Strength [MPa]	41.4
Elongation [%]	40.75

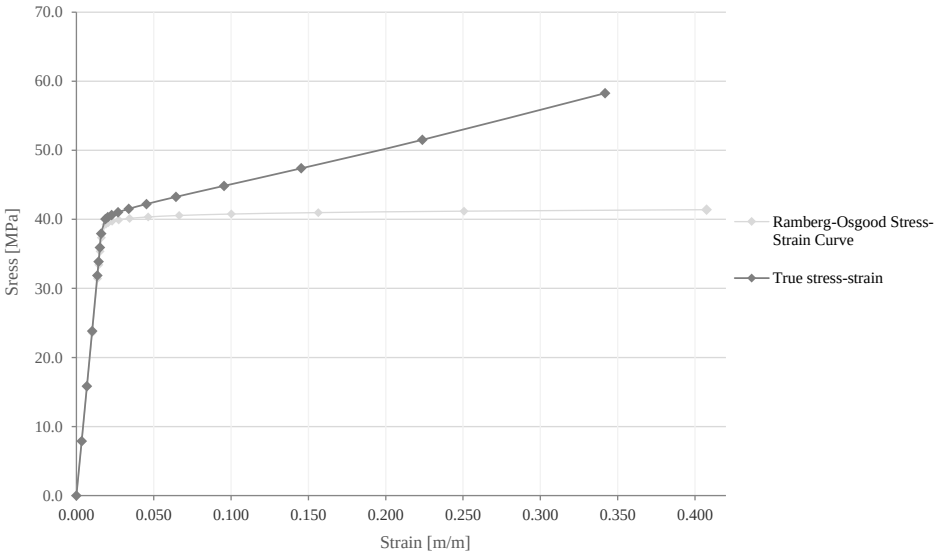


Figure 9.1: ABS stress-strain relationship, true and engineering curves (Adapted from [144]).

By the introduction of the above-mentioned properties in Ansys® and subsequential assignment for all the components that constitute the BPE, the following individual and overall weights were achieved (Table 9.2).

Table 9.2: Mass associated with the ABS BPE model of Phase 2

Part	Material	Density [kg/mm^3]	Volume [mm^3]	Mass [kg]
Top Cover	ABS	$1.185e-6$	9864525	11.69
Bottom Cover	ABS	$1.185e-6$	81358780	96.41
Bigger Longeron	ABS	$1.185e-6$	2439721	2.89
Smaller Longeron (6x)	ABS	$1.185e-6$	5036321	5.97
			Total	$\approx$ 116.96

Note that, evidently, the volumes of the components remain the same, given the fact that the geometry of the model remained untouched. This significant reduction in the total mass, from 267 kg in the "Original model" to the now 117 kg, occurs solely based on the assignment of a less dense material to the BPE.

As can be seen, the switch to this thermoplastic led to an extremely effective weight reduction, approximately 57%. The following analyses assess the influence of this material change on the behaviour of the structure. Note that although a BPE lightweight design is desired for BEVs, if it is verified that its mechanical properties are worsened to a point where it can no longer fulfil its functions, the design should be discarded as the component is not applicable for its intended use.

Lastly, it is worth noting that if this solution yields positive results, additional price and ease of production advantages can be obtained.

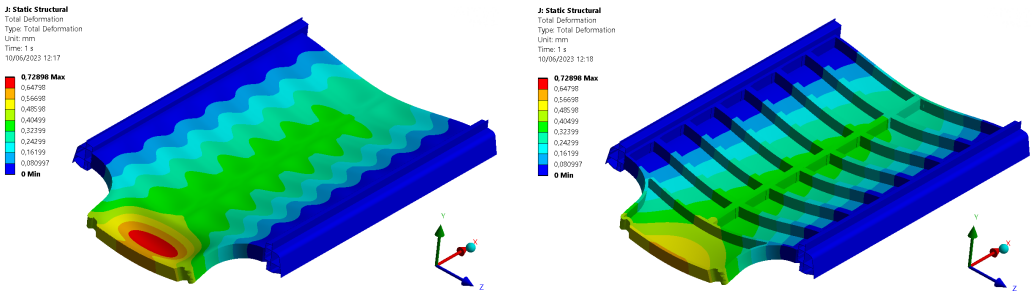
9.2 Phase 2: Static Analysis

The mesh parameters input in the program, and thus, the mesh quality achieved for the model of Phase 2, are in everything similar to those of Phase 1. This originates from the fact that the geometry of the structure remained the same, and only the material of the BPE components was altered. Thus, in each of the five analyses that will be discussed in this Chapter, the considerations related to the meshing of the model (mesh definitions, element types and number, mesh quality, etc.) can be found in Chapter 8.

Regarding the static analysis in particular, after introducing in the analysis module all the relevant settings, the model was ready to be run. The solver took 1 minute to yield the solution to the problem.

9.2.1 Total and Directional Deformation

As was done in Phase 1, and for the same reasons, an overview of the total and directional (in y) deformations in the structure are presented in Figures 9.2 and 9.3, respectively. Note, however, that in the illustrations concerning the total deformation, a scale of 360 was employed in this case to enable an improved understanding of the deflection of the BPE. This scaling value represents a tenth of the used in Phase 1.



(a) **(b)**

Figure 9.2: Static analysis of Phase 2: total deformation of the BPE (scale of 360). **(a)** BPE with cover. **(b)** BPE without cover.

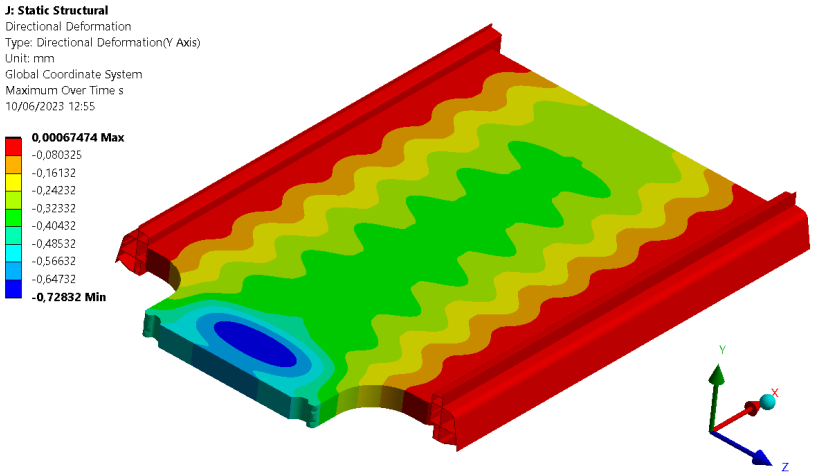


Figure 9.3: Static Analysis of Phase 2: directional deformation in y (true scale).

By examination of the Figures above, it can be concluded that the change of the material assigned to the BPE does not alter the overall behaviour of the structure: the bending of the BPE, the symmetry of the deformation distribution, and the most deformed zones remain the same. It does, however, influence the order of magnitude of the deformations, which changes from the hundredth of a millimetre to the tenth of that. This justifies the fact that the scale applied to observe the total deformation is one-tenth smaller than that of one of Phase 1, and even so, the bending visualised on the structure is more apparent. This increase in deformation is expected, considering the increased flexibility of the ABS BPE structure. At the same time, the stiffness of the rocker panels remained untouched, as Al 6061-T6 was once more assigned to these vehicles' components.

The maximum value of total deformation, 0.73 mm, emerging in the frontal region of the top cover is, nevertheless, still an extremely small value of deformation that surely does not affect the well-being of the internal battery pack components. Therefore, the deformation caused by the weight of the structure is negligible and does not affect its structural integrity, as expected and mandatory for any automotive structure of this kind.

9.2.2 Equivalent von Mises Stress

As can be observed in Figure 9.4, the stress distribution in the ABS structure remains the same as it was in the structure manufactured from aluminium alloy. The most stressed

regions remain in the same locations, i.e., in the proximity of the contact regions of the rocker panels and BPE, as a result of the rigid boundary conditions applied in the model.

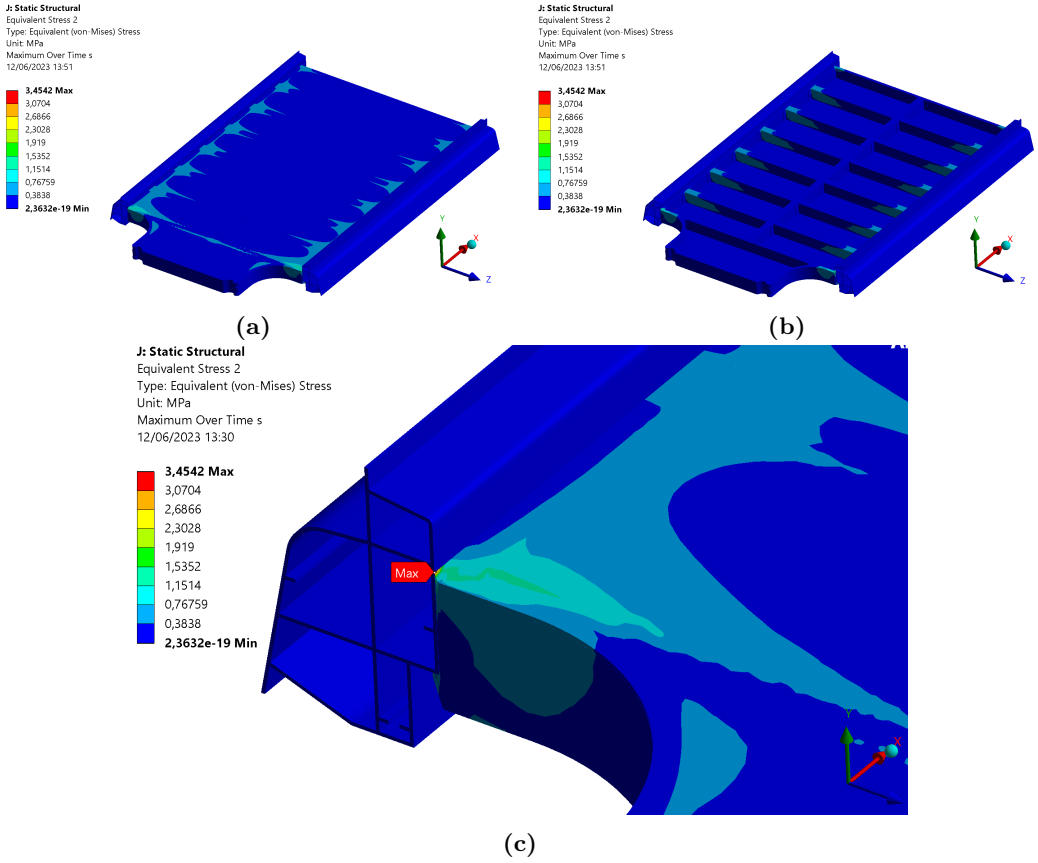


Figure 9.4: Static analysis of Phase 2: equivalent von Mises stress (true scale). **(a)** BPE with cover. **(b)** BPE without cover. **(c)** Most stressed region.

In addition to similar behaviour, the ABS BPE presents an identical maximum value of stress resulting solely from the standard earth gravity acting on the structure, with regards to the one retrieved for the "Original model". This contributes, furthermore, to the validation of this model since a similar (or enhanced) mechanical and impact behaviour of the BPE is desired.

9.3 Phase 2: Modal analysis

The mesh parameters input in the Modal module in Ansys® for Phase 2 correspond to those of Phase 1 since the same model geometry was used. Thus, all aspects related to the mesh of the model were already addressed in the previous Chapter.

A numerical simulation was then initiated, and the results presented in the next subsection were obtained after 112 minutes.

9.3.1 Natural Mode Shapes: Deformation

The natural modes of vibration, and particularly the natural mode shapes, were evaluated for the ABS model. This was done to evaluate the potential differences in the structure's behaviour owing to the alteration of the material assigned to the BPE. The modal analysis

was then used to provide the initial conditions of the next analysis, a transient structural one.

Hence, in Figure 9.5, the system's first six natural mode shapes, associated with the six first natural frequencies, are presented. Once again, a scaling of 20 was employed to display the natural mode shapes. This facilitates the direct comparison between the behaviour of the models of different Phases.

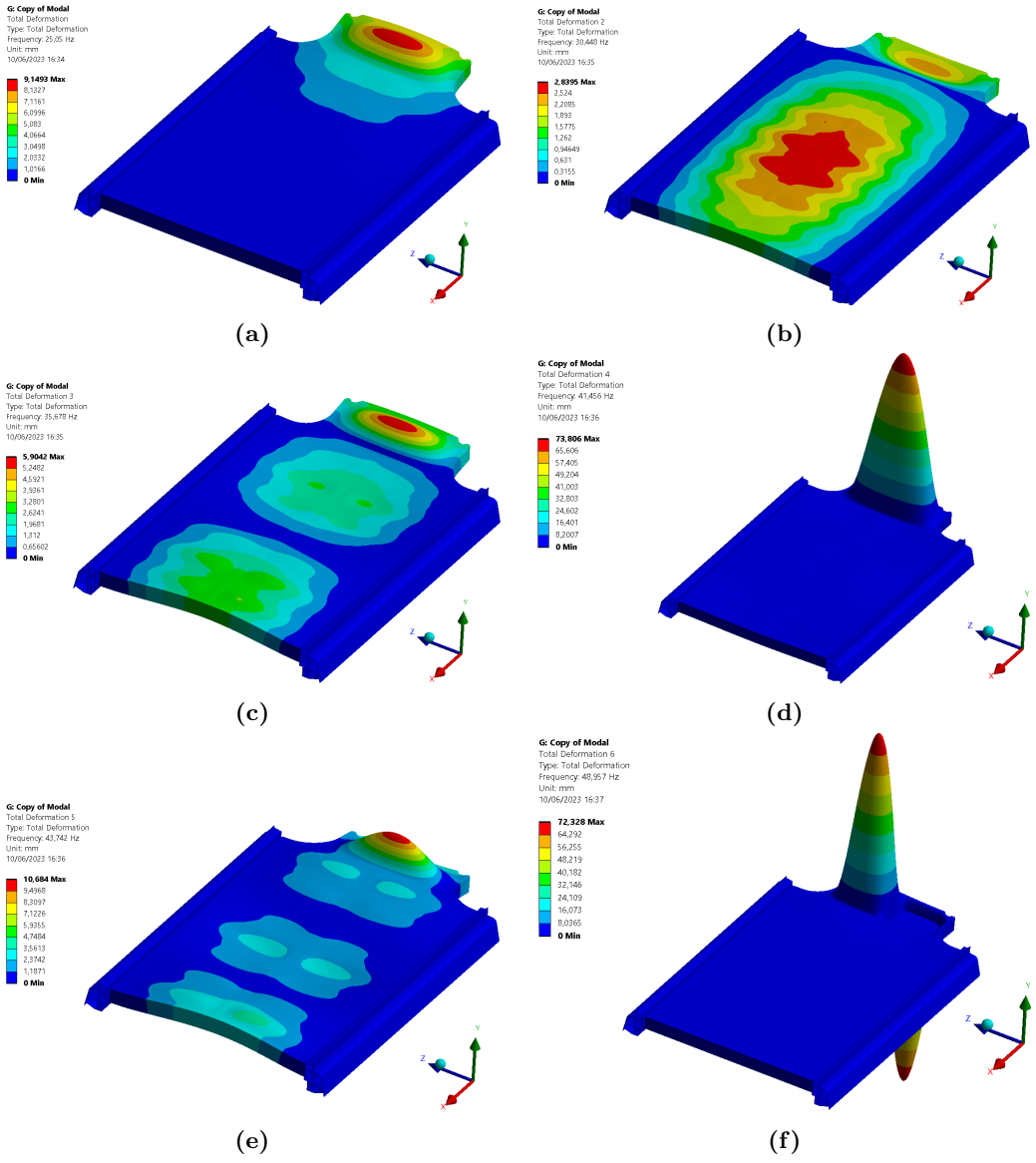


Figure 9.5: Modal analysis of Phase 2: natural mode shapes coupled with the first six natural frequencies (scale of 20). **(a)** 25.05 Hz. **(b)** 30.448 Hz. **(c)** 35.678 Hz. **(d)** 41.456 Hz. **(e)** 43.742 Hz. **(f)** 48.957 Hz.

The 400 modes of vibration retrieved from the modal analysis of Phase 2 captured a frequency range starting from 25.05 Hz, coupled to the fundamental frequency, to 419.14 Hz, associated with the 400^{th} mode of vibration. Recall that this range in Phase 1 was from 113.85 Hz to 1593.6 Hz. The obtainment of smaller values for the fundamental natural frequency and the other ones in this Phase is consistent with what was anticipated.

Currently, it is well understood that the natural frequencies of a system depend on

its mass and stiffness. Their relation is described in a simple system with one DoF by Equation 6.7, and for a generic system of n DoF as shown in Equation 6.10. Thus, since the stiffness of the ABS structure is much smaller than that of the aluminium alloy BPE, even with the associated decrease in mass enabled by the thermoplastic, the fundamental natural frequency of the system will be decreased, as will the other ones. This is, of course, undesirable since the present system will most likely be more vulnerable than the previous one with regard to the occurrence of vibrations in the vehicle. In addition, recall that for an undamped system, the resonance frequencies, where the amplitudes of vibration tend to an infinite value, correspond to the natural frequencies. It is important to note that an undamped system like the one being evaluated now does not correspond to the reality in most automotive components associated with a suitable damping ratio.

The values of deformation of the ABS model, associated with the six first modes of vibration, range from 5 mm to 74 mm, as compared to the maximum value of 48 mm obtained for the same modes in Phase 1. It is possible to state that these differences emerge from the distinct material properties of the two structures.

An initial thought could be to anticipate that the stresses emerging on the BPE for the following analyses would be higher for this Phase than those of Phase 1; however, likely, the opposite will occur. This is explained by the fact that the polymer, of reduced stiffness compared to the studied aluminium alloy, is a more flexible material, enabling more deformation in the structure. Moreover, this characteristic facilitates the distribution of the loads potentially acting on the structure over a larger area of the structure, which, as a result, will likely lead to the obtainment of lower values of stress. In conclusion, lower values of stress in the model of Phase 2, about that of Phase 1, are anticipated for the following analyses.

Lastly, it is worth mentioning that even though the exact values of deformation obtained in the modal analysis are of limited interest for the current study (since the real component does not correspond to an undamped system), the qualitative comparison between the magnitude of this quantity across the different Phases is relevant, as was seen in the paragraph above. In addition, an insight into the structure's dynamic behaviour was captured, and the obtained results of this analysis can now be used to interpret those retrieved in the transient analysis of the model, where an industry-based equivalent damping coefficient was employed, as stated in the numerical procedure discussion.

9.4 Phase 2: Transient Analysis

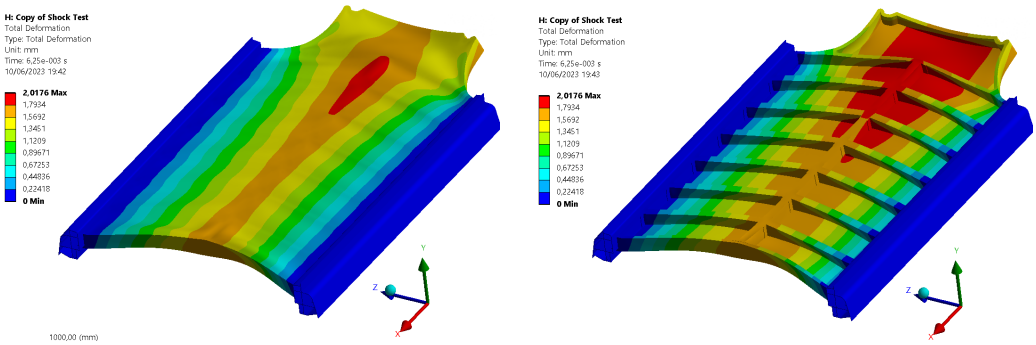
Recalling the fact that by inputting the modal analysis as an initial condition of the transient one, all the analysis settings of the former are transferred to the latter, no matter regarding the model set-up remains non-discussed. The mesh definitions and quality metrics can be consulted once more in the previous Chapter concerning the modal analysis section.

This simulation of Phase 2 took 127 minutes to yield the solution to the analyst.

9.4.1 Total and Directional Deformation

As per usual, the discussion of results starts from the evaluation of the distribution of deformations within the structure.

In Figure 9.6, the distribution of the total deformation can be observed for the entire automotive structure. In this Phase, a scaling of 100 was employed in the model, as it was deemed sufficient to provide the reader with a comprehensive understanding of the BPE's behaviour to the crash incident being simulated. Recall that a scaling factor of 1000 was employed in the "Original model" of Phase 1 for the examination of this same quantity.



(a) **(b)**

Figure 9.6: Transient analysis of Phase 2: total deformation distribution in the BPE and rocker panels (scale of 100). **(a)** BPE with cover. **(b)** BPE without cover.

Despite the fact that, in this case, a scaling factor corresponding to a tenth of that is employed to visualise the total deformation in Phase 1, a much more visually evident deformation of the structure is represented. In fact, by changing the material of the BPE structure from Al 6061-T6 to ABS, the maximum value of total deformation within the structure changes from 0.06 mm to 2 mm. Although it is still an extremely small value and can still be considered negligible, this alteration in the order of magnitude of this quantity is, once more, a witness of the decreased stiffness and more flexible behaviour characteristic of the ABS in comparison to the one of the aluminium alloy utilised in Phase 1.

With regards to the distribution of total deformation in the structure, the profile remained identical to that showcased in the Al 6061-T6 BPE, with the most deformed zones being those localised in the proximity of the symmetry axis of the structure, particularly the frontal region of the structure. The lesser deformed and undeformed zones also stayed the same, in the extremities of the structure, owing to the employed boundary conditions. Furthermore, the zones characterised by the highest deformations are reminiscing of those suggested by the modal analysis.

As was done for Phase 1, in Figure 9.7, the distribution of total deformation for each component of the automotive structure can be consulted.

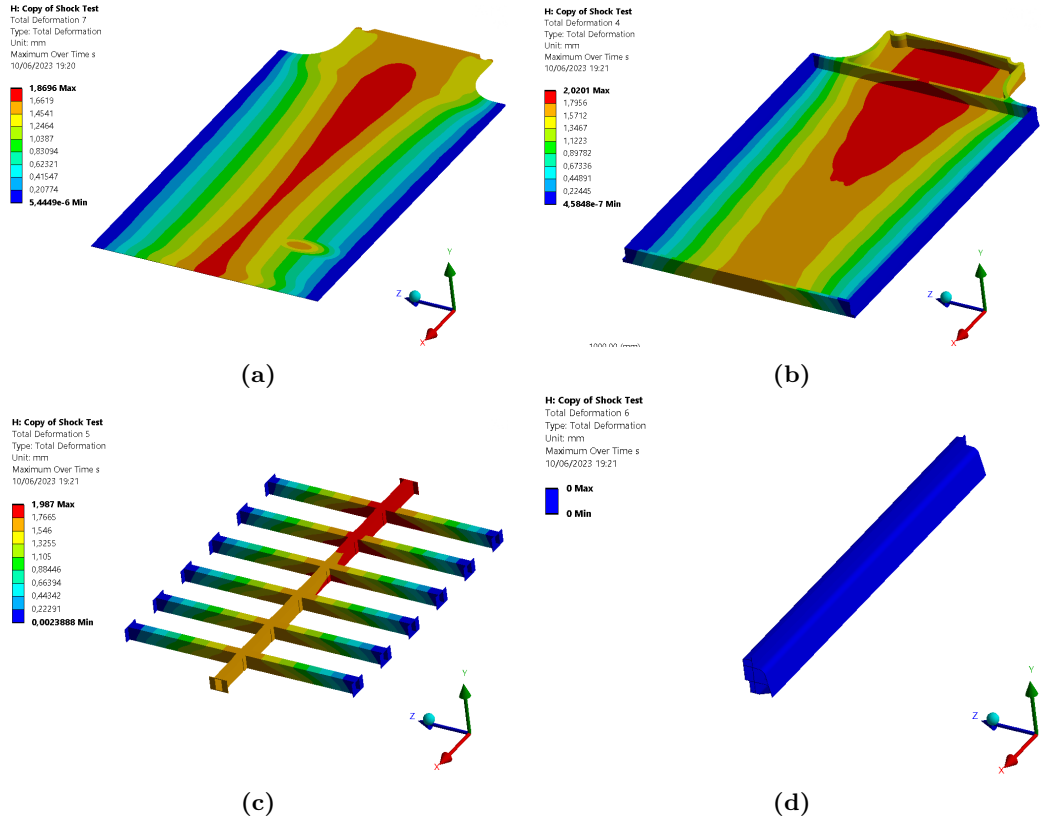


Figure 9.7: Transient analysis of Phase 2: total deformation distribution at the component level (true scale). **(a)** Bottom case **(b)** Top cover. **(c)** Reinforcements. **(d)** Rocker panel.

In opposition to what was the case in Phase 1, the maximum deformation is now found in the bottom case of the BPE, closely followed by the most deformed zones of both the internal skeleton and the top case. The primary structural element of the BPE exhibits its most significant deformation in the uttermost frontal region, specifically towards the middle of the structure. This deformation pattern aligns with the applied load and boundary conditions discussed earlier.

In the illustration showcasing the reinforcements, it is possible to observe a significantly gradual distribution of deformations within the component. This is likely a result of the loads emerging from the frontal crash event travelling through the reinforcements, leading to its deformation throughout the defined load path of the structure. These start by acting more severely in the longitudinal reinforcement, particularly in its frontal end, owing to the direction of the acceleration. From there, they are distributed through the multiple transversal reinforcements, which causes their magnitude to attenuate and, thus, the deformations originating from them to be less pronounced in a gradual manner the further the considered cross-section is from the start of their propagation in the internal skeleton, both longitudinally and orthogonally.

Lastly, the rocker panels remain undeformed, as was expected, given the applied constraints in the structure.

Once again, most of the deformation the BPE endures is in the y direction, as verified by bending the structure towards the middle in Figure 9.6. Thus, in Figure 9.8, the distribution of this directional deformation is presented, both at component and structure levels.

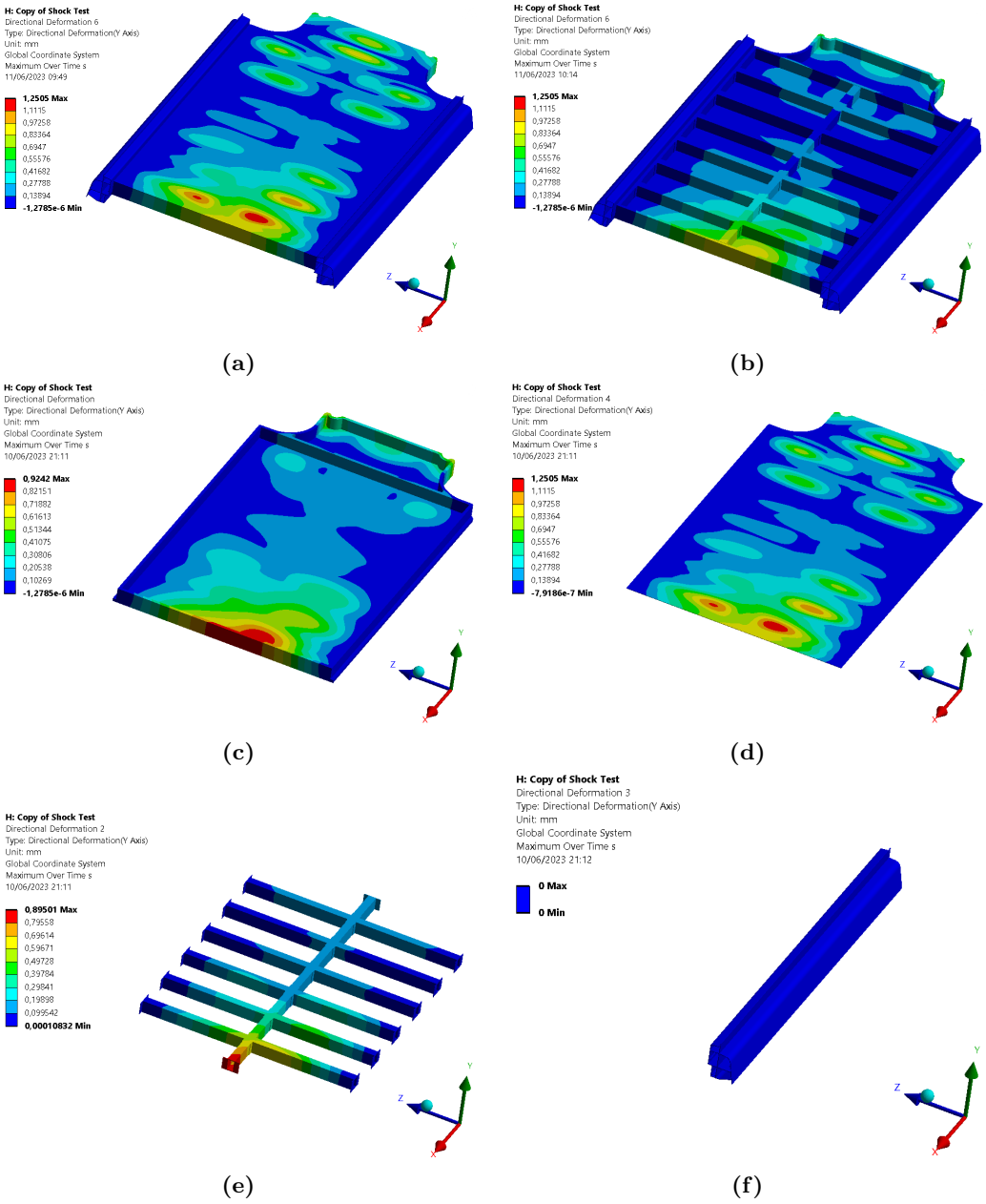


Figure 9.8: Transient analysis of Phase 2: directional deformation distribution in y, at the global and component levels (true scale). **(a)** BPE with cover. **(b)** BPE without cover. **(c)** Bottom case. **(d)** Top cover. **(e)** Reinforcements. **(f)** Rocker panel.

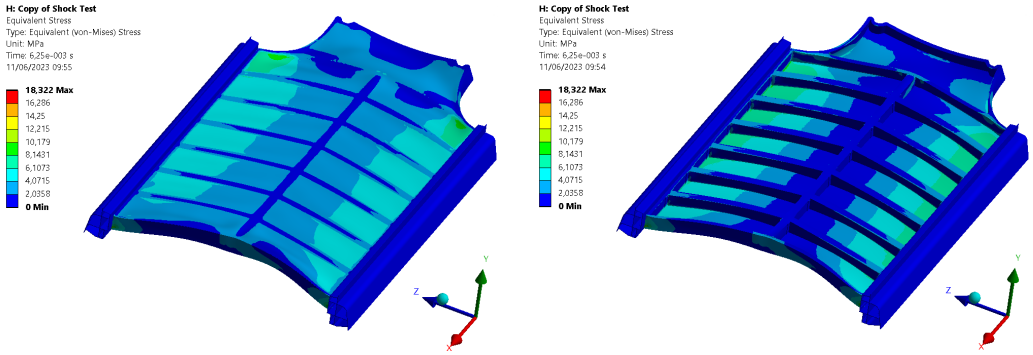
The distribution of this directional quantity, like it was the case for the total deformation, is equivalent to the profile displayed by the Al 6061-T6 BPE model of Phase 1 for the corresponding analysis to this one. In this case, however, a maximum magnitude of 1.25 mm was achieved, as opposed to 0.0033 mm. Equal was also the component where this maximum deformation value was verified, the top cover, given its smaller thickness compared to the rest of the housing components.

Moreover, the greatest vertical deflections observed on the structure remain in the front and rear of the BPE, in this case being even greater in the back region. This is oftentimes the behaviour of a generic structure to crash, and as already hypothesised, results from

redistribution and transfer of the impact energy throughout the BPE.

9.4.2 Equivalent von Mises Stress

In Figure 9.9, the stress distribution in the BPE model can be consulted. The bending behaviour of the structure can also be observed by the application of the same scaling factor of 100.



(a) **(b)**

Figure 9.9: Transient analysis of Phase 2: equivalent von Mises stress distribution in the BPE and rocker panels (scale of 100). **(a)** BPE with cover. **(b)** BPE without cover.

As can be concluded, the obtained symmetric stress profile of the structure is similar to the corresponding one of Phase 1, the difference relying on the fact that the overall magnitudes of this quantity are slightly increased. For the ABS BPE, the highest stress value is 18.3 MPa, compared to the similar 16.9 MPa obtained for the Al 6061-T6 model. However, the exact value of maximum stress is not of much interest since, once again, it results from merely numerical matters and does not represent the real maximum stress value emerging in the structure from the crash phenomenon.

Accordingly, to perform a more detailed examination of the stress arising in the structure, the distribution of this physical quantity is illustrated for each component in Figure 9.10.

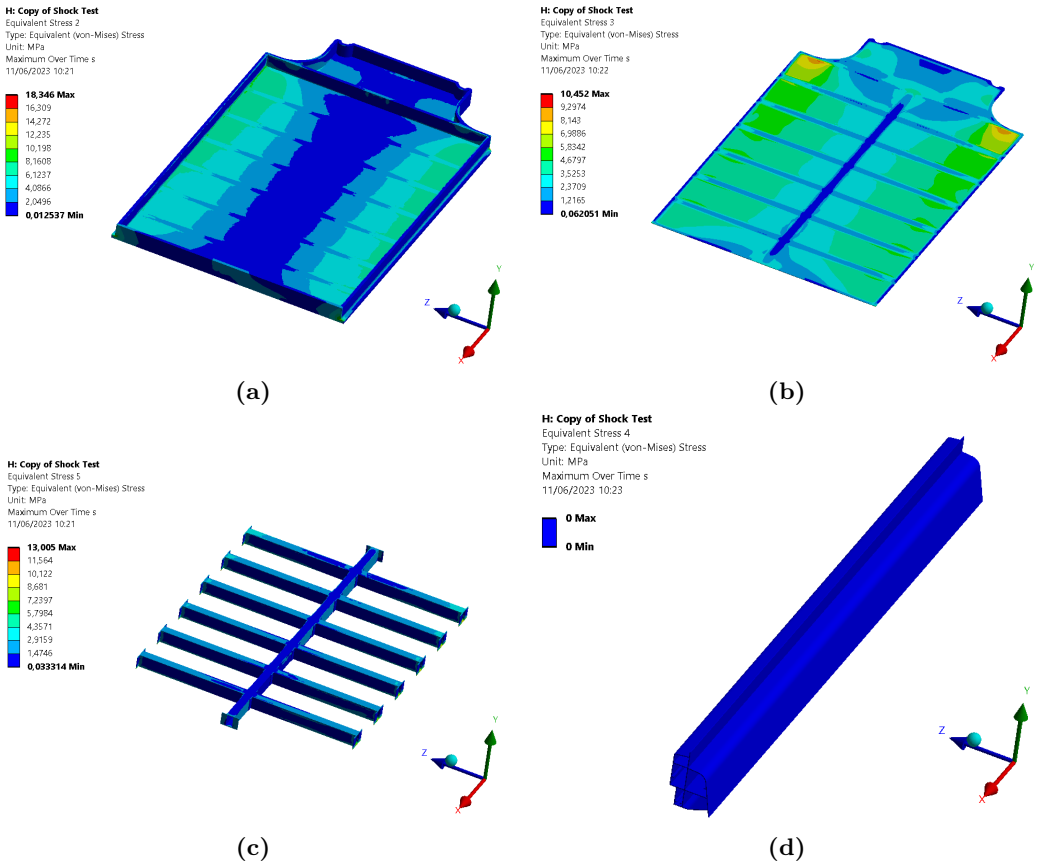


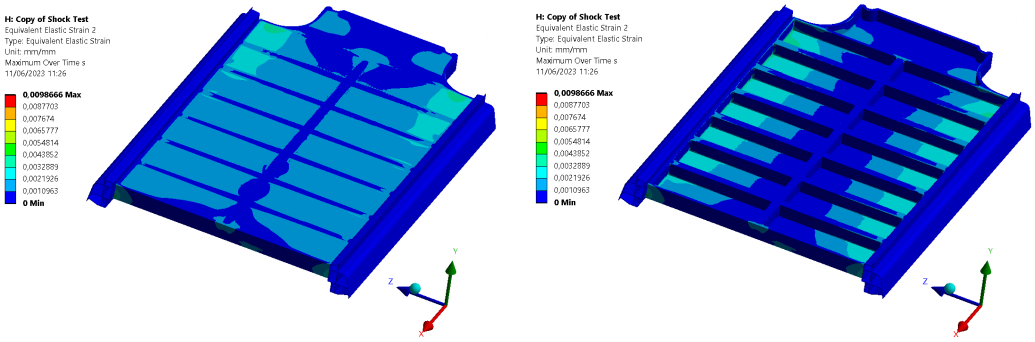
Figure 9.10: Transient analysis of Phase 2: equivalent von Mises stress distribution at the component level (true scale). **(a)** Bottom case. **(b)** Top cover. **(c)** Reinforcements. **(d)** Rocker panel.

Likewise, the distribution of stress for each of the components is equivalent to the one presented in Phase 1: the most stressed region is the bottom case, while the rocker panels remain free of any stress. The stress is increased the further the zones being considered are localised from the symmetry axis of the structure, as evidenced by the distribution of the reinforcements, top cover, and bottom case.

Recall, however, that evaluating the stress levels in the proximity of the regions where the rigid boundary conditions were applied to the structure does not yield physically-significant values. Instead, "contaminated" maximum values by this numerical implication are found. Nevertheless, as addressed in Phase 1, if even these "maximum" values are considered low and significantly far from the yield strength of the ABS, then the stresses effectively acting on the BPE are even smaller and do not constitute any threat to the internal components of the battery pack.

9.4.3 Equivalent von Mises Strain

The equivalent von Mises strains' distribution in the structure can be consulted in Figure 9.11.



(a) **(b)**

Figure 9.11: Transient analysis of Phase 2: equivalent von Mises strain distribution in the BPE and rocker panels (true scale). **(a)** BPE with cover. **(b)** BPE without cover.

As per usual, a symmetric distribution of the mentioned quantity was obtained.

The simulated frontal crash results in minimal strain values throughout the structure, with the maximum strain magnitude of 0.009 occurring in the regions next to where the boundary conditions were applied. Recall that, once again, these strain values have no physical significance and are likely artefacts of the applied boundary conditions. Therefore, it can be concluded that the strains induced in the structure by the event of a frontal crash are negligible.

In summation, just like for the model of Phase 1, it can be concluded that the constructed ABS BPE is capable of enduring the emerging deformations, stresses and strains that act upon it as a result of the occurrence of a severe frontal crash event.

Therefore, at least for the frontal impact, for now, the weight reduction associated with the material change of the BPE did not influence or deteriorate the properties of the structure for a crash, as was sought. The same must now be evaluated for the event of a side impact by means of the following explicit analyses.

9.5 Phase 2: Explicit Dynamics Analysis

9.5.1 Side Impact at 32 km/h

The explicit dynamics simulation of Phase 2, for which a constant velocity in z of 32 km/h was applied to the model, was characterised by a total elapsed time of 172 minutes, about three hours.

As per usual, the evaluation of the results of the explicit analysis will start with the consultation of the energy summary plot of the system. This energy graph is represented in Figure 9.12.

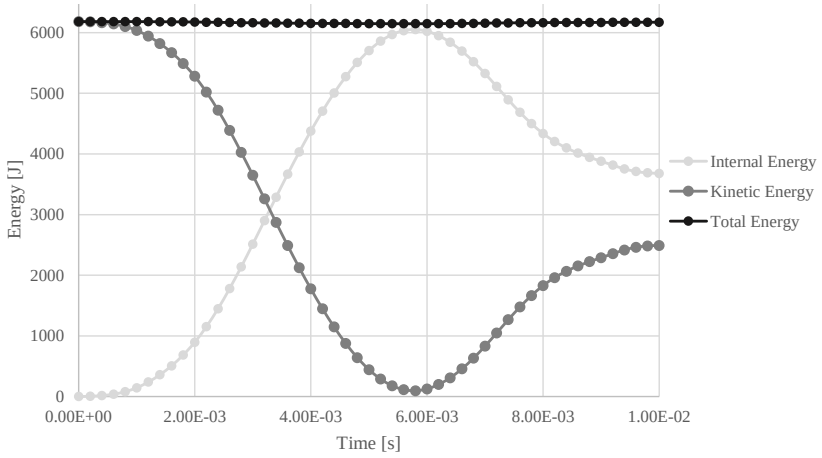


Figure 9.12: Explicit analysis of Phase 2, at 32 km/h: energy summary.

As expected and desired, the obtained energy plot is equivalent to those achieved in Phase 1.

The law of conservation of energy is verified, and a constant total energy of approximately 6200 J is verified for the entirety of the analysis time. In the instant of maximum compression of the contacting bodies, in this analysis achieved at $t = 5.8$ ms, this energy value is mostly related to the strain energy absorbed by the automotive assembly. Once again, this moment corresponds to the moment where the kinetic energy (and, therefore, the velocity) of the moving structure reaches its minimum value, and the "rebounce" of the latter commences.

It is worth noting that the total value of energy present in the currently evaluated system corresponds to about half of that achieved for this particular analysis of the previous Phase. Also, the timestamp of maximum intrusion of the pole into the rocker panel now takes place earlier, in relation to the above-mentioned analysis, which enables a more comprehensive visualisation of the energy transformations associated with the "bounce back" of the automotive assembly, where the system tends to reach an equilibrium situation. Lastly, another difference observed in the two energy summary plots is the now more notorious energy conversion rate after the $t = 5.8$ ms timestamp is passed. The stated disparities are deeply coupled to the distinct materials assigned to the BPE in the two analyses.

The kinetic energy, and hence the total energy, associated with the structure at $t = 0$ s is, for this analysis, less than it was in the corresponding analysis of Phase 1 since the mass associated with the structure suffered a reduction of about 50%. This corresponds roughly to the reduction of the total energy of this system in relation to one of the first Phases of this work, explaining this difference.

Furthermore, the other disparities observed within the two Phases, the first one deeply related to the other, are related to the more rapid energy transfer and conversion associated with the ABS material, due to its intrinsic impact properties, compared to those presented by the Al 6061-T6.

9.5.1.1 Total and Directional Deformations

Figures 9.13 and 9.14 strive to provide the reader with a considerable understanding of how the automotive assembly reacts to the side-impact it experiences against the rigid pole. The former Figure portrays an overview of the aforesaid structure from an above point of view, while the latter portrays its deflection in the $y - z$ plane. Once again, a scaling factor of 2 was employed for both illustrations.

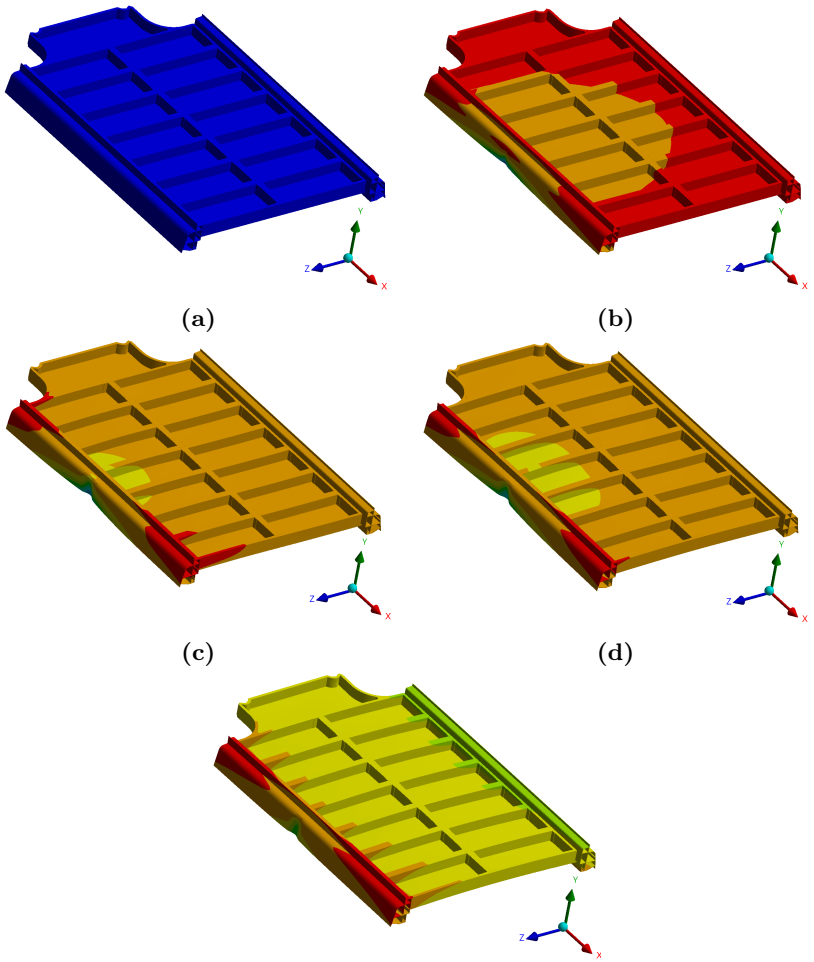


Figure 9.13: Explicit dynamic analysis of Phase 2, at 32 km/h: overview of the deformation of the BPE in time frames (scale of 2). **(a)** $t = 0$ s. **(b)** $t = 2.5e - 3$ s. **(c)** $t = 5e - 3$ s. **(d)** $t = 7.5e - 3$ s. **(e)** $t = 1e - 2$ s.

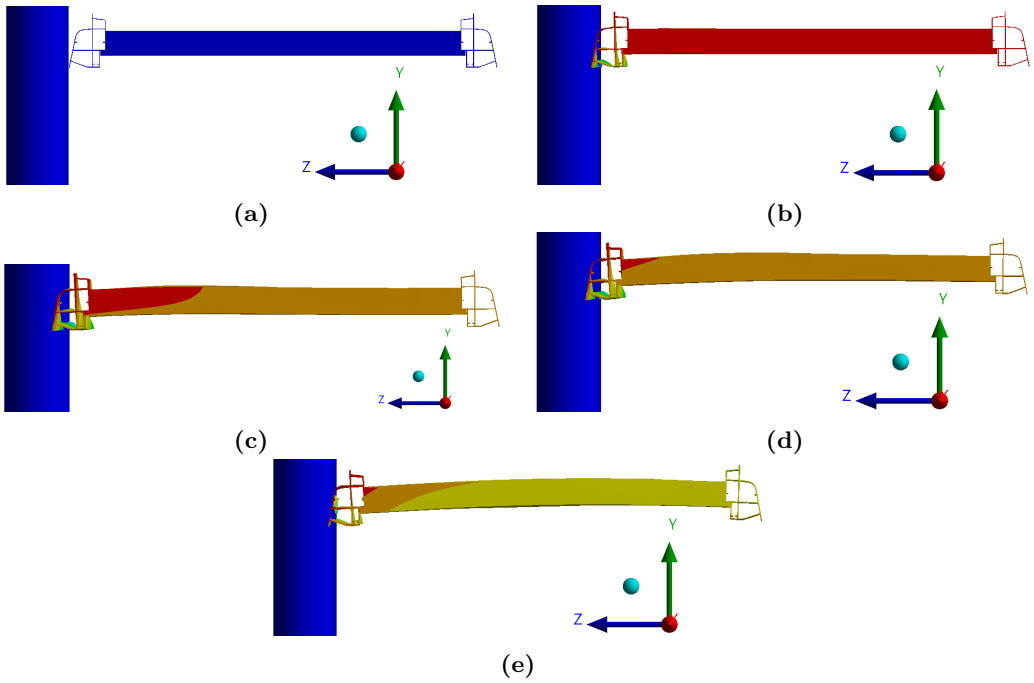
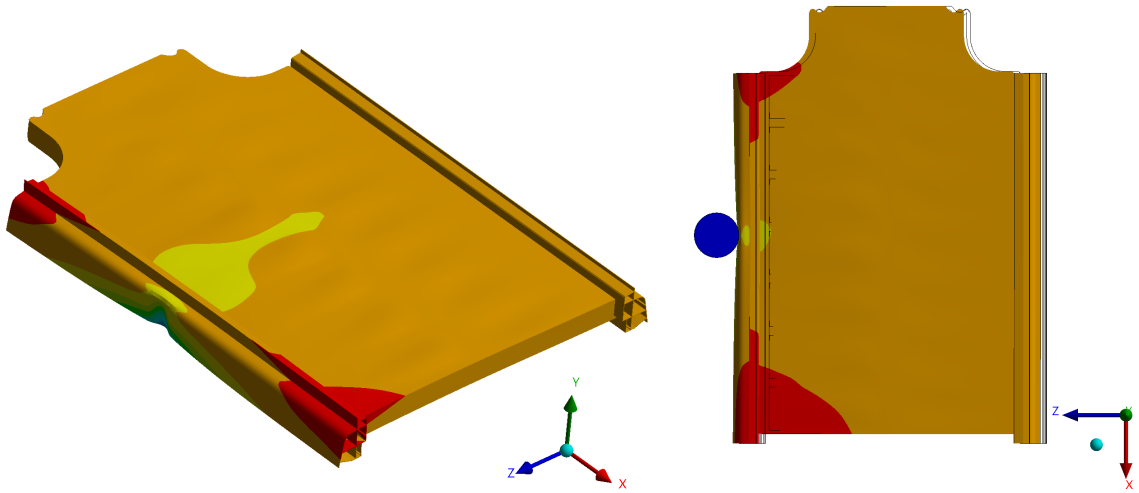


Figure 9.14: Explicit dynamic analysis of Phase 2, at 32 km/h: overview of the deformation of the BPE, in the $z-y$ plane, in time frames (scale of 2). **(a)** $t = 0$ s. **(b)** $t = 2.5e-3$ s. **(c)** $t = 5e-3$ s. **(d)** $t = 7.5e-3$ s. **(e)** $t = 1e-2$ s.

Disregarding the colour map that characterises the deformation of the structure scaled for each specific timestamp and focusing solely on the structure's configuration for each of those, it is evident that the BPE endures a much more severe upwards deflection, starting from the extremity where the rocker panel meets the pole, until the other end of the assembly.

Once again, this behaviour can be attributed to improved flexibility of the ABS structure, originating from its significantly reduced stiffness characteristics. This leads the BPE to deform to a greater extent and, therefore, to transmit the impact energy and distribute the corresponding loads faster, as observed in the energy graph characterising this system. The Al 6061-T6 BPE is much stiffer, which limits the deflections observed in the structure.

As per usual, to gift the reader with a representation of the realistic behaviour of the structure after the occurrence of the impact, now in true scale, both the intrusion and the qualitative z directional deformation of the BPE are presented in Figure 9.15. These are comparable to the ones found in the corresponding illustration of Phase 1 (Figure 8.17) in the sense that they are, once more, of minor significance.



(a) **(b)**

Figure 9.15: Explicit dynamics analysis of Phase 2, at 32 km/h: intrusion of the pole into the automotive structure (true scale). **(a)** Global view. **(b)** Deformation in the z direction.

Next, to obtain the exact values of total deformation that the automotive structure suffers, in Figure 9.16, the distribution of this quantity is presented, both at global and individual levels.

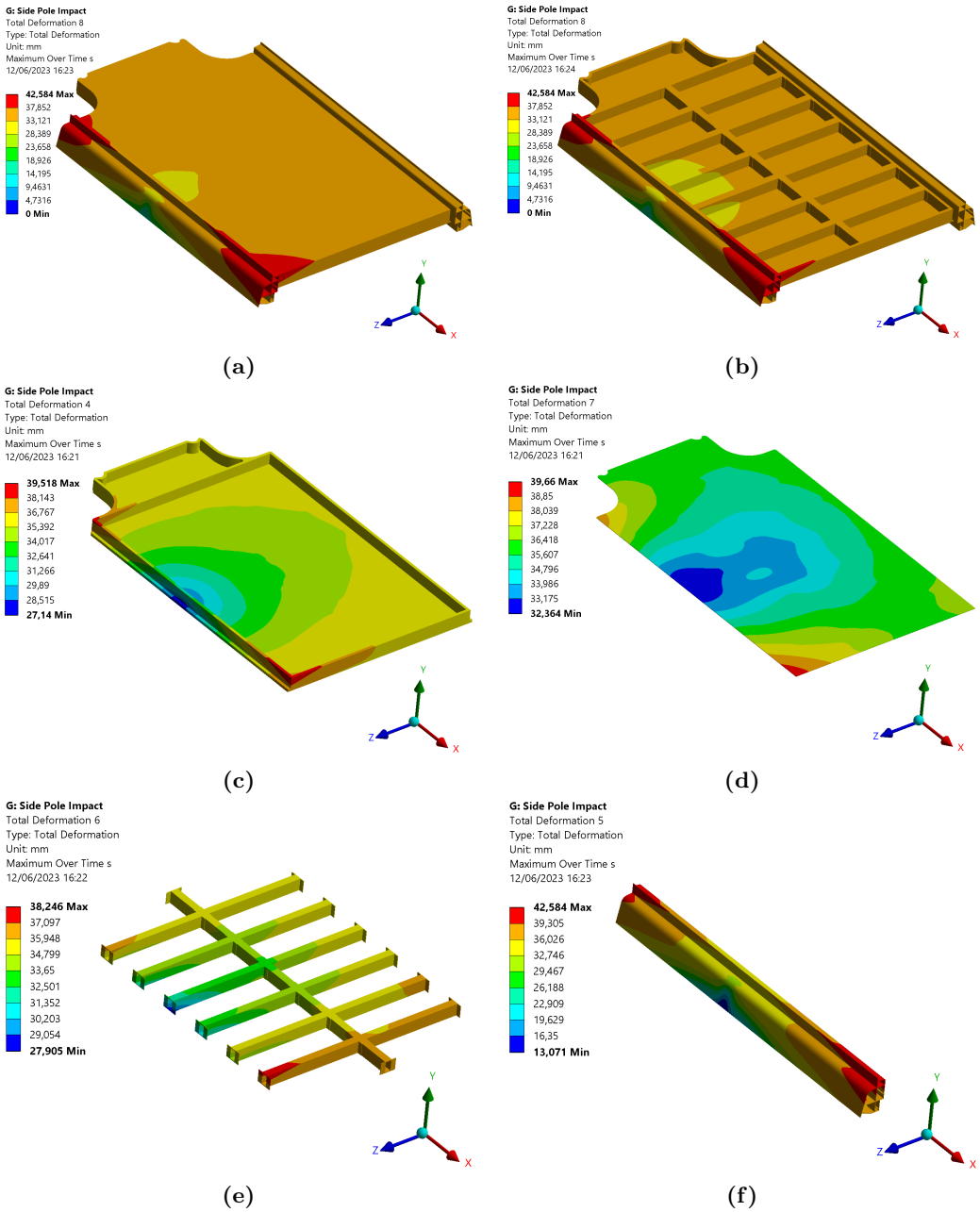


Figure 9.16: Explicit dynamics analysis of Phase 2, at 32 km/h: total deformation distribution at global and component levels (true scale). **(a)** BPE with top cover. **(b)** BPE without top cover. **(c)** Bottom case. **(d)** Top cover. **(e)** Reinforcements. **(f)** Rocker panel.

Once again, the total deformation values account for the displacement of the BPE towards the rigid pole; thus, this information should be assessed carefully. Other than that, it is possible to observe a symmetric distribution of deformation of the structure, which corresponds to what was seen in Phase 1 and was expected. In addition, it is retrieved that the various components of the BPE present values of maximum total deformation extremely close to each other.

As was done for the "Original model", it is relevant to evaluate the deformation of the BPE in the y direction, even more so now, as it has been concluded that the structure presents a more prominent vertical deflection. This is provided in Figure 9.17.

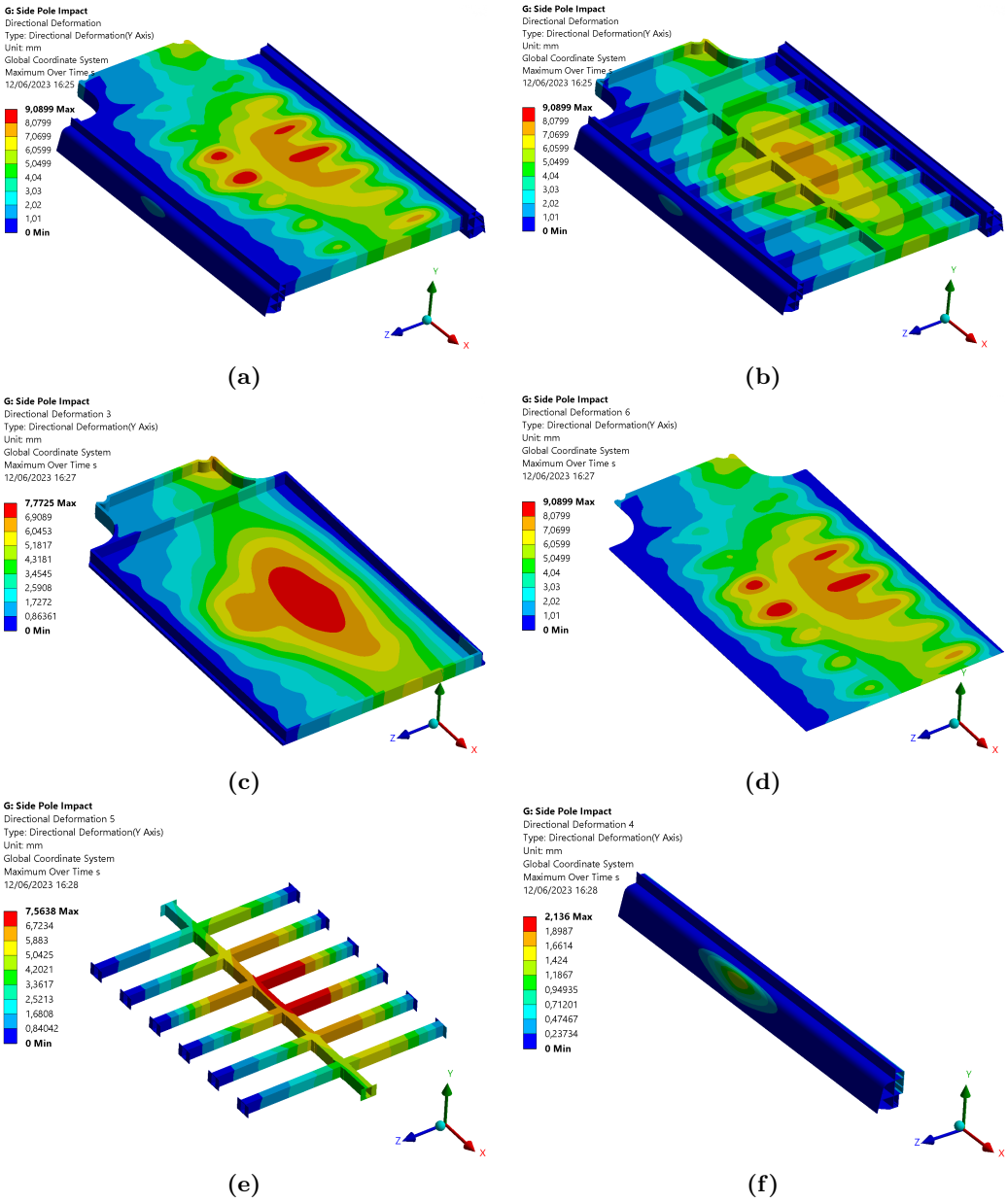


Figure 9.17: Explicit dynamics analysis of Phase 2, at 32 km/h: directional deformation distribution in the y direction at global and component levels (true scale). **(a)** BPE with top cover. **(b)** BPE without top cover. **(c)** Bottom case. **(d)** Top cover. **(e)** Reinforcements. **(f)** Rocker panel.

(a) BPE with top cover. (b) BPE without top cover. (c) Bottom case. (d) Top cover. (e) Reinforcements. (f) Rocker panel.

From the presented Figure is possible to retrieve a maximum directional deformation value of 9 mm within the entire automotive assembly, which occurs on the central zone of the thin top cover of the BPE.

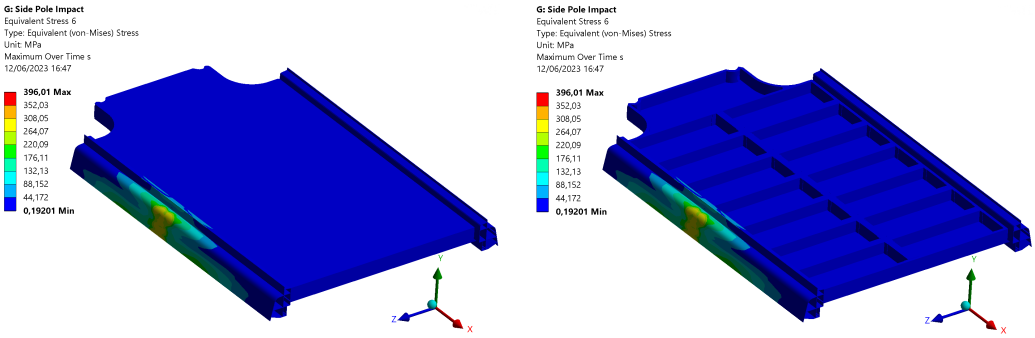
Contrary to what occurred for the Phase 1 simulation of a side impact at 32 km/h, in which the impacted rocker panel presented the maximum deformation of 21 mm in y, this component is the least deformed in the present analysis. This has to do with the fact that the two members of the assembly are "manufactured" by distinct materials in the two

models. In this solution, a much more flexible material was assigned to the battery housing in comparison to the one presented by the rocker panels, thereby facilitating the occurrence of more prominent deformations in the BPE, particularly bending in the central zone of the bottom case, given its enhanced capacity of energy absorption. Once again, the battery housing parts present very close values of deformation. The maximum value in the top cover can be justified by its much thinner cross-section with respect to the rest of the BPE parts.

Lastly, taking into consideration the obtained values of deformation in y, it is worth mentioning that the central region of the BPE will be carefully evaluated in the results yielded for the next investigated physical quantities. While a deflection of approximately 9 mm may not necessarily indicate a problematic region, as it does not correspond to a significant value, examining this zone's stress and strain values will provide a more comprehensive understanding of its behaviour.

9.5.1.2 Equivalent von Mises Stress

The equivalent von Mises stresses are represented in a global light in Figure 9.18, and for each component in Figure 9.19.



(a) **(b)**

Figure 9.18: Explicit dynamics analysis of Phase 2, at 32 km/h: equivalent von Mises stress (true scale). **(a)** BPE with top cover. **(b)** BPE without top cover.

From the evaluation of Figure 9.18, it can be concluded that the distribution of stresses within the entire automotive assembly is quite localised in the impact zone and neighbouring regions. The maximum value of stress found in the rocker panel is about 396 MPa. On the contrary, the BPE structure presents for most of its span relatively low-stress levels in comparison. Hence, it is extremely pertinent to investigate this sudden stress reduction and how this quantity is distributed across each of the components of the assembly (Figure 9.19).

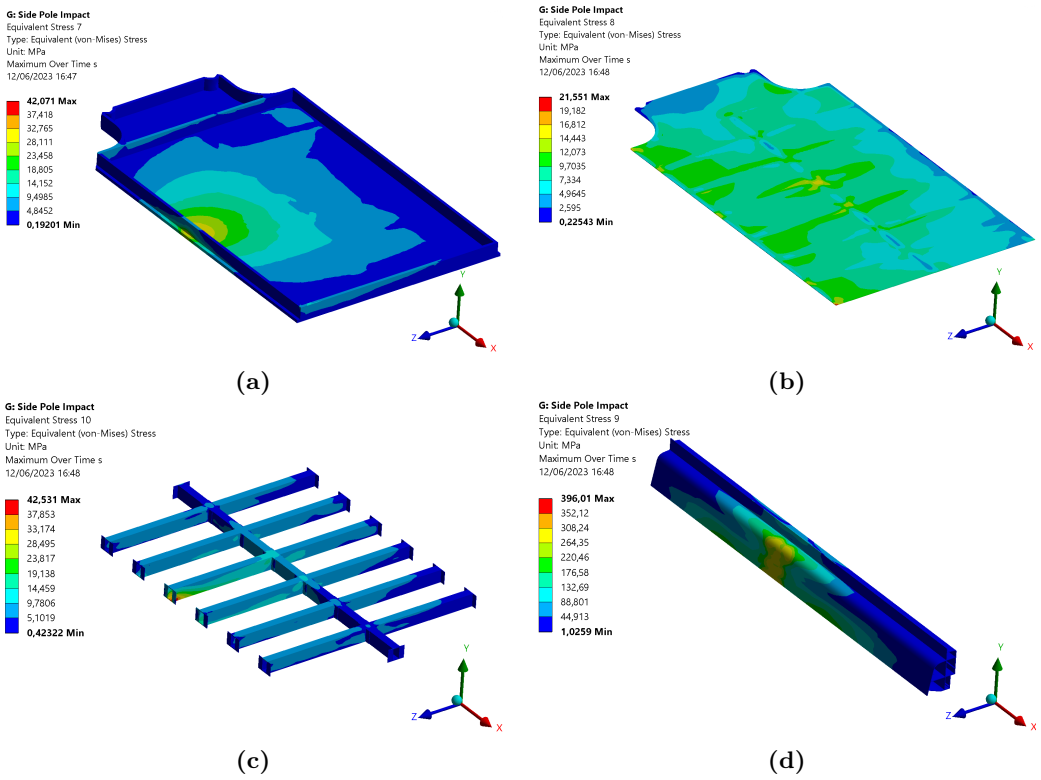


Figure 9.19: Explicit dynamics analysis of Phase 2, at 32 km/h: equivalent von Mises stress (true scale). **(a)** Bottom case. **(b)** Top cover. **(c)** Reinforcements. **(d)** Rocker panel that endures the impact.

Although the maximum value of stress reoccurs in a similar magnitude in the region of the rocker panel, an interesting aspect to note is that the stresses on the BPE components are significantly smaller compared to those achieved in the corresponding analysis of Phase 1. For instance, the bottom case endured a value of 42 MPa compared to the 97 MPa of the previous analysis. Furthermore, while in the analysis of the first Phase, the internal reinforcements were the least stressed components of the BPE, now they are the opposite.

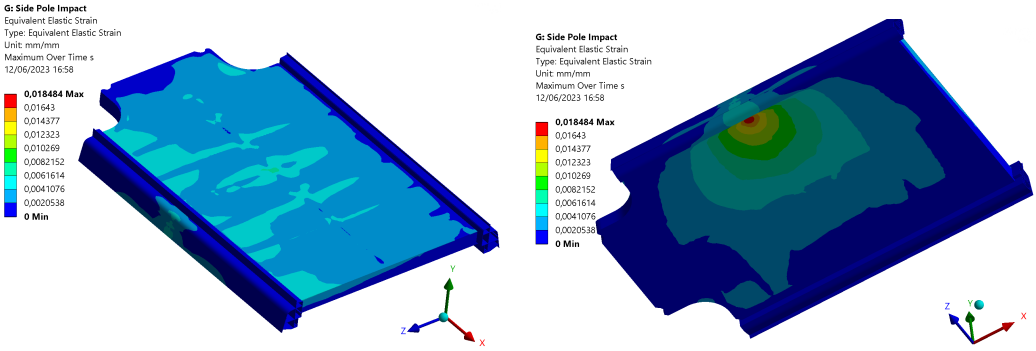
The substantially reduced values of stress that resulted from this analysis are a direct result of the replacement of the Al 6061-T6 for the ABS in the battery housing structure. As was already explained in section 9.3, a flexible construction effectively absorbs and distributes impact energy, resulting in lower stress concentrations. A more rigid structure, on the other hand, may experience higher localised stresses because it resists deformation and transmits impact forces through fewer locations or components. As a result, a more flexible structure can aid in stress reduction and lower the likelihood of structural damage or failure during an impact, which is desired for an automotive component.

Recall, however, that the ABS was introduced in the analysis' engineering data as behaving as an elastic material, which corresponds to a heavy assumption. Given the fact that the yield stress of the material is close to the maximum stress found in two extremely localised points of the bottom case and reinforcements, it is possible that the BPE presents equally localised yielding in these regions. The assessment of the specific ABS material used in manufacturing this automotive component is, thus, essential to achieve a conclusion on this matter. Furthermore, it would need to be evaluated if the small permanent deformation resulting from this phenomenon would pose any threat to the correct functioning of the battery modules. Since no information is available regarding this matter, and due to the

fact that these potential points of plastic deformation are massively localised, for now, it will be considered that the ABS BPE is capable of enduring the given impact event. This will, nevertheless, constitute one of the points of further discussion during the conclusions and limitations of this work.

9.5.1.3 Equivalent Elastic Strain and Equivalent Plastic Strain

The equivalent von Mises strain is discussed next. For illustration purposes, the distribution of this quantity is illustrated in Figure 9.20. In **(a)**, the elastic strain distribution across the entire model is provided, while in **(b)**, the zone where the maximum value for this quantity can be found is represented.



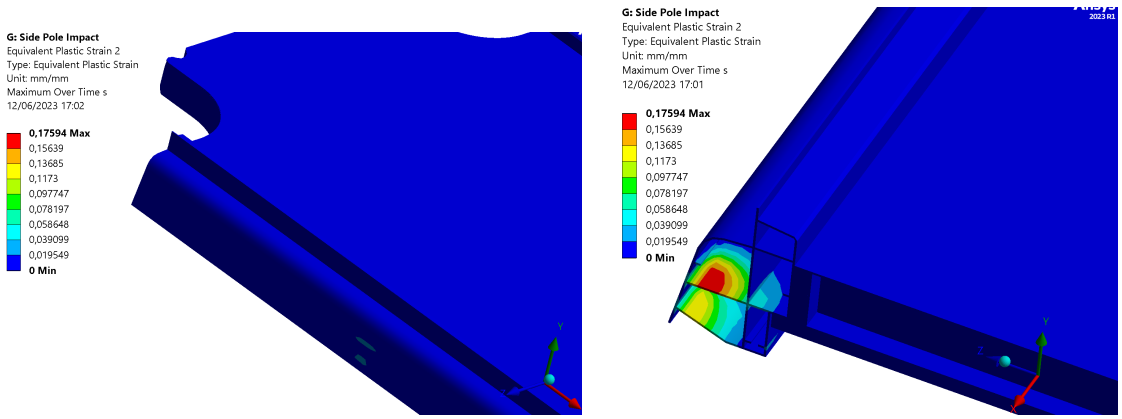
(a) **(b)**

Figure 9.20: Explicit dynamics analysis of Phase 2, at 32 km/h: equivalent von Mises strain (true scale). **(a)** Rocker panels and BPE. **(b)** Bottom view.

In contrast to the findings of the corresponding Phase 1 analysis, the maximum elastic strain values are now located in the bottom case of the BPE.

The maximum intensity of the elastic strain now corresponds to double the value of this quantity in the analysis of Phase 1. Furthermore, this strain presents a much more pronounced distribution within the BPE, and the strain magnitudes in the BPE are similar to those of the impact region of the rocker panel. As anticipated, the discrepancies in material properties between ABS and Al 6061-T6 resulted in the observed differences.

In Figure 9.21, the zone of maximum equivalent plastic strain can be found.



(a) **(b)**

Figure 9.21: Explicit dynamics analysis of Phase 2, at 32 km/h: plastic strain (true scale). **(a)** Rocker panels and BPE. **(b)** Plastic strain in the rocker panel cross-section.

Similarly to the observations in Phase 1, the plastic strain remains extremely localised in the impact zone of the rocker panel to the pole, exhibiting an even more pronounced concentration in the current analysis. The maximum value of plastic strain in the rocker panel is reduced from 0.25 to 0.18, nevertheless still very close values.

Considerations regarding the potential localised yielding occurring in the BPE structure were already discussed in the previous subsection; therefore, nothing is left to assess regarding this matter.

From the multiple results assessed in this section regarding the structure's behaviour to the simulation of Euro NCAP's "Side Pole" test, it can thus be concluded that this model is capable of enduring the test conditions enforced in the analysis settings.

The potentially problematic zones discriminated in section 9.5.1.1 towards the middle of the assembly can be classified as non-problematic since the vertical deflection of 9 mm, which by itself is not substantial, is associated with reduced values of stress and elastic strain of the vehicle, less than 15 MPa and 0.004, respectively.

In summation, it can now be concluded that a colossal improvement to the weight efficiency of the BPE was achieved without significant changes or losses to its mechanical and impact properties. The proposed model is now validated as capable of resisting the Euro NCAP's side crash test, for which it was proposed. This constitutes the achievement of the principal objective of this work and something that aims to be replicated in Phase 3, in which another strategy for the obtainment of weight reductions in the BPE structure is explored.

Finally, it is of great interest to investigate whether the optimised model can withstand an equivalent side pole impact at triple the velocity. This evaluation will be conducted in the following section.

9.5.2 Side Impact at 100 km/h

The results from the Euro NCAP "Side Pole" crash test simulation are not only relevant by themselves but also enable the obtainment of valuable information regarding the influence of the BPE material properties on the crashworthiness of the automotive structure. Furthermore, simulating this crash test for more than one velocity enables a deeper insight into the structure's behaviour for this event.

The simulation portraying the side impact of the automotive assembly into a pole at 100 km/h took 248 minutes, about 4 hours, to run, more or less the corresponding time of the last examined analysis.

The energy summary characteristic of this explicit dynamics simulation is presented in Figure 9.22.

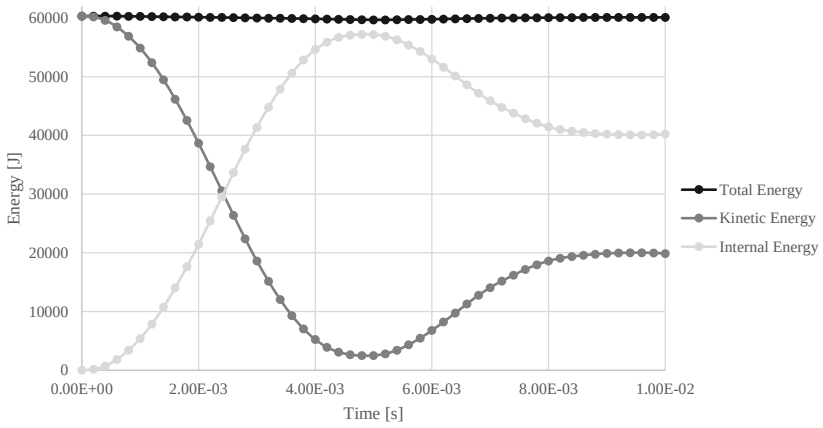


Figure 9.22: Explicit analysis of Phase 2, at 100 km/h: energy summary.

The retrieved plot corresponds, once more, to the anticipated graph for an impact event, and therefore, all the energy considerations discussed for the already presented energy plots remain pertinent to this one.

The maximum compression of the BPE assembly against the rigid pole occurs at the $t = 4.8e-3$ instant, from which the peaks of both the minimum and maximum of the kinetic and internal energy, respectively, decrease in intensity and start to stabilise. In this case, the total energy of the system corresponds to a value of $6e4$ J approximately, about ten times more than that observed in the explicit analysis of this Phase at 32 km/h, something that was also observed in the preceding Phase of this work and can be directly connected to the increase in velocity applied in the model. For the same reason, the impact of the bodies occurs earlier, as does the instant of maximum compression of the rocker panel against the pole, for the same global mechanical properties of the structure in the two simulations of this Phase.

Furthermore, the conversion rate observed in this plot is notably lower compared to the previously presented one, as can be determined by calculating the slope of the energy conversions during the "rebounce" period of the structure. This is consistent with what was also found while comparing the two explicit analyses of Phase 1, and the reasoning for this, which has already been explained, can be found in Chapter 8. Lastly, since the above-mentioned events occurred earlier, a more extensive visualisation of the stabilisation of the two energy quantities is observed

With respect to Figure 8.25, where the energy graph of the Phase 1 simulation at 100 km/h is provided, the total energy of the system is now about half of the $1.2e5$ associated with the former. Moreover, the rate of energy conversion after the situation of maximum compression of the impacting bodies is now much more significant. As explained during the discussion of the previous explicit dynamics simulation results, this is mostly related to the distinct material properties utilised in the BPE solution, as anticipated.

9.5.2.1 Total and Directional Deformations

To provide a more comprehensive understanding of the automotive assembly under the impact, as per usual, in Figures 9.23 and 9.24, frames representing the pole's intrusion in the rocker panels and BPE model, as well as the vertical deflection of the latter, are provided. For uniformity purposes, the scale factor of 2 was employed once more.

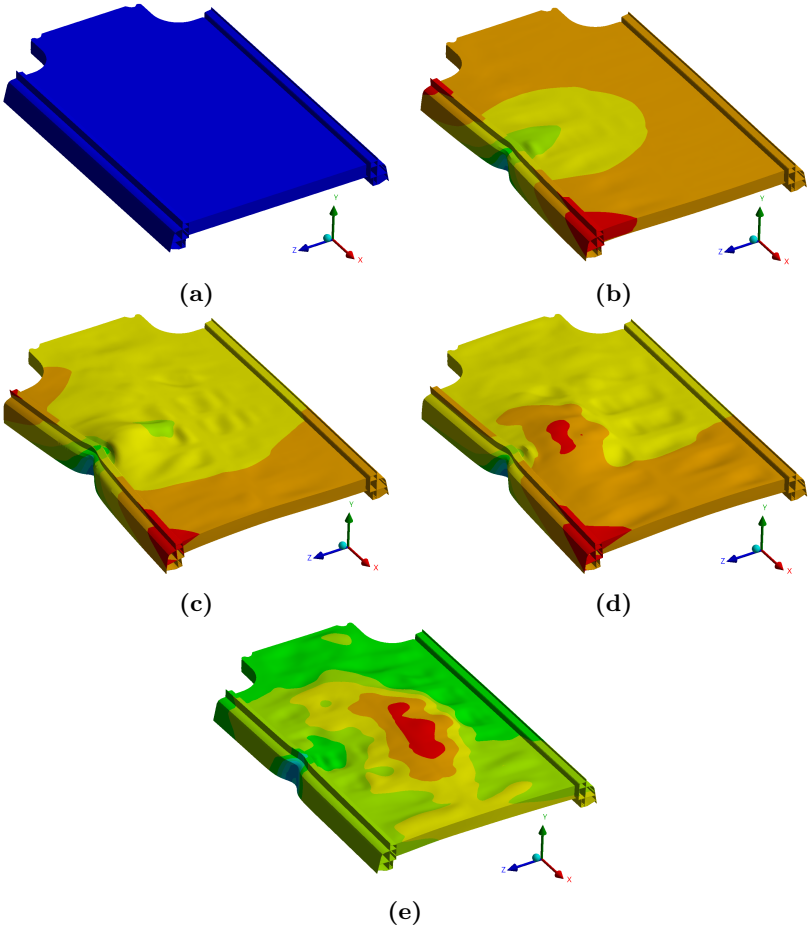


Figure 9.23: Explicit dynamic analysis of Phase 2, at 100 km/h: overview of the deformation of the BPE in time frames (scale of 2). **(a)** $t = 0$ s. **(b)** $t = 2.5e-3$ s. **(c)** $t = 5e-3$ s. **(d)** $t = 7.5e-3$ s. **(e)** $t = 1e-2$ s.

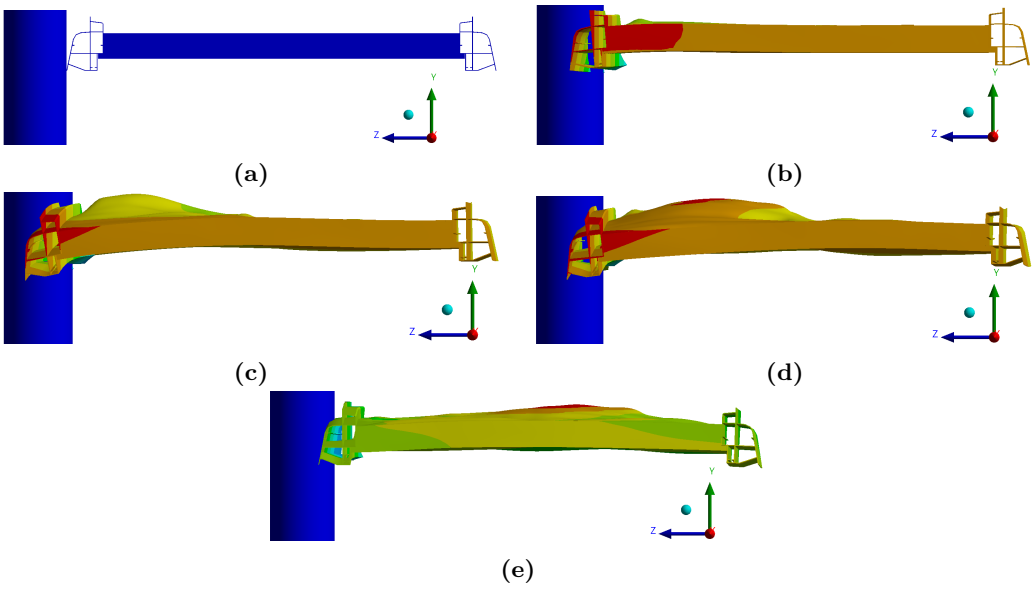
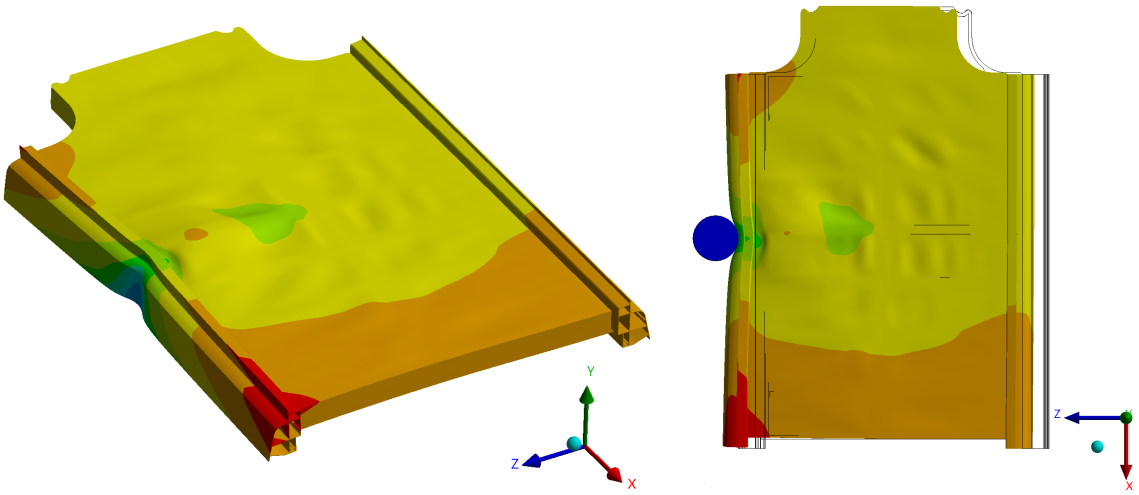


Figure 9.24: Explicit dynamic analysis of Phase 2, at 100 km/h: an overview of the deformation of the BPE, in the $z-y$ plane, in time frames (scale of 2). **(a)** $t = 0$ s. **(b)** $t = 2.5e-3$ s. **(c)** $t = 5e-3$ s. **(d)** $t = 7.5e-3$ s. **(e)** $t = 1e-2$ s.

As can be observed in the Figures above, the deformations of the BPE structure are now much more prominent, with respect to both the preceding explicit simulation of this Phase and particularly to the corresponding one in Phase 1. For the first case, this is explained by the considerable increase of the constant velocity applied to the model and the consequent increase of kinetic energy absorbed by the structure in the impact. The second comparison has to do with the change of the BPE material for a much less rigid and much more flexible one. Thus, this is consistent with what was expected, and the verified behaviour is correct.

Recall, however, that the frames above are associated with a scale factor of 2. To provide an illustration of the real behaviour and deformation of the model, particularly in terms of the intrusion and deflection in z, this is represented in Figure 9.25, in true scale. Globally, similar behaviour of the structure is found, however, with what appears to be a less noticeable intrusion and in-plane deflection, compared to those of Phase 1, for the same velocity impact.



(a) **(b)**

Figure 9.25: Explicit dynamics analysis of Phase 2, at 100 km/h: the intrusion of the pole into the automotive structure (true scale). **(a)** Global view. **(b)** Deformation in the z direction.

The distribution of total deformations within the model is presented on global and individual levels in Figure 9.26.

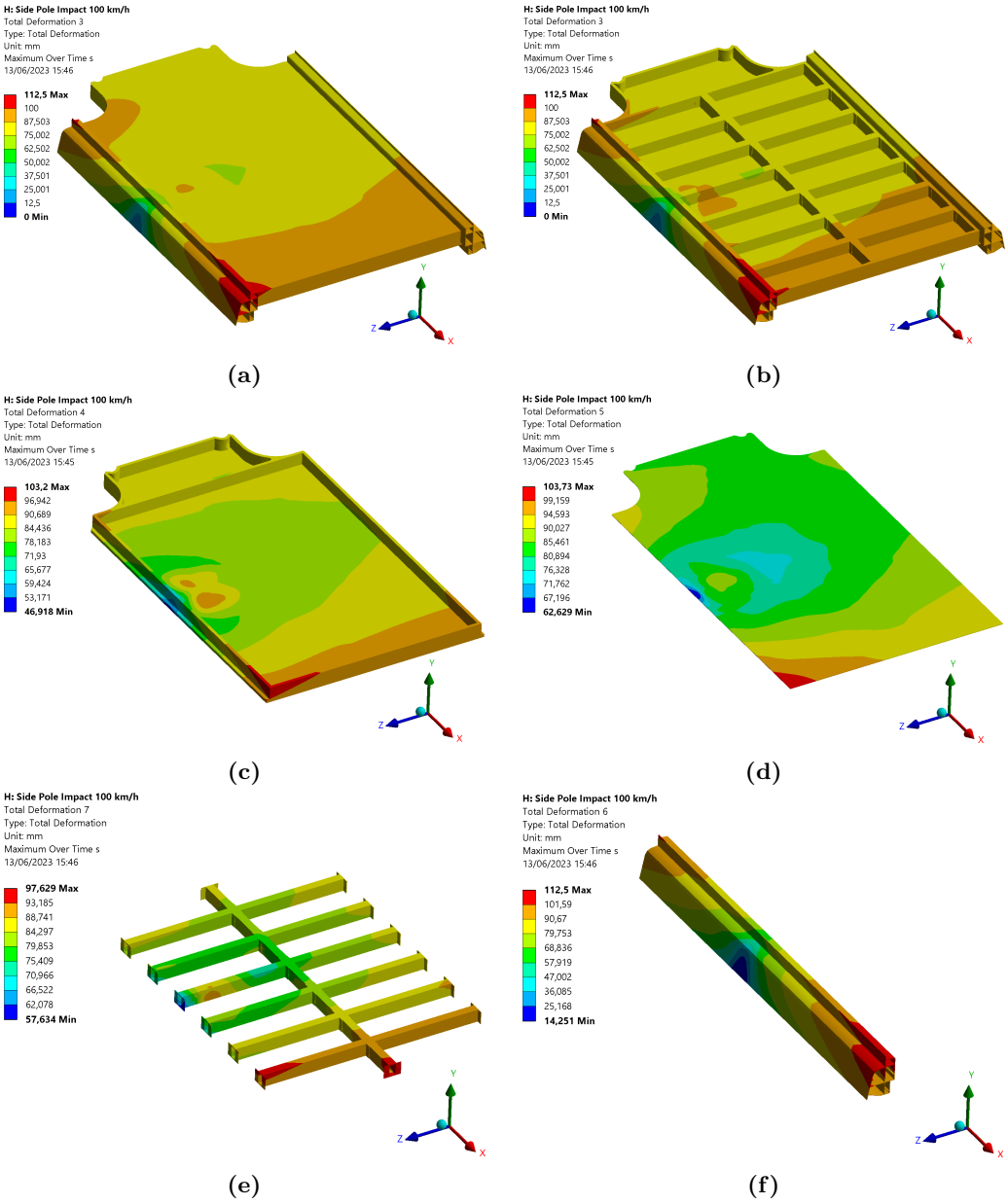


Figure 9.26: Explicit dynamics analysis of Phase 2, at 100 km/h: total deformation distribution at global and component levels (true scale). **(a)** BPE with top cover. **(b)** BPE without top cover. **(c)** Bottom case. **(d)** Top cover. **(e)** Reinforcements. **(f)** Rocker panel.

Regarding the assessment of the directional deformation in y, in Figure 9.27, the distribution of this quantity in the modelled automotive assembly can be observed.

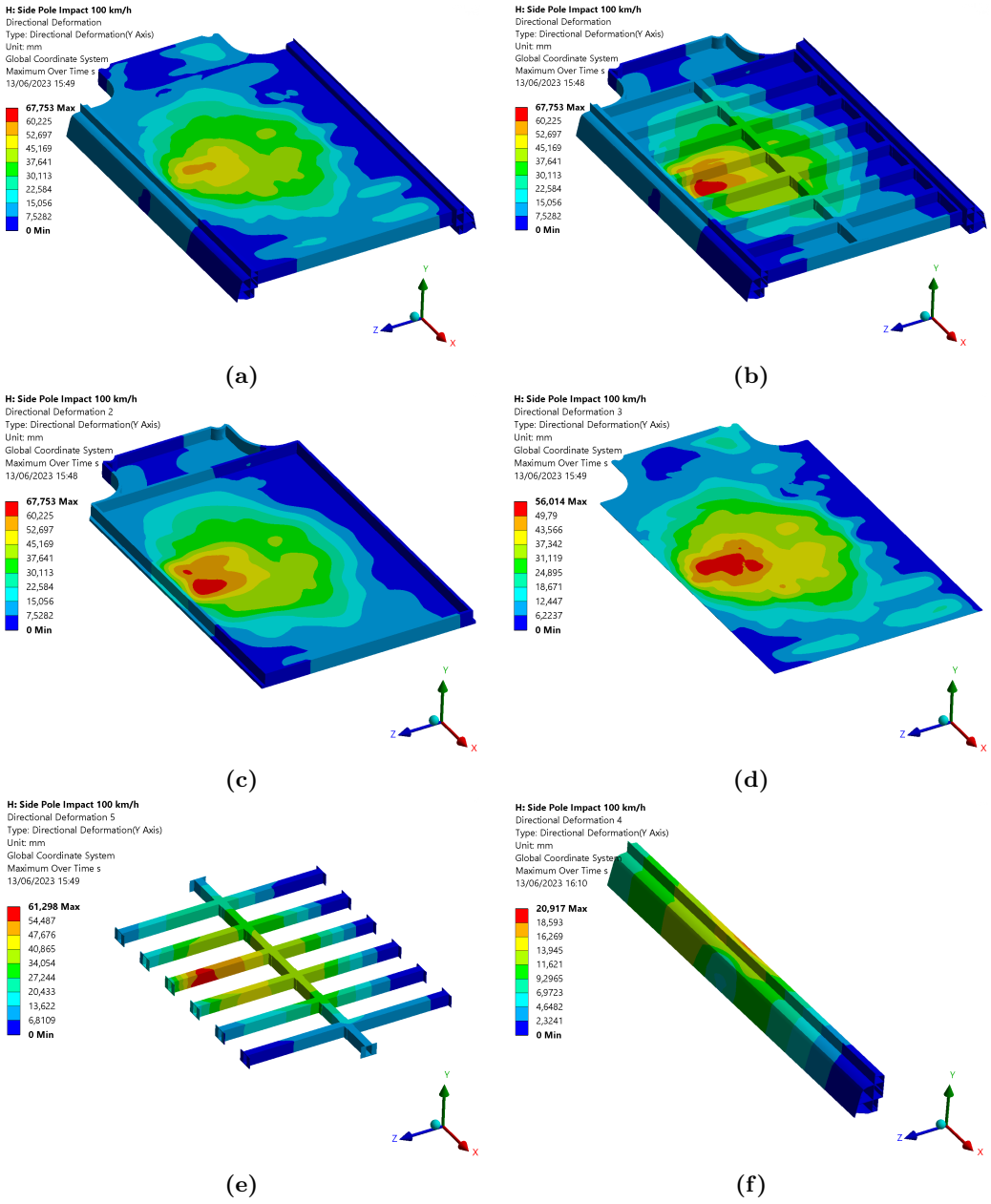


Figure 9.27: Explicit dynamics analysis of Phase 2, at 100 km/h: directional deformation distribution in the y direction at global and component levels (true scale). **(a)** BPE with top cover. **(b)** BPE without top cover. **(c)** Bottom case. **(d)** Top cover. **(e)** Reinforcements. **(f)** Rocker panel.

The disposition of the emerging deformations in the structure is similar to those verified in the earlier explicit simulation. As expected, however, much greater values of this directional deformation are achieved in this analysis when compared to the previously assessed one. For this case, the maximum value of total deformation was found to be around 112 mm, and it is verified in the impacted rocker panel. While this value was identically located in the latter, it corresponded to a significantly lower magnitude of 43 mm. This increase in the orders of magnitude of the deformations of the structure is consistent with the different initial conditions applied to the model.

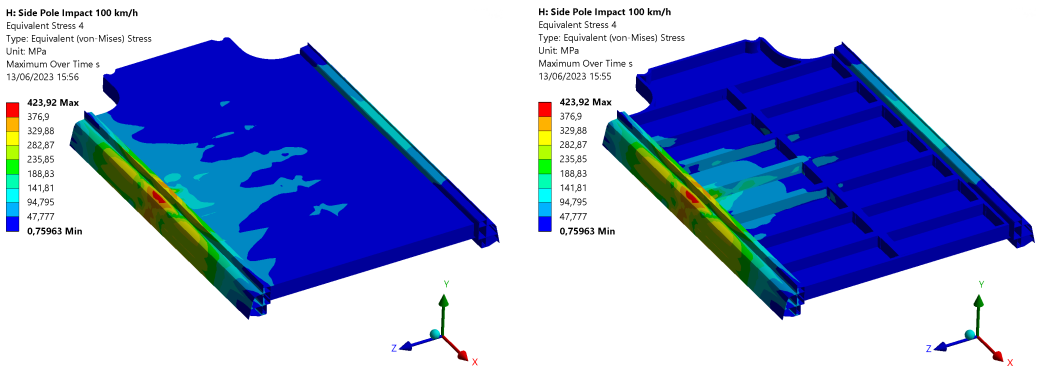
Focusing particularly on the vertical deformation of the structure in y, where the obtained

values of deformation are more meaningful for the already explained reasons, for an initial velocity of 100 km/h being applied in the vehicle, the maximum vertical deflection taking place in a BPE component presents a magnitude of 67 mm, close to the region of the impact of the rocker panel. Similar values can be found in the rest of the battery housing.

This corresponds to a significant level of deformation, much more significant than those of both the previous simulation and the corresponding analysis of Phase 1. This indicates the necessity of further investigation to determine whether the identified zone is indeed a critical area of the BPE structure for the given impact, as it is possible that the integrity of the BPE and the proper functioning of the battery modules may possibly be at risk in this particular region. Therefore, it is crucial to conduct a detailed analysis and assessment to evaluate the potential consequences and implications of the observed deformation in terms of the structural integrity and safety of the battery pack.

9.5.2.2 Equivalent von Mises Stress

To assess the von Mises stress distribution and magnitude present in the complete automotive assembly, consult Figure 9.28.



(a) **(b)**

Figure 9.28: Explicit dynamics analysis of Phase 2, at 100 km/h: equivalent von Mises stress (true scale). **(a)** BPE with top cover. **(b)** BPE without top cover.

A maximum stress value of 424 MPa is observed, primarily concentrated in the impacted rocker panel, as anticipated from a direct impact to the component. In addition, similarly to previous findings, there is a nearly symmetric distribution of stress around the z axis for the entire assembly resulting from the placement of the pole with regard to the automotive structure. In this analysis, however, the stress distribution extends further into the BPE. This is due to the increased transfer of loads into the battery housing, resulting in higher stress levels in those areas.

The maximum value of stress found in the automotive components is evidently increased with respect to the equivalent explicit simulation conducted at 32 km/h. However, it remains approximately the same compared to the value found in the previous Phase (427 MPa).

The stress distribution is now evaluated for the individual components of the assembly in Figure 9.29.

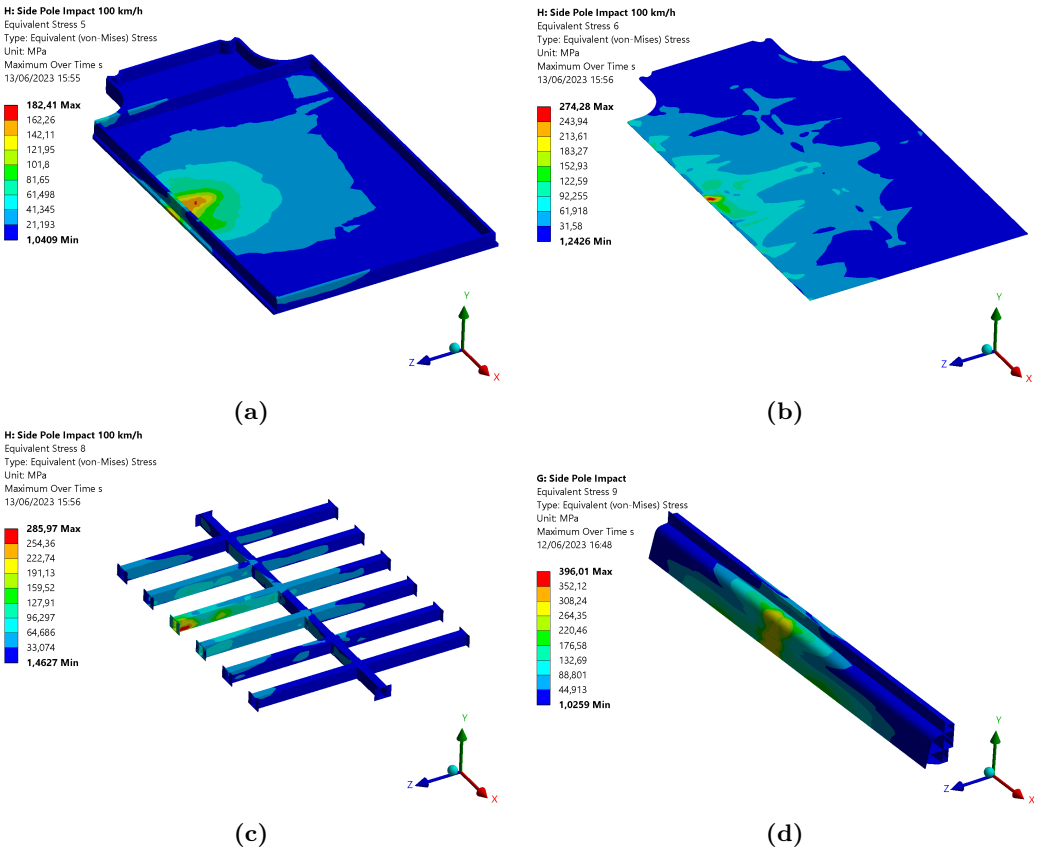


Figure 9.29: Explicit dynamics analysis of Phase 2, at 100 km/h: equivalent von Mises stress (true scale). **(a)** Bottom case. **(b)** Top cover. **(c)** Reinforcements. **(d)** Rocker panel that endures the impact.

The maximum value of stress in the BPE is found in its internal skeleton, in the proximity of the zone of impact of the rocker panel, where the adjacent components, like this one, are compressed. The highest value found for this quantity corresponds to 286 MPa; however, significant values of stress are also verified in the other components of the battery housing.

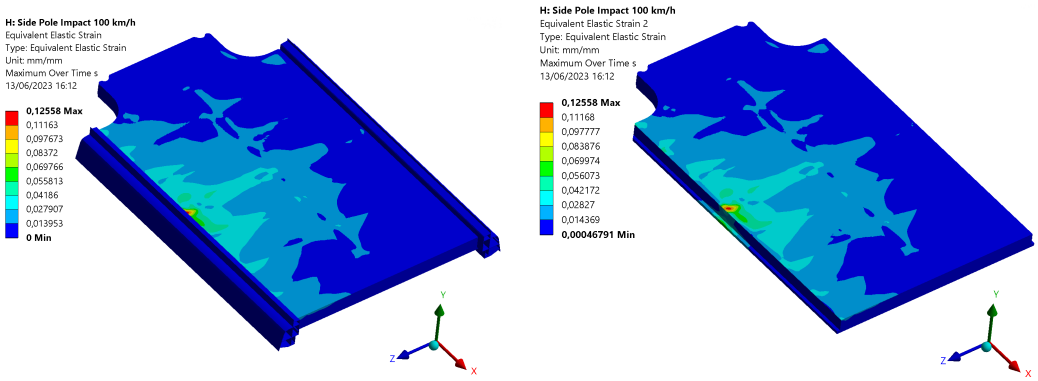
It is important to note that despite the polymer being introduced as elastic material in the engineering data for this analysis, the components to which this material was assigned present stress levels that exceed the yielding stress of the material by as far as 700%. This suggests that the material may have exceeded its elastic limit under the applied loads. Hence, it can be concluded that all the BPE components endure yielding at significantly localised points of maximum compression in the immediate neighbouring regions of the impact.

Finally, when comparing the stress values in the currently assessed battery housing with those obtained in the corresponding Phase 1 analysis, it is noticeable that lower stress levels are found in the ABS BPE. As previously discussed, this can be directly linked to the material properties and characteristics of the ABS BPE of this analysis that cause it to absorb and distribute the impact energy more effectively. This finding further validates the results obtained in the current simulation.

9.5.2.3 Equivalent Elastic Strain and Equivalent Plastic Strain

Lastly, it is interesting to assess the distribution of strains within the structure, both related to the elastic and plastic regimes. To fulfil this purpose, Figure 9.30, regarding the

elastic strain, and Figure 9.31, for the plastic strain, are presented.

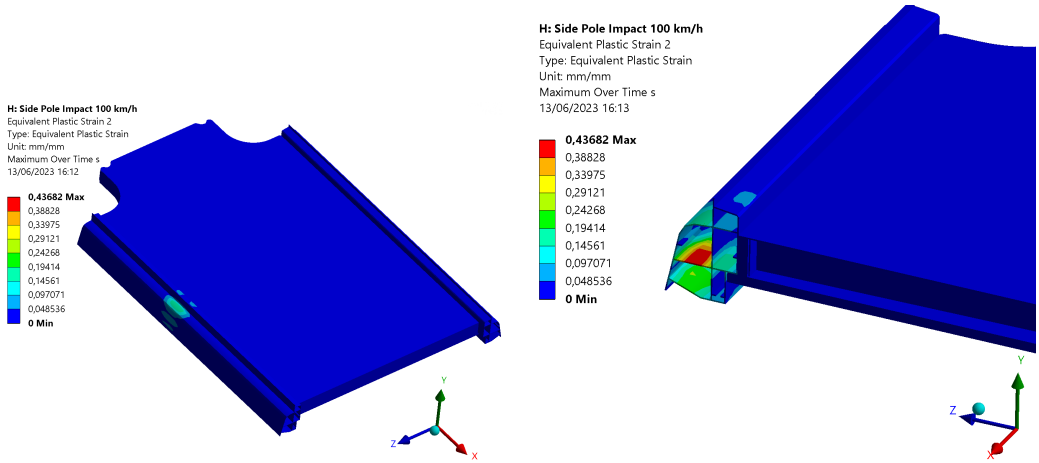


(a) **(b)**

Figure 9.30: Explicit dynamics analysis of Phase 2, at 100 km/h: equivalent von Mises strain (true scale). **(a)** Rocker panels and BPE. **(b)** Exclusively the BPE structure.

The maximum value of elastic strain is found to be around 0.13, and extensive distribution of this quantity within the complete automotive assembly can be observed.

Recall that the highest value of elastic strain occurring on the Al 6061-T6 BPE of Phase 1 for this particular analysis was about 0.006, two orders of magnitude below the currently obtained. This can be justified, once again, by the intrinsic properties of the ABS and Al-SiC foam that enable the occurrence of more prominent and extensive deformations in the structure, thereby due to a more effective absorption and distribution of the strain energy.



(a) **(b)**

Figure 9.31: Explicit dynamics analysis of Phase 2, at 100 km/h: plastic strain (true scale). **(a)** Exterior region of the impacted rocker panel. **(b)** Rocker panel cross-section.

As expected, there is localised plastification in the rocker panel, particularly in the region of maximum compression of the rocker panel against the rigid pole. The highest value obtained for this quantity corresponds to 0.44 and is mostly localised in this vehicle's integral member's interior surfaces. This was consistent with what was seen across all the explicit analyses until this moment.

It must be noted that while no plastic strain is explicitly represented in the BPE solution, yielding occurs in specific areas of the structure, as discussed in the antecedent subsection.

The absence of plastic strain representation is attributed to the assumption of the ABS material being treated as an elastic material, as already explained. Further evaluation of this aspect will be conducted in Chapter 11, where the overall results and limitations of this work will be thoroughly discussed.

Chapter 10

Phase 3: Multimaterial Honeycomb Geometry

This Chapter concerns the third Phase of this work. The present Phase comprises the particular analysis settings and results related to the study of a multimaterial model with a novel geometry.

10.1 Phase 3: Novel Geometry and Al-SiC Material Properties

The aim of this BPE model optimisation was to propose an equally efficient weight reduction methodology as that of Phase 2, but now resorting to the use of a promising emerging material: metal foams.

According to Parveez et al. [145], metal foams are cellular structures that consist of solid materials with a significant volume of gas-filled pores. Their cellular structure makes them materials of exceptional mechanical and physical properties, including lightweight characteristics, high compressive strength, low specific weight, high stiffness, and excellent energy absorption capabilities. This makes them extremely desirable for the aerospace and automotive industries and has attracted massive attention recently. One important advantage of these materials is that they can also be tailored in terms of, for instance, geometry, pore size, and foaming material, which allows for control over their mechanical properties.

Aluminium and aluminium alloys are vastly used in metal foam fabrication, offering advantages such as non-flammability, thermal and sound insulation, mechanical damping, lightweight panels, and impact resistance. Their recyclability further boosts their appeal [145]. As can be concluded, their potential in structural and functional applications, particularly their high specific strength and energy absorption capacity, composes the rationale for their utilisation in this optimisation route.

As was performed to find the ABS utilised in Phase 2, the Granta® [117] material database was used. The same parameters were input as the search constraints, and from the group of resulting materials, the aluminium-silicon carbide (Al-SiC) foam with a density of 0.54 kg/m^3 was chosen.

Some relevant properties of the selected material are presented in Table 10.1, some of which were used to plot an estimate of the stress-strain curve of the material, in Figure 10.1, where the elastic and plastic regimes of the foams are represented.

Table 10.1: Al-SiC foam mechanical properties [117]

Mechanical Property	Value
Young's Modulus, E [GPa]	2.8
Poisson's Coefficient, [-]	0.29
Density [kg/m^3]	540
Yield Strength [MPa]	7.35
Ultimate Strength [MPa]	11.5
Elongation [%]	45

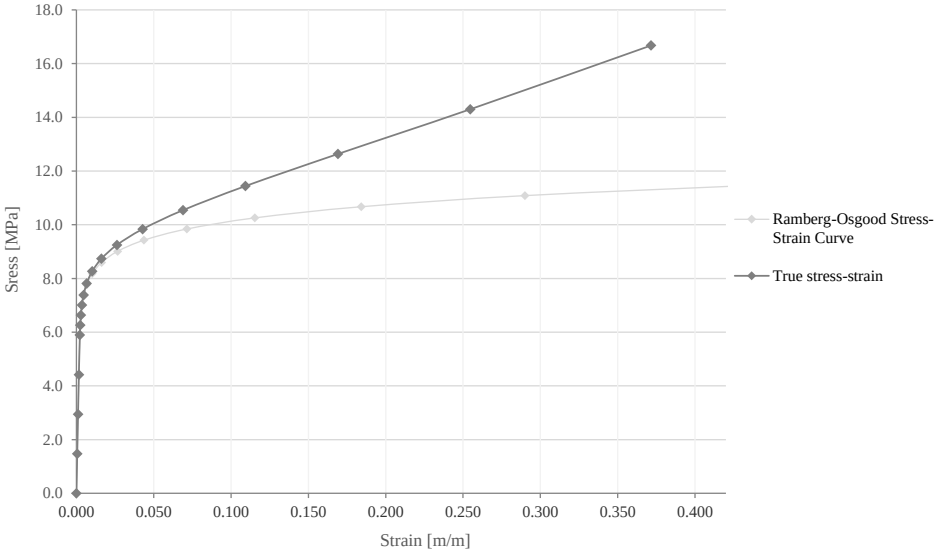


Figure 10.1: Al-SiC foam stress-strain relationship, true and engineering curves (Adapted from [144]).

As was done for the ABS, this material was introduced in Ansys'® engineering data as an assumed exclusively elastic material. Thus, a similar approach will be employed to indirectly evaluate the potential occurrence of yielding of the material in this Honeycomb geometry for a certain load case, as was done for the ABS BPE solution.

The idea behind the employment of this material was to use it in manufacturing a core component for the BPE by replacing the internal reinforcements of the studied geometry until this point. Further enhance the weight efficiency of this newly designed BPE structure in comparison to the "Original model", given the overall satisfactory results achieved in the model of Phase 2, the external components of the BPE, i.e., the top cover and bottom case, would remain in ABS (whose properties can be retrieved in Table 9.1 of the previous Chapter).

The question then relied on the design of the metal foam structure. The design of the metal foam structure was inspired by the illustration provided in Figure 10.2 from the US Patent 8,833,499 B2 [128], attributed to the same automotive manufacturer as the industry solution that influenced both the material and geometry of the model of Phase 1.

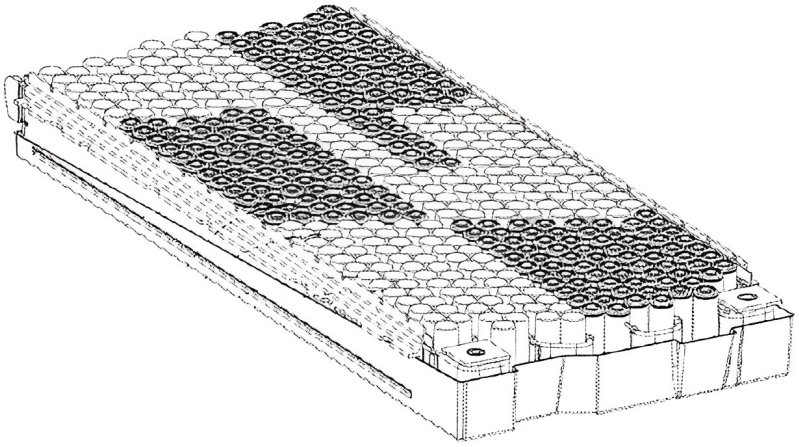
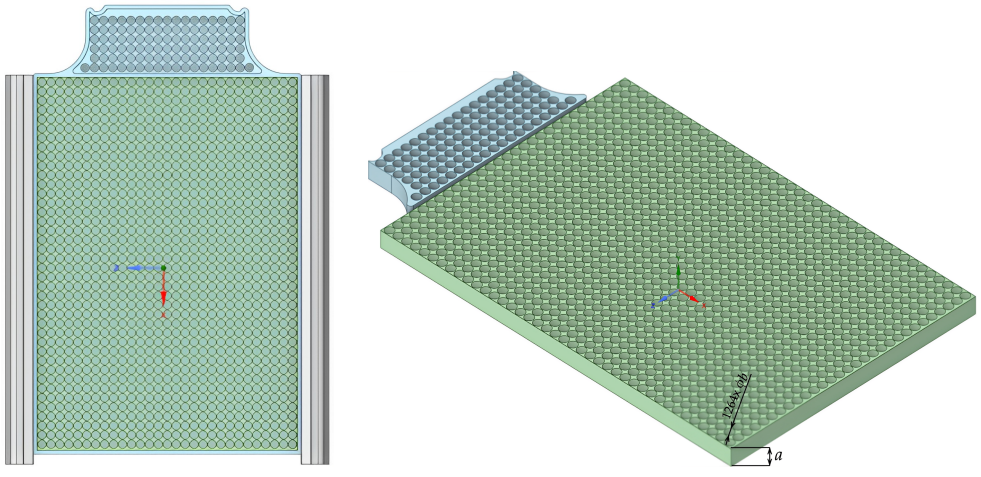


Figure 10.2: Inspiration for the BPE of Phase 3 [128].

The idea for this design was to remove the battery cells from the modules and display them individually and vertically throughout the whole battery pack. Incorporating an internal metal foam structure would serve the purpose of proper positioning and secure attachment of the battery cells and significantly contribute to its mechanical strength and structural rigidity. This ensures the overall integrity and stability of both the battery pack and the vehicle it is inserted in, enhancing the impact properties of the BPE [128].

Moreover, even though this matter is mostly out of the scope of this work, given the excellent thermal isolation provided by the metal foams, the discussed internal structure would act as a thermal barrier. This would only add to the already improved avoidance of thermal runway caused by cell segregation [128].

Finally, the geometry of the Honeycomb-like structure, as it will often be termed in this work, was designed in SpaceClaim and is presented in Figure 10.3. The integration of the geometry into the BPE, along with its relevant dimensions, is illustrated. The measurements themselves can be consulted in Table 10.2.



(a) **(b)**

Figure 10.3: Geometry of the BPE model of Phase 3. **(a)** Top view of the integration of the metal foam component in the BPE. **(b)** Metal foam component with relevant dimensions.

Table 10.2: Dimensions of the cell cavities of the internal metal foam components of Phase 3

Dimension	Value [mm]
a	80
b	46

As can be seen, there are, in fact, two honeycomb components, a major one in the region where fourteen of the fifteen modules laid before, and a minor one in the localisation of the frontal module cavity. The battery cells are evidently placed in both, and in the current design, a total number of 1264 cell cavities can be found.

Both the diameter and length of the cell cavities were selected using as inspiration a particular battery cell solution: the 4680 battery cell, whose name results from its measurements for the aforesaid dimensions. These cells are more robust than other typical industry solutions [146]. Nevertheless, this was simply done to provide a realistic example of possible cell technologies to be utilised in the constructed design. This configuration is solely exemplary of a preferred cell embodiment. It could easily accommodate the usage of different cell chemistries and a different number of the primary battery elements, smaller or greater, as required for the vehicle's performance and coupled constraints [128].

Lastly, it is important to emphasise that no modifications were made to the external geometry of the BPE. This decision was deliberate, as it was deemed crucial to preserve the original integration schemes of the BPE with the BEV (i.e., its connection to the rocker panels, for instance, but not only). This was the rationale for not changing the material of the rocker panels, for example. One of the primary purposes of this work was to achieve weight reduction exclusively through modifications to the BPE without necessitating alterations to the geometry or material of the vehicle's body in white. This approach is convenient and avoids the need to redesign the entire EV or specific subassemblies or components affected by changes in BPE geometry and integration.

In the end, the total mass associated with the model, after the assignment of the suitable materials to each component (i.e., the metal foam to the major and minor core structures, the ABS to the top cover and bottom case), was computed. Table 10.3 shows the achieved individual and total values.

Table 10.3: Mass associated with the BPE model of Phase 3

Part	Material	Density [kg/mm^3]	Volume [mm^3]	Mass [kg]
Top Cover	ABS	$1.185e-6$	9864525.33	11.69
Bottom Cover	ABS	$1.185e-6$	81358780.23	96.41
Foam Core Major	Al-SiC Foam	$5,4e-7$	70951900.35	38.31
Foam Core Minor	Al-SiC Foam	$5,4e-7$	10203485.92	5.51
			Total	≈ 151.92

While the achieved mass of 152 kg is, of course, higher than the 117 kg obtained in the model of Phase 2, it is important to highlight that this optimisation route is more ambitious and laborious. Therefore, if the BPE model produces satisfactory results in the subsequent analyses, it remains an extremely compelling solution for implementation in a BEV. Ultimately, it still achieves a considerable total mass reduction of 100 kg compared to the initial 267 kg of the "Original model" (and, consequently, compared to the estimated

weight of the real BPE solution that inspired this study). Percentage-wise, this corresponds to a reduction of 43% with regard to the mass of the model of Phase 1.

Lastly, it is worth mentioning that the methods employed to represent the weight of the, in this case, battery cells correspond to those of the previous Phases. The same total value of 375.6 kg was considered, discarding any possible small mass difference resulting from the employment of diverse cell chemistries. Furthermore, a methodology that resorted to the use of distributed masses was employed for the static, modal and transient analyses. At the same time, an equivalent pressure to that was applied in the explicit models. The calculations that resulted in the applied magnitudes of the mentioned quantities are presented next for the two approaches.

For the analyses where the distributed masses were applied, the procedure consisted essentially of the application of the total mass value in the 1264 bottom surfaces of the cell cavities. To do this, a projection of the edges of the interior metal foam component in the bottom case was performed. The resulting independent surfaces were then selected, and the value of total mass associated with the primary battery elements was applied.

For the explicit analysis, a pressure equivalent to this value was input in the structure. Instead of calculating the pressure value acting on each of the bottom surfaces of the cell cavities, as was done for Phases 1 and 2 due to the reduced number of cavities, in this case, the total value of pressure acting on the structure due to the presence of the cells was calculated. Therefore, after the projection of the circular edges of the metal foam component into the bottom case of the BPE, all of the surfaces were selected, and the obtained value of pressure was introduced (Equations 10.1 to 10.3).

$$F_{cells\,total} = m_{total} * G = 375.6 * 9.8066 = 3683.36\ \mathbf{N} \tag{10.1}$$

$$A_{total_{bottom\ surf}} = \pi\frac{b^2}{4} * 1264 = \pi\frac{0.046^2}{4} * 1264 = 2.10\ \mathbf{m^2} \tag{10.2}$$

$$P_{cells\,total} = \frac{3683.36}{2.1} = 1753.44\ \mathbf{Pa}\ \simeq 1.753e-3\ \mathbf{MPa} \tag{10.3}$$

The last matter to address is the meshing of this model. To accommodate the significant changes brought by this novel geometry, the mesh parameters introduced in the diverse analyses varied slightly for some of the analyses conducted. Therefore, the employed mesh and the meshed structure's achieved quality will be addressed for each analysis type.

10.2 Phase 3: Static Analysis

Prior to the presentation of the addressed static analysis results, it is relevant to discuss the mesh employed in the model. Recall that for the models of Phase 2, meshes identical to those employed in the models of Phase 1 were used, owing to the fact that both models were characterised by the same geometry. In the current Phase, this equivalency of geometry does not persist. Therefore, a validated mesh is necessary to accommodate the geometry differences that took place in Phase 3.

It was verified, nevertheless, that the mesh utilised in the previous Phases yielded a satisfactory mesh quality, and, thus, the following equivalent mesh parameters were input in the model:

- As was done for the corresponding models of the other Phases, the Physics Preference and the Element Order definitions were left in their default definitions of mechanical and program-controlled, respectively. A global sizing of 25 mm was defined.

- The Automatic method was utilised for all the bodies of the model.
- An element size of 15 mm was defined for all the BPE components, with the exception of the bottom case, owing to its inherently less complex geometry.

For this particular geometry, the spatial discretisation of the model entailed a number of 1164200 nodes and 509433 elements. Once more, the same Tet10, Hex20, and Wed15 quadratic solid elements can be found in the meshed model.

The achieved quality of the mesh, assessed by the element quality, aspect ratio, and skewness mesh metrics, yielded the values presented in Table 10.4.

Table 10.4: Phase 3: Static analysis mesh metrics

	Element Quality	**Aspect Ratio**	**Skewness**
Minimum	$2.7651e-2$	1.1792	$1.3057e-10$
Maximum	0.99978	55.423	0.99955
Average	0.55873	3.1042	0.48152
Standard Deviation	0.20099	1.8618	0.24436

The mesh quality in this newly designed BPE assessment yielded quality values similar to those of Phase 1, with slight improvements in the average values of the element quality and aspect ratio metrics and a small skewness worsening. Overall, despite the existence of a scarce number of distorted elements, this mesh was deemed suitable to be utilised in the analysis. Illustrations of the employed mesh are presented in Figure 10.4 for both global and detailed views.

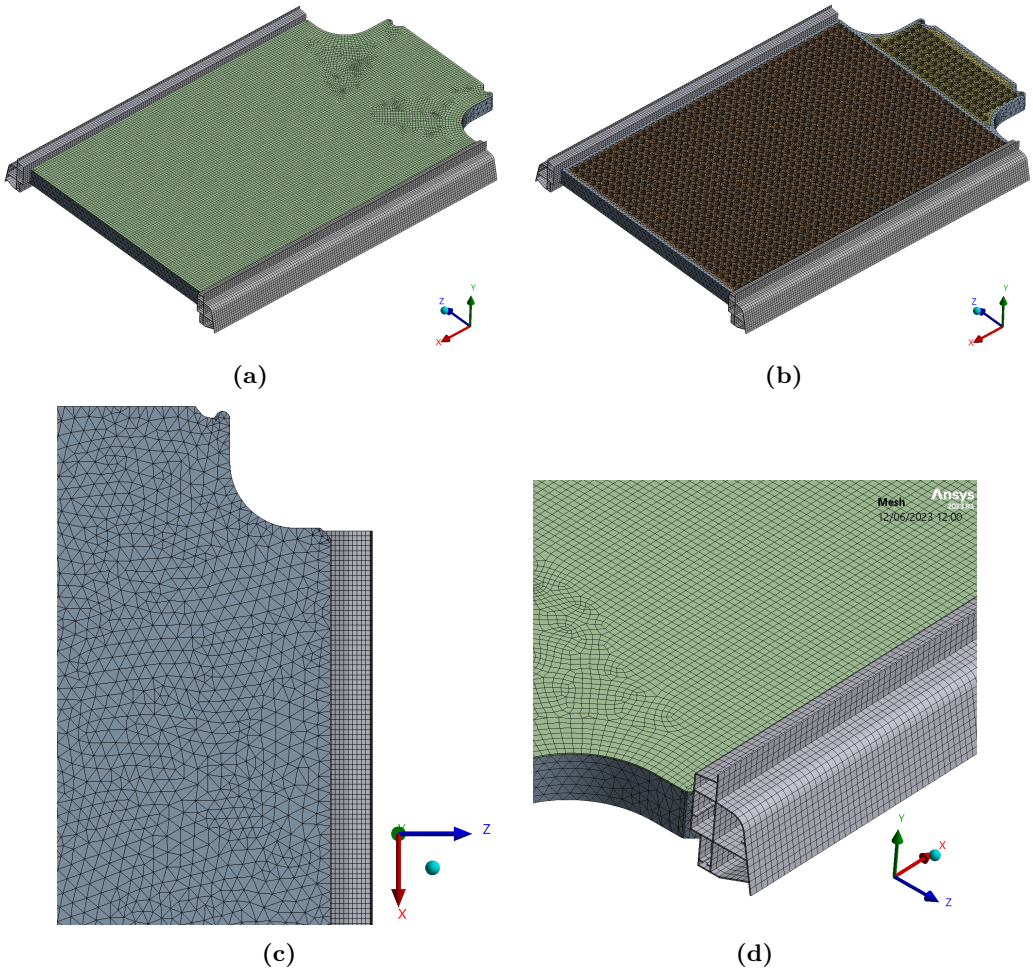


Figure 10.4: Static analysis of Phase 3: mesh applied in the model. **(a)** BPE with cover. **(b)** BPE without cover. **(c)** Bottom case detail. **(d)** Rock panel and top cover detail.

As can be seen in the Figure presented above, it was possible to implement a mapped mesh in most of the model. Hexagonal elements were mostly used in the more simple geometries, while tetrahedrons can, once more, be found in those of more complex designs as they are the best suited for this purpose.

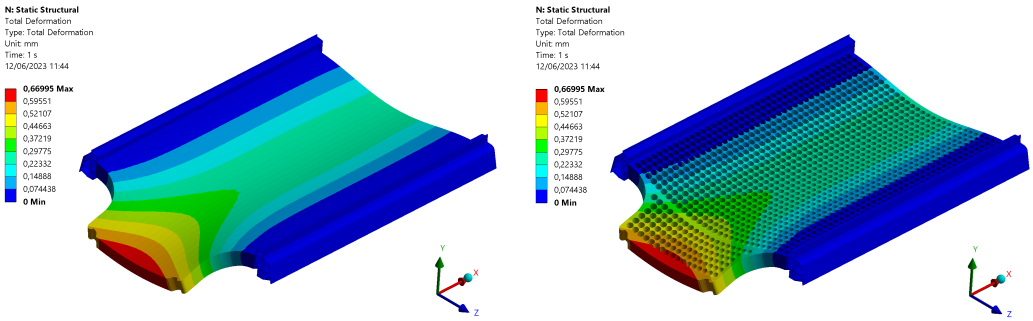
Having finished the complete process of analysis settings definition, the model was left to run, and after 2 minutes, the program yielded results. Although this analysis' elapsed time is still extremely small, especially when compared to the magnitude of those characterising the conducted transient and explicit analyses, note that its value is significantly bigger than that obtained for the static analyses of Phase 1 and 2 (i.e., 28 seconds and 1 minute, respectively). This increase in the elapsed time is a consequence of this model's more complex geometry, and, as such, it is anticipated that the rest of the conducted analysis will also be characterised by lengthier simulation times.

10.2.1 Total and Directional Deformation

Due to the alternations of the internal geometry of the BPE, something that did not take place in Phase 2, it is anticipated that more evident differences in relation to the results of the "Original model" will be obtained in comparison to the ABS model.

Once again, the discussion of the results will initiate from the assessment of the total

deformation endured by the structure and the visualisation of its overall behaviour, enabled by suitable scaling. Both aspects are illustrated in Figure 10.5, where a scale of 360 (the same as of Phase 2) was utilised.



(a) **(b)**

Figure 10.5: Static analysis of Phase 3: total deformation of the BPE (scale of 360). **(a)** BPE with cover. **(b)** BPE without cover.

As can be concluded from the Figure above, the change in the internal geometry of the BPE, just like the material alterations, did not have a significant effect on the behaviour of the structure subjected exclusively to the standard earth gravity. The bending presented by the structure in the previous Phases remains, and the most severe (downwards) deflections are still found in the frontal zone of the automotive structure. Nevertheless, the maximum deformations now occur in a region much closer to the frontal extremity of the BPE instead of directly above the middle zone where the minor metal foam component lies. This is explained by the fact that what was previously the naked module cavity is now filled by an internal reinforcement structure that occupies most of its volume and equips this region with improved stiffness properties. In addition, the maximum value of total deformation in the BPE is approximately 0.67 mm, identically to that of Phase 2, constituting an extremely small quantity that is of negligible magnitude.

Most deformations occur along the y axis; hence, this directional deformation is assessed again for completeness. The distribution of this quantity in the model can be consulted in Figure 10.6.

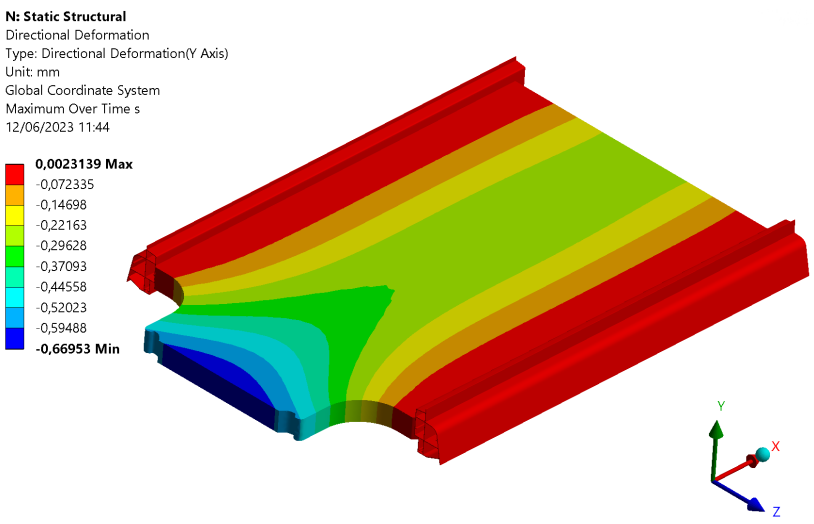


Figure 10.6: Static Analysis of Phase 3: directional deformation in y (true scale).

The symmetric distribution of this directional deformation is also similar to the ones characteristic of the previous Phases, as the symmetry of the geometry and boundary conditions is maintained. As expected, the maximum deformation in y occurs in the same region as the above-mentioned total deformation. In addition, just like the total deformation, this deformation value can be disregarded.

The distribution of this directional quantity is now much "smoother" than the ones obtained for this work's first two numerical Phases. This is a result of the replacement of the reduced number of internal reinforcements by a more uniformly voluminous internal structure. It is relevant to recall, however, that were the modules to be physically represented in Phases 1 and 2, hence contributing to filling the volume of the interior of the BPE, it is likely that a more smooth distribution would also be found for those cases.

10.2.2 Equivalent von Mises Stress

The equivalent von Mises stress is evaluated next, with the distribution of this quantity in the model being illustrated in Figure 10.7.

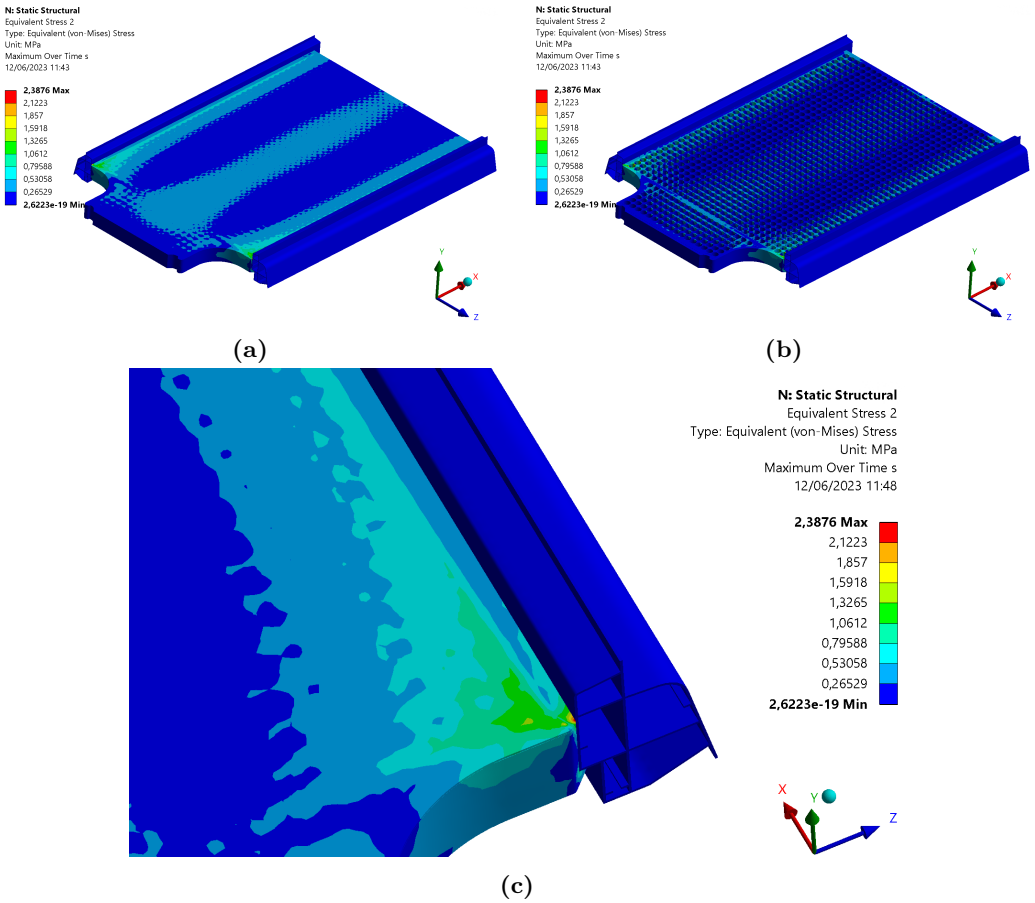


Figure 10.7: Static analysis of Phase 3: equivalent von Mises stress (true scale). **(a)** BPE with cover. **(b)** BPE without cover. **(c)** Most stressed region.

As anticipated and desired, similar behaviour of the structure is verified, and identically reduced values of stress are found in the structure.

Since the boundary conditions remain untouched across all Phases, a stress concentration zone is still found in the structure's corner regions, where the BPE's top cover and bottom

case meet the rocker panels due to the rigidity of the applied constraints. As declared earlier, evaluating the stress in the proximity of the zones of application of concentrated loads and rigid boundary conditions is incorrect; therefore, this maximum value of stress is ignored.

Note, however, that even if this artificial maximum magnitude of stress had any real meaning, it is extremely reduced. Hence, the even smaller real values of stress acting on the structure, studied in regions far from the aforementioned critical zones, can be considered negligible.

In conclusion, the structure is well-capable of withstanding its own weight, which corresponds to one of the basic requirements of a structural automotive component, evidently.

10.3 Phase 3: Modal Analysis

Similarly to what was performed for the static analysis, a novel mesh was created specifically for this Phase's modal and transient analysis. This mesh was designed to accommodate the intricate internal geometry of the BPE and to suit the requirements of these particular analysis types.

This new mesh was defined according to the following parameters:

- In the mesh details, as per usual, the Physics Preference and Element Order were left in their default definitions of mechanical and program-controlled. A global sizing of 10 mm was employed, as it was found that the 12 mm employed in the geometry of Phases 1 and 2 yielded poor quality for the currently assessed one.
- The Patch Conforming Method was utilised to mesh the new metal foam structure, as it was proven to obtain the highest quality meshed for the complex geometry.

These resulted in a mesh with 2858181 nodes and 1256878 elements. Nevertheless, the same element shapes and formulations of the last two Phases were employed. The achieved mesh is represented in Figure 10.8

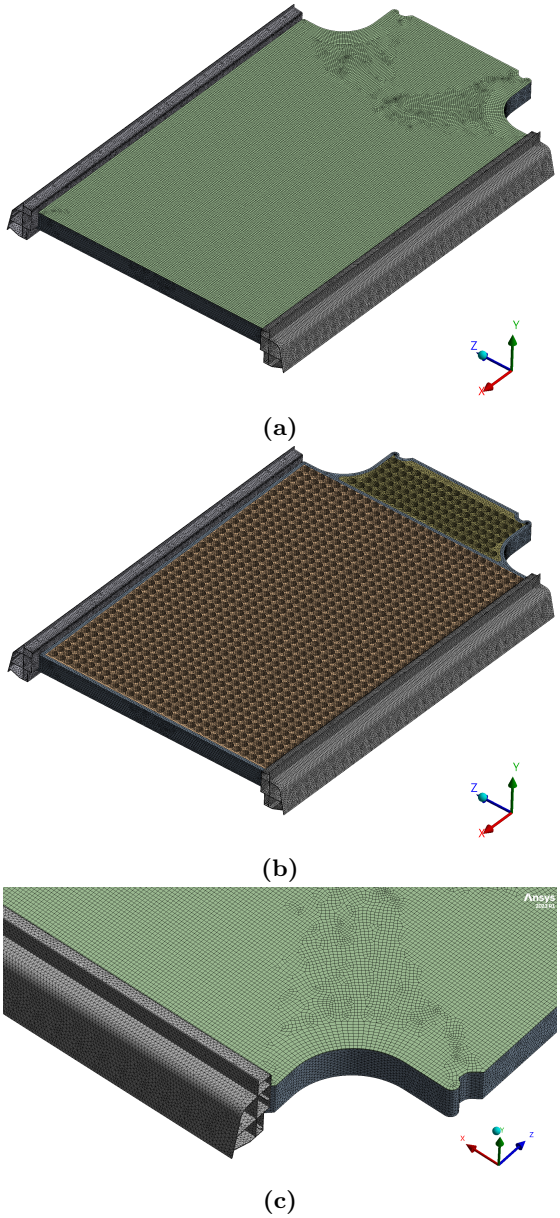


Figure 10.8: Modal analysis of Phase 3: mesh applied in the model. **(a)** BPE with cover. **(b)** BPE without cover. **(c)** Top cover and rocker panels detail.

The mesh was then evaluated, resorting to the relevant mesh metrics. The obtained values for the three quality indicators are presented in Table 10.5.

Table 10.5: Phase 3: Modal and transient analyses mesh metrics

	Element Quality	**Aspect Ratio**	**Skewness**
Minimum	$3.6077e-2$	1.0429	$1.3057e-10$
Maximum	1	115.41	0.99989
Average	0.71109	2.4024	0.35951
Standard Deviation	0.18094	1.0742	0.21914

The mesh quality values obtained for the current analysis were considered adequate for

the present model and are comparable to those obtained in the previous phases. Although there is a scarce number of extremely distorted elements in the mesh, the achieved mesh solution is globally uniform and symmetric, which naturally contributes positively to its quality.

The model was then left to solve for 180 minutes, 3 hours. Note that the time taken for the solver to reach the solution of the modal problem was significantly increased in relation to the two other performed modal analyses. This has to do with the more complex internal geometry of the BPE, as anticipated.

10.3.1 Natural Mode Shapes: Deformation

As performed in the other analysis, the first six natural modes of vibration, and hence the first natural frequencies, of the undamped system were captured and are presented in Figure 10.9. Once more, a scaling of 20 was applied to enable a more direct comparison of the oscillations of the structure across all Phases of this work.

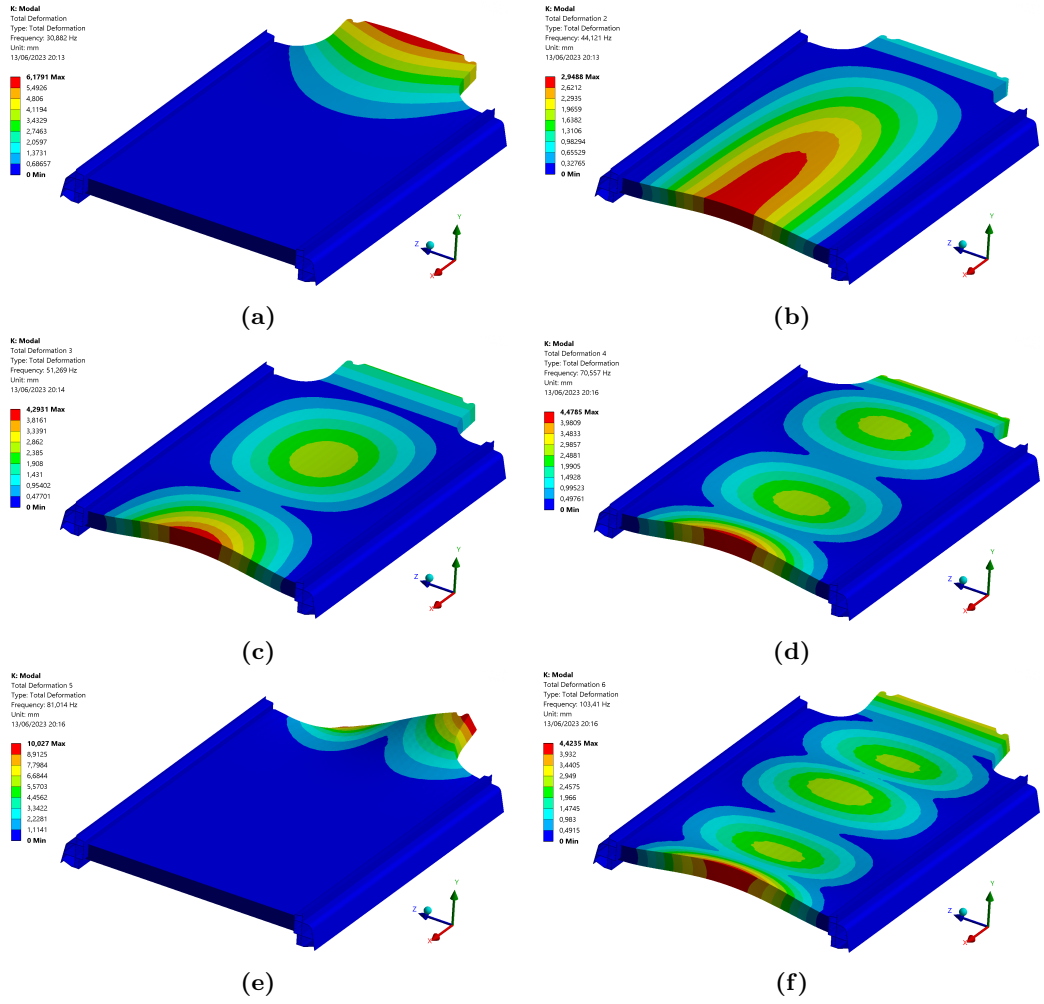


Figure 10.9: Modal analysis of Phase 3: natural mode shapes coupled with the first six natural frequencies (scale of 20). **(a)** 30.882 Hz. **(b)** 44.121 Hz. **(c)** 51.269 Hz. **(d)** 70.557 Hz. **(e)** 81.014 Hz. **(f)** 103.41 Hz.

The 400 natural modes of vibration retrieved from this modal analysis captured a fre-

quency range starting from 30.882 Hz, the fundamental frequency, to 1315.8 Hz, associated with the 400^{th} mode of vibration. Associated with these, deformation ranging from 2 mm to 11 mm is observed within this range of frequencies. However, this quantity's upper value is significantly smaller than those found in the preceding modal analyses associated with the previously assessed BPE models. This is most likely the result of filling most of the internal value of the BPE with the novel internal structure, which leaves less room for the oscillation associated, for instance, with the top cover of the BPE, the component associated with the smallest thickness. This may also indicate that smaller deformation values will be found in the dynamic analyses presented next in this work.

Furthermore, note that the fundamental natural frequency of this system is, in this case, smaller than the one found in Phase 1, which is undesirable, of course, and slightly higher than that of Phase 2. This indicates that the currently assessed system, and therefore automotive structure, will likely present a dynamic behaviour more similar to the one of Phase 2 as a result of more similar mass and stiffness properties.

In addition, from the Figure above, it is possible to anticipate that the more deformed zones in the subsequent transient analysis will be the zone in the foreground of the BPE, as well as the centre of BPE, along the x axis.

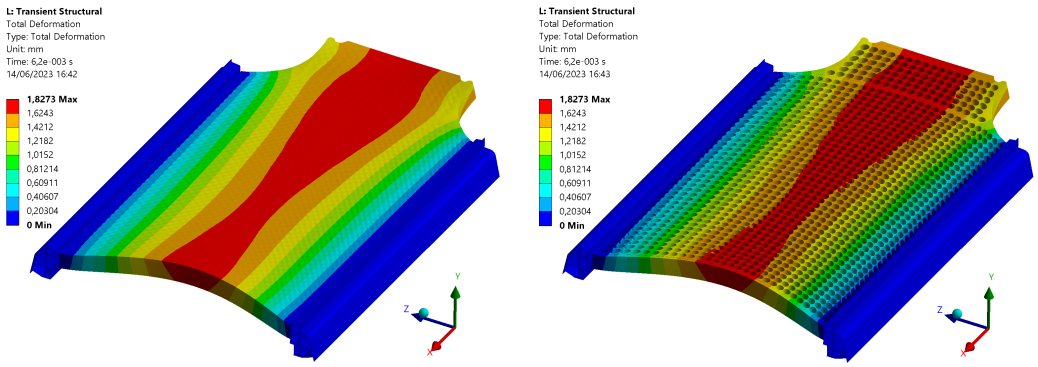
10.4 Phase 3: Transient Analysis

After obtaining the modal analysis and gathering a fundamental understanding of the structure's dynamic behaviour, a transient analysis was conducted, which utilised the set-up and results of the former as initial conditions.

As foreseen, the transient analysis of Phase 3 ran for 210 minutes, considerably more than in the corresponding transient analyses of other Phases.

10.4.1 Total and Directional Deformation

Figure 10.10 illustrates the total deformation endured by the automotive assembly subjected to a frontal crash event, simulated by a peak acceleration of 50 G. Once again, to provide a more direct comparison between the magnitude of this quantity across each of the three transient analyses of this work, a scaling factor of 100 was employed to interpret the achieved results.



(a) **(b)**

Figure 10.10: Transient analysis of Phase 3: total deformation distribution in the BPE and rocker panels (scale of 100). **(a)** BPE with cover. **(b)** BPE without cover.

In the instant at which the structure presents its highest values of total deformation, $t = 6.2e - 3$ s, a maximum constant magnitude of 1.8 mm is observed along the symmetry axis of the geometry across its entire span. Once again, the anterior modal analysis provided significant insight into the behaviour of the structure. This represents an increase from the 0.06 mm yielded in Phase 1 and about the same as the 2mm found in Phase 2. This evidences the similarities in the reduced rigidity of the two polymeric BPE solutions and how they behave differently as compared to the all-metallic assembly. Note, notwithstanding, that the aforesaid value of total deformation is negligible, as it was in the previously discussed transient analyses.

Figure 10.11 allows a more detailed examination of the distribution of this quantity for each of the components of the model.

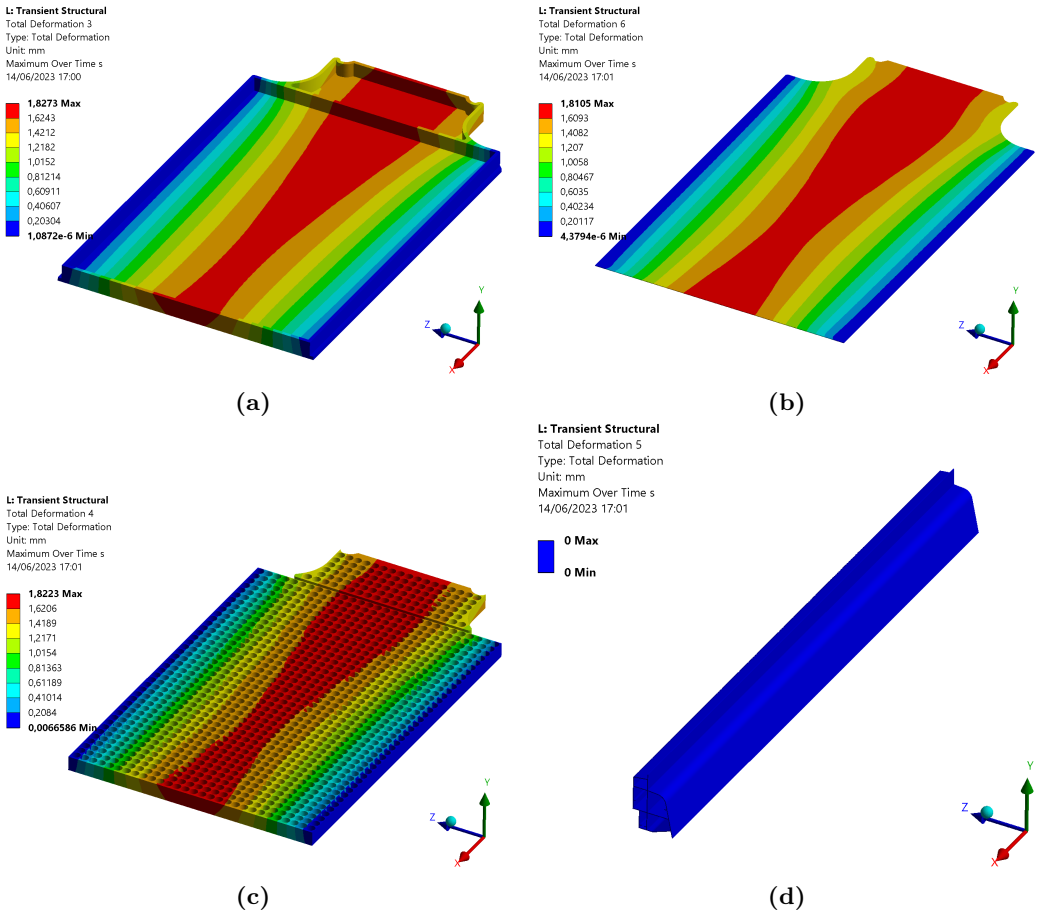


Figure 10.11: Transient analysis of Phase 3: total deformation distribution at the component level (true scale). **(a)** Bottom case **(b)** Top cover. **(c)** Reinforcements. **(d)** Rocker panel.

As concluded in the transient analyses of the preceding Phases, owing to the boundary conditions introduced in the model that aimed at simulating a realistic frontal crash of the structure, each of the components of the BPE presents extremely low values of deformation. This was in line with the expected outcome, given the fact that equivalent findings were found in the earlier assessed transient analyses, as well as due to the fact that, in a real frontal impact to the BEV, the BPE is heavily protected from direct impacts and, subsequently, from the resulting deformations and stresses.

To assess the deflection of the structure in y, similarly to what was performed before,

this quantity is illustrated in Figure 10.12, both at global and individual levels.

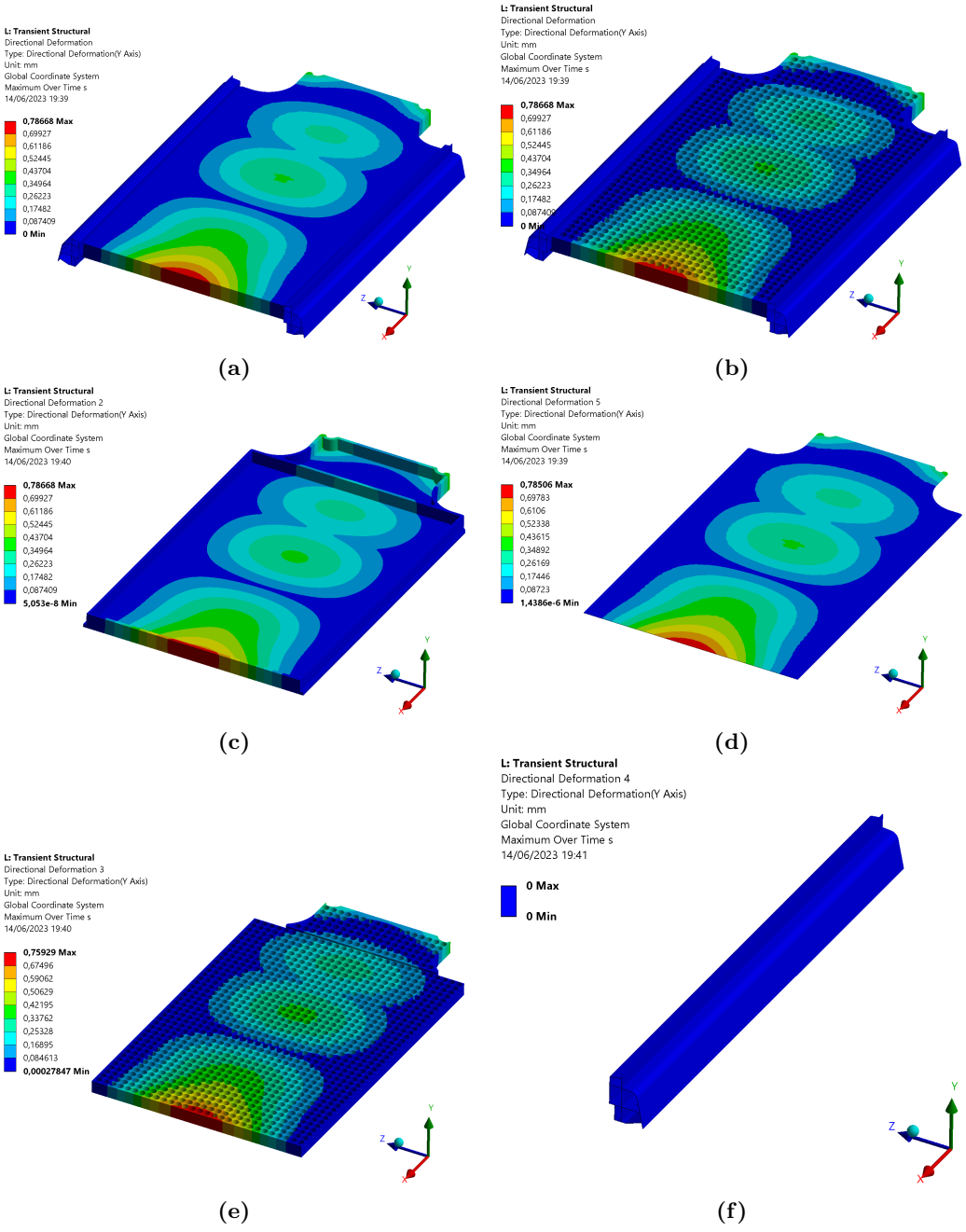


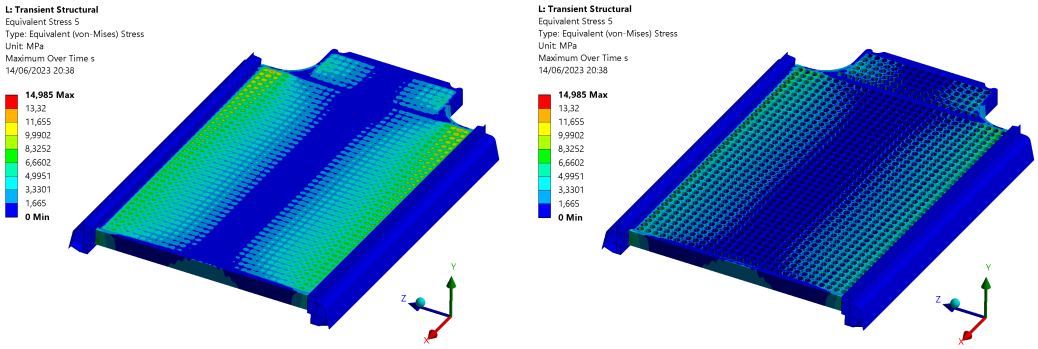
Figure 10.12: Transient analysis of Phase 3: directional deformation distribution in y, at the global and component levels (true scale). **(a)** BPE with cover. **(b)** BPE without cover. **(c)** Bottom case. **(d)** Top cover. **(e)** Reinforcements. **(f)** Rocker panel.

The zones of maximum deflection of the structure in y correspond to those found in the modal analysis, which justifies the rationale for its performance prior to a transient structural simulation.

The maximum values of this quantity in the model corresponds to about 0.79 mm and can be found in the central regions of all of the BPE parts.

10.4.2 Equivalent von Mises Stress

The assessment of the von Mises stress in the model starts, as usual, at the global level. Figure 10.13 illustrates the distribution of this physical quantity in the entire model.



(a) **(b)**

Figure 10.13: Transient analysis of Phase 3: equivalent von Mises stress distribution in the BPE and rocker panels (scale of 100). **(a)** BPE with cover. **(b)** BPE without cover.

The first inference to be extracted from the Figure above is that the disposition of the stresses in the structure is identical to those observed in the models of Phases 1 and 2, provided with a distinct internal geometry. This is consistent since the novel internal part safeguards the symmetry of the BPE.

The highest value of stress originating in the structure is of 15 MPa, slightly smaller but overall comparable to the corresponding values yielded in the other transient analyses.

To further investigate the stresses actuating in each of the components of the BPE solution, Figure 9.10 can be consulted.

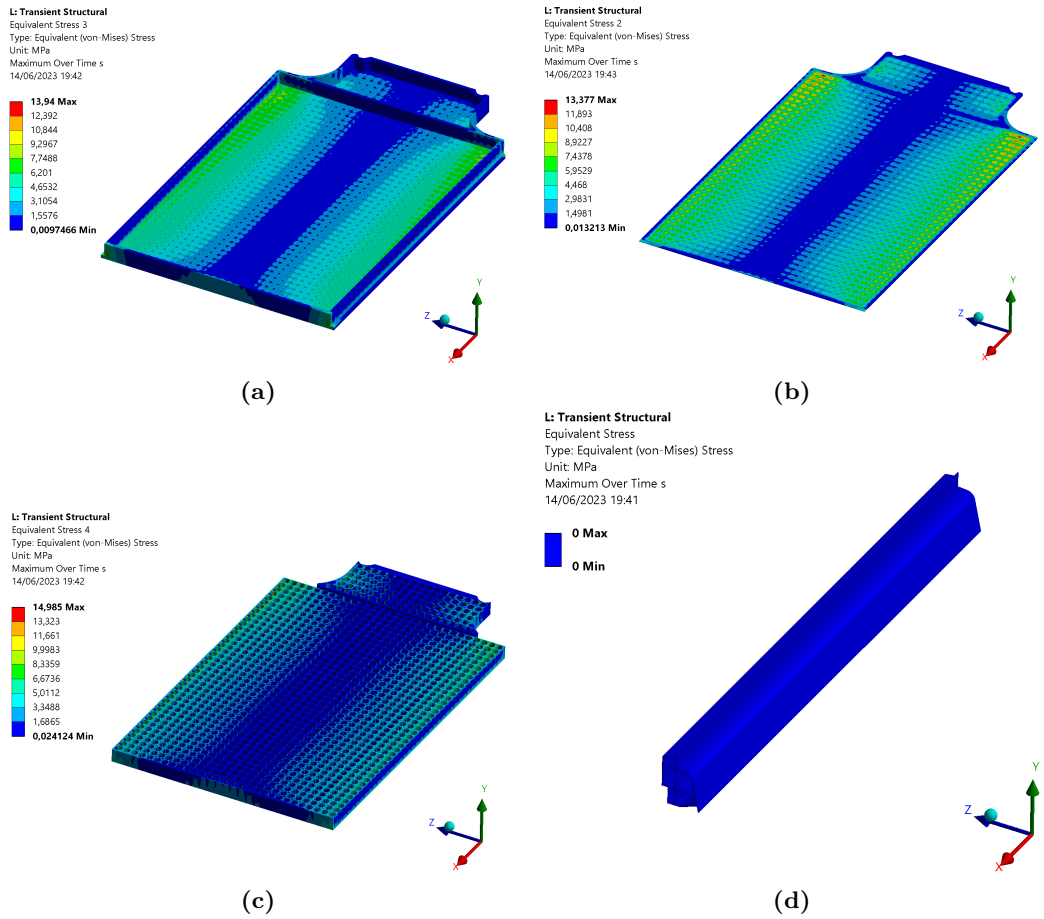


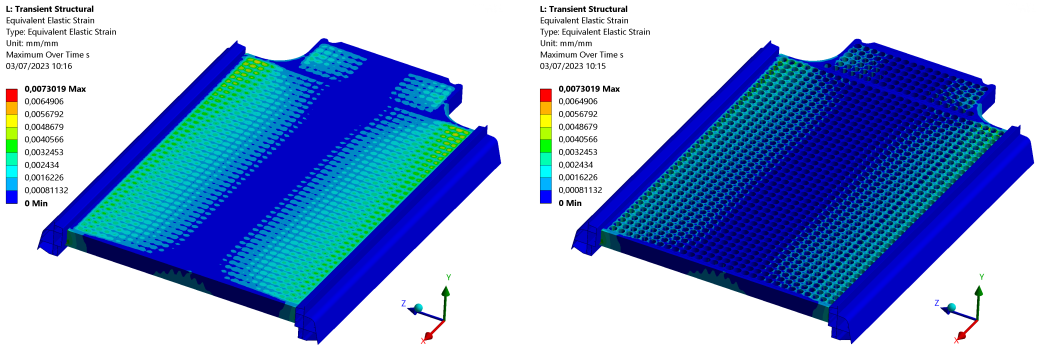
Figure 10.14: Transient analysis of Phase 3: equivalent von Mises stress distribution at the component level (true scale). **(a)** Bottom case. **(b)** Top cover. **(c)** Reinforcements. **(d)** Rocker panel.

The maximum stress values observed in the structure are concentrated in the same regions as in the other models. These stress concentrations are once more attributed to numerical artefacts arising from the application of rigid constraints to the structure and potential considerations related to the spatial discretisation of the model.

In summation, it can be concluded that, for the simulated crash situation, the stresses originating in the Honeycomb BPE do not exceed those corresponding to the elastic limit of the materials assigned to its manufacture, as desired.

10.4.3 Equivalent von Mises Strain

The last aspect to address related to the transient analysis of Phase 3 corresponds to the elastic strains. The distribution of this quantity in the model is showcased in Figure 10.15.



(a) **(b)**

Figure 10.15: Transient analysis of Phase 3: equivalent von Mises strain distribution in the BPE and rocker panels (true scale). **(a)** BPE with cover. **(b)** BPE without cover.

Once again, the frontal crash simulation results in extremely small strain values, the biggest of which is solely 0.01. This justifies that the elastic strains are not only exclusively presented at a global level but also that the plastic strains are not assessed, as they are nonexistent in the structure.

Moreover, the strain distribution obtained is in everything similar to those yielded in the other Phases, which further contributes to the identification of the present BPE as an ambitious yet valid approach.

10.5 Phase 3: Explicit Dynamics Analysis

The Euro NCAP "Side Pole" test was then simulated at its stipulated velocity and 100 km/h, similar to what was performed in the preceding analysis.

The model was meshed using the same parameters as those introduced in the static simulation of this Phase, following the same approach employed in Phases 1 and 2. As a result, the inherent alterations in the default definitions of the Physics Preference and Element Order of the mesh, arising from variations in the underlying formulations of the analyses, were kept as explicit and linear, as suggested by the program.

The aforesaid alterations in the mesh details lead to the obtainment of alternative element types and different element quality values, although a visually identical mesh is found in the model. The model was then meshed using linear elements, Tet4, Hex8, and Wed6.

Overall, 213246 nodes and 211323 elements can be found in the mesh. The quality of the obtained spatial discretisation of the model was then evaluated, resorting to the pertinent mesh metrics for this particular analysis, as presented in Table 10.6.

Table 10.6: Phase 3: Explicit analysis mesh metrics

	Element Quality	**Aspect Ratio**	**Characteristic Length [mm]**
Minimum	0.13828	1.0038	0.97856
Maximum	0.99997	45.102	24.045
Average	0.64234	2.9162	8.7062
Standard Deviation	0.20506	1.3585	4.9732

It can be stated that an identical mesh quality to those achieved in the already assessed explicit analysis was reached. The minimum characteristic length found for an element, which limits the time step size according to the CFL stability condition, is still around 1

mm. The average aspect ratio is also similar, at 2.9, and the average element quality achieved is now about 0.64. This is adequate for the present analysis type.

The model was now fully ready to be run for the stated constant velocities.

10.5.1 Side Impact at 32 km/h

Starting with the assessment of the simulation of the rigid pole side impact at 32 km/h, it is pertinent to note that Autodyn took 388 minutes, approximately 6 hours and a half, to reach the solution to the problem. Recall that the corresponding analysis of Phase 1 and Phase 2 took 236 minutes and 172 minutes for the same purpose. The increasingly complex geometry of this analysis and the small alterations in the mesh parameters justify this disparity between the elapsed times.

As per usual, the energy plot representative of the event being simulated is presented in Figure 10.16.

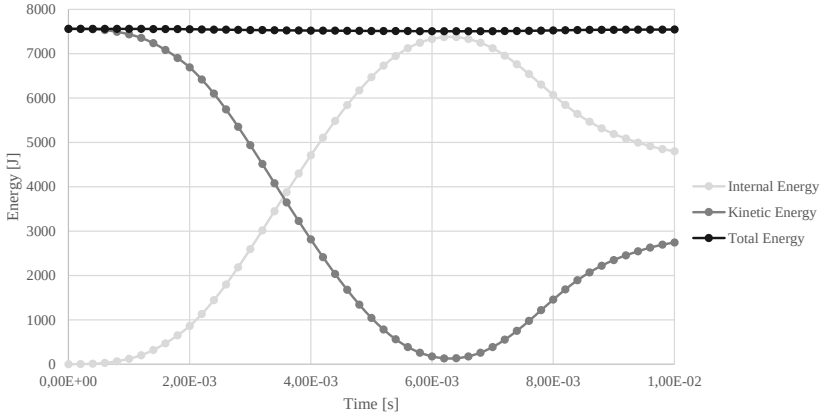


Figure 10.16: Explicit analysis of Phase 3, at 32 km/h: energy summary.

The total value of the energy of the system corresponds, in this case, about 7500 J, as opposed to the 12402 J of the corresponding analysis of Phase 1 and 6000 J of Phase 2. The instant of maximum intrusion of the pole into the rocker panel corresponds to $t = 6.20e - 3$ s, about 1 ms earlier than in Phase 1 and about 0.4 ms after than in Phase 2, of similar total energy. The increased proximity of these factors to the ones obtained in Phase 2 of this work attests, once again, to the similarity of their global mechanical properties, especially when compared to the metallic BPE solution.

A rapid conversion between the kinetic and internal energies of the system is observed, both before and after the timestamp of maximum compression of the automotive assembly. In fact, there is a rapid "rebounce" of the structure after this instant, which is related to the substantially contained deformation and, therefore, energy absorption of the automotive structure at the induced velocity. This rapid energy diffusion within the model is similar to the one observed in Phase 2. It can therefore be related to the reduced intrinsic stiffness of these solutions compared to the more rigid solution of Phase 1.

10.5.1.1 Total and directional deformation

Figures 10.17 and 10.18 portrays the intrusion of the pole into the rocker panel and the deflection observed in the BPE, at different instants of the analysis time. To aid with the visualisation of both within the model and to facilitate the establishment of comparisons

and conclusions regarding the behaviour of the other BPE solutions for this specific analysis, the scaling factor of 2 remained employed. Moreover, to provide a deeper comprehension of the behaviour of this particular model without the need to accommodate the aforesaid comparisons, the deformations in the structure can be consulted in true scale in Figure 10.19, along with its behaviour in z, from the top view of the BPE. A small indentation accompanied by an equally reduced deflection of the structure in the aforesaid direction is verified, as was expected from the already assessed Phases of this work.

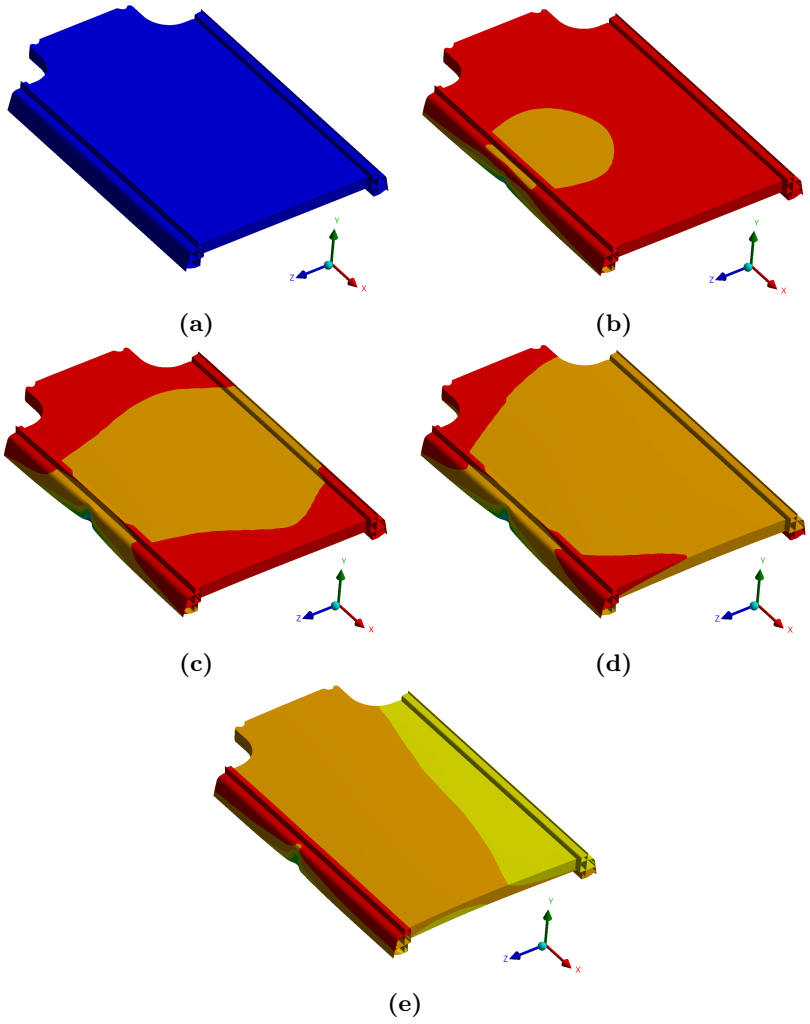


Figure 10.17: Explicit dynamic analysis of Phase 3, at 32 km/h: overview of the deformation of the BPE in time frames (scale of 2). **(a)** $t = 0$ s. **(b)** $t = 2.5e - 3$ s. **(c)** $t = 5e - 3$ s. **(d)** $t = 7.5e - 3$ s. **(e)** $t = 1e - 2$ s.

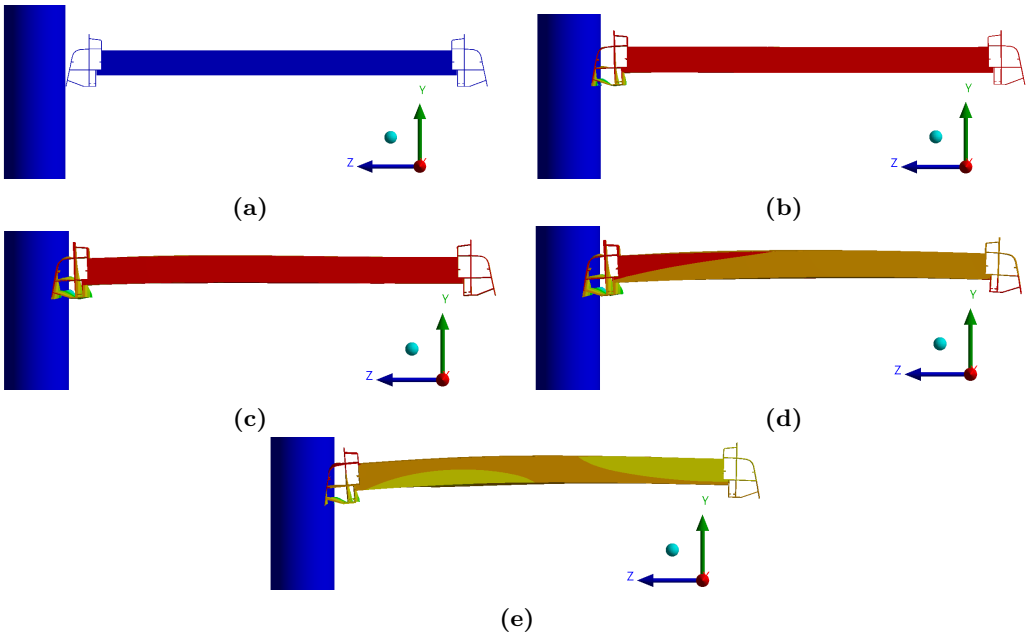


Figure 10.18: Explicit dynamic analysis of Phase 3, at 32 km/h: overview of the deformation of the BPE, in the $z-y$ plane, in time frames (scale of 2). **(a)** $t = 0$ s. **(b)** $t = 2.5e-3$ s. **(c)** $t = 5e-3$ s. **(d)** $t = 7.5e-3$ s. **(e)** $t = 1e-2$ s.

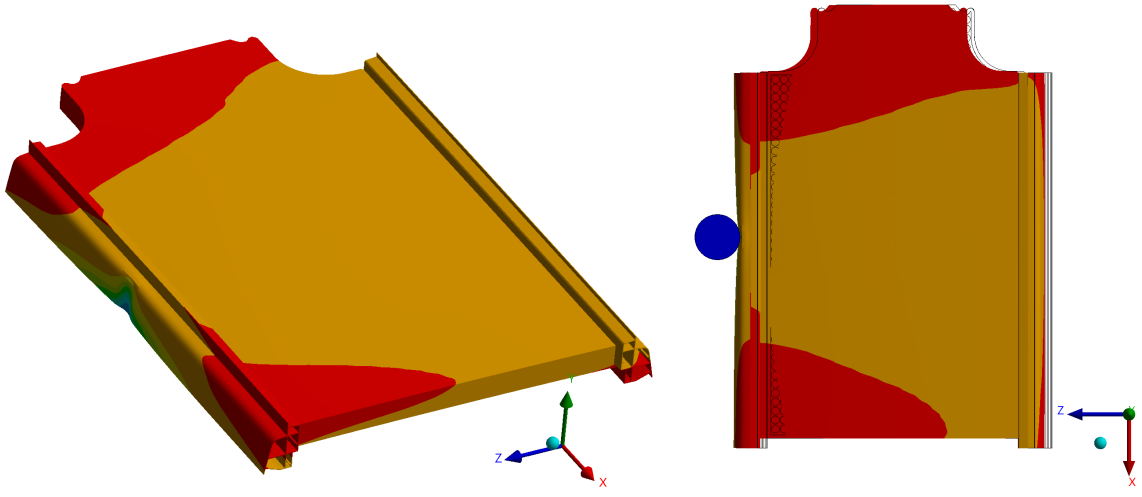


Figure 10.19: Explicit dynamics analysis of Phase 3, at 32 km/h: intrusion of the pole into the automotive structure (true scale). **(a)** Global view. **(b)** Deformation in the z direction.

As can be concluded from the scaled Figures, the Honeycomb BPE presents a deflection in y and an intrusion visually similar to that observed in the ABS solution for the same applied velocity. Al 6061-T6 presented, in turn, a much more rigid behaviour, as was already foreseen from the energy plot. Therefore, both the stated similarity and disparity were to be expected, given that the overall mechanical properties of the BPE of Phase 3 are much more similar to the one manufactured in ABS than the metallic one. This makes sense since the external parts of the currently assessed BPE solution are also "manufactured" in the above-mentioned thermoplastic.

Next, it is pertinent to assess the distribution of total deformations within the model, both at global and individual levels. These are illustrated in Figure 10.20.

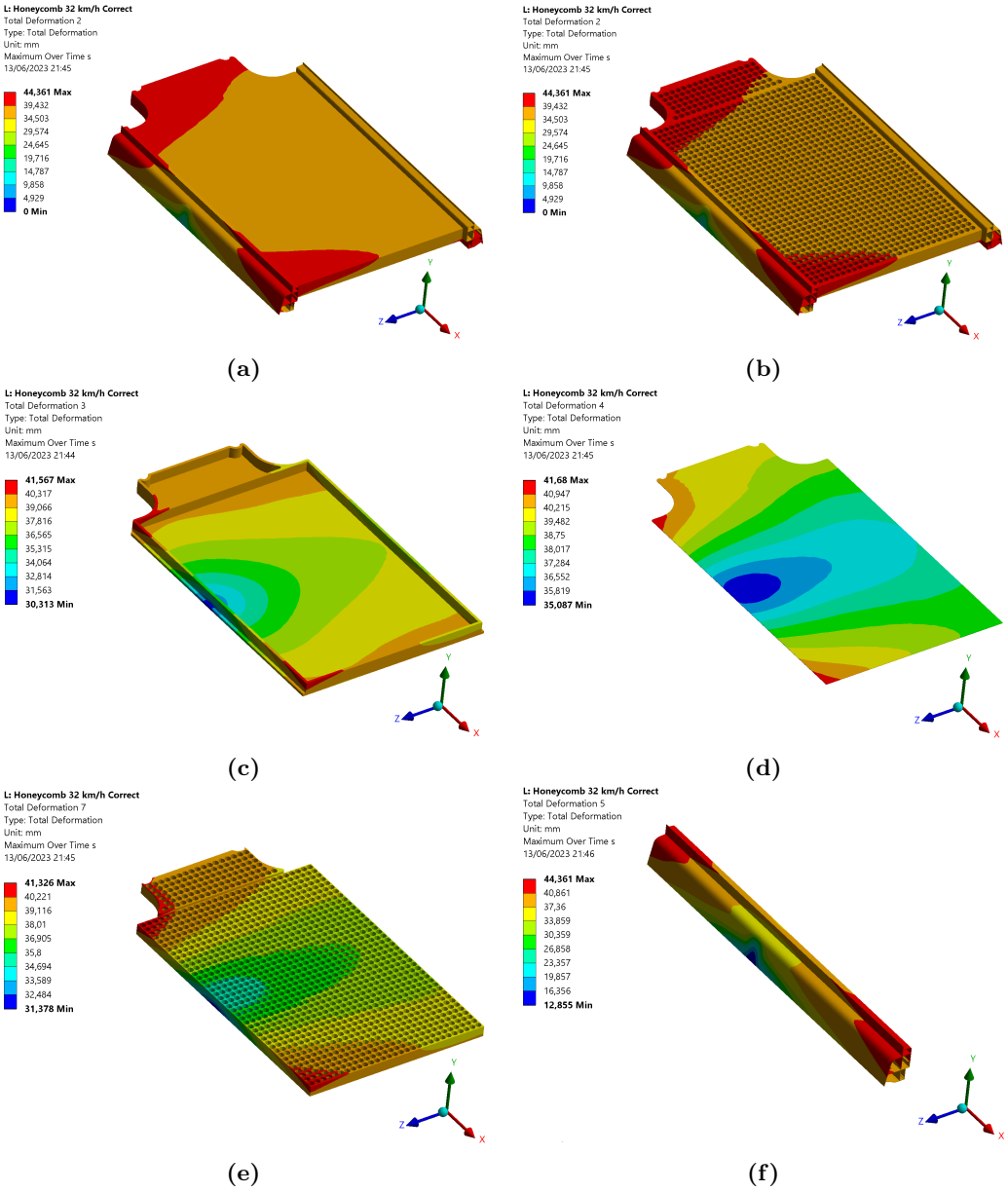


Figure 10.20: Explicit dynamics analysis of Phase 3, at 32 km/h: total deformation distribution at global and component levels (true scale). **(a)** BPE with top cover. **(b)** BPE without top cover. **(c)** Bottom case. **(d)** Top cover. **(e)** Reinforcements. **(f)** Rocker panel.

The obtained values of total deformation are not only similar to the ones achieved in Phase 2 but also to the ones found in Phase 1. However, the symmetric distribution of this quantity, both in the complete structure and within each component, is more comparable to the ones resulting from Phase 2. This is once again justified by similarities of the employed materials. Owing to this similarity, both in the properties and in the behaviour of the global structure, any remaining considerations regarding comparing this BPE solution to the Al 6061-T6 one can be found in the discussion of the corresponding analysis in Phase 2.

Regarding the assessment of the directional deformation in y, the distribution of this

quantity in the modelled automotive assembly is displayed in Figure 10.21.

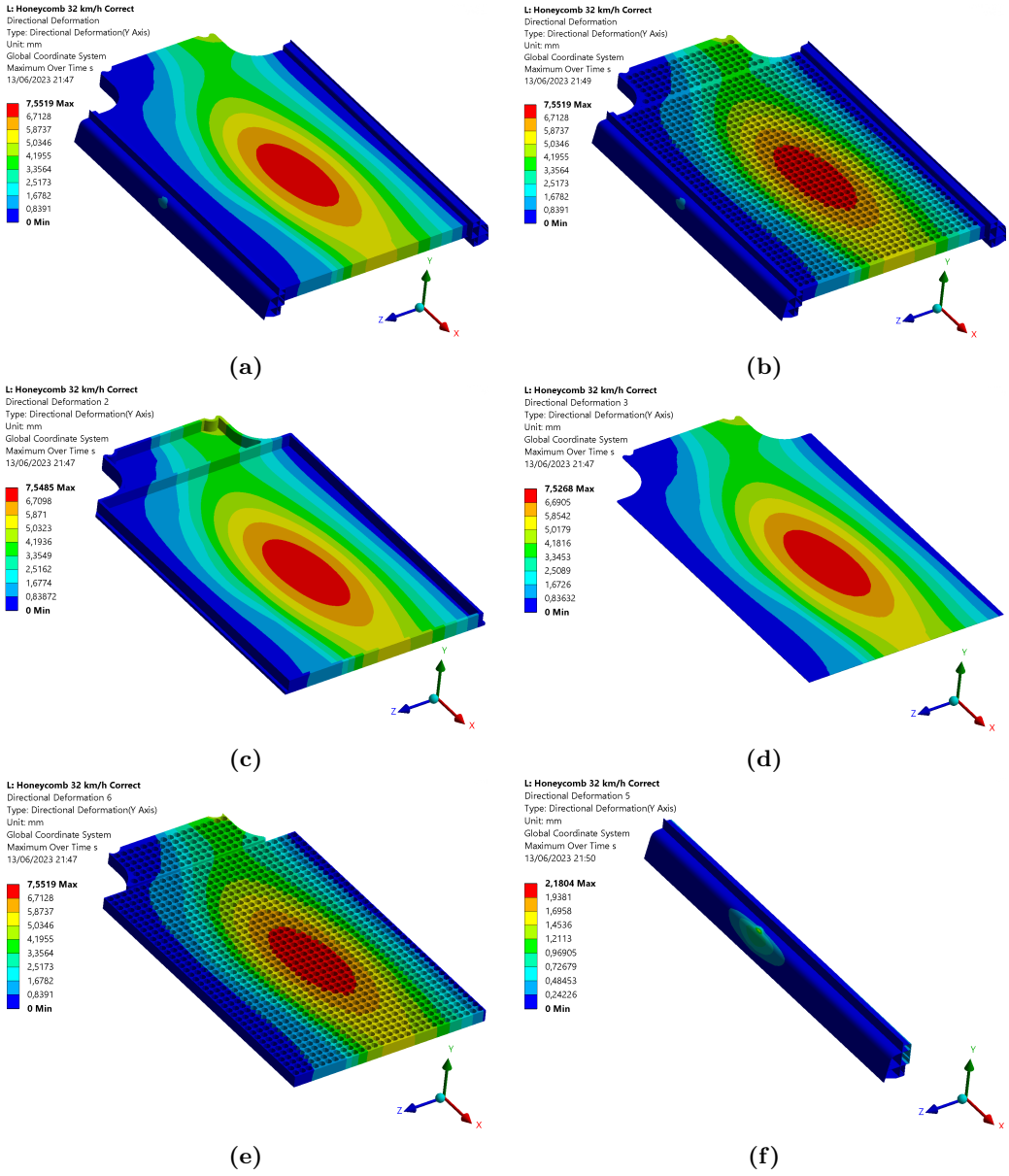


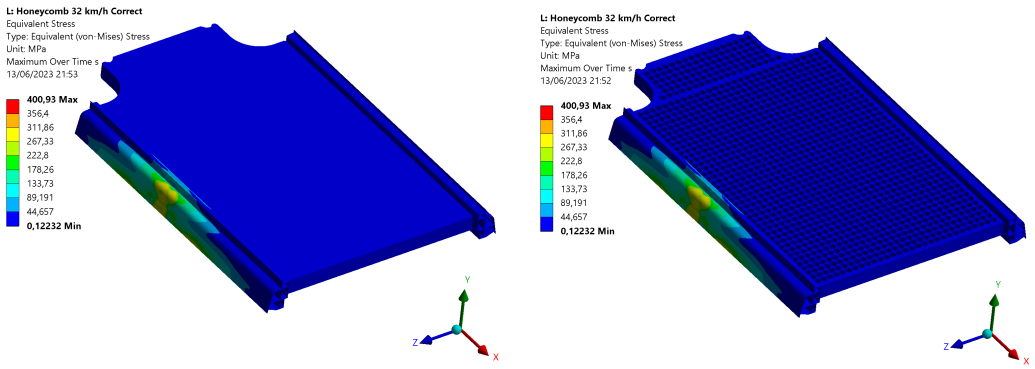
Figure 10.21: Explicit dynamics analysis of Phase 3, at 32 km/h: directional deformation distribution in the y direction at global and component levels (true scale). **(a)** BPE with top cover. **(b)** BPE without top cover. **(c)** Bottom case. **(d)** Top cover. **(e)** Reinforcements. **(f)** Rocker panel.

As was observed in the evaluation of total deformation, the deflection results in y in this structure are similar to those achieved in Phase 2, both in their assortment in the structure and maximum magnitudes for each of the components. The highest deformations found in the BPE structure correspond, once more, to approximately 8 mm, found in the centre of the model. The corresponding value in Phase 1 was approximately 3 mm.

Hence, it can be concluded that the alteration of the internal geometry and material brought by the BPE proposed in this Phase did not significantly influence the total and directional deformations presented by the structure.

10.5.1.2 Equivalent von Mises Stress

As presented for the other stages of this numerical work, the global stress distribution within the whole automotive model can be found in Figure 10.22. The distribution of this same quantity can be found for each relevant component in Figure 10.23



(a) **(b)**

Figure 10.22: Explicit dynamics analysis of Phase 3, at 32 km/h: equivalent von Mises stress (true scale). **(a)** BPE with top cover. **(b)** BPE without top cover.

As observed in the other Phases of this work, the maximum stress emerging in the automotive structure is of around 400 MPa. The rocker panel, directly impacted by the rigid pole, exhibits the highest maximum values of this physical quantity in the model.

The stresses arising in the immediate proximity of the impact region are colossally higher than those found in the remaining assembly, as can be concluded from the evaluation of the global illustrations of this physical quantity. This is, of course, consistent with what has been previously assessed. Hence, as per usual, it is crucial to examine the stress distribution within each component of the BPE. This approach allows for a more comprehensive analysis and a deeper understanding of the stress state in the structure.

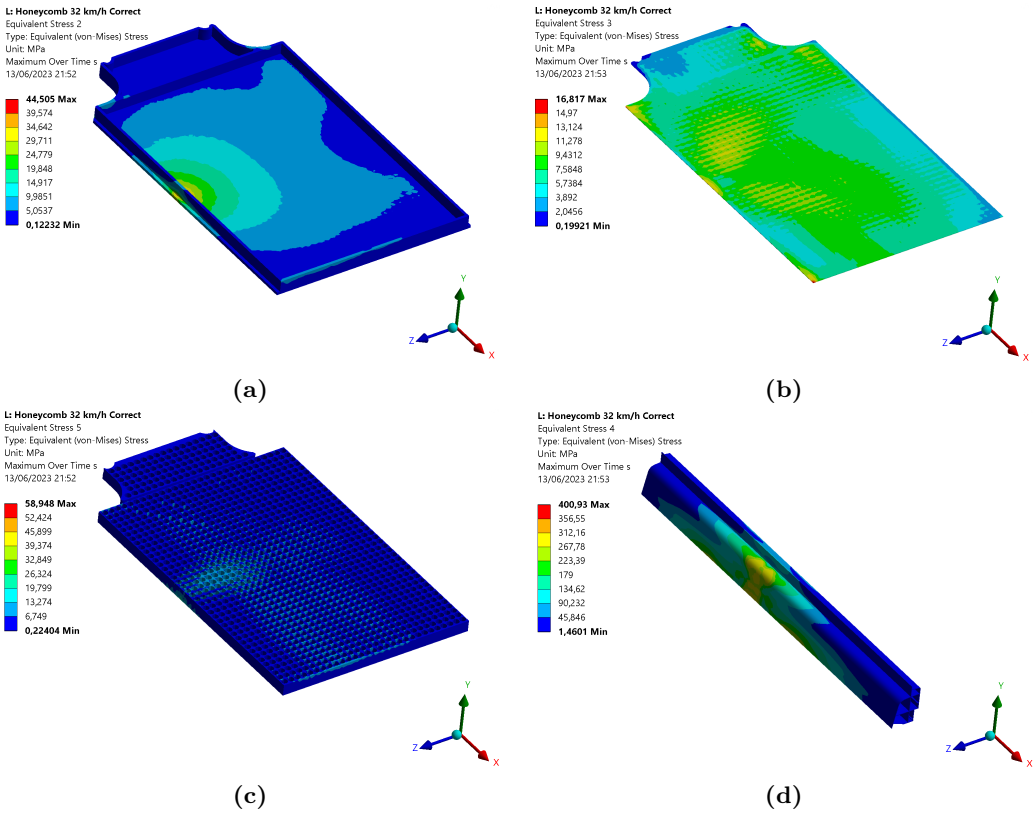


Figure 10.23: Explicit dynamics analysis of Phase 3, at 32 km/h: equivalent von Mises stress (true scale). **(a)** Bottom case. **(b)** Top cover. **(c)** Reinforcements. **(d)** Rocker panel that endures the impact.

The stresses found for each individual component are, once more, identical to those arising in the ABS solution for the same velocity, without many differences resulting from the introduction of the alternative metal foam internal reinforcement. As anticipated, the highest stresses in the BPE are observed in the metal foam component. These stresses have a magnitude of 59 MPa, which is 17 MPa higher than that observed in Phase 2, not constituting an alarming difference.

The extremely localised maximum stresses in the corners of the top cover (that originate from the rigid boundary conditions defined in the model) drop from 22 MPa to 16 MPa, and the maximum magnitude of this quantity remains almost untouchable in the bottom case, in relation to the ABS BPE.

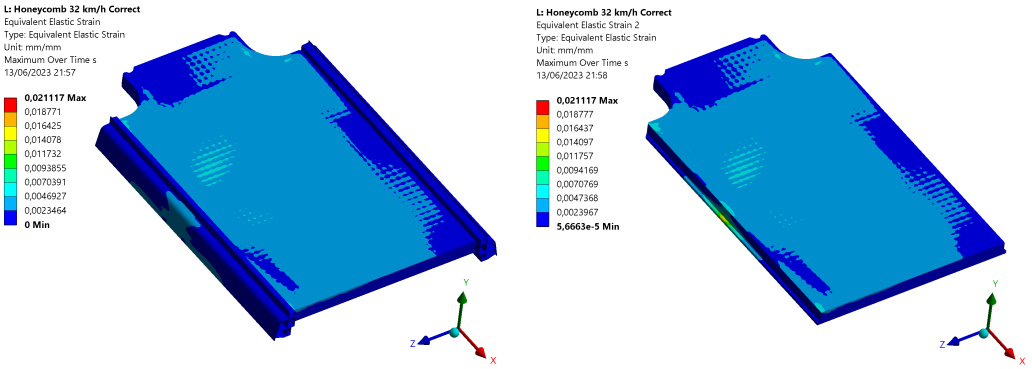
Concerning the corresponding analysis of Phase 1, the obtained values are not as consistent. In the aforesaid Phase, the following stress levels were verified in the BPE components: 97 MPa in the bottom case, 67 MPa in the top cover and 53 MPa. Thus, while the maximum value for this quantity in the internal parts of both BPEs is quite similar, the same cannot be said for the external components, where the highest stresses are far more severe in the current solution.

Finally, in the following subsection, the possibility of the occurrence of plasticization in the BPE assembly arising from the exceedance of the yield strength of the materials assigned to the structure will be assessed when discussing the plastic strains.

10.5.1.3 Equivalent von Mises Strain

The last matter to assess regarding this explicit dynamic analysis are the strains originating in the structure from this simulated side-impact event, both in the elastic and plastic regimes.

In Figure 10.24, the distribution of the equivalent von Mises strains within the overall structure and solely in the BPE components can be found.



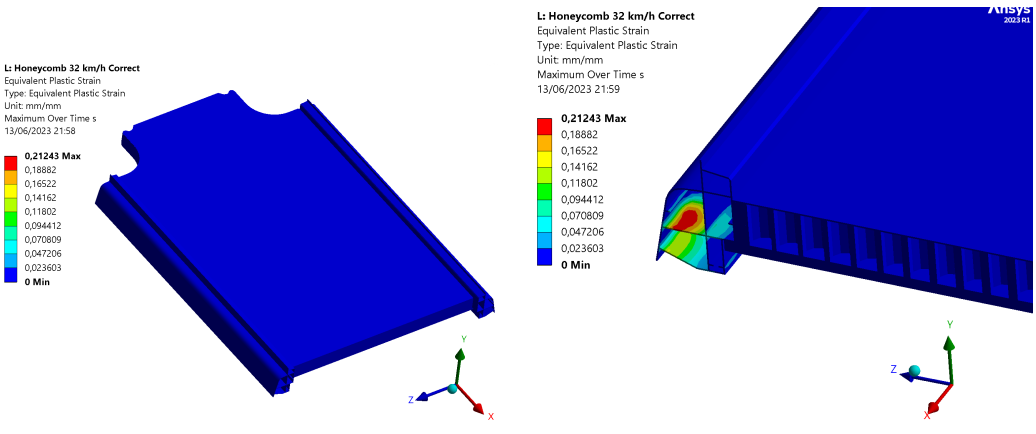
(a) **(b)**

Figure 10.24: Explicit dynamics analysis of Phase 3, at 32 km/h: equivalent von Mises strain (true scale). **(a)** Rocker panels and BPE. **(b)** Exclusively the BPE structure.

As expected, a concentration of elastic strains in the BPE region next to the impact zone of the rocker panel is verified. The maximum value of 0.02 is observed in the BPE in an extremely localised point in the aforesaid region. Overall, excluding this zone almost directly affected by the impact, the rest of the structure presents elastic strains generally below the magnitude of 0.005.

It is worth mentioning that the presence of peaks of this quantity in the corner regions of the BPE results, once again, from the contact settings defined between the rocker panel and the BPE, as well as from possible mesh considerations.

In Figure 10.25, the presence of plastic strains in the automotive assembly is assessed.



(a) **(b)**

Figure 10.25: Explicit dynamics analysis of Phase 3, at 32 km/h: plastic strain (true scale). **(a)** Exterior region of the impacted rocker panel. **(b)** Rocker panel cross-section.

In the aforementioned Figure, the recurrence of highly localised plastic strains resulting

from the compression of the impacted rocker panel during the side impact can be observed. Furthermore, the maximum value of this quantity corresponds to 0.2, which is representative of those in the corresponding analyses of Phases 1 and 2.

The evaluation of the occurrence of yielding within the BPE, since both the ABS and the Al-SiC foams were introduced in the simulation as elastic materials, must be performed indirectly, considering the yield strength of each of those materials.

Recall that the yield strength of the ABS employed in the structure's top cover and bottom case is about 40 MPa. The maximum stress from the simulation concerning the BPE's top cover corresponded to a value of 17 MPa, less than 50% of the yield stress. In the bottom component, however, a maximum stress of 44 MPa is found in a very concentrated point of this part, the rest of it presenting values of this quantity smaller than 34 MPa. Considering this information, it would be pertinent to further evaluate if this point would, in fact, present any permanent deformation and possibly constitute a problem to the mechanical resistance of the structure. For that, however, more data regarding the specific ABS selected to be utilised in the BPE would need to be available.

In the internal body of the BPE, to which a metal foam material with a yield strength of about 8 MPa was assigned, it is possible to observe that a maximum value of stress of 59 MPa is found. Although this value exceeds the material's elastic limit by about 7 times, note that it can also only be found in a particularly confined point of the part. Most of the structure endures stresses with an associated magnitude of far less than 7 MPa. Thus, it was stated for the potentially problematic zone of the bottom case, more investigation should follow to deeply analyse the behaviour of the structure to this impact situation.

Moreover, in the forthcoming explicit analysis, which will involve a significantly higher velocity, the response of the solution will be examined. This comprehensive evaluation will provide a deeper understanding of the material and structural behaviour. It is anticipated that higher stresses will occur in the battery housing, potentially leading to more extensive plastic deformation of the structure over a larger area, which, if verified, has the capacity to compromise the integrity of the BPE certainly.

10.5.2 Side Impact at 100 km/h

The simulation representing the event of a side impact at 100 km/h to the automotive assembly took 470 minutes, about 8 hours, to yield a solution. This is, without a doubt, notably higher than all of the explicit analyses conducted previously.

In each of the three Phases that compose this numerical work, the time it took for the 100 km/h simulations to run was considerably greater than in those where a velocity of 32 km/h was introduced. Furthermore, the utilisation of an increasingly complex geometry at this stage, identically to what was witnessed in the previous explicit analysis, leads to a longer elapsed time for the simulation.

As was done for the six explicit dynamics simulations, Figure 10.26 represents the energy summary of this analysis.

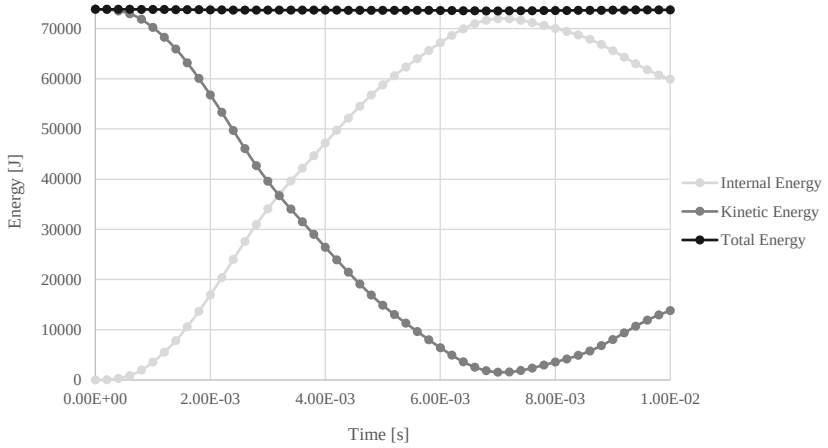


Figure 10.26: Explicit analysis of Phase 3, at 100 km/h: energy summary.

The maximum contact established between the two clashing bodies occurs at the instant $t = 7$ ms for this explicit dynamics simulation. The value of the total energy of the system is uniformly maintained at 74000 J throughout this small time interval right after the impact instant, therefore indicating that the law of conservation of energy is fulfilled by the system. The latter is found to be about ten times higher than the total energy of the simulation at 32 km/h, which is correct and consistent with what has been found in the other Phases of this numerical work.

Comparing this plot to that of Phase 2, it is observed that the instant of maximum compression of the rocker panel occurs now substantially later, at a timestamp more similar to that of Phase 1. However, the system's total energy is in the order of magnitude of Phase 2. The conversion rate between the kinetic and strain energy of the system, prior to and after the instant of maximum contact of the bodies, is, in this case, faster than that verified in the second Phase and slower than the one characterising the corresponding analysis of Phase 1. These discrepancies can be attributed to the unique characteristics of the Honeycomb model, including its distinct geometry and materials.

10.5.2.1 Total and Directional Deformations

To offer a deeper insight into the automotive assembly's response to the impact scenario, Figures 10.27 and 10.28 present visual frames depicting the intrusion of the pole into the rocker panels, along with the corresponding vertical deflection of the BPE, respectively. In order to maintain consistency, a scale factor of 2 was applied.

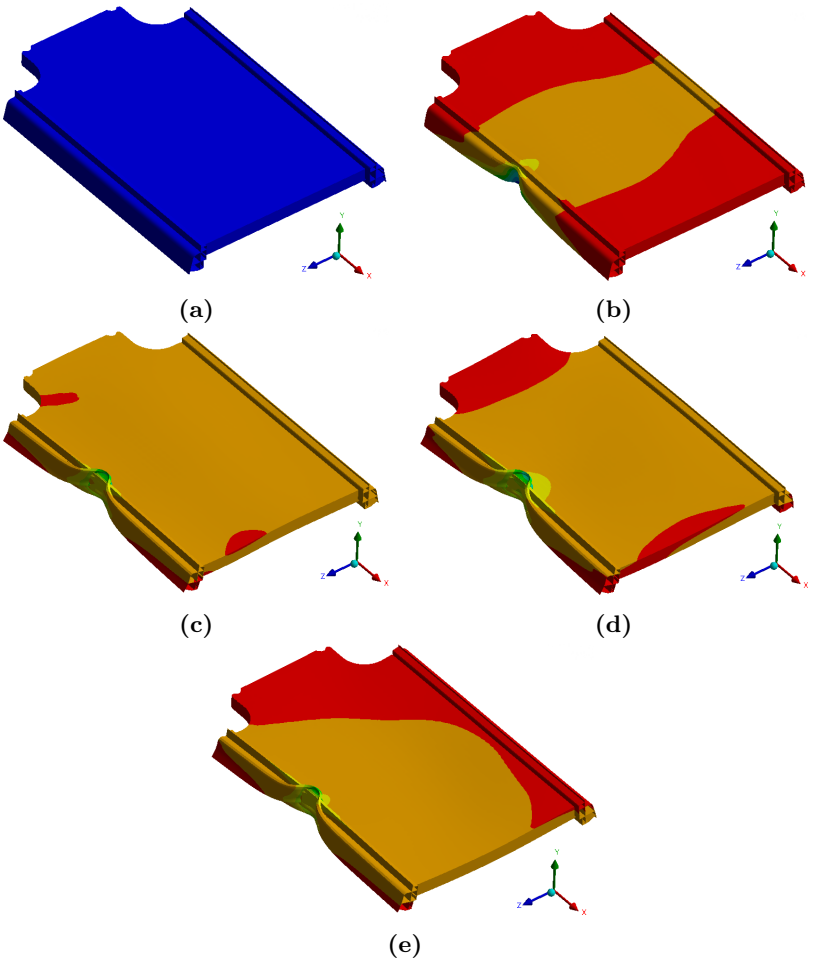


Figure 10.27: Explicit dynamic analysis of Phase 3, at 100 km/h: overview of the deformation of the BPE in time frames (scale of 2). **(a)** $t = 0$ s. **(b)** $t = 2.5e-3$ s. **(c)** $t = 5e-3$ s. **(d)** $t = 7.5e-3$ s. **(e)** $t = 1e-2$ s.

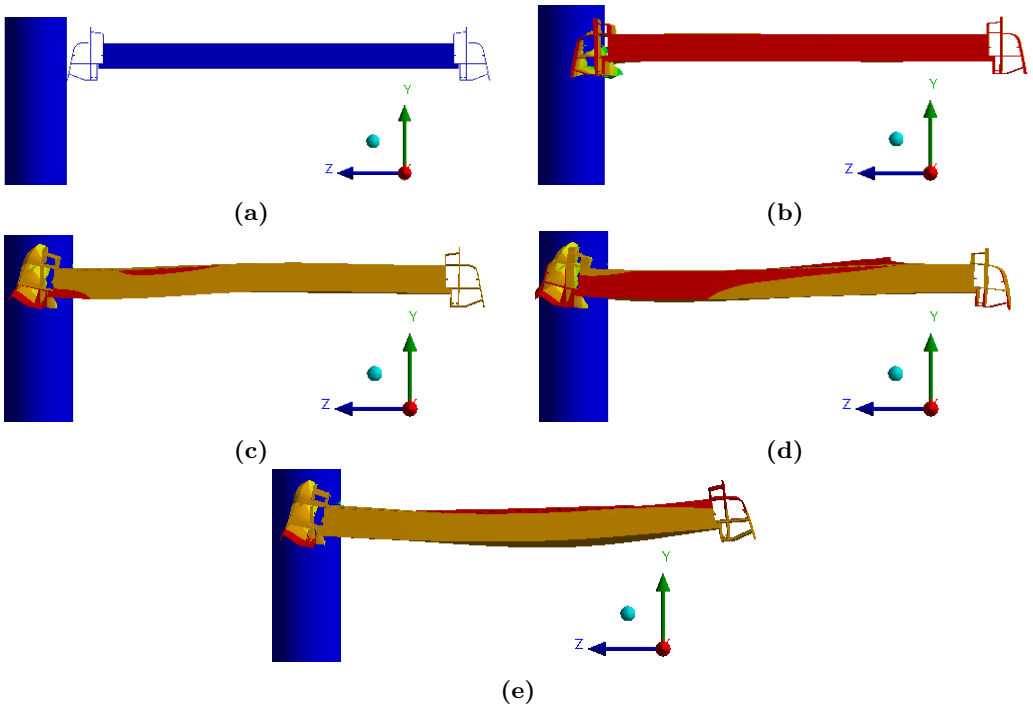
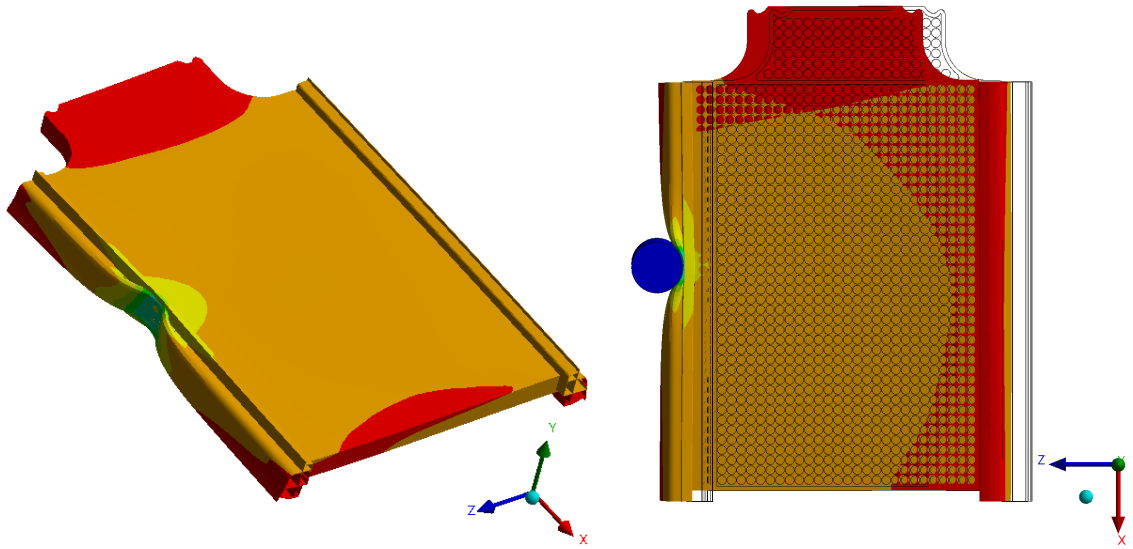


Figure 10.28: Explicit dynamic analysis of Phase 3, at 100 km/h: overview of the deformation of the BPE, in the $z-y$ plane, in time frames (scale of 2). **(a)** $t = 0$ s. **(b)** $t = 2.5e-3$ s. **(c)** $t = 5e-3$ s. **(d)** $t = 7.5e-3$ s. **(e)** $t = 1e-2$ s.

As anticipated from the introduction of triple the velocity of the previous analysis for this simulation, the deformation that the system undergoes is now much more significant. Through the application of the scaling factor of 2, the oscillatory behaviour of the automotive structure in the y axis after the impact with the pole is extremely noticeable. This contrasts considerably with the behaviour of the rigid Al 6061-T6 BPE when subjected to impact at the same velocity.

Comparing the behaviour of the Honeycomb model to the one observed in Figure 9.14 regarding the ABS BPE model (of similar global stiffness), the differences originating from the replacement of the internal skeleton of the BPE with the metal foam part are extremely noticeable at this velocity. In this case, the top cover presents less deflection in y due to the addition of the internal structural body in the BPE, which evidently restricts its oscillation in this direction. As already addressed, the observed deformation would be significantly smaller if the modules were explicitly modelled in the BPEs of Phases 1 and 2.

It is important to recall that the frames presented above are associated with a scale factor of 2. In order to accurately represent the actual behaviour and deformation of the present model from a top view, Figure 10.29 depicts the model in true scale. These are, once more, comparable to the ones presented by the already assessed models. Nevertheless, much smaller vertical deflections of the thin ABS top cover can be observed for this case in comparison to the same component of Phase 2.



(a) **(b)**

Figure 10.29: Explicit dynamics analysis of Phase 3, at 100 km/h: intrusion of the pole into the automotive structure (true scale). **(a)** Global view. **(b)** Deformation in the z direction.

The distribution of total deformations within the model is presented on global and individual levels in Figure 10.30. The examination of the directional deformations of the structure in y will be performed resorting to Figure 10.31.

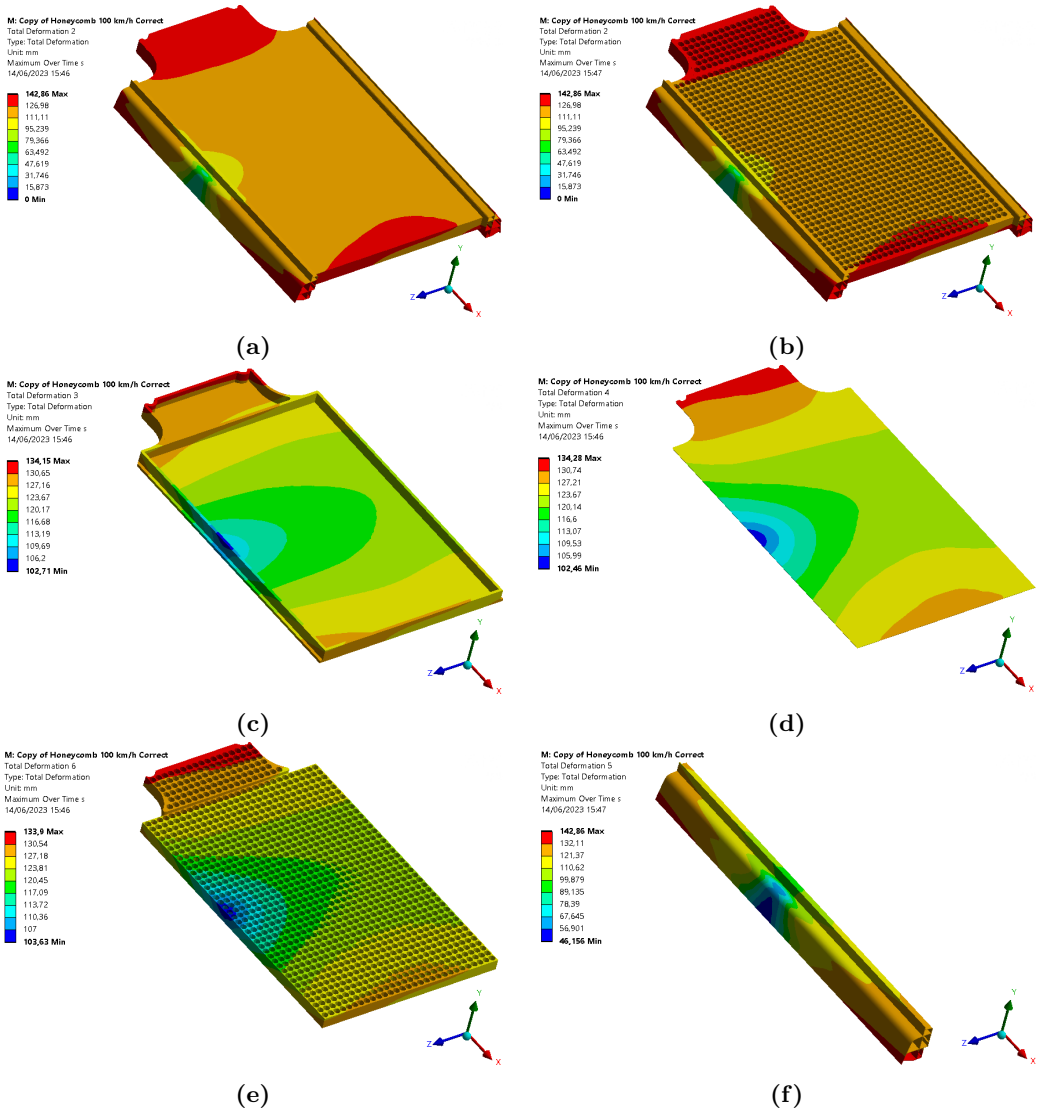


Figure 10.30: Explicit dynamics analysis of Phase 3, at 100 km/h: total deformation distribution at global and component levels (true scale). **(a)** BPE with top cover. **(b)** BPE without top cover. **(c)** Bottom case. **(d)** Top cover. **(e)** Reinforcements. **(f)** Rocker panel.

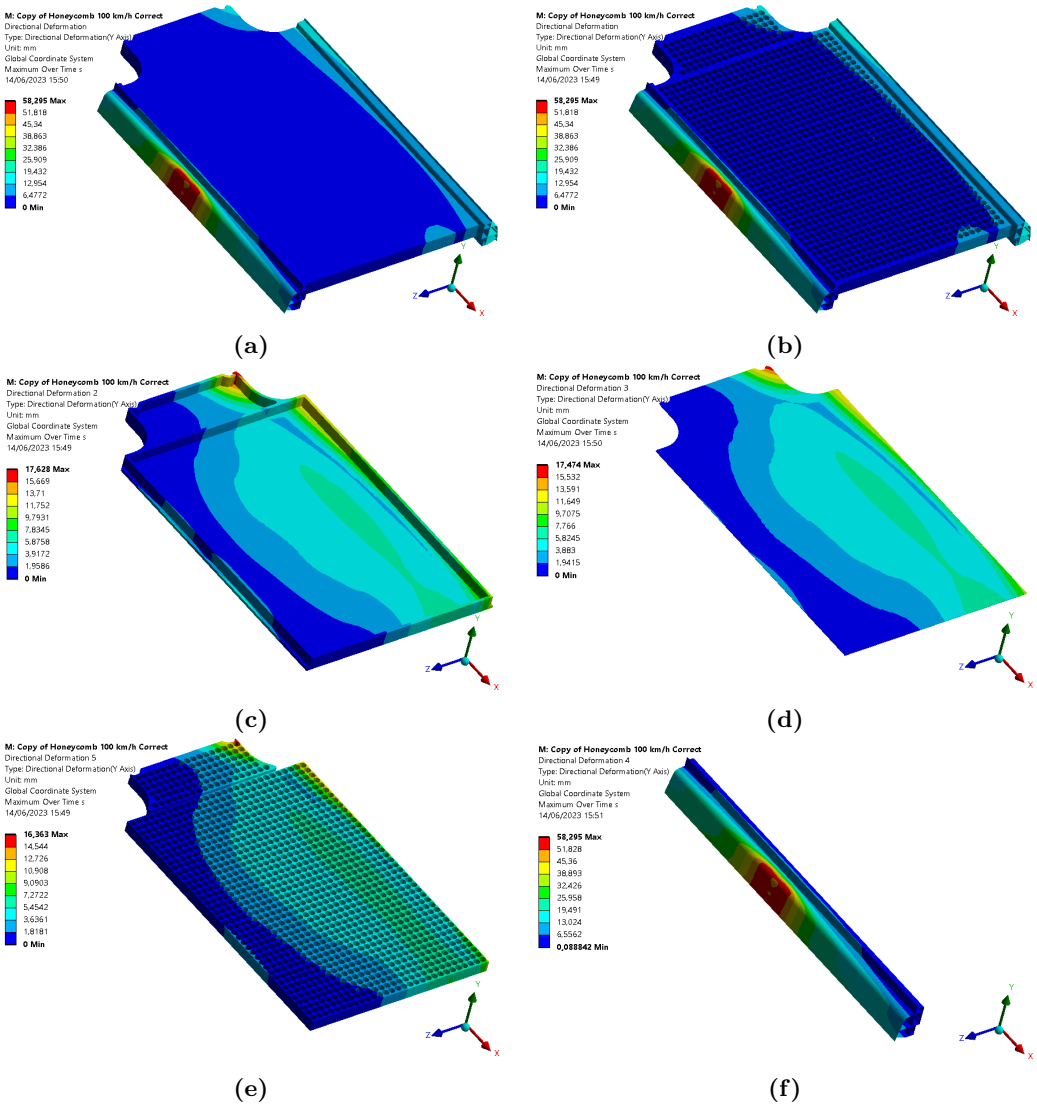


Figure 10.31: Explicit dynamics analysis of Phase 3, at 100 km/h: directional deformation distribution in the y direction at the global level (true scale). **(a)** BPE with top cover. **(b)** BPE without top cover. **(c)** Bottom case. **(d)** Top cover. **(e)** Reinforcements. **(f)** Rocker panel.

Out of all the explicit analyses conducted, this particular case exhibits the highest levels of total deformation in the structure. The structure's highest value of total deformation is found on the directly impacted component and corresponds to 143 mm. Limiting this search to the BPE components only, a maximum value of 134 mm is found, which is a significant quantity if evaluated by itself. Recall, nevertheless, that this value accounts for the rigid body motion of the automotive structure toward the pole, which is not of interest to this analysis.

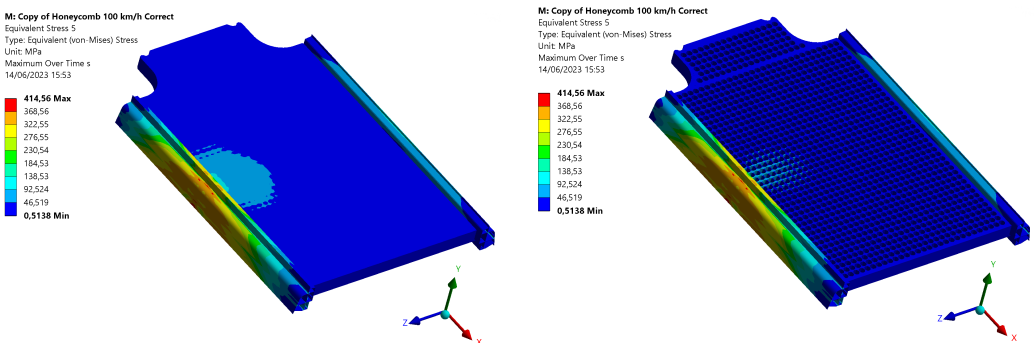
To conduct a more tangible analysis of the deformation, the deflection in the y direction was evaluated, as per usual. This led to more favourable outcomes in comparison to the ABS BPE solution. Indeed, the maximum magnitude of this directional deformation observed in the BPE components is approximately 18 mm across all of the components. In Phase 1, it corresponded to 5 mm, and in Phase 2, to 68 mm. These differences can be attributed to the substantial variation in flexibility between the two BPE solutions in the first comparison. In the second comparison, the discrepancies primarily arise from the inclusion of the metal foam

part, which fills the internal volume of the BPE structure, limiting the vertical deflection of the structure, particularly of the top cover.

10.5.2.2 Equivalent von Mises Stress

This section concerns the discussion of results related to the distribution of the von Mises stresses across the rocker panel and BPE assembly.

In Figure 10.32, the above-mentioned matter is illustrated for the whole structure.



(a) **(b)**

Figure 10.32: Explicit dynamics analysis of Phase 3, at 100 km/h: equivalent von Mises stress (true scale). **(a)** BPE with top cover. **(b)** BPE without top cover.

As anticipated, higher stress values, now reaching 415 MPa, are found in the model compared to those emerging in the simulation at 32 km/h. Moreover, a more evident presence of stresses in the BPE is now observed in the neighbouring regions to the impact zone.

To some extent, the stress levels observed in the six explicit analyses conducted, taking into account various material and geometry combinations, did not exhibit significant differences. In fact, the lowest maximum stress acting on the assembly in these, of about 396 MPa (found in the simulation at 32 km/h in Phase 2) and the highest of 468 MPa (in Phase 1, at 100 km/h). This suggests that logical reasoning and thoughtful evaluation support the alternative BPE solutions proposed in this work.

The stress distribution is now evaluated for each of the relevant individual components of the assembly in Figure 10.33.

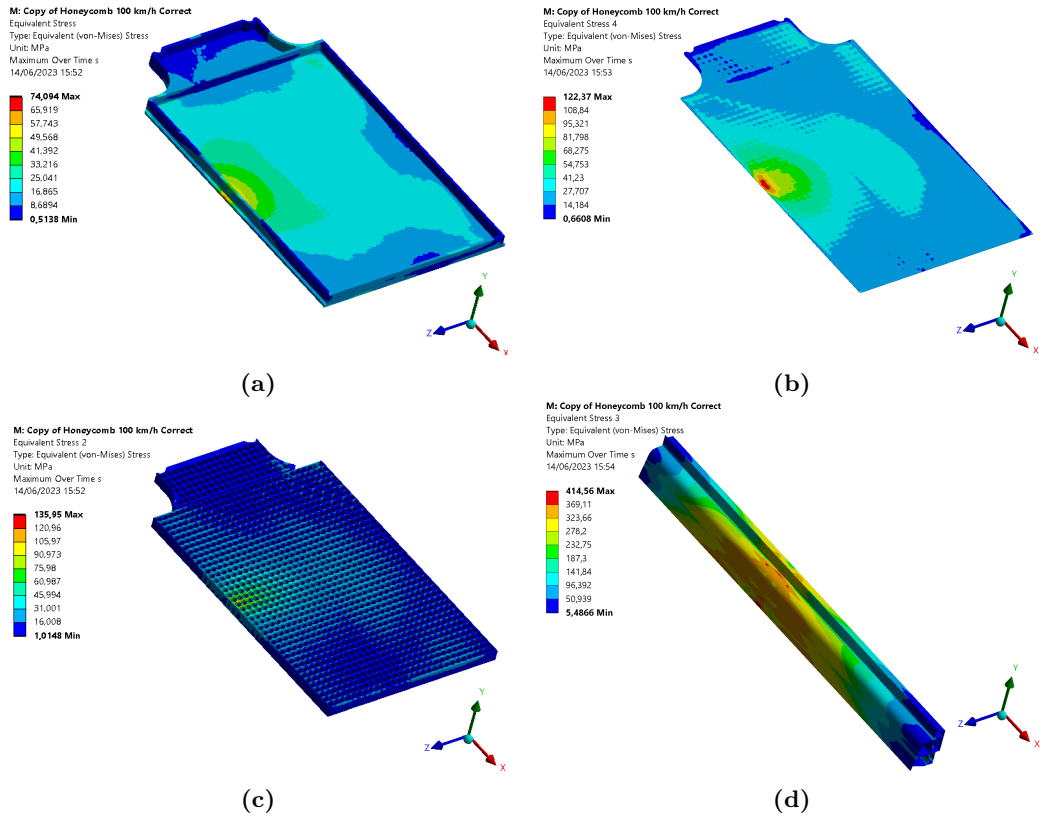
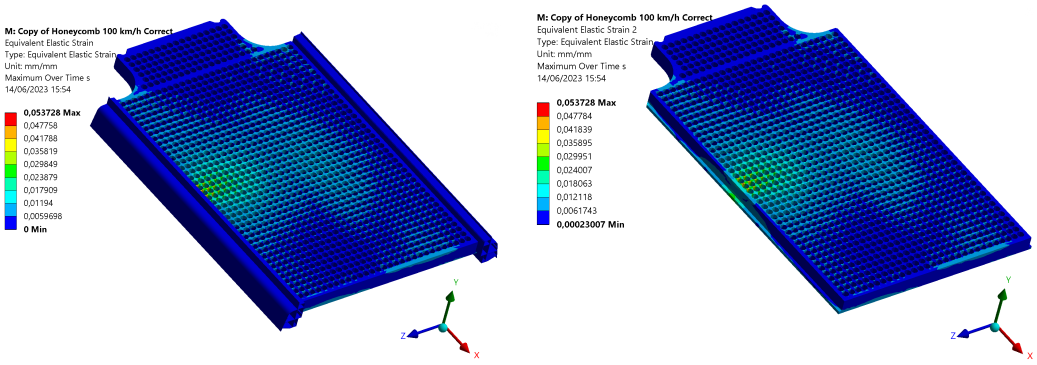


Figure 10.33: Explicit dynamics analysis of Phase 3, at 100 km/h: equivalent von Mises stress (true scale). **(a)** Bottom case. **(b)** Top cover. **(c)** Reinforcements. **(d)** Rocker panel that endures the impact.

The von Mises stresses acting in each of the BPE components achieve their maximum values in the top cover and metal-foam parts, reaching magnitudes of approximately 130 MPa in extremely localised points of both. The highest value of this quantity in the bottom cover is of 74 MPa, in the zone where it endures maximum compression due to the crash. These elevated stress levels, however, are not found across the majority of the span of the components, where significantly lower stresses are mostly found. For example, although the maximum stress value within the Honeycomb model is observed in the internal metal foam part, the majority of regions within this component exhibit stress values below 10 MPa.

10.5.2.3 Equivalent Elastic Strain and Equivalent Plastic Strain

In Figure 10.34, the distribution of the elastic strains is presented for both the global assembly and exclusively for the BPE components.

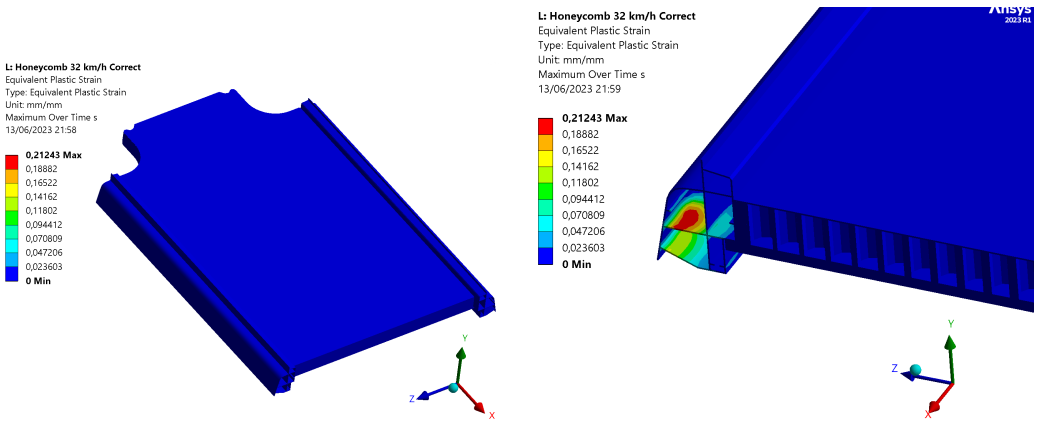


(a) **(b)**

Figure 10.34: Explicit dynamics analysis of Phase 3, at 100 km/h: equivalent von Mises strain (true scale). **(a)** Rocker panels and BPE. **(b)** Exclusively the BPE structure.

Evidently, higher values of this physical quantity are found in relation to the previously assessed explicit simulation. 0.05 corresponds to the maximum magnitude of this quantity in the BPE, in its most stressed zone. Note that this is about ten times higher than the maximum elastic strains found in the corresponding analysis of Phase 1. This was expected since the BPE Honeycomb model is much more flexible than the Al 6061-T6 one, thus preventing increased deformation.

The plastic stresses arising in the assembly are represented in Figure 10.35.



(a) **(b)**

Figure 10.35: Explicit dynamics analysis of Phase 3, at 100 km/h: plastic strain (true scale). **(a)** Exterior region of the impacted rocker panel. **(b)** Rocker panel cross-section.

Once again, due to the limitations associated with introducing both the ABS and the Al-SiC metal foam as elastic materials in the analysis' engineering data, the presence of the plastic strains in the BPE is visually nonexistent. In fact, according to the Figure above, only the rocker panel presents permanent deformation in the immediate proximity of impact of about 0.2.

Considering the yield strengths of both the ABS and metal foam components that constitute the BPE and the values of von Mises stresses found in the battery housing, it is evident that particularly localised yielding will occur in the three components of the BPE. In fact, in the BPE's external components, both in ABS, the yield strength of the material was exceeded by 85% and 205% in the bottom case and top cover, respectively. In the in-

ternal part, this value is even bigger. Notwithstanding, these plastification zones are, once more, extremely localised within the whole span of the structure and may potentially not compromise the integrity of the structural assembly.

In conclusion, it is important to evaluate the implications of plastic strain occurring within these zones and its influence on the integrity of the primary components of the battery pack. While it was not feasible to perform such an evaluation within the scope of this work, potential strategies to enhance the structural strength of the BPE will be proposed in Chapter 11, where a reflection regarding the performed work will be performed.

Chapter 11

Conclusions

With the completion of all the tasks outlined in this study, it is now appropriate to address this work's overall accomplishments and limitations. Likewise, a more detailed analysis of the results obtained for each proposed BPE solution will be presented.

Starting off from the state-of-the-art and theoretical background Chapters, ranging from 1 to 5, owing to the profound level of knowledge demanded for the conduction of this work considering the multitude of fields at hand, extensive and thorough research was executed. In fact, this serves as a bibliographical review of the current state of the industry (concerning BEVs, battery packs and BPEs, and the utilisation of FEM for crashworthiness-related problems) that will be passed on for use in potential projects within CES, as will the methodology presented in the numerical portion of this thesis. In fact, the established workflow, including expertise in various analysis types and best practices, will enhance CES's confidence in analysing new projects for the automotive industry, particularly those related to the subject matter.

From this expository stage, by analysing the state-of-the-art industry solutions for all aspects above-mentioned, it was possible to conclude that the automotive industry, particularly the field concerned with electric mobility, will continue pursuing lightweight design and material solutions in the coming years. This results from the evident commercial advantages brought on by the performance improvements associated with these, as well as the ever-evolving technologies linked to BEVs, batteries, and most other electrical components. Furthermore, adding to the arising challenges and opportunities coupled to these desired solutions that must, evidently, ensure or exceed the mechanical and crash behaviour of the current ones, it appears obvious that sustainability will compose a factor of an increased importance level [109].

In the numerical portion of this study, which was introduced in Chapter 6 and concluded in Chapter 10, the pertinence of conducting FEM analysis for predicting the crashworthiness of vehicles and components was evident. Through firsthand experience, it was observed that FEM simulations can capture and represent the nonlinear and highly complex dynamics of vehicle crash events, offering a cost-effective and time-efficient alternative to physical crash tests. Hence, through the execution of this work, it is now well-understood why this method has proven to be such a valuable tool in product development within the automotive industry [20].

The first step of this numerical work encompassed the obtainment of a CAD that corresponded to the real-life well-positioned BPE solution that served as inspiration for this study. A process of reverse engineering provided the degree of realism sought for the geometry of the latter, which constitutes one of the novelties of this thesis. Subsequently, this

geometry was introduced in a FEM model that was later subjected to a series of carefully chosen analyses as to achieve the objectives of this study.

The simulations performed within the scope of this work in total ran for 26445 minutes, roughly 44 hours. Nevertheless, this value does not account for all the preliminary analyses that did not achieve the intended and realistic results for this specific problem. In fact, particularly with regards to the explicit dynamics analyses, given the inexperience of the analyst, as many as four analyses were simulated prior to the presented ones. In those, the analysis settings were tuned to achieve physically meaningful results. This was the reason for resorting to the Flanagan Belytschko hourglass damping instead of the program-controlled definition and selecting the analysis type as "Low Velocity", for instance. Indeed, in summation, approximately 81 hours of computational work were performed, which heavily contributed to the author's familiarity with the never-before-used FEM software, as well as to consolidate the previously addressed theoretical foundations of the method. In the end, it was possible to retrieve satisfactory and consistent results across all the conducted analyses.

In the case of the Al 6061-T6 BPE model, in Phase 1, notable conclusions could be drawn. As the model was strongly influenced by an existing and well-established real-life solution, the observed behaviour of the model aligned with the previous expectations, given the industry-foundation of the real BPE. Indeed, the evaluation of deformation, stress, strain, and energy in the "Original model" demonstrated that the designed structure could easily withstand the resulting values. This validation provided confidence in the assumptions and setup employed for the model. No significant deformation or stress values were found in the static and transient analyses. The latter, which aims to simulate the Euro NCAP's "Full Width Rigid Barrier" crash test, is particularly meritorious since the harm to the BPE was negligible for the realistic boundary conditions and the considered worst-case scenario conditions applied. This behaviour is expected in most frontal crashes involving BEVs, as the energy of the impact is primarily absorbed and distributed through the frontal deformation zone of the vehicle. Next, regarding the explicit dynamics analyses, by which the Euro NCAP's "Side Pole" crash test is being simulated, the highest values of deformation, strains and stresses are evidently found in the rocker panel closer to the pole, as it is directly impacted. In this component, stresses of about 400 MPa emerged in all the explicit analyses across all Phases. Something else found through the six conducted explicit analyses is the fact that no significant transmission of these quantities to the BPE is verified in the impact simulations at 32 km/h. In comparison, this phenomenon is observed for the ones where a speed of 100 km/h was induced.

Due to the available access to the full explicit characterisation of the aluminium alloy, it was possible to directly visualise the potential presence of permanent deformation in the BPE model in the explicit dynamics analyses of Phase 1. Localised yielding of the structure was only observed in the higher-velocity simulations at a speed of 100 km/h. In contrast, no yielding was found in the simulation at 32 km/h, corresponding to the velocity defined in the crash test technical sheet. This is consistent for two reasons: 1) a side-impact incident is, typically, far more severe to the battery pack than a frontal one due to the nonexistence of the above-mentioned crumple zone in the lateral zones of the energy storage system; 2) the BPE model was subjected to a velocity three times higher than that defined in the regulation's crash test. This increased velocity leads to more significant consequences for the battery housing, identically to the potential outcomes of real-life accidents of this magnitude.

As the industry does not provide specific information regarding the limitations of battery cells in terms of deformation and allowable stress, a direct evaluation of the well-being of the battery's primary components is not possible. Noting, however, that the highest values of all accessed quantities in the BPE are highly localised and, in addition, the modules in

which the cells are arranged often present housings themselves, which constitutes another layer of protection to impact (as do the internal polymeric foam gaps, for instance), it was considered that this BPE solution assured the correct functioning of these cells.

In Phase 2, which involved a BPE solution manufactured in ABS material, a less dense and stiff material, a colossal weight reduction of 57% was achieved in relation to Phase 1. The analysis of various physical quantities, such as deformation, stress, and strain, revealed minimal values and the behaviour of the ABS BPE solution was found to be similar to that observed in Phase 1, in the static, modal, and transient analyses. For the explicit ones, higher values of deformation and lower values of stress were verified in this BPE. This is explained by the fact that ABS is much more flexible than aluminium alloy, efficiently transmitting and distributing the strain energy throughout the battery housing. In the explicit simulation, especially elevated deformation values were found, particularly in the top case of the BPE. Nevertheless, it is possible to speculate that were the module cases physically represented in the model, these maximum values would be relatively smaller than the retrieved ones.

Because of the introduction of the thermoplastic as a linear elastic isotropic material in Ansys® for this analysis, the plastic strains potentially present in the BPE solution cannot be directly visualised. Notwithstanding, relating the stresses that emerged in the two explicit simulations to the yield strength of the material, approximately 40 MPa, it was concluded that the structure might present yielding at some points, particularly for the higher-velocity impact. In the latter, the yield strength was surpassed by 20% in a particular region of the bottom case, which makes sense for the load path emerging in the structure for the defined impact conditions, as well as for the fact that this is the main structural component of the BPE.

In Phase 3, a new BPE model was introduced with a unique honeycomb-like internal geometry, which was manufactured with Al-SiC metal foam. The external components of the battery housing remained in ABS material, leveraging the knowledge gained from Phase 2. These modifications to the BPE design resulted in a mass reduction of 43% in comparison to the "Original model". It is possible to state that the new internal part and material did not induce notorious changes in the behaviour of the structure for any of the analyses conducted, particularly in relation to the ABS BPE of more similar mechanical properties. Like it was done in Phase 2, the Al-SiC was introduced in the program as an exclusively elastic material; therefore, the plastic stains possibly present in the BPE needed to be indirectly assessed. By juxtaposition to the yield strength of the material, about 8 MPa in this case, it was concluded that extremely localised yielding of the internal material could potentially take place in the low-velocity impact and will likely occur in the higher one.

In summation, it is possible to state that tremendous changes were not observed in the three studied models for each of the analyses performed. This is evidently positive since the last two BPE solutions present significant weight reductions compared to the first. Regarding the potential occurrence of yielding in the BPE, nevertheless, it is known that the assessment of the distribution and intensity of plastic strain can, in fact, help the analysts and engineers to identify critical regions that may need reinforcements or design modifications. Note, however, that this plastic quantity alone cannot be used to reach any conclusion regarding the well-being of the battery cells, particularly when some relevant industry information is confidential and when some other protection elements within the interior of the battery pack are not considered. Furthermore, recall that owing to the same data unavailability, average values were introduced for the mechanical properties of the employed ABS and Al-SiC materials. Were real-life specific materials utilised for this study, particularly those positioned in the upper limits of the stiffness and strength ranges of these material classes, the results would be even closer to those obtained in the "Original model".

Considering the achieved results in the three assessed models and assuming that the performance of the solutions may be conditioned when a certain level of speed of the vehicle is reached (higher than the ones of the assessed regulations), some strategies to improve the crashworthiness of the structure while enabling a degree of weight reduction are provided. These may entail:

- Material treatments to improve the properties of the materials assigned to the structure. For instance, material grading, optimising in terms of density and strength the performance of the battery housing components in particular regions, according to their specific requirements.
- A hybrid structure manufactured, for example, in Al 6061-T6 in the external components and ABS in the internal ones.
- The employment of thin ribs localised in the sides of the BPE's external components. This process can also be coupled with topology optimisation.
- A thickness optimisation algorithm to obtain the optimal thickness of the multiple BPE components: increasing the thickness in the most critical regions, and reducing it in the least stressed ones.

The above-mentioned points compose some possible future projects related to this work, as well as different approaches that would have been explored if it was not for the limited time imposed on the duration of this project. In addition to these, the performance of practical tests, simulations including the chassis and BIW of the BEV, and the exploration of more exotic materials (provided with a full explicit characterisation) would be of outstanding worth.

Lastly, in Figure 11.1, a BPE generic optimisation methodology, based on the proposal of novel geometry and material combinations, similar to the procedure followed in this work and based on the findings of the latter, is presented. This may be useful for further works on the currently assessed theme.

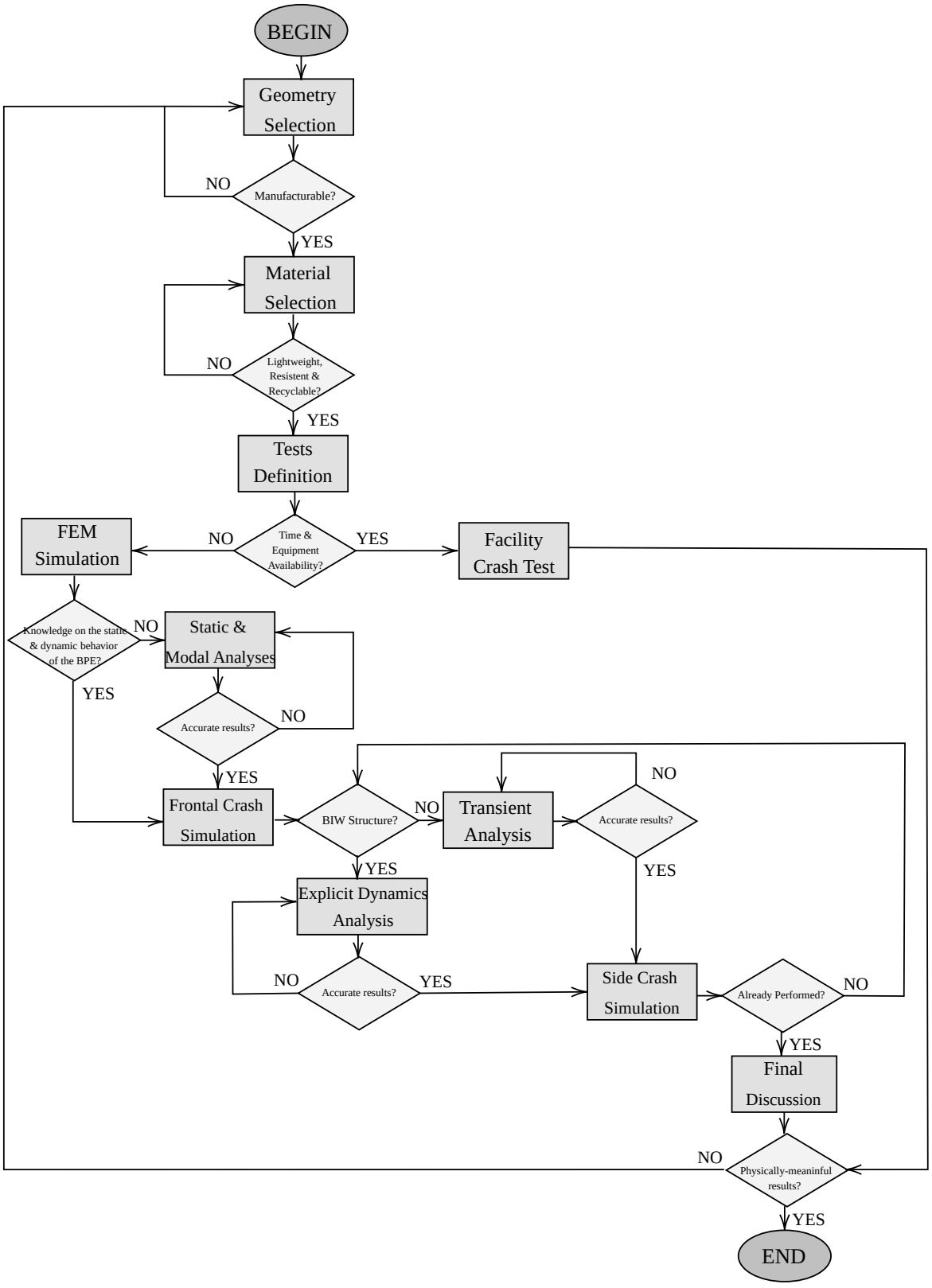


Figure 11.1: BPE optimisation methodology, based on novel material and geometry solutions.

Bibliography

[1] Ioan Szabo, Liviu I. Scurtu, Horia Raboca, and Florin Mariasiu. Topographical optimization of a battery module case that equips an electric vehicle. *Batteries*, 9(2), 2023.

[2] S. Winkler, James Anderson, L. Garza, W. Ruona, R. Vogt, and T. Wallington. Vehicle criteria pollutant (PM, NOx, CO, HCs) emissions: how low should we go? *Climate and Atmospheric Science*, 1, 12 2018.

[3] European Environmental Agency (EEA). Greenhouse gas emissions from transport in Europe, 2020. https://www.iea.org/topics/transport (Accessed on 15-02-2023).

[4] Pius Victor Chombo, Yossapong Laoonual, and Somchai Wongwises. Lessons from the electric vehicle crashworthiness leading to battery fire. *Energies*, 14(16):4802, 2021.

[5] Ahmad Faraz, A. Ambikapathy, Saravanan Thangavel, K. Logavani, and G. Arun Prasad. *Battery Electric Vehicles (BEVs)*, pages 137–160. Springer Singapore, Singapore, 2021.

[6] Jan Fischer-Wolfarth and Gereon Meyer. *Advanced Microsystems for Automotive Applications 2013: Smart Systems for Safe and Green Vehicles*. Springer Science & Business Media, 2013.

[7] Heide Budde-Meiwes, Julia Drillkens, Benedikt Lunz, Jens Muennix, Susanne Rothgang, Julia Kowal, and Dirk Uwe Sauer. A review of current automotive battery technology and future prospects. *Proceedings of the Institution of Mechanical Engineers, Part D: Journal of Automobile Engineering*, 227(5):761–776, 2013.

[8] Miguel Díaz, Jacobo. Costas. *Crashworthiness*, pages 469–486. Springer Berlin Heidelberg, Berlin, Heidelberg, 2020.

[9] Paul Du Bois, Clifford C Chou, Bahig B Fileta, Tawfik B Khalil, Albert I King, Hikmat F Mahmood, Harold J Mertz, Jac Wismans, Priya Prasad, and Jamel E Belwafa. Vehicle crashworthiness and occupant protection.

[10] Yuqing Chen, Yuqiong Kang, Yun Zhao, Li Wang, Jilei Liu, Yanxi Li, Zheng Liang, Xiangming He, Xing Li, Naser Tavajohi, and Baohua Li. A review of lithium-ion battery safety concerns: The issues, strategies, and testing standards. *Journal of Energy Chemistry*, 59:83–99, 2021.

[11] National Highway Traffic Safety Administration (NHTSA). Vehicle electrification standards, 2017. nhtsa.gov/sites/nhtsa.gov/files/documents/12848-lithiumionsafetyhybrids_101217-v3-tag.pdf (Accessed on 20-03-2023).

[12] Bhavya Kotak, Yash Kotak, Katja Brade, Tibor Kubjatko, and Hans-Georg Schweiger. Battery crush test procedures in standards and regulation: Need for augmentation and harmonisation. *Batteries*, 7, 09 2021.

[13] Markus Spielbauer, Philipp Berg, Michael Ringat, Oliver Bohlen, and Andreas Jossen. Experimental study of the impedance behavior of 18650 lithium-ion battery cells under deforming mechanical abuse. *Journal of Energy Storage*, 26:101039, 2019.

[14] Enrique Machuca, Fabian Steger, Johanna Vogt, Katja Brade, and Hans-Georg Schweiger. Availability of lithium-ion batteries from hybrid and electric cars for second use: how to forecast for germany until 2030. *Journal of Electrical Engineering*, 6(3):129–143, 2018.

[15] ISO 6469. Electrically propelled road vehicles — Safety specifications — Part 1: Rechargeable energy storage system (RESS), 2019.

[16] UL 2580. Batteries for Use in Electric Vehicles, 2013.

[17] UN/ECE Regulation No. 100.02. Uniform Provisions Concerning the Approval of Vehicles with Regard to Specific Requirements for the Electric Power Train, 2019.

[18] Lingxi Kong, Chuan Li, Jiuchun Jiang, and Michael G. Pecht. Li-ion battery fire hazards and safety strategies. *Energies*, 11(9), 2018.

[19] Celina Mikolajczak, Michael Kahn, Kevin White, and Richard Thomas Long. *Lithium-ion batteries hazard and use assessment*. Springer Science & Business Media, 2012.

[20] Gulshan Noorsumar, Svitlana Rogovchenko, Kjell G Robbersmyr, and Dmitry Vysochinskiy. Mathematical models for assessment of vehicle crashworthiness: a review. *International journal of crashworthiness*, 27(5):1545–1559, 2022.

[21] Andrzej Erd and Jozef Stoklosa. Energy dependencies in li-ion cells and their influence on the safety of electric motor vehicles and other large battery packs. *Energies*, 13(24), 2020.

[22] Laetitia Theodora Aarts, JJ Commandeur, Ruth Welsh, S Niesen, Markus Lerner, Pete Thomas, Niels Bos, and Ragnhild Johanna Davidse. Study on serious road traffic injuries in the EU. *Luxembourg: Publications Office of the European Union*, 2016.

[23] European New Car Assessment Programme (Euro NCAP). Vehicle electrification standards, 2023. https://www.euroncap.com/en (Accessed on 25-03-2023).

[24] Brian O'Neill. Preventing passenger vehicle occupant injuries by vehicle design—a historical perspective from iihs. *Traffic Injury Prevention*, April 2009.

[25] Society of Automotive Engineers (SAE). Safety protocol for crash tests involving electric and hybrid vehicles, 2017. https://www.sae.org/publications/technical-papers/content/2017-26-0010/ (Accessed on 27-03-2023).

[26] European New Car Assessment Programme (Euro NCAP). Testing of high voltage electric vehicles, 2022. https://cdn.euroncap.com/media/67949/tb-011-testing-of-electric-vehicles-v11.pdf (Accessed on 27-03-2023).

[27] S. Palvoelgyi and P. Stangl. Crashworthiness of the electric G-van. *SAE Technical Paper 900579*, 1990.

[28] Hayata Uwai, Atsushi Isoda, Hideaki Ichikawa, and Nobuhiko Takahashi. Development of body structure for crash safety of the newly developed electric vehicle. In *22nd Enhanced safety of vehicles conference, Washington*, 2011.

[29] EVERSAFE. Recommendations and guidelines for battery crash safety and post-crash safe handling, 2014. https://www.diva-portal.org/smash/get/diva2:1367933/FULLTEXT01.pdf (Accessed on 30-03-2023).

[30] Sean P. O'Malley, David S. Zuby, Matthew Moore, Michael P. Paine, and David Paine. Crashworthiness testing of electric and hybrid vehicles. 2015.

[31] Andrzej Åuchowski. Results of the crash tests of electric cars. *Journal of KONES*, 25(1):483–490, 2018.

[32] Polestar. Polestar 2's first crash test. the crash labs are installing a pool, 2020. https://www.polestar.com/us/news/polestar-2-s-first-crash-test/ (Accessed on 30-03-2023).

[33] G. P. Nikishkov. *Introduction to the Finite Element Method*. University of Aizu, Aizu-Wakamatsu 965-8580, Japan, 2004.

[34] Lovely Sabat and Chinmay Kumar Kundu. *History of Finite Element Method: A Review*. Springer Singapore, Singapore, 2021.

[35] Walter Ritz. Über eine neue methode zur lösung gewisser variationsprobleme der mathematischen physik. *Journal für die reine und angewandte Mathematik*, 135:1–61, 1909.

[36] Iredia Erhunmwun and Usiosefe Ikponmwosa. Review on finite element method. *Journal of Applied Sciences and Environmental Management*, 21:999, 11 2017.

[37] Erwin Stein. *The History of Theoretical, Material and Computational Mechanics-Mathematics Meets Mechanics and Engineering*, volume 1. Springer Science & Business Media, 2013.

[38] B.G. Galerkin. *Rods and Plates: Series in Some Questions of Elastic Equilibrium of Rods and Plates*. National Technical Information Service, 1968.

[39] Alexander Hrennikoff. Solution of problems of elasticity by the framework method. 1941.

[40] Richard Courant. Variational methods for the solution of problems of equilibrium and vibrations. *Bulletin of the American Mathematical Society*, 49:1–23, 1943.

[41] Wing Kam Liu, Shaofan Li, and Harold S Park. Eighty years of the finite element method: Birth, evolution, and future. *Archives of Computational Methods in Engineering*, 29(6):4431–4453, 2022.

[42] J.H. Argyris and S. Kelsey. *Energy Theorems and Structural Analysis: A Generalised Discourse with Applications on Energy Principles of Structural Analysis Including the Effects of Temperature and Non-linear Stress-strain Relations*. Butterworth's scientific publications. Butterworths, 1960.

[43] Morris J. Turner. Stiffness and deflection analysis of complex structures. *Journal of the Aeronautical Sciences*, 23:805–823, 1956.

[44] Junuthula Narasimha Reddy. *Introduction to the Finite Element Method*. McGraw-Hill Education, 2019.

[45] R.W. Clough. *The Finite Element Method in Plane Stress Analysis*. American Society of Civil Engineers, 1960.

[46] O.C. Zienkiewicz and R.L. Taylor. *The Finite Element Method for Solid and Structural Mechanics*. The Finite Element Method. Elsevier Science, 2013.

[47] IA Magomedov, M SU Khaliev, and AA Elmurzaev. Application of finite element analysis in medicine. In *Journal of Physics: Conference Series*, volume 1679, page 022057. IOP Publishing, 2020.

[48] Nathan M Newmark. A method of computation for structural dynamics. *Journal of the engineering mechanics division*, 85(3):67–94, 1959.

[49] E.L. Wilson and R.W. Clough. *Dynamic Response by Step-by-step Matrix Analysis*. 1962.

[50] Hans M. Hilber, Thomas J. R. Hughes, and Robert L. Taylor. Improved numerical dissipation for time integration algorithms in structural dynamics. *Earthquake Engineering & Structural Dynamics*, 5(3):283–292, 1977.

[51] John C. Houbolt. A recurrence matrix solution for the dynamic response of elastic aircraft. *Journal of the Aeronautical Sciences*, 17(9):540–550, 1950.

[52] I. Farhoomand. *Nonlinear Dynamic Stress Analysis of Two-dimensional Solids*. University of California, Berkeley, 1970.

[53] Thomas J.R. Hughes, Karl S. Pister, and Robert L. Taylor. Implicit-explicit finite elements in nonlinear transient analysis. *Computer Methods in Applied Mechanics and Engineering*, 17-18:159–182, 1979.

[54] Thomas J.R. Hughes, Robert L. Taylor, Jerome L. Sackman, Alain Curnier, and Worsak Kanoknukulchai. A finite element method for a class of contact-impact problems. *Computer Methods in Applied Mechanics and Engineering*, 8(3):249–276, 1976.

[55] Giovanni Belingardi and Jovan Obradovic. Design of the impact attenuator for a formula student racing car: Numerical simulation of the impact crash test. *Journal of the Serbian Society for Computational Mechanics*, 4:52–65, 01 2010.

[56] *Influence of Wheels on Frontal Crash Response of Small Lightweight Electric Vehicle*, volume Volume 12: Transportation Systems of *ASME International Mechanical Engineering Congress and Exposition*, 11 2015. V012T15A009.

[57] Lorenzo Berzi, Niccolò Baldanzini, Daniele Barbani, Massimo Delogu, Ramses Sala, and Marco Pierini. Simulation of crash events for an electric four wheel vehicle. *Procedia Structural Integrity*, 12:249–264, 01 2018.

[58] Yuan Chen, Xinying Teresa Cheng, and Kunkun Fu. Multi-material design of a vehicle body considering crashworthiness safety and social effects. *International Journal of Crashworthiness*, 25:1–10, 05 2019.

[59] Z. Li, L. B. Duan, A. G. Cheng, Z. P. Yao, T. Chen, and W. Yao. Lightweight and crashworthiness design of an electric vehicle using a six-sigma robust design optimization method. *Engineering Optimization*, 51(8):1393–1411, 2019.

[60] A. B. Navale, S. P. Chippa, D. A. Chougule, and P. M. Raut. Crashworthiness aspects of electric vehicle design. *International Journal of Crashworthiness*, 26(4):368–387, 2020.

[61] Junyuan Zhang, Linan Ning, Yumin Hao, and Tao Sang. Topology optimization for crashworthiness and structural design of a battery electric vehicle. *International Journal of Crashworthiness*, 26(6):651–660, 2021.

[62] Steven Kirkpatrick, Robert MacNeill, and Robert Bocchieri. Development of an LS-DYNA occupant model for use in crash analyses of roadside safety features. 01 2003.

[63] I Putu Alit Putra. *An Average Female Head-Neck Finite Element Model with Reflexive Neck Muscles*. PhD thesis, 04 2020.

[64] J Kukreja, T Nguyen, T Siegmund, W Chen, W Tsutsui, K Balakrishnan, H Liao, and N Parab. Crash analysis of a conceptual electric vehicle with a damage tolerant battery pack. *Extreme Mechanics Letters*, 9:371–378, 2016.

[65] Roland Uerlich, Karthik Ambikakumari Sanalkumar, Tjorben Bokelmann, and Thomas Vietor. Finite element analysis considering packaging efficiency of innovative battery pack designs. *International Journal of Crashworthiness*, 25(6):664–679, 2020.

[66] Yongjun Pan, Yue Xiong, Wei Dai, Keshan Diao, Lei Wu, and Jinrong Wang. Crush and crash analysis of an automotive battery-pack enclosure for lightweight design. *International Journal of Crashworthiness*, 27:1–10, 10 2020.

[67] Weigao Qiao, Lei Yu, Zhanxi Zhang, and Tongyu Pan. Study on the battery safety in frontal collision of electric vehicle. *Journal of Physics: Conference Series*, 2137(1):012008, dec 2021.

[68] Guanqiang Ruan, Changqing Yu, Xing Hu, and Jing Hua. Simulation and optimization of a new energy vehicle power battery pack structure. *Journal of Theoretical and Applied Mechanics*, 59(4):565–578, 2021.

[69] Michael Alfred Stephenson Biharta, Sigit Puji Santosa, Djarot Widagdo, and Leonardo Gunawan. Design and optimization of lightweight lithium-ion battery protector with 3D auxetic meta structures. *World Electric Vehicle Journal*, 13(7), 2022.

[70] Ashvin Dhoke and Amol Dalavi. A critical review on lightweight design of battery pack enclosure for electric vehicles. *International Journal of Sustainable Transportation Technology*, 4:53–62, 10 2021.

[71] E.P. Popov and T.A. Balan. *Engineering Mechanics of Solids*. Prentice Hall, 1998.

[72] Massachusetts Institute of Technology. *Mecânica dos Sólidos e Resistência dos Materiais*. 2021.

[73] J.F. Silva Gomes. *Mecânica dos Sólidos e Resistência dos Materiais*. Edições INEGI, 2021.

[74] José Dias Rodrigues. Didactic support material for the curricular unit of *Finite Element Method*, 2018.

[75] S.S. Rao. *The Finite Element Method in Engineering*. Elsevier Science, 2010.

[76] Miguel Couto Aires. Elastoplastic analysis of 2D and 3D structural elements using meshless methods, 2019.

[77] Francisco Pires. Didactic support material for the curricular unit of *Finite Element Method*, 2021.

[78] S.P. Venkateshan and Prasanna Swaminathan. Chapter 9 - Numerical integration. In S.P. Venkateshan and Prasanna Swaminathan, editors, *Computational Methods in Engineering*, pages 317–373. Academic Press, Boston, 2014.

[79] Ryan G. McClarren. Chapter 16 - Gauss quadrature and multi-dimensional integrals. In *Computational Nuclear Engineering and Radiological Science Using Python*, pages 287–299. Academic Press, 2018.

[80] ANSYS Inc. *Ansys Explicit Dynamics*. 2021.

[81] Shen Wu and Lei Gu. Introduction to the explicit finite element method for nonlinear transient dynamics. *Introduction to the Explicit Finite Element Method for Nonlinear Transient Dynamics*, 07 2012.

[82] David Benson. *Explicit Finite Element Methods for Large Deformation Problems in Solid Mechanics*. 10 2007.

[83] J. Michael Chang, Tau Tyan, Marwan El-bkaily, James Cheng, Amar Marpu, Qiang Zeng, and Julien Santini. Implicit and explicit finite element methods for crash safety analysis. *SAE Transactions*, 116:1025–1037, 2007.

[84] KT Chau and Ching Chuen Chan. Emerging energy-efficient technologies for hybrid electric vehicles. *Proceedings of the IEEE*, 95(4):821–835, 2007.

[85] Jia Ying Yong, Vigna K Ramachandaramurthy, Kang Miao Tan, and Nadarajah Mithulananthan. A review on the state-of-the-art technologies of electric vehicle, its impacts and prospects. *Renewable and sustainable energy reviews*, 49:365–385, 2015.

[86] Sid-Ali Amamra, Yashraj Tripathy, Anup Barai, Andrew D. Moore, and James Marco. Electric vehicle battery performance investigation based on real world current harmonics. *Energies*, 13(2), 2020.

[87] Kunal Wagh and Pankaj Dhatrak. A review on powertrain subsystems and charging technology in battery electric vehicles: Current and future trends. *Proceedings of the Institution of Mechanical Engineers, Part D: Journal of Automobile Engineering*, 236(4):479–496, 2022.

[88] International Energy Agency (IEA). Improving the sustainability of passenger and freight transport, 2023. https://www.eea.europa.eu/ims/greenhouse-gas-emissions-from-transport (Accessed on 15-02-2023).

[89] IEA. Global EV Outlook 2022.

[90] Wenbo Li, Ruyin Long, Hong Chen, and Jichao Geng. A review of factors influencing consumer intentions to adopt battery electric vehicles. *Renewable and Sustainable Energy Reviews*, 78:318–328, 2017.

[91] European Commission. Zero emission vehicles: first 'Fit for 55' deal will end the sale of new CO2 emitting cars in Europe by 2035, 2022. https://www.iea.org/topics/transport (Accessed on 15-02-2023).

[92] Jonn Axsen, Jennifer TyreeHageman, and Andy Lentz. Lifestyle practices and pro-environmental technology. *Ecological Economics*, 82:64–74, 2012.

[93] European Environmental Agency (EEA). Electric vehicles and the energy sector - impacts on Europe's future emissions, 2021. https://www.eea.europa.eu/publications/electric-vehicles-and-the-energy (Accessed on 15-02-2023).

[94] Adrian König, Lorenzo Nicoletti, Daniel Schröder, Sebastian Wolff, Adam Waclaw, and Markus Lienkamp. An overview of parameter and cost for battery electric vehicles. *World Electric Vehicle Journal*, 12(1):21, 2021.

[95] V. Raja, Ignatius Raja, and Rahul Kavvampally. Advancements in battery technologies of electric vehicle. *Journal of Physics: Conference Series*, 2129:012011, 12 2021.

[96] Jerome Dumortier, Saba Siddiki, Sanya Carley, Joshua Cisney, Rachel M. Krause, Bradley W. Lane, John A. Rupp, and John D. Graham. Effects of providing total cost of ownership information on consumer's intent to purchase a hybrid or plug-in electric vehicle. *Transportation Research Part A: Policy and Practice*, 72:71–86, 2015.

[97] C. Linse and R. Kuhn. 10 - Design of high-voltage battery packs for electric vehicles. In Bruno Scrosati, Jargen Garche, and Werner Tillmetz, editors, *Advances in Battery Technologies for Electric Vehicles*, Woodhead Publishing Series in Energy, pages 245–263. Woodhead Publishing, 2015.

[98] Florian Pampel, Stefan Pischinger, and Moritz Teuber. A systematic comparison of the packing density of battery cell-to-pack concepts at different degrees of implementation. *Results in Engineering*, 13:100310, 2022.

[99] Li Shui, Fangyuan Chen, Akhil Garg, Xiongbin Peng, Nengsheng Bao, and Jian Zhang. Design optimization of battery pack enclosure for electric vehicle. *Structural and Multidisciplinary Optimization*, 58, 07 2018.

[100] Ghassan Zubi, Rodolfo Dufo-López, Monica Carvalho, and Guzay Pasaoglu. The lithium-ion battery: State of the art and future perspectives. *Renewable and Sustainable Energy Reviews*, 89:292–308, 2018.

[101] Jie Deng, Chulheung Bae, Adam Denlinger, and Theodore Miller. Electric vehicles batteries: requirements and challenges. *Joule*, 4(3):511–515, 2020.

[102] Shashank Arora, Weixiang Shen, and Ajay Kapoor. Review of mechanical design and strategic placement technique of a robust battery pack for electric vehicles. *Renewable and Sustainable Energy Reviews*, 60:1319–1331, 2016.

[103] Meher Chaitanya Kamaraju Abhishek Bala. Design and optimization of battery housing in electric cars, 2020.

[104] Ashvin Dhoke and Amol Dalavi. A critical review on lightweight design of battery pack enclosure for electric vehicles. *International Journal of Sustainable Transportation Technology*, 4:53–62, 10 2021.

[105] Iceberg by Caresoft Global. https://iceberg3.caresoftglobal.com/ (Accessed on 20-05-2023).

[106] Society of Automotive Engineers (SAE). Vehicle electrification standards, 2023. https://www.sae.org/standards (Accessed on 20-03-2023).

[107] Joerg Bakker, Christian Sachs, Dietmar Otte, Rainer Justen, Lars Hannawald, and Flavio Friesen. Analysis of fuel cell vehicles equipped with compressed hydrogen storage systems from a road accident safety perspective. *SAE International Journal of Passenger Cars-Mechanical Systems*, 4(2011-01-0545):332–342, 2011.

[108] Andreas Afseth. Aluminum battery enclosure design, 2021. https://www.cargroup.org/wp-content/uploads/2021/02/Aluminum-Battery-Enclosures-Constellium-February-2021-FINAL.pdf (Accessed on 25-04-2023).

[109] Timothy E Lipman and Petra Maier. Advanced materials supply considerations for electric vehicle applications. *MRS Bulletin*, 46(12):1164–1175, 2021.

[110] Vivek Patel, Jeroen De Backer, Henrik Hindsefelt, Mattias Igestrand, Saeed Azimi, Joel Andersson, and Jãrgen Sãll. High speed friction stir welding of AA6063-T6 alloy in lightweight battery trays for ev industry: Influence of tool rotation speeds. *Materials Letters*, 318:132135, 2022.

[111] Ducker Carlisle. 2023 North American light vehicle aluminum content and outlook, April 2023. https://drivealuminum.org/wp-content/uploads/2023/04/Ducker-ATG-2023-Aluminum-Study-Summary-Report-April-2023-Final.pdf (Accessed on 01-05-2023).

[112] K. Kirwan and B.M. Wood. 11 - Recycling of materials in automotive engineering. In Jason Rowe, editor, *Advanced Materials in Automotive Engineering*, pages 299–314. Woodhead Publishing, 2012.

[113] Matthias Hartmann, Martin Roschitz, and Ziad Khalil. Enhanced battery pack for electric vehicle: Noise reduction and increased stiffness. *Materials Science Forum*, 765:818–822, 07 2013.

[114] Sunarto Kaleg and Amin . 1P15S lithium battery pack: Aluminum 5052-0 strength of material analysis and optimization. pages 1–5, 10 2016.

[115] Chen Chen, Fei Xiong, Fengchong Lan, and Songsong Kuang. Crush simulation and optimisation study of power battery pack. *International Journal of Vehicle Safety*, 11(1):37–55, 2019.

[116] A.P. Mouritz. *Introduction to Aerospace Materials*. AIAA education series. American Institute of Aeronautics and Astronautics, 2012.

[117] ANSYS Inc. Ansys GRANTA Edupack software, 2021. https://www.ansys.com/products/materials/granta-edupack (Accessed on 15-05-2023).

[118] José Joaquim da Mota Machado. Impact strength optimization with cohesive zone elements of multi-material bonded structures used in the automotive industry, 2019.

[119] M. Shome and M. Tumuluru. 1 - Introduction to welding and joining of advanced high-strength steels (ahss). In Mahadev Shome and Muralidhar Tumuluru, editors, *Welding and Joining of Advanced High Strength Steels (AHSS)*, pages 1–8. Woodhead Publishing, 2015.

[120] J. Rowe. 1 - Introduction: advanced materials and vehicle lightweighting. In Jason Rowe, editor, *Advanced Materials in Automotive Engineering*, pages 1–4. Woodhead Publishing, 2012.

[121] Yongjun Pan, Yue Xiong, Lei Wu, Keshan Diao, and Wei Guo. Lightweight design of an automotive battery-pack enclosure via advanced high-strength steels and size optimization. *International Journal of Automotive Technology*, 22:1279–1290, 2021.

[122] C Ungureanu, S Das, and I. Jawahir. Life-cycle cost analysis: Aluminum versus steel in passenger cars. *TMS Annual Meeting*, 01 2007.

[123] Christian Schludi and Jürgen Joos. Lightweight and safe composite battery housings. *Lightweight Design worldwide*, 12:44 – 47, 2019.

[124] Carl-Christoph Hãhne, Philipp Blaess, Sergej Ilinzeer, and Patrick Griesbaum. New approach for electric vehicle composite battery housings: Electromagnetic shielding and flame retardancy of pur/up-based sheet moulding compound. *Composites Part A: Applied Science and Manufacturing*, 167:107404, 2023.

[125] Tobias Trautwein, Stefan Henn, and Klemens Rother. Weight spiral adjusting lever in vehicle engineering. *ATZ worldwide eMagazine*, 113:30–35, 05 2011.

[126] Gibson Chirinda and Stephen Matope. The lighter the better: Weight reduction in the automotive industry and its impact on fuel consumption and climate change. pages 520–533, 12 2020.

[127] Pall Kornmayer. Tesla Model X: center underbody, 2023. https://www.pallkornmayer.com/work/model-x-biw (Accessed on 20-04-2023).

[128] Peter Dore Rawlinson. Integration System for a Vehicle Battery Pack, 2014. US Patent 8,833,499 B2. Tesla Motors, Inc.

[129] ANSYS Inc. Ansys Engineering Data: Explicit Materials, 2023. From Equation of State and Strength Properties of Selected Materials D. Steinberg.

[130] ANSYS Inc. LS-DYNA support: Equation of state. https://www.dynasupport.com/howtos/general/equation-of-state (Accessed on 27-05-2023).

[131] William Andrew Publishing. Chapter 18 - Mechanical Fastening. In Michael J. Troughton, editor, *Handbook of Plastics Joining (Second Edition)*, pages 175–201. Boston, second edition edition, 2009.

[132] Ansys Inc. Global mesh controls: Mesh metric, 2023. https://ansyshelp.ansys.com/account/secured?returnurl=/Views/Secured/corp/v231/en/wb_msh/msh_metrics.html?q=mesh%20metrics (Accessed on 20-05-2023).

[133] José Dias Rodrigues. *Apontamentos de Vibrações de Sistemas Mecânicos*. Faculty of Engineering of the University of Porto, DeMec, 2021.

[134] ANSYS Inc. *Ansys Innovation Courses: Modal Analysis*. 2020.

[135] European New Car Assessment Programme (Euro NCAP). Full width rigid barrier, 2015. https://www.euroncap.com/en/vehicle-safety/the-ratings-explained/adult-occupant-protection/frontal-impact/full-width-rigid-barrier/ (Accessed on 25-03-2023).

[136] International Electrotechnical Commission (IEC). International standard IEC 60068-2-27: Environmental testing – part 2-27: Tests – test ea and guidance: Shock, 2008.

[137] Andrew Zimmerman Jones. The physics of a car collision, 2015. https://www.thoughtco.com/what-is-the-physics-of-a-car-collision-2698920 (Accessed on 25-04-2023).

[138] European New Car Assessment Programme (Euro NCAP). Side pole, 2020. https://www.euroncap.com/en/vehicle-safety/the-ratings-explained/adult-occupant-protection/lateral-impact/side-pole/ (Accessed on 25-03-2023).

[139] Ansys Inc. Ansys Learning Hub, 2023. https://www.ansys.com/services/ansys-learning-hub (Accessed on 10-05-2023).

[140] Shen R Wu. Convergence Study on Explicit Finite Element for Crashworthiness Analysis. *SAE Transactions*, pages 527–536, 2006.

[141] ANSYS Inc. *Lesson 4: Energy Balance in Explicit Dynamics*. 2021.

[142] ANSYS Inc. Selecting elements for your analysis, 2018. https://www.mm.bme.hu/ gyebro/files/ans_help_v182/ans_elem/Hlp_E_CH3_Classifications.html (Accessed on 22-05-2023).

[143] Horacio Vieyra Ruiz, Joan Manuel Molina-Romero, Juan de Dios Calderón-Nájera, and Alfredo Santana-Díaz. Engineering, recyclable, and biodegradable plastics in the automotive industry: A review. *Polymers*, 14(16):3412, 2022.

[144] VDOKUMENTS. Etk material curves 20121018, 2022. https://vdocuments.mx/etk-material-curves-20121018.html?page=1 (Accessed on 15-05-2023).

[145] Bisma Parveez, Nur Ayuni Jamal, Hazleen Anuar, Yusilawati Ahmad, Abdul Aabid, and Muneer Baig. Microstructure and mechanical properties of metal foams fabricated via melt foaming and powder metallurgy technique: A review. *Materials*, 15(15):5302, 2022.

[146] Fred Lambert. Tesla unveils new 4680 battery cell: bigger, 6x power, and 5x energy, 2020. https://electrek.co/2020/09/22/tesla-4680-battery-cell-bigger-power-energy/ (Accessed on 20-05-2023).